UNIVERSITÀ DEGLI STUDI DI CAGLIARI

DOTTORATO DI RICERCA
Fisica Nucleare, Subnucleare e Astrofisica
Ciclo XXV

Spectral Comparisons of Neutron Star Low-Mass X-Ray Binaries with Black Hole X-Ray Binaries

Settore scientifico disciplinare di afferenza
FIS/05 Astronomia e Astrofisica

Tesi di dottorato di
Elise EGRON

discussa il 3 Aprile 2013

Relatori: Prof. Luciano BURDERI
Dr. Tiziana DI SALVO

Coordinatore Dottorato: Prof. Paolo RUGGERONE

Esame finale anno accademico 2011-2012

A toi, Maman, ma plus belle Etoile...

Le seul véritable voyage, le seul bain de Jouvence, ce ne serait pas d'aller vers de nouveaux paysages, mais d'avoir d'autres yeux, de voir l'univers avec les yeux d'un autre, de cent autres, de voir les cent univers que chacun d'eux voit, que chacun d'eux est.

A la recherche du temps perdu
Marcel Proust (1871-1922)

Acknowledgements

First of all, I would like to thank my supervisors, *Tiziana Di Salvo* and *Luciano Burderi*, for their guidance and valuable assistance during the three years of my PhD. Thank you so much for allowing me to work on a great subject and for helping me complete this study.

I am extremely thankful to *Joern Wilms* and *Sera Markoff* for organizing the European ITN 215212 "Black Hole Universe" network that funded my research, and for making this great adventure possible.
Thank you so much, *Joern*, for your kindness, for being available whenever I needed your help, and for your hospitality at the observatory of Bamberg during one month. It was a pleasure and an honor to work with your group.
I would like to thank *Jerome Rodriguez* and *Stephane Corbel* for their support and helpful advice since the beginning of my PhD. Thank you very much *Jerome* for your precious comments on my thesis.
Many thanks to my colleagues in the ITN network: *David, Pablo, Yi-Jung, Ivica, Salome, Refiz, Yoon Young, Pieter, Teo, Holger* and *Tao*. It was great to meet all of you, and extremely enriching to have discovered all of your cultures. We have become like a small family, without you, the PhD experiment would never have been the same.

My sincere thanks to the referee of my thesis, *Giorgio Matt*, for his constructive criticism and excellent advice.

Additionally, I thank the great people I met during conferences, workshops, and schools. I will always remember *Malcom Longair* and *Hale Braadt*, with their sparkling eyes full of passion and enthusiasm. Many thanks for your generosity in transmitting so much to the new generation, and for your fantastic books!

Moreover, I would like to thank the people with whom I did my first steps in research during my Master's studies at the Observatory of Paris, and from whom I learnt so much. In particular, thank you *Jacques Le Bourlot, Jean-Michel Martin, Nicole Coudreau, Andrea Zech* at the Observatory of Meudon, and *Sylvain Chaty* at CEA Saclay.

I would like to thank my colleagues at the University and Observatoy of Cagliari. First, thank you so much to post-docs *Alessandro Papitto* and *Alessandro Riggio*, for their availability, help, and constructive discussions about XMM-Newton data analysis.
Many thanks to *Giovanna, Elisa, Vasco, Antonio, Masha, Cristina, Ester, Alberto, Noemi, Sabrina, Valentina, Caterina, Carlo, Andrea, Christian, Amit*; thanks to all of you, my years in wonderful Sardinia have been exceptional! Special thanks to *Marco* who shared my office for more than two years; thank you so much for

Abstract

The study of high-resolution X-ray spectra of neutron star low-mass X-ray binaries (LMXBs) allows the investigation of the innermost parts of the accretion disk and immediate surroundings of the compact object. The weak magnetic field of old neutron stars present in such systems allows the accretion disk to approach very close to the compact object, like in black hole X-ray binaries.

Using data from X-ray satellites such as XMM-Newton, RXTE, and BeppoSAX, I studied the reflection component in two neutron star LMXBs: MXB 1728-34 and 4U 1735-44. I showed that the iron line at $6.4 - 7$ keV is broad and relativistically smeared, as in black hole binary systems and active galactic nuclei. This is compatible with an interpretation where the line is emitted in the innermost part of the accretion disk. Moreover, I studied the changes in the spectral parameters in 4U 1705-44, in both the hard and soft states of the source. I derived physical and geometrical parameters for the system in both states, such as the state of ionization of the disk, the inner radius of the disk, the inclination angle of the system, and the temperature of the electrons composing the corona.

Contents

Part I

Introduction

High energy astrophysics is a relatively new discipline in astronomy that regards the study of high energy processes releasing electromagnetic radiation in X-rays and gamma-rays. The matter present in such environments, like for instance those close to black holes, neutron stars and supernovae, is under extreme physical conditions (extremely hot and extremely energetic), which cannot "yet" be reproduced in laboratories.

Black holes and neutron stars are very exciting and intriguing objects in the Universe, not only because of their compact nature, but also because of their influence on the surrounding matter. The observational evidence for their existence comes from the study of active galactic nuclei (AGN), X-ray binaries, or pulsars. These systems are among the brightest sources in the X-ray sky.

Binary systems are very common since the star formation process involves the collapse and fragmentation of interstellar clouds, favouring the formation of protostars in close proximity to each other. If the system is close enough, a mass transfer can occur, which gives rise to accretion. This process liberates gravitational potential energy, making accreting objects potentially powerful sources of energy.

Black holes and neutron stars in LMXB systems are expected to show similar spectra. Indeed, these compact objects have similar gravitational potentials since the radius of a neutron star is about three Schwarzschild radii, very close to the last stable orbit of material around the neutron star or a black hole of similar mass. Therefore, the accretion flow is expected to be similar in both cases. On the other hand, the discovery of any difference in the behavior of the accretion flow around black holes and neutron stars will prove the existence of event horizons in black holes. The spectral analysis of X-ray photons coming from these systems offers a unique opportunity to understand their physics and investigate their properties.

The main objective of this thesis is to compare X-ray spectra of neutron LMXB systems to those of the much better-known black hole systems, specifically by studying the so-called reflection component in neutron star LMXBs.

The first part is devoted to an introduction to X-ray binary systems, in particular their formation, the role that accretion plays in these systems, and the physical processes occuring in such sources.

The second part concerns the data analysis. I first explain the progression from the detection of photons to the data analysis. Then, I present the work I performed on two LMXB systems containing a neutron star, MXB 1728-34 and 4U 1705-44, and the tests I carried out on the reflection model Xillver.

The third part regards the conclusions about these sources, and a discussion of the comparison between the X-ray spectra of neutron star LMXBs and black hole binaries.

X-ray binary systems

Contents

More than half of all stars in our Galaxy are in binary systems. In a small fraction of these systems, the two stars are close enough to considerably affect the evolution of each other. Binary periods can be extremely different, ranging from a few hours for close binaries to thousands of years [Griffin 1985]. Discovered in the 1960's [Giacconi 1971, Giacconi 1972, Tananbaum 1972], X-ray binaries are among the most luminous objects in the X-ray sky. At present, more than 400 X-ray binaries have been identified.

1.1 Formation and evolution

X-ray binary systems consist of two objects: a compact object (black hole or neutron star) and a companion star, which both orbit the center of mass of the system. The term cataclysmic variables (CVs) is reserved for binary systems composed of a white dwarf and a normal star, where the accretion efficiency is much lower than in X-ray binaries (see [Warner 1995, Hellier 2001] for a review).

In these systems, the matter that leaves the companion star (also called the donor star) is accreted onto the compact object. The X-ray emission originates from the conversion of the gravitational energy of the accreted matter into light, through viscous processes or shocks occuring in the accretion disk. Depending on the mass of the companion star, X-ray binaries are classified as low-mass X-ray binaries or high-mass X-ray binaries (hereafter LMXBs or HMXBs). In the first class, the matter is accreted onto the compact object by Roche lobe overflow via an accretion disk, whereas in the second class, the matter is mainly accreted by a

stellar wind (see Fig 1.1). Several other classifications exist. One of them is based on the X-ray variability, where steady and transient sources constitute two categories. In steady sources, the X-ray emission remains stable whereas in transient sources (XRT), outburst phases are alterned with quiescence phases.
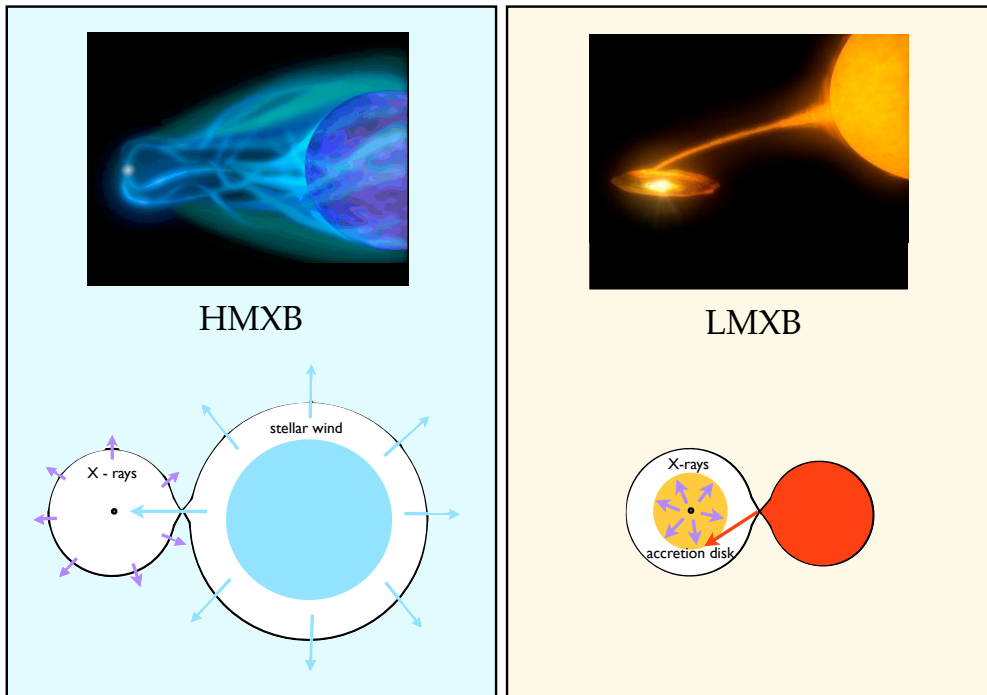
Figure 1.1: Comparison of HMXB and LMXB. Each panel presents an artist's view (top) and a schematic view (bottom) of the systems to illustrate the different accretion modes, respectively by stellar wind and by Roche lobe overflow via an accretion disk (indicated in yellow on the schematic view and seen from the top).

An interesting point related to X-ray binary sources is their evolutionary history, from their origin until their final stages. Different scenarios are proposed and show the difficulty in finding the origin of a system, in particular because of mass exchange between both stars [Karttunen 2007]. Indeed, a star should follow its "normal" evolution, depending only on its inital mass. However, due to the interactions with the other star, the evolution is different.

The presence of a compact object in the binary system means that the progenitor was a massive star that underwent a supernova explosion. During this violent process, a considerable amount of mass is expelled from the system, implying the binary may be disrupted after this event. To maintain the binary system, different explanations are proposed, as discussed by [Verbunt 1993]. Another important point regards the link between X-ray binaries and radio pulsars [Verbunt 1993].

1.1.1   Low mass X-ray binary systems (LMXBs)

At present, 187 LMXBs have been observed in the Galaxy and Magellanic clouds [Liu 2007]. The companion star in such systems is a low-mass star (in general $M \leq 1$ $M_{\odot}$), older than the ones present in HMXBs, and associated with a late-type main-sequence star or a white dwarf. The optical counterparts of LMXBs are intrinsically faint objects.

Formation

An LMXB system can be formed by different processes: a) two stars may be directly gravitationally bound from birth, or b) the system may be formed by capture of a second star.

In the first case, the more massive star evolves faster to reach the giant phase, during which a large portion of its envelope is either transferred to the companion, lost from the binary as the companion spirals in, or lost from the binary by stellar wind. Then, it undergoes a supernova explosion. If less than half of the binary mass is lost in this extremely violent event, the binary survives. In the opposite case, the binary can only survive if a kick velocity from the explosion happens in the right direction. In conclusion, if the binary system survives the supernova explosion, the system remains bound, and contains the new-born compact object and the companion star. Fig. 1.2 illustrates this scenario.

In the second case, a massive star lives alone and becomes a compact object. Because of a high star density environment, a star can be captured (in a close encounter). This happens mainly in globular clusters. However, the vast majority of the binaries which exist in our Galaxy must have been born in a bound state.

Roche lobe overflow

The companion star in an LMXB system is usually a main-sequence star, much smaller than its Roche lobe. The Roche lobe is defined as the quasi-sphere influence within which the matter is gravitationally bound. However, in one of the possible evolutionary tracks of binary systems, the star follows its evolution and expands to fill its Roche lobe when it reaches the red giant phase. The matter exceeding the Roche lobe is no longer gravitationally bound to the star and can be accreted by the compact object through the inner Lagrange point L_1.

In a reference frame in rotation with the binary system, a test mass m in the system is subjected to a force $F = -m\nabla\Phi_R$, which is expressed in terms of the Roche potential Φ_R:

$$\Phi_R(r) = -\frac{GM_1}{|r - r_1|} - \frac{GM_2}{|r - r_2|} - \frac{1}{2}(w \times (r - r_c))^2, \tag{1.1}$$

where r_1 and r_2 are the distances from the centers of masses M_1 and M_2 to the test mass at r, w is the angular velocity of the binary system with respect to an inertial
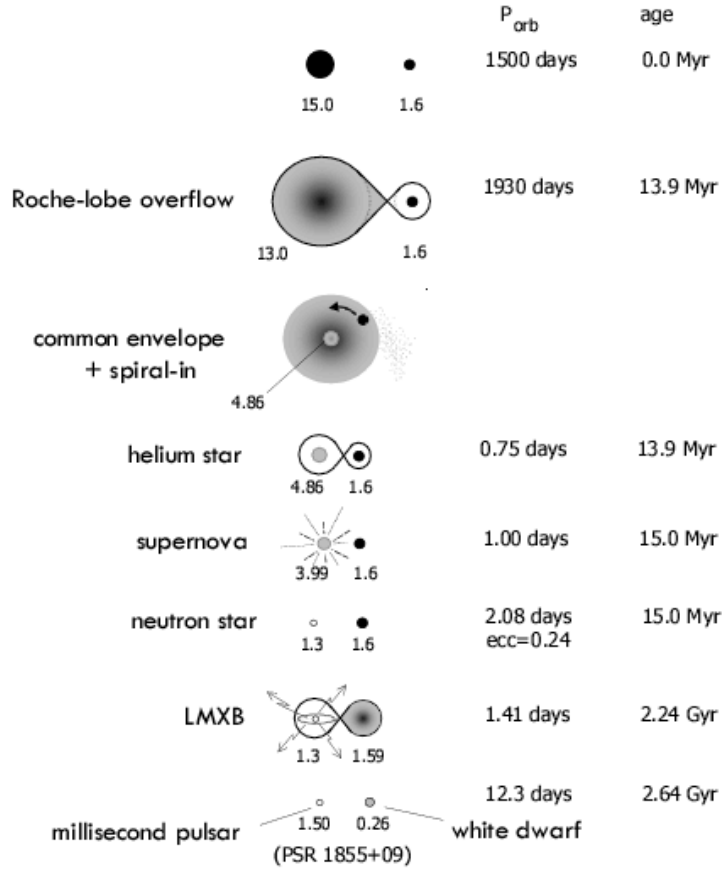
Figure 1.2:   An example of evolution of stars in a binary system leading to the formation of an LMXB. Credit: Tauris & van den Heuvel 2004.

frame, $w = \left(\frac{G(M_1 + M_2)}{a^3}\right)^{1/2}$, and a is the binary separation. This results in equipotential surfaces ($\Phi_R = $ constant) which correspond to the sum of the equipotential surfaces for each star (defined by their gravitational potential) and a centrifugal potential associated with the rotation of the stars about the common center of mass.

The transferred matter has a large amount of angular momentum, therefore forms an accretion disk around the compact object instead of being accreted radially. The masses of the two stars may change considerably with the accretion process. This leads to modifications in the star separation and orbital period. This accretion mode is called Roche Lobe overflow and is typical of LMXBs.

NS LMXB

Neutron stars present in LMXBs have a rather low magnetic field ($B \leq 10^{10}$ G), indicating old compact objects. Many LMXBs show type I X-ray bursts, which are thermonuclear flashes on the neutron star surface. They are interpreted as material
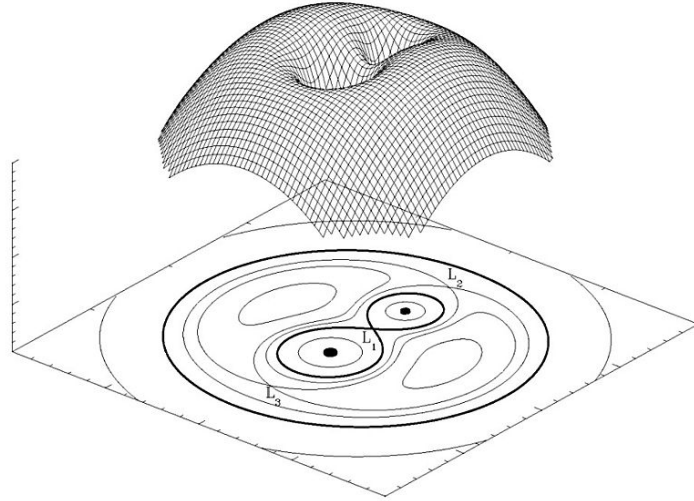
Figure 1.3: Representation of the Roche potential in a binary system (with a mass ratio of 2). Bottom of the figure: equipotential surfaces plotted in the equatorial plane. L1, L2 and L3 are the Lagrange points where the effects of gravity vanish. Mass can flow through the saddle point L1 from one star to its companion when the star fills its Roche lobe. Author: Marc van der Sluys, 2006.

accreted onto the surface that reaches densities and temperatures sufficient for nuclear ignition. The burning is unstable and propagates around the star, resulting in an X-ray burst. The detection of these bursts is proof that the compact object is a neutron star, since a black hole does not have any physical surface.

An interesting point in the evolution of NS LMXBs is that with the transfer of mass, angular momentum spins up the neutron star. When the mass transfer stops, a millisecond pulsar may be detected, resulting in a very old "recycled" neutron star, with low magnetic fields (see Fig. 1.2).

1.1.2 High mass X-ray binary systems (HMXBs)

HMXBs were among the first X-ray sources observed by the UHURU mission in the 1970's. At present, 114 HMXBs have been identified in the Galaxy, and 128 in the Magellanic Clouds [Liu 2006]. HMXBs are binary systems that contain a young and high-mass companion star ($M > 5$ M$_\odot$) of spectral type O or B. These stars generate very strong winds which are captured by the compact object orbiting the massive star and converted into X-ray emission (e.g., Vela X-1 [Nagase 1986]). Wind accretion yields to mass-loss rate of $\sim 10^{-4}-10^{-6}$ M$_\odot$/yr. Roche lobe overflow may represent a small fraction of accretion in addition to the accretion due to wind, however it cannot be the only accretion process since it becomes unstable after $\sim 10^5$ years if the ratio between the mass of the compact object and the mass of the companion star is greater than unity [Lewin 1983]. This would lead to the inspiral

of the compact object into the massive star. Fig 1.4 shows a possible scenario for the formation of an HMXB system.

HMXBs can be divided into two subgroups: Be/X-ray binaries and SG/X-ray binaries. In the first group, the companion star is a Be star i.e. a massive star on the main sequence (type V), whereas in the second one, it is an evolved supergiant (SG) O or B star.
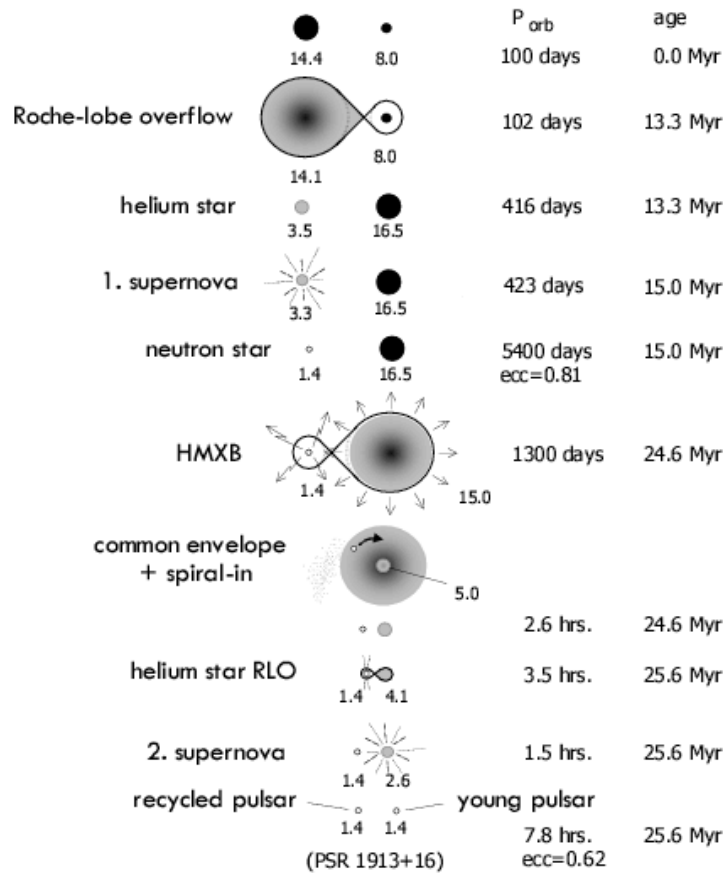
Figure 1.4: An example of star evolution in a binary system leading to the formation of an HMXB. Credit: Tauris & van den Heuvel 2004.

Be/X-ray binaries

A large fraction of X-ray binaries (about 60% of HMXBs) belongs to the Be/X-ray binary systems, in which the donor is a Be star and the compact object is a neutron star (see [Reig 2011] for a review). These systems may present very eccentric orbits, leading to transient behavior as the neutron star moves closer or farther away from its orbital companion. Their X-ray activity originates from a disk of material surrounding the equator of the rapidly-rotating Be star.

HMXB X-ray pulsars

HMXBs are young systems, since the life of an OB star is short. If the compact object is a neutron star with high magnetic fields ($B \geq 10^{10}$ G) (a newly-born neutron star keeps a large fraction of the magnetic field from its progenitor star), the material will fall onto the magnetic poles [Lewin 1995]. If the magnetic and rotation axes are misaligned, X-ray pulsations can be observed when the beamed emission crosses the line of sight of the observer. The majority of HMXBs are X-ray pulsars, most notably Centaurus X-3 and Vela X-1. The evolution of an HMXB X-ray pulsar can then lead to the formation of a double neutron star system, and possibly a double pulsar system (PSR J0737-3039 [Burgay 2003, Lyne 2004]), when the companion star undergoes a supernova explosion (see Fig 1.4). The final evolution of this system is the collapse of the two neutron stars into a single object (probably a black hole), from which gravitational waves may be detectable.

1.2 Compact objects

During its life, a star is in equilibrium between its gravitation and thermal pressure of gas. The main source of energy arises from nuclear fusion processes in the central regions. The more massive a star, the more rapid its life, and the heavier the elements synthesized by different nuclear reactions (H, He, C, Ne, O, Si, Fe). When thermonuclear reactions are no longer possible because of the lack of nuclear fuel, the gravitational collapse is inevitable since no force can oppose it. This results in the formation of a compact object. Compact objects represent the last stage of the life of a star, their nature depending on the initial mass of the star.

Defined by a mass confined to an extremely small size, compact objects are classified into three categories: white dwarf, neutron star, and black hole, by order of increasing compactness. The ratio M/R of an object increases with its compactness, which can be calculated by the compactness parameter $R_{\rm Sch}/R$, where $R_{\rm Sch}$ is the Schwarzschild radius defined as

$$R_{\rm Sch} = \frac{2\,GM}{c^2} = 3\left(\frac{M}{M_\odot}\right)\,{\rm km}. \tag{1.2}$$

This consists in comparing the radius of an object with that of a static black hole of the same mass. This parameter is also called the relativity parameter since it shows the importance of relativistic effects for an object.

The physics of these objects is completely different from what exists on Earth. They represent invaluable laboratories for studying the behavior of matter under extreme conditions. In white dwarfs and neutron stars, the density is so high that formulae for classical gases are not appropriate anymore. These stars are held up by electron and neutron degeneracy pressure, respectively, which counterbalances gravity. As far as black holes are concerned, they are observed indirectly at different scales by the motion of the matter in their vicinity and represent the most exotic objects in the Universe, since no force can support their gravity.

In the following sections, only neutron stars and black holes are being discussed since this work is about X-ray binaries. However Table 1.1 presents a comparison of the main characterisitics of compact objects, including also white dwarfs.

Table 1.1: Main characteristics of typical white dwarfs, neutron stars and stellar-mass black holes. Note: "Counterbal. of self-grav." means "Counterbalance of self-gravity" and "deg. press." means "degeneracy pressure".

	White Dwarf	**Neutron Star**	**Black hole**
Progenitor Mass ($M_\odot$)	$0.1 - 8$	$8 - 25$	≥ 25
End stage of star	Red giant	Supernova	Supernova
Mass M ($M_\odot$)	$0.1 - 1.4$	$1 - 3$	≥ 3
Radius R (km)	$10^4 \sim$ Earth	10	R_{Sch}
Density ρ (kg m^{-3})	10^{9-10}	10^{18}	-
Compactness param.	10^{-4}	$0.2 - 0.4$	1
Counterbal. of self-grav.	electron deg. press.	neutron deg. press.	-

1.2.1 Neutron stars

Neutron stars are some of the densest objects known in the Universe. They exhibit conditions and phenomena not observed elsewhere (such as hyperon, deconfined quark matter, superfluidity, and superconductivity), and contain matter of supranuclear density in their interior with most likely a large fraction of neutrons. These relativistic objects represent ideal astrophysical laboratories for testing theories of dense matter physics, and provide connections among nuclear physics, particle physics and astrophysics.

With typical masses $M \sim 1.4\,M_\odot$ and radii $R \sim 10$ km, neutron stars possess an enormous gravitational energy E_{grav},

$$E_{\text{grav}} \sim GM^2/R \sim 0.2\,Mc^2, \tag{1.3}$$

where G is the gravitational constant. Their mass being close to the solar mass for a radius $\sim 10^5$ times smaller than the solar radius. Their mean mass density is

$$\rho = 3M/(4\pi R^3) \sim 6 \times 10^{17}\,\text{kg}\,\text{m}^{-3} \sim 5\,\rho_{\text{n}}, \tag{1.4}$$

where ρ_{n} is the mass density of nucleon matter in heavy atomic nuclei:

$$\rho_{\text{n}} = \frac{m_{\text{n}}}{\frac{4}{3}\pi r_{\text{n}}^3} = 1.2 \times 10^{17}\,\text{kg}\,\text{m}^{-3}, \tag{1.5}$$

with r_{n} and m_{n} the radius and mass of a neutron. The central density of neutron stars is even larger, reaching $(10 - 25)\rho_{\text{n}}$.

The gravity of a neutron star is so large that free electrons are forced to combine with the protons in the nuclei of atoms to form neutrons through the inverse beta decay process:

$$p + e^- \rightarrow n + \nu_e. \tag{1.6}$$

Generated mainly in the neutron star core by the direct Urca processes, neutrinos carry away energy and provide an efficient way to cool neutron stars.

Additionally, neutron stars show a variety of temperatures and magnetic fields, which depend on their age. Young neutron stars can reach temperatures and magnetic fields higher than 10^{10} K and 10^{15} G, respectively, whereas old neutron stars have generally much lower values of the order of $T \sim 10^7$ K and $B \sim 10^8$ G.

The following sections are devoted to the formation, discovery, internal composition, and mass-radius relations of neutron stars.

Formation of a NS

A neutron star can be obtained by two different scenarios : 1) the end of a massive star or 2) a white dwarf with a mass that exceeds the Chandrasekhar limit.

In the first case, the neutron star corresponds to the final product of stellar evolution. When a massive star is at the stage of giant or supergiant, it eventually exhausts the nuclear fuel in its core. It follows that the core undergoes gravitational collapse and becomes a neutron star, while the outer layers are blown away by an expanding shock wave, producing supernova remnants. The whole event is usually referred to as a type-II supernova explosion (see, e.g. [Imshennik 1988, Arnett 1996] and references therein).

In the second case, the neutron star is formed via accretion-induced collapse of an accreting white dwarf in a binary system. During the course of mass transfer, the white dwarf mass reaches the Chandrasekhar limit ($M_{\rm Ch} = 1.4$ $M_\odot$), which constitutes the critical mass above which the star is gravitationally unstable, and collapses to form a neutron star [Bhattacharya 1991].

Discovery and evidence for NSs

One year after the discovery of the neutron by Sir James Chadwick, the existence of neutron stars was proposed by Walter Baade and Fritz Zwicky in 1934. They also suggested that supernovae could be at the origin of these compact stars [Baade 1934].

Scorpius X-1 was the first X-ray source ever detected outside the Solar System. Discovered in 1962, it was latter classified as a high-luminosity LMXB containing a neutron star with a low magnetic field. It constitutes the first detection of a system with a neutron star, although the presence of the compact object in this system has not yet been identified.

The actual discovery of neutron stars was performed through the detection of pulsars, which are highly-rotating, magnetized neutron stars. In 1967, Jocelyn Bell discovered the first radio pulses from isolated radio pulsars [Hewish 1968]. The pulses are assumed to originate from beams of radio emission emitted along the

magnetic axis, which is misaligned with respect to the rotation axis (see Fig 1.5).
The radio beam shows a behavior similar to a lighthouse beam that an observer
on Earth can detect as brief and regularly-spaced pulses of radio emission. One
year later, the discovery of two young pulsars in the Crab Nebula and in the Vela
supernova remnant proved that neutron stars were formed in supernova explosions.
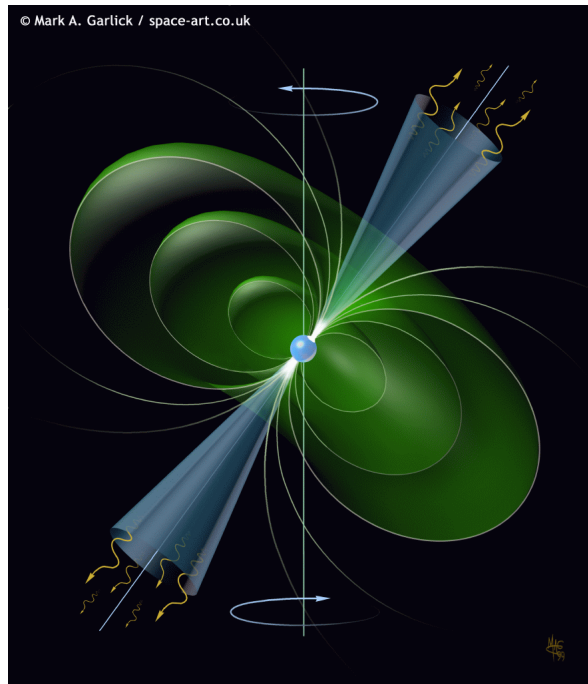
Figure 1.5: Illustration of a pulsar. The magnetic axis is inclined with respect to
the rotational axis. The pulsar acts like a lighthouse becoming visible when the
beam intersects the line of sight of the observer.

Then in 1971, another important event happened: the first evidence for the
presence of a neutron star in a binary system (such as Centaurus X-1) came using the
Uhuru X-ray observatory [Giacconi 1971]. The period of X-ray pulsations showed
sinusoidal variations, which suggests that the sources are members of accreting X-
ray binary systems. The changes in the period of the pulses are due to the Doppler
shift of the X-ray pulses in the binary orbit. In 1975, a binary system containing two
neutron stars, of which one is a pulsar, was detected by [Hulse 1975]. This binary
pulsar, known as PSR B1913+16, can be used for very sensitive tests of general
relativity. In 1982, [Backer 1982] observed a millisecond pulsar (B1937+21) for the
first time. These objects show very stable pulse periods and weak magnetic fields.
They are old neutron stars which are said to be "recycled" following the accretion
of the matter from a companion star. In 2003, [Burgay 2003] discovered an amazing
system, the double pulsar PSR J0737-3039 (see also [Lyne 2004]).

Consequently, neutron stars have been found to be multiwavelength emitters.
They are now observed in radio, infrared, optical, ultraviolet [Mignani 2011], X-ray

and gamma-ray spectral bands, but also emit high-energy particles, neutrinos and gravitational waves. They can be detected as isolated neutron stars (radio pulsars, magnetars, compact central objects in supernova remnants "CCOs"), or in binary systems, the companion star being either a non-degenerate star, a white dwarf or another neutron star.

Equation of state and structure

The observation of neutron stars offers the unique opportunity to test theories of matter under extreme physical conditions. To determine the structure of these exotic objects, one needs to understand the relations between pressure and density at different stages in the neutron star interior. These relations constitute the so-called equations of state (EOS). Many aspects of these equations are discussed in [Shapiro 1983] and more recently in [Haensel 2007].

Since neutron stars are mainly composed of strongly degenerate fermions (neutrons, protons, electrons), the temperature dependence is mostly negligible and the EOS can be calculated at $T = 0$. The methods employed to calculate the EOS are different from the neutron star surface to the center. Atomic structure and plasma theories are used for surface layers, whereas nuclear theory combined with plasma physics in very exotic density-temperature regimes are required in deeper layers of the neutron star crust. The core, where the composition of matter is largely unknown, necessitates the many-body theory of dense strongly-interacting systems, together with the physics of strong interactions of elementary particles. However, the associated EOS remain strongly unconstrained, and this constitutes the main mystery regarding neutron stars.

Based on the EOS, many stellar models are proposed and imply different maximum masses, from $M_{\max} \sim 1.4$ M$_\odot$ for the softest EOS to $M_{\max} \sim 2.5$ M$_\odot$ for the stiffest ones. These models become still more numerous when the density increases. Although its internal structure is not fully known, a neutron star is thought to be subdivided into four zones of different density, plus a gaseous atmosphere less than 10 cm thick forming a surface layer [Zavlin 2002]. Fig 1.6 illustrates the structure of a neutron star.

- The first zone is a thin outer crust which extends from the atmosphere bottom to the layer of density $\rho \sim 4 \times 10^{14}$ kg m^{-3}. Electrically conductive, the matter is similar to that found in white dwarfs, i.e. composed mainly of heavy nuclei together with relativistic degenerate electrons. This layer is about 300 m thick. As the density increases, electrons have an energy large enough to induce stable inverse β-decay, which enriches the number of neutrons in nuclei.

- A second zone called the "inner crust" is defined between $\rho \sim 4 \times 10^{14}$ kg m^{-3} and $\rho \sim 4 \times 2^{17}$ kg m^{-3} and is about 600 m thick. It consists of neutron-rich nuclei, free degenerate neutrons and a degenerate gas of relativistic electrons. With growing density, the fraction of free neutrons increases and the neutron fluid provides most of the pressure.

- The outer core also named the "neutron liquid phase" constitutes the largest zone, being about $9.7\,\mathrm{km}$ thick, until matter reaches $\rho \sim 10^{18}$ kg m^{-3}. The matter consists of neutrons with a few percent of protons, electrons and possibly muons, all strongly degenerate. The electrons and muons form almost ideal Fermi gases, whereas neutrons and protons (interacting via nuclear forces) constitute a Fermi liquid and can be in a superfluid state.

- The inner core occupies the central regions of massive neutron stars (in case of low-mass neutron stars, the outer core extends to the center). This region is defined by an extremely high density $\rho \sim 3 \times 10^{18}$ kg m^{-3} and a radius of several km. Different exotic models have been proposed to describe its composition of dense matter. They predict a hyperionization of matter with the appearance of hyperons, pion condensation, kaon condensation, and quark matter composed of u, d, s quarks. Note that the pion and kaon condensation processes have not yet been discovered in the laboratory. The implications of exotic forms of matter on the structure and stability of neutron stars are discussed by [Camenzind 2007].

Mass and radius

Binary systems offer the opportunity to directly measure the mass of a neutron star thanks to the orbital motions of the nearby companion. The mass function gives a lower limit on the mass of a compact star :

$$M_{\mathrm{X}} = \frac{K_{\mathrm{opt}}^3 P \left(1 - e^2\right)^{3/2}}{2\pi G \sin^3 i} \left(1 + \frac{1}{q}\right)^2 , \tag{1.7}$$

where $\mathrm{K_{opt}}$ is the semi-amplitude of the radial-velocity curve, P the period of the orbit, e the eccentricity of the orbit, i the inclination of the orbital plane to the line of sight, and q the mass ratio of the compact object to the companion star, which is equivalent to the ratio of the semi-amplitude of the radial-velocity curve of the companion star to the compact object.

The mean mass of a neutron star is estimated to be about 1.4 M$_\odot$, which coincides with the Chandrasekhar limit on mass for a white dwarf. The minimum mass limit of a stable neutron star can be $M \lesssim 1$ M$_\odot$. Such low-mass neutron stars are thought to result from the fragmentation of rapidly-rotating proto-neutron stars [Imshennik 1992]. Additionally, the maximum mass of a neutron star is estimated to be 3 M$_\odot$, which can be explained by the accretion of matter from a secondary companion. In principle, a larger mass should not exist, since the nuclear and degeneracy pressures could not withstand the force of gravity anymore. This is called the Oppenheimer-Volkoff limit and is analogous to the Chandrasekhar limit for white dwarf stars. Hence the neutron star would collapse to form a black hole. Fig. 1.7 presents the estimates of the masses of compact object in several systems.

When a binary system contains a pulsar, its mass is determined with great accuracy. The most precise values have been obtained for the double pulsar system
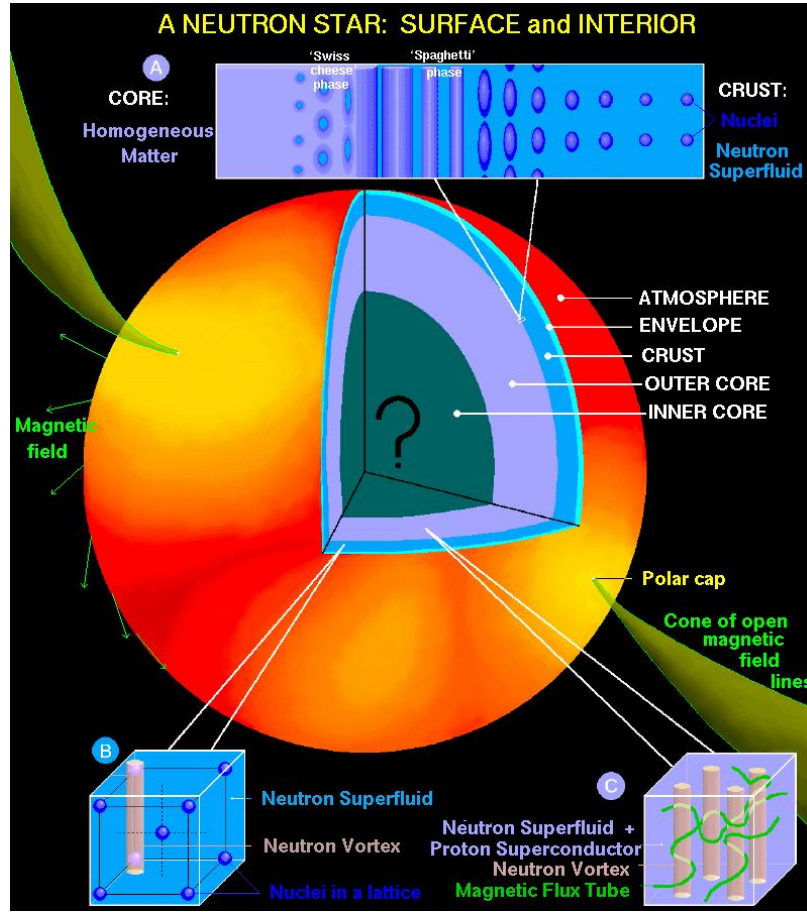
Figure 1.6: Structure of a neutron star. Credit: http://www.astro.umd.edu/miller/nstar.html

PSR J0737-3039A/B ($M_A = 1.3381 \pm 0.0007$ M$_\odot$ and $M_B = 1.2489 \pm 0.0007$ M$_\odot$ [Kramer 2008]).

The radius of a neutron star can be estimated in different ways:

- from the density of nuclear matter,

$$R_{NS} = \left(\frac{3\,M}{4\pi\rho} \right)^{1/3},$$

(1.8)

- from the neutron degeneracy pressure,

$$P_{deg} = \frac{h^2}{2\pi^2} \left(\frac{Z}{A} \right)^{5/3} \frac{\rho^{5/3}}{m_n^{8/3}},$$

(1.9)

hence by equating $P_{deg} = P_{grav}$, the mass-radius relation gives

$$R_{NS} = \left(\frac{2}{\pi} \right) \left(\frac{3}{4\pi} \right)^{5/3} \left(\frac{Z}{A} \right)^{5/3} \frac{h^2}{G m_n^{8/3}} M^{-1/3},$$

(1.10)
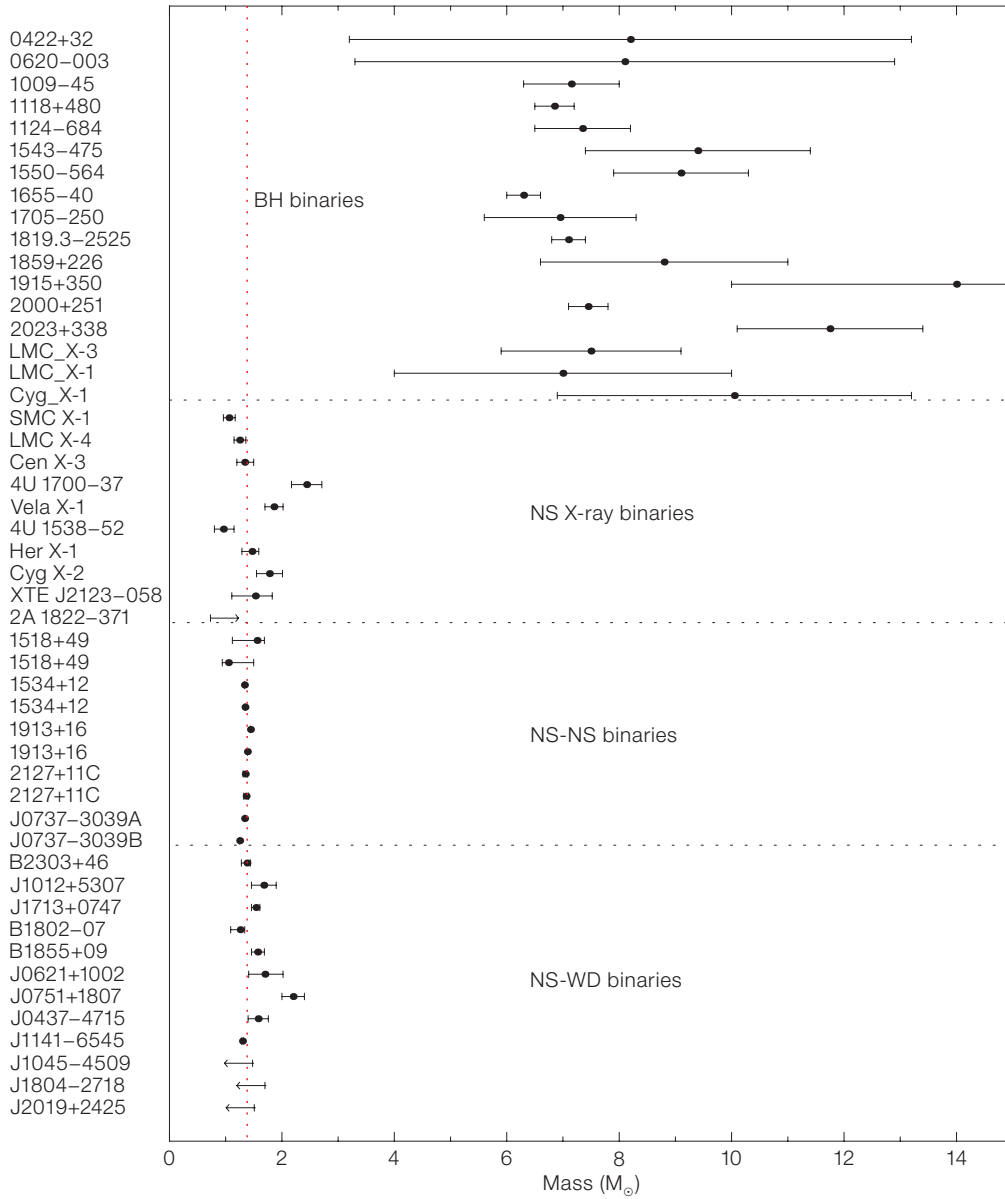
Figure 1.7: Mass distribution of neutron stars and black holes, based on measurements collected from the literature [Stairs 2004, McClintock 2006]. The neutron stars occupy a relatively narrow mass range near 1.4 $M_\odot$. The error bars correspond to 1σ errors. Note that there are some uncertainties on the nature of the compact object of 4U 1700-37, which could be a black hole. Figure from [Kaper 2006].

where Z is the atomic number, A the mass number, and h the Planck constant.

- from observational measurements of X-ray bursts of X-ray binaries containing an old and weakly magnetized neutron star, or from the inner disk radius,

which provides upper limits on the neutron star radius thanks to the iron line profile. X-ray bursts, also called type I X-ray bursts, are associated with brief thermonuclear flashes ($\sim$ 1 min) which arise when the matter accumulated onto the neutron star surface reaches a critical mass. The bursts provide a rare opportunity for the observer to measure the radius of a neutron star, which radiates like a spherical blackbody of luminosity:

$$L_{\mathrm{burst}} = 4\pi R_{\mathrm{NS}}^2 \sigma T^4 = f_{\mathrm{X}} 4\pi d^2, \tag{1.11}$$

where d is the distance to the neutron star, f_{X} the flux of the burst, T the temperature from the peak wavelength of the spectrum of the burst, and σ the Stefan-Boltzmann constant.

All of these methods provide comparable results. The typical size for a neutron star is $R_{\mathrm{NS}} \sim 10$ km, however it can vary, in a quite narrow range, with the mass of the compact object. This value is also consistent with the models derived from the EOS.

1.2.2 Black holes

Black holes are among the most mysterious objects in the Universe, although from a physics point of view, they can be considered to be very simple. Indeed, a black hole is characterized by only three parameters: the mass M, the angular momentum J, and the electric charge Q. A null value is often ascribed to the last parameter, since as soon as a black hole gets a net charge, it quickly attracts an equal number of opposite charges. Any other information is lost during black hole formation.

Black holes are classified into three categories: supermassive, intermediate, and stellar-mass black holes. The main parameter which differs between these classes is the mass. Moreover, the formation processes seem to be different. Characterized by a mass $M > 10^6$ M$_\odot$, supermassive black holes are present in the center of most (or possibly all) galaxies [King 2003]. However their origin is still unclear: were they born before the galaxies or after? Are they the result of accretion of matter or merging black holes? Simulations are performed in order to understand their formation, and the role that they play in galaxies. A second class of these objects is composed of stellar-mass black holes, which are associated with the end life of a supermassive star. They are created by gravitational collapse when the star does not have enough nuclear fuel to counterbalance gravitation forces. In that sense, black holes are an extension of neutron stars, since they are more compact and with a deeper potential well. In our Galaxy those for which we have an estimate of the mass do not exceed 20 M$_\odot$. The third class corresponds to intermediate mass black holes. Their understanding is important in order to put constraints on the origin and properties of black holes. With a mass larger than stellar-ass black holes, but much smaller than supermassive ones ($M = 10^2 - 10^4$ M$_\odot$), intermediate mass black holes are expected to be present in ultraluminous X-ray sources (ULXs) [Miller 2004a, Roberts 2007]. The existence of intermediate mass black holes was

strengthened by the detection of the brightest ULX source HLX1 in the nearby galaxy ESO 243-49 [Lasota 2011].

Detection of black holes

A black hole cannot be observed directly since it does not emit any radiation, which is why it is called a "black" object. Therefore, it can be discovered only through its gravitational influence on the neighbouring star or on the ambient gas medium [Salpeter 1964]. To fully explain the term "black hole", the second word is associated with the singularity that represents a hole in space-time; no matter or light can emerge from it [Wheeler 1968].

Supermassive black holes were detected indirectly by observing the elliptic motion of stars accelerated around a dark zone. They are also evident in active galactic nuclei (AGN). In such galaxies, the supermassive black hole is very active because of the large amount of accreted matter.

Stellar-mass black holes are detected in X-ray binaries thanks to the X-ray emission coming from matter in the accretion disk (for a comprehensive review on black hole binaries, see [Remillard 2006] and references therein). In 1971, Cygnus X-1 was the first object recognized as a black hole [Bolton 1972, Webster 1972]. At present, about 20 X-ray binary are believed to contain a compact object too massive to be a neutron star binary and are called black-hole binaries. Different studies were performed to estimate the number of these systems in the Galaxy; they are estimated at $\sim 10^8 - 10^9$ [Brown 1994, Timmes 1996]. A similar result was obtained for neutron stars in the Galaxy [van den Heuvel 1992, Timmes 1996].

As in the case of neutron stars, black hole masses can be determined from the dynamics of their companion stars. Fig 1.7 and Fig 1.8 present the mass estimates and a schematic representation of black-hole candidates.

When radio jets are detected in X-ray binaries that harbor a black hole, the system is called a microquasar, a term that is used to refer to the similarity of these objects and quasars (a class of AGN), which also show jets. The processes are similar, but energetic and typical times scales with the mass of the black hole (see the illustration in Fig 1.9). Therefore accreting black holes offer the opportunity to study AGN indirectly.

All these sources are multiwavelength emitters. It is extremely interesting to perform simultaneous observations of a source in different energy bands in order to better understand the physics and the connections between a black hole and the matter in its vicinity.

Event horizon

The event horizon of a black hole represents the radius of the sphere surrounding the collapsed mass at which the escape speed equals the speed of light. It is defined as:

$$R_{\mathrm{H}} = \frac{GM}{c^2}[1 + (1 - a^2)^{1/2}] \tag{1.12}$$
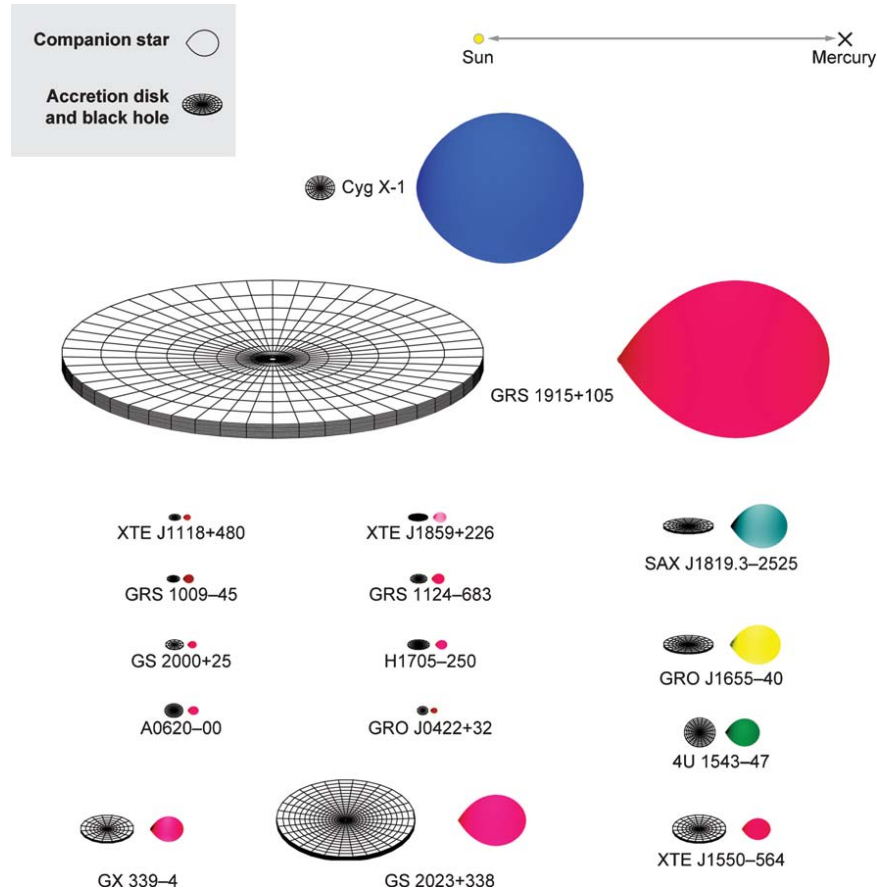
Figure 1.8: Representation of 16 black holes binaries in the Milky Way [Remillard 2006]. The distance between the Sun and Mercury is indicated on the top (0.4 AU). The inclination of the systems is indicated by the tilt of the accretion disk. The color of the companion star indicates its surface temperature. Credits: J. Orosz.

where a measures the spin of the black hole, which expresses the amount of its angular momentum J:

$$a = \frac{cJ}{GM^2}. \tag{1.13}$$

The event horizon is usually expressed in units of the Schwarzschild radius R_{Sch}.

This zone cannot be seen by an outside observer, since a photon travelling into this zone cannot escape to infinity. Hence it defines a region of space-time from which it is not possible to get any information. Because matter can fall in but never leave, the mass of a black hole can only increase. As a consequence, the surface area of the associated event horizon would always increases (apart from the Hawking radiation). Immediately outside the event horizon, the region of space-time has an extremely strong gravitational field.
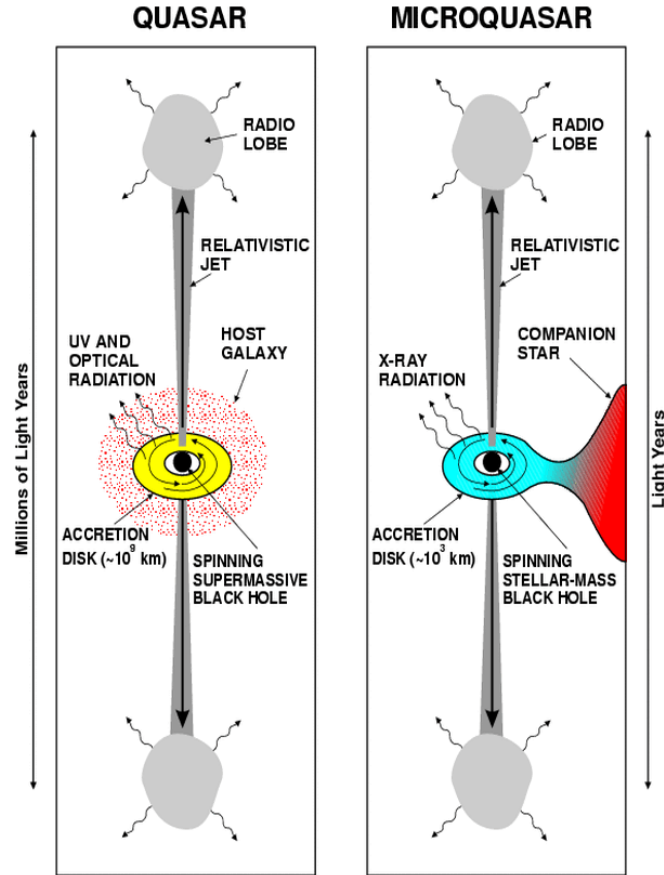
Figure 1.9: Schematic comparison of quasars and microquasars [Mirabel 1998]. Microquasars can be viewed as a smaller version of quasars.

Schwarzschild black holes

A non-rotating black hole with a null charge ($J = Q = 0$) is named a Schwarzschild black hole. It is formed when a mass M collapses within a sphere of radius R_{Sch}. Thereby a Schwarzschild black hole has an event horizon $R_{\mathrm{H}} = R_{\mathrm{Sch}}$. In the case of an AGN, considering for example a black hole of mass $M = 10^8$ M$_\odot$, R_{Sch} equals 3×10^8 km, whereas a stellar-mass black hole with $M = 3$ M$_\odot$ has $R_{\mathrm{Sch}} = 9$ km. The accreting material orbits the black hole before it crosses the Schwarzchild radius. In general relativity, R_{ISCO} defines the innermost stable circular orbit [Shapiro 1983, Kato 1998]. Closer to the compact object, a stable orbit does not exist, and material plunges towards the event horizon quickly. In Schwarzschild black holes, R_{ISCO} is three times farther than the event horizon, that is $R_{\mathrm{ISCO}} = 3\,R_{\mathrm{Sch}}$.

One can estimate the accretion efficiency onto a Schwarzschild black hole by assuming that accreting material follows Kepler orbits in an accretion disk and slowly drifts inwards. The inner edge of the accretion disk coincides with the last

stable circular orbit. The correct general relativistic result for the accretion efficiency of a Schwarzschild black hole which accretes from a geometrically thin accretion disk is $\eta_{\mathrm{acc}} = 5.7\,\%$.

The space-time metric associated with non-rotating black holes was derived by Schwarzschild in 1916:

$$\mathrm{d}s^2 = \alpha\,\mathrm{d}t^2 - \frac{1}{c^2}\left[\alpha^{-1}\mathrm{d}r^2 + r^2(\mathrm{d}\theta^2 + \sin^2\theta\,\mathrm{d}\phi^2)\right] \tag{1.14}$$

where

$$\alpha = \left(1 - \frac{2\,GM}{rc^2}\right) \tag{1.15}$$

This metric describes the interval between events in curved space-time and is described only by the mass of the black hole.

Kerr black holes

Because the majority of stars acquire angular momentum when they form, black hole remnants are expected to rotate too, unless an effective braking mechanism removes it. The Schwarzschild solution of Einstein's field equations for non-rotating black holes can be generalized in the form of the Kerr solution [Kerr 1963] to describe rotating black holes, or Kerr black holes. The Kerr metric depends upon the mass and the angular momentum of the black hole. It can be written in the Boyer-Lindquist coordinates:

$$\begin{aligned}
\mathrm{d}s^2 = {} & \left(1 - \frac{2\,GMr}{\rho c^2}\right)\mathrm{d}t^2 - \frac{1}{c^2}\left[\frac{4\,GMrj\sin^2\theta}{\rho c}\mathrm{d}t\,\mathrm{d}\phi + \frac{\rho}{\Delta}\,\mathrm{d}r^2\right. \\
& \left. + \rho\,\mathrm{d}\theta^2 + \left(r^2 + j^2 + \frac{2\,GMrj^2\sin^2\theta}{\rho c^2}\right)\sin^2\theta\,\mathrm{d}\phi^2\right]
\end{aligned} \tag{1.16}$$

where
$\Delta = r^2 - (2GMr/c^2) + j^2$,
$\rho = r^2 + j^2\cos^2\theta$,
$j = J/mc$ is the angular momentum of the black hole per unit mass which has dimensions of distance.

The Newton angular momentum is defined as $J = MvR$. One can calculate the maximum angular momentum J_{max} for a black hole by considering the entire mass of the black hole M, the speed $v = c$, and the orbital radius which corresponds to the event horizon of a Kerr black hole:

$$R_{\mathrm{H}} = \frac{GM}{c^2} = \frac{1}{2}\,R_{\mathrm{Sch}}. \tag{1.17}$$

with the spin parameter $a = \pm1$ in the formula of the event horizon, so that

$$J_{\mathrm{max}} = Mc\,\frac{GM}{c^2} = \frac{GM^2}{c}. \tag{1.18}$$

A significant property of accreting Kerr black holes is that the radius of the innermost stable circular orbit of matter orbiting the compact object depends on

whether the matter moves in the direction of rotation of the black hole (prograde) or in the opposite direction (retrograde). In the case of maximally-rotating Kerr black holes ($a = \pm 1$) where both the compact object and the accreting matter rotate in the same direction,

$$R_{\mathrm{ISCO}} = R_+ = \frac{GM}{c^2} = \frac{1}{2} R_{\mathrm{Sch}}, \tag{1.19}$$

which is half of the radius of a Schwarzschild black hole of the same mass, whereas in the case of counter-rotating particles,

$$R_{\mathrm{ISCO}} = R_- = 9 R_+ = 9 \frac{GM}{c^2}. \tag{1.20}$$

One can estimate the accretion efficiency using the innermost stable circular orbit in the Newton method:

$$\eta_{\mathrm{acc}} = \frac{1}{2} \frac{GM}{Rc^2} \sim 50\,\%, \tag{1.21}$$

with $R = 0.5\,R_{\mathrm{Sch}}$. The correct general relativistic result is $\eta_{\mathrm{acc}} = 42\,\%$.

Both Schwarzschild and Kerr black holes represent gravitational singularities where the curvature of spacetime is infinite. In the case of Kerr black holes, this singularity is a ring in the plane perpendicular to the rotational axis, while it is a single point for a Schwarzschild black hole. Both types have a spherical event horizon where the escape speed is equal to the speed of light. However the event horizon of a Kerr black hole is surrounded by a second critical surface called the static limit, which has the shape of an oblate spheroid and which touches the event horizon at its poles. The space between these two surfaces is called the ergosphere.

1.3 Accretion

Known since the 1940's, accretion is an important concept in astrophysics, whose pioneers were Bondi, Hoyle and Lyttelton. Present in different fields at different scales, accretion plays a crucial role in the interstellar medium, AGN, and X-ray sources, through the accretion of gas or matter onto a star, a supermassive black hole, and a stellar compact object (black hole, neutron star or white dwarf) respectively. To give a simple definition, accretion represents the accumulation of matter onto an object under the effects of gravity. When matter approaches a gravitational body, in particular a compact object, it liberates gravitational potential energy, making the accreting object a powerful source of energy [Frank 1992].

1.3.1 Accretion as a source of energy

As was said previously, accretion can be seen as a powerful gravitational energy extractor. When matter falls onto a compact object, its kinetic energy increases at the expense of its gravitational potential energy which becomes more negative.

In the close vicinity of the compact object, particularly in the case of a black hole or a neutron star, velocities are expected to be highly relativistic

[Mukhopadhyay 2012]. Then, when matter reaches the surface of the neutron star, it rapidly decelerates and the kinetic energy is radiated as heat. In the case of a black hole, there is no solid surface, but matter drifts inward until it reaches the last stable orbit. According to classical calculations, this occurs when the rotational energy of the matter is less than half the gravitational potential energy, i.e. :

$$\frac{L^2}{2\,I} < \frac{GMm}{2\,r_{\mathrm{ISCO}}}, \tag{1.22}$$

where L is the angular momentum of a mass of element m and $I = mr_{\mathrm{ISCO}}^2$ is its moment of inertia at the last stable orbit. The condition that matter fall into the black hole can be given in terms of the specific angular momentum $J = L/m$:

$$J < (GMr_{\mathrm{ISCO}})^{1/2}. \tag{1.23}$$

Accretion luminosity

The gravitational potential energy of a test mass m in the gravitational field of a compact object of mass M and radius R such that $m << M$, situated at a distance r is:

$$E_{\mathrm{grav}}(r) = -\frac{GMm}{r}. \tag{1.24}$$

As the test mass moves from a very large distance $r \to \infty$ to the surface $r = R$ of the central body, the energy difference $\Delta E_{\mathrm{grav}} = E_{\mathrm{grav}}(r \to \infty) - E_{\mathrm{grav}}(R)$ is released, hence

$$\Delta E_{\mathrm{grav}} = \frac{GMm}{R}. \tag{1.25}$$

Considering that the central body accretes matter continuously at a rate $\dot{M}$ in the time interval Δt, it therefore accretes the mass $\Delta M = \dot{M} \times \Delta t$ and liberates the energy

$$\Delta E_{\mathrm{grav}} = \frac{GM\Delta M}{R}. \tag{1.26}$$

If the energy is radiated away at the same rate at which it is liberated, the luminosity of the object due to the accretion process is:

$$L_{\mathrm{acc}} = \frac{GM\dot{M}}{R}. \tag{1.27}$$

The quantity L_{acc} is called the accretion luminosity. For a fixed mass accretion rate, the accretion luminosity obviously increases with the compactness M/R of the accreting object. This reflects the fact that for a given mass M, the depth of its gravitational potential well increases with decreasing radius R.

To illustrate the power of accretion, the efficiency η_{acc}, defined by the expression

$$L_{\mathrm{acc}} = \eta_{acc}\dot{M}c^2, \tag{1.28}$$

where c is the speed of light, expresses the accretion luminosity as a function of the rest mass of the accreted matter.

To calculate the accretion luminosity of the accretion disk, a factor $1/2$ is included to take into account the fact that half of the gravitational potential energy is converted into kinetic energy and half of the energy is available to be radiated away by the disk itself:

$$L_{\text{disk}} = \frac{1}{2}\frac{GM\dot{M}}{R}. \tag{1.29}$$

Eddington luminosity

The Eddington limit plays a major role in accreting neutron stars. In such systems, the matter coming from the companion star is accreted onto the compact object and generates large luminosities. However if the matter accreted becomes too important, the radiation pressure limits the accretion rate and therefore the observed luminosity. The limiting luminosity is called the Eddington luminosity. This occurs when the inward gravitational forces balance the outward radiation pressure on electrons and protons constituting the ionized plasma:

$$F_{\text{grav}} = F_{\text{rad}} \Leftrightarrow \frac{GMm_{\text{p}}}{D^2} = \frac{L\sigma_{\text{T}}}{4\pi D^2 c} \tag{1.30}$$

where σ_{T} is the Thomson scattering cross-section for the electron. The Eddington luminosity is therefore:

$$L_{\text{Edd}} = \frac{4\pi GMm_{\text{p}}c}{\sigma_{\text{T}}}, \tag{1.31}$$

$$L_{\text{Edd}} = 1.26 \times 10^{31} \left(\frac{M}{M_{\odot}}\right) \text{W}, \tag{1.32}$$

The mass accretion rate that corresponds to the Eddington luminosity can be deduced from the previous equations:

$$\dot{M}_{\text{Edd}} = 1.26 \times 10^{31} \frac{R}{GM_{\odot}}. \tag{1.33}$$

It is important to note that $\dot{M}_{\text{Edd}}$ does not depend on the mass of the star, but only on its radius, whereas the Eddington luminosity is proportional to the mass. For instance, the maximum accretion rate of a neutron star of radius $R = 10$ km is $\dot{M}_{\text{Edd}} = 1.5 \times 10^{-8}$ $M_{\odot}/\text{yr}$. Any additional mass is blown off by the radiation pressure. In practice, magnetic fields and accretion disks modify the theoretical values, although they remain a good approximation.

1.3.2   From the accretion disk to the compact object

Accreting matter from the companion star does not directly fall on the compact object. Because of the conservation of angular momentum, it spirals around the central object to form a flat structure, the so-called accretion disk. Friction forces induced by the matter striking itself make its temperature increase to reach the very high values responsible for the disk X-ray emission [Pringle 1972, Shakura 1973,

Lynden-Bell 1974]. Thus, the accretion disk acts like a machine that extracts gravitational potential energy and angular momentum from plasma. The latter follows circular Keplerian orbits around the compact object with speed $v_K = (GM/R)^{1/2}$. The orbit of a blob of plasma in the accretion disk slowly decreases until it reaches the accretor, losing gravitational potential energy while gaining kinetic energy.

Depending on the nature of the compact object, matter can arrive more or less close to the compact object. In the case of a black hole, matter reaches the last stable orbit, which depends on the spin of the black hole and on the direction of rotation of the disk with respect to the compact object (see the previous part dedicated to Kerr and Schwarzchild black holes). As far as neutron stars are concerned, magnetic fields play an important role in the way the matter approaches and falls onto the compact object. In the presence of strong magnetic fields, the matter follows the field lines such that the matter falls onto the magnetic poles generating pulses, when the direction of the magnetic axis is not aligned with the rotation axis, which cross the line of sight of the observer. In this configuration, the inner accretion disk is truncated at the magnetosperic or Alfven radius. Regarding low magnetized neutron stars, the matter can reach the neutron surface. The boundary layer represents the region which does the connection between the accretion disk and the neutron star surface, and is an important source of luminosity.

Physics of binary systems

Contents

As explained in the previous chapter, accretion disks play a major role in the X-ray emission of LMXBs. However, to fully understand the physics of X-ray binaries and to account for the spectra obtained from these sources, one has to mention the crucial role of the corona composed of hot plasma that surrounds the accretion disk.

In the following sections, the accretion disk and the corona are discussed in more detail. We discuss in particular the different types of interactions occuring between photons and matter, the geometry of the disk/corona, and the states observed in X-ray binary sources.

2.1 Different components

X-ray spectra of accreting binary systems typically exhibit a soft-thermal component (a blackbody) associated with the accretion disk, and a hard X-ray component that usually dominates the spectrum. The hard component is thought to result from soft photons emitted by the disk that get Compton upscattered by high-energy electrons that form a corona. This component can be fitted either by a power law with a high-energy cutoff when the source is in the so-called hard state, or by a blackbody when the source is in the soft state. A reflection component is often detected in the spectra of such sources, and is thought to be due to the interaction between the Comptonized photons and the cold matter in the accretion disk. All of these components are illustrated in Fig. 2.1.
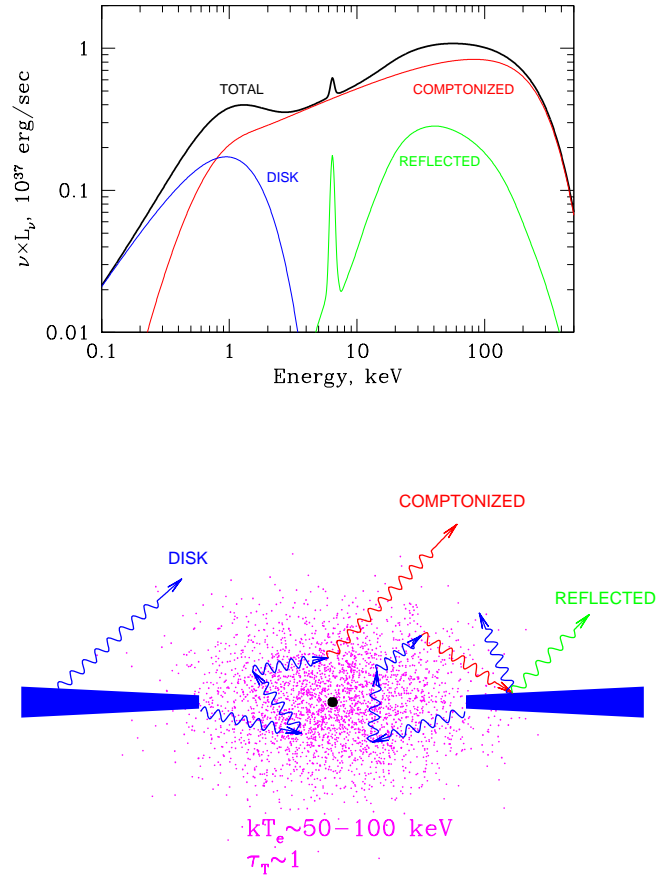
Figure 2.1: The three main components of the X-ray emission corresponding to an accreting black hole (top) and a plausible geometry of the accretion flow in the hard spectral state (bottom, side-view), where the black point, the blue slabs, and the pink points represent the compact object, the accretion disk, and the corona of electrons, respectively. From [Gilfanov 2010].

2.1.1 The accretion disk

The accretion disk consists of stellar plasma (from the external envelope of the companion star), i.e. ionized gas whose properties are determined by ions and electrons. Depending on the temperature, the matter is fully ionized or may recombine to form neutral atoms at lower temperatures. The mass accretion rate and viscosity seem to play major roles in the accretion disk structure and geometry.

There exist different solutions to the equations of accretion flow around the compact object, leading to many models. One can distinguish different classes of models, such as accretion flows radiatively efficient and radiatively inefficient, depending mainly on three criteria: 1) the ratio between the heating rate and cooling rate, 2) the opacity of the gas, and 3) the dominant pressure (gas or radiation).

Whatever the configuration, they all involve an optically thick geometrically thin accretion disk.

Standard model of thin accretion disks

Developed by [Pringle 1972] and [Shakura 1973], the standard accretion disk, which is geometrically thin and optically thick (with $H \ll r$ where H is the thickness of the disk and r its radius) is one solution among others. It corresponds to the radiatively efficient case, where the disk is gas pressure dominated. The heating produced by viscosity is radiated locally. The flow being optically thick, it is cooled efficiently and its temperature is close to that of a blackbody.

Viscosity plays an important role in determining the accretion disk structure. To infer more precisely the type and the influence of viscous forces, one can calculate the Reynolds number $R \sim L^2/\nu T \sim VL/\nu$, where L, T and V are the typical dimensions of length, time and velocity of the flow, and ν is the kinematic velocity. If the Reynolds number is less than 1, viscous forces play a central role, whereas if $R > 10^3$, the flow becomes turbulent [Landau 1987]. By inserting values in the case of an accretion disk around a neutron star, $R \sim 10^{12}$ [Longair 2011]. This implies that molecular viscosity does not play a major role in determining the structure of the accretion disk; turbulent viscosity does. Thus the flow is strongly turbulent, and the transport of momentum depends on the turbulence in the plasma. The turbulent viscosity is often described as $\nu = \alpha\, v_s H$, where α is the viscosity parameter and v_s the sound speed in the disk [Shakura 1973]. Turbulent swirls and velocities have dimensions much smaller than the thickness of the disk and the speed of sound, respectively. Hence, thin accretion disks are referred to as $\alpha-$disks.

Moreover, the accretion disk is very likely magnetized [Balbus 1991], which is important to understand the transport of momentum on large scales. Magnetohydrodynamic turbulence generated in the disk is deeply studied in this context.

An optically thick accretion disk implies that photons scatter many times before escaping the disk, so particles and photons continuously share their kinetic energies. In perfect thermal equilibrium, the average particle's kinetic energy equals the average photon energy, and a unique temperature T may be defined. Thus the disk radiates from its top and bottom surfaces and the heat dissipated between r and $r + \Delta r$ can be approximated by a blackbody emission from these surfaces, such as: $2\sigma T^4 \times 2\pi r \Delta r$, where σ is the Stefan-Boltzmann constant:

$$\sigma T^4 = \frac{3G\dot{m}M}{8\pi r^3}, \tag{2.1}$$

M being the mass of the accreting object, r the radial distance from the center, and $\dot{m} = 2\pi r v_r \Sigma$ the mass transfer rate through the optically thick disk of surface density Σ, at the velocity v_r [Frank 1992]. Each annulus of the disk radiates like a blackbody of temperature T that depends on the associated radius r, as $T \sim r^{-3/4}$. The temperature of the disk increases towards the compact object.

The total intensity of the disk is proportional to the surface area at temperature

T and to the blackbody intensity at that temperature:

$$I(\nu) = \int 2\pi r\, B(T, \nu) dr \qquad (2.2)$$

where

$$B(T, \nu) = \frac{2h\nu^3}{c^2} \frac{1}{(e^{h\nu/kT} - 1)} \qquad (2.3)$$

is the Planck function. It results that the spectrum of a thin, optically thick accretion disk has the form $I(\nu) = \nu^{1/3}$ [Frank 1992]. At low frequencies, well below the peak ($h\nu \ll kT$), the Planck function can be approximated by

$$B(T, \nu) \sim \frac{2\nu^2 kT}{c^2} \sim \nu^2 T, \qquad (2.4)$$

which constitutes the Rayleigh-Jeans approximation. At frequencies well above the peak, $e^{h\nu/kT} \gg 1$, the spectrum decreases exponentially

$$B(T, \nu) \sim \frac{2h\nu^3}{c^2} e^{-h\nu/kT}. \qquad (2.5)$$

This is known as the Wien approximation.

As a result, the spectrum of the accretion disk in binaries is often fitted by a blackbody which peaks at ~ 1 keV ($T_{\text{disk}} \sim 10^7$ K), or by a multi-color blackbody which approximates the black body emission at each radius of the disk, as illustrated in Fig 2.2.
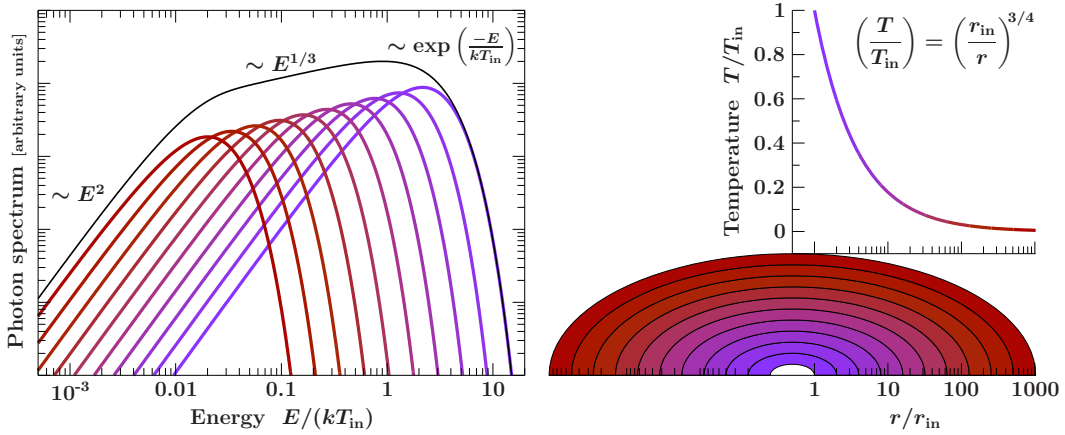
Figure 2.2:   Spectrum resulting from the superposition of black-body components originating from individual rings in the optically-thick accretion disk. Figure from [Hanke 2011].

Accretion flow dominated by advection

Another family of models was proposed, since the standard disk model was not able to reproduce the spectral energy distribution of some sources, especially low rate accreting sources [Esin 1996]. Initially proposed by [Ichimaru 1977], the Advection Dominated Accretion Flow (ADAF) model assumes that the inner region of the accretion disk close to the compact object becomes optically thin and is replaced by a hot flow [Narayan 1994, Narayan 1995b, Narayan 1995a, Abramowicz 1995, Chen 1995]. This model has successful applications in particular with respect to X-ray transients [Esin 1997], some AGN [Lasota 1996], and the Galactic center [Manmoto 1997].

Because the accretion flow is not cooled efficiently by radiation, the viscous energy is stored in the gas as thermal energy and is advected radially with the flow onto the compact object [Ichimaru 1977]. Only a small fraction of the energy is radiated away [Narayan 1996]. Therefore the radiation efficiency is significantly lower than that of the standard disk model (see [Narayan 1998], for a review and references therein, [Kato 1998]). ADAF is very useful for inefficient accretion in black holes because part of the accretion energy is advected into the black hole. In neutron stars, the energy is eventually released by the surface of the neutron star, and thus accretion is efficient there.

Advection-dominated accretion flows can occur in two regimes, depending mainly on the accretion rate and the optical depth. In the case defined as the "slim accretion disk", the accretion rate is high and the optical depth becomes very high too; the radiation is trapped in the gas [Abramowicz 1998]. In the second regime where the accretion rate is very low, the accretion flow is optically thin [Narayan 1994, Abramowicz 1995].

Additionally, the magnetic field seems to play an important role on the structure of hot flow since the flow is highly ionized [Balbus 1998, Shadmehri 2005, Abbassi 2008].

Alternative models are proposed and derived from the ADAF, which is a hot and inefficiency accretion flow model. For instance one can cite ADIOS (Advection Dominated Inflow-Outflow Solution; the advected energy is expelled in outflow instead of crossing the event horizon as in case of ADAF [Blandford 1999]), LHAF (Luminous Hot Accretion Flow; it consists of an efficiency accretion flow [Yuan 2001]), or CDAF (Convection Dominated Accretion Flow; the convection transports angular momentum toward the inner part of the flow [Quataert 2000]). It is still not obvious which of the different proposed geometrical configurations is the correct one.

2.1.2 The corona

The corona is composed of hot electrons ($T > 10^9$ K), as opposed to the "cold" accretion disk, and is responsible for producing the high-energy spectrum by Comptonization. (This process is described more in more detail later). Energetic electrons would occupy regions more or less important on the top and bottom of the disk,

and not instead of it, as in the case of ADAFs where the corona is the inner part of the accretion flow.

Different theoretical models have been proposed to account for its existence. A first model suggests that the corona may be formed by evaporation of hot material from the surface of the accretion disk [Shakura 1973]. Another one proposes that the accretion disk would inject energy into an outer tenuous layer of its atmosphere to form a hot corona [Liang 1977]. By the mechanism of magnetic reconnections, this would lead to a very hot, magnetically-confined structured corona analogous to the observed structure of the solar corona [Galeev 1979].

Moreover, there are still strong uncertainties regarding the corona geometry. Three main models are proposed: a) a "slab" or "sandwich" geometry, above and under the accretion disk on the plane-parallel , b) a "sphere" geometry around the compact object (ADAF like), and c) a "patchy" or "pill box" corona. These models are illustrated in Fig. 2.3. It is not extremely clear where the hard photons are produced in the different states, and this may also be linked to changes in coronal geometry.
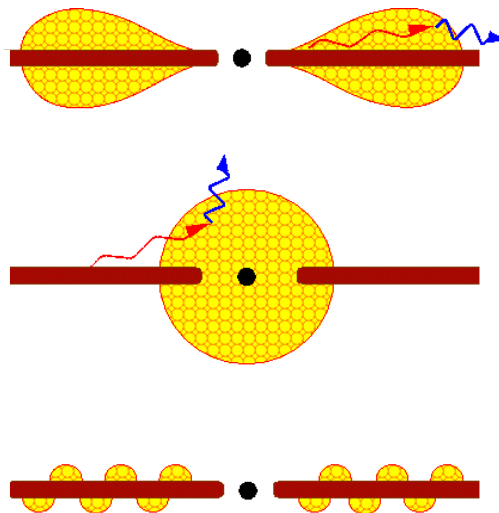
Figure 2.3: Illustration of the possible geometries of the accretion disk (red) corona (yellow): "slab" or sandwich geometry (top), "sphere" geometry, ADAF like (middle), and "patchy" geometry (bottom) [Stern 1995].

Acretion disk corona (ADC)

The simplest models able to reproduce the spectral features in AGNs and X-ray binaries constitute the accretion disk corona (ADC) models [White 1982]. The standard optically thick and geometrically thin accretion disk [Shakura 1973] extends close to the compact object and is sandwiched between two plane-parallel of hot plasma that form the corona.

Until recently, this model was largely accepted [Galeev 1979, Haardt 1994].

Truncated disk model

The truncated disk model where the thin accretion disk is truncated and replaced by an inner advection-dominated accretion flow (ADAF) represents an alternative to the ADC model [Esin 1997, Done 2007]. In this model, a hot corona above the disk is a continuation of the inner ADAF.

The global configuration of the thin accretion disk, the inner hot flow, and the corona change with the mass accretion rate. At low mass accretion rates, the inner ADAF is radiatively inefficient and the outer thin disk is found at large radii. At high mass accretion rates, the ADAF becomes radiatively efficient and the system more luminous. The ADAF progressively shrinks in size, whereas the thin accretion disk approaches closer to the compact object. The truncated disk model accounts for the spectral changes in X-ray sources (see the section dedicated to the spectral states for more details).

2.2 Physical processes in the accretion disk/corona system

As explained previously, the accretion disk and the corona form a complex system. Since some regions of the hot corona are in contact with or in the close vicinity of the disk of cold matter, important interactions take place. The main processes involved in the interaction of high-energy photons with atoms, nuclei, and electrons are photoelectric absorption, Compton scattering, and electron-positron pair production. There is a competition between these processes, based on their efficiency of cooling the medium at a certain energy. The efficiency of cooling depends on the probability of interactions and is therefore directly linked to the cross-sections of interaction (see Fig. 2.4).

In the following, the physical processes that dominate X-ray spectra of AGN and X-ray binary sources are discussed. For more details about these processes and the full demonstrations of the formulae, see [Rybicki 1979, Bradt 2008, Longair 2011].

2.2.1 Compton scattering - Comptonization

Inverse Compton scattering plays a preponderant role in the formation of the high-energy spectrum of compact objects. How can a thermal (Maxwellian) distribution of electrons produce a power-law spectrum? The basic reason is the superposition of many orders of Compton scattering spectra, each one corresponding to a single scattering process, when they are not too much separated in energy (i.e. for not too large temperatures); the sum is a smooth power law.

First let us present a brief overview on the scattering of a photon by an electron. Scattering is the simplest interaction between photons and free electrons. Depending on the initial photon energy with respect to that of the electron, different regimes are
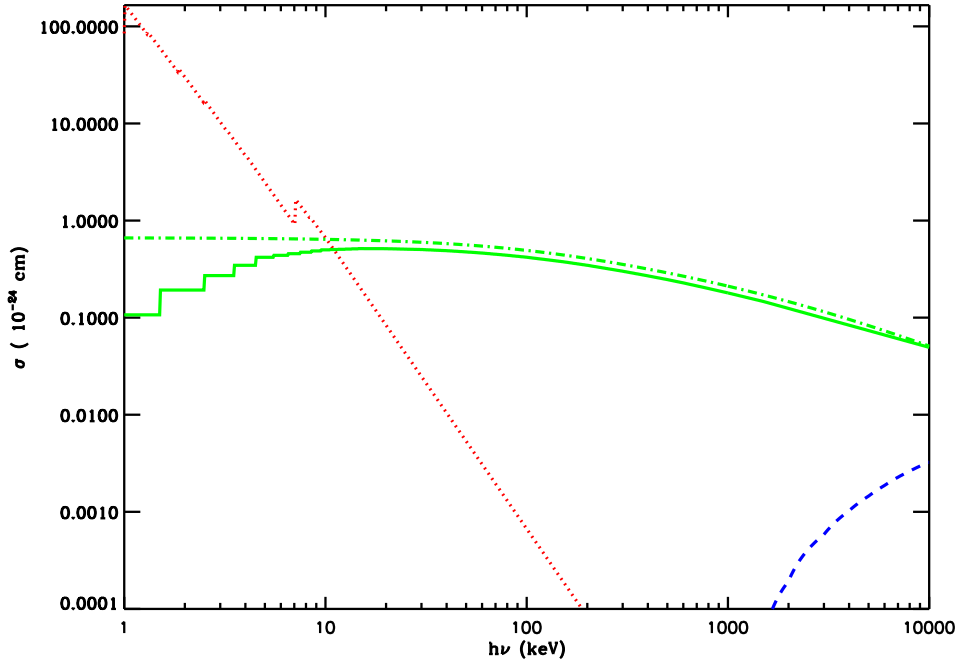
Figure 2.4:   Comparison of photoionization (red dotted line, [Morisson 1983]),
Compton scattering (on bound electrons and of Klein-Nishina in green solid line
[Storm 1967] and green dashed-dotted line, respectively), and pair production (blue
dashed line, [Storm 1967]) cross sections. The cross sections are given in barn for a
hydrogren atom with cosmic abundances [Malzac 1999].

discerned, such as Thomson scattering, Compton scattering, and inverse Compton
scattering.

Compton scattering

For low photon energies ($h\nu \ll m_e c^2$), scattering of a photon by an electron at rest
is reduced to the classical case of Thomson scattering. In this process, the photon
is scattered in a random direction, and no change in the frequency of the radiation
is observed.

If the photon energy is comparable to, or greater than the electron energy, non-
classical effects have to be taken into account; this process is called Compton scat-
tering. The scattering is then modified by quantum effects through a change in
kinematics of the collision (because of the energy and the momentum of the pho-
ton), and an angle dependence of the cross-section (Klein-Nishina regime).

Compton scattering is not elastic since a recoil of the charge is observed, hence
a transfer of energy occurs. This implies that the initial and the scattered photon
energy are different. Let us consider that the incident photon has an energy $h\nu$ and
a momentum $h\nu/c$, and the scattered photon has an energy $h\nu'$ and a momentum

$h\nu'/c$. The inital energy of the electron is its rest energy $m_\mathrm{e}c^2$. Its recoil energy is $\gamma m_\mathrm{e}c^2$, and its momentum associated is $p_\mathrm{e} = \gamma\beta m_\mathrm{e}c = \gamma m_\mathrm{e}v$, where v is its recoil speed, m_e is its mass, β is the speed parameter defined as $\beta = v/c$, and γ is the Lorentz factor $\gamma = (1 - \beta^2)^{1/2}$. The photon scattering angle is θ.

The following relations are derived from energy and momentum conservation, with both the electron and the photon treated as particles. Two equations are required for the momentum, along the x and the y axis. The three conservation equations give

$$h\nu + m_\mathrm{e}c^2 = h\nu' + \gamma m_\mathrm{e}c^2 \tag{2.6}$$

$$\frac{h\nu}{c} = \frac{h\nu'}{c}\cos\theta + \gamma\beta m_\mathrm{e}c\cos\phi \tag{2.7}$$

$$0 = \frac{h\nu'}{c}\sin\theta + \gamma\beta m_\mathrm{e}c\sin\phi. \tag{2.8}$$

The initial (i.e. before the interaction) momenta and energy are on the left sides. The longitudinal and transverse components of momentum are defined relative to the direction of the incident photon. By combining these equations, the energy of the Compton scattered photon is obtained:

$$h\nu' = \frac{h\nu}{1 + \frac{h\nu}{m_\mathrm{e}c^2}(1 - \cos\theta)}. \tag{2.9}$$

The relation explicitly shows how the scattered photon energy is significantly shifted as the incident photon energy $h\nu$ becomes comparable to the rest energy $m_\mathrm{e}c^2$ of the electron. At much lower energies, the photon is scattered without significant reduction in energy. At a given incident photon energy, the decrease in energy is greatest when the photon is back scattered ($\theta \sim \pi$ radians). Conversely, at very high-photon energies ($h\nu \gg m_\mathrm{e}c^2$), a back scattered photon has energy $m_\mathrm{e}c^2/2$ irrespective of the incoming photon's energy.

This energy change results in an increase of the wavelength of the photon given by

$$\lambda' - \lambda = \frac{h}{m_\mathrm{e}c}(1 - \cos\theta). \tag{2.10}$$

The quantity $h/m_\mathrm{e}c = 2.426 \times 10^{-12}$ m is known as the Compton wavelength λ_C. The equivalent frequency and photon energy are 1.23×10^{20} Hz and 0.511 MeV, respectively. The equivalent energy turns out to be the rest energy of the electron, $m_\mathrm{e}c^2 = 0.511$ MeV.

The wavelength shift $\lambda' - \lambda$ is independent of the incident wavelength. The fractional shift $(\lambda' - \lambda)/\lambda$ becomes substantial only if the incoming wavelength λ is so short as to be comparable to 10^{-12} m, at which point the photon energy approaches that of the electron rest energy. For long wavelengths $\lambda \gg \lambda_\mathrm{C}$ (so $h\nu \ll m_\mathrm{e}c^2$), the scaterring is closely elastic; there is no change observed in the photon energy.

Compton scattering is not isotropic, i.e. the probability for a photon to be scattered through a certain solid angle $d\Omega$ is not constant. Indeed, the probability of scattering is higher when θ is close to 0, which means that the photon has more chance to be scattered (head-on collision). The angular distribution of the electron after the scattering event or the differential cross section for Compton scattering are given by the Klein-Nishina formula ([Klein 1929], [Rybicki 1979])

$$\frac{d\sigma_{KN}}{d\Omega} = \frac{3}{16\pi}\sigma_T \left(\frac{\nu'}{\nu}\right)^2 \left(\frac{\nu}{\nu'} + \frac{\nu'}{\nu} - \sin^2\theta\right) \tag{2.11}$$

where

$$\sigma_T = \frac{8\pi}{3}r_0^2 = \frac{8\pi}{3}\left(\frac{e^2}{m_e c^2}\right)^2 = 6.652 \times 10^{-25} \text{ cm}^2 \tag{2.12}$$

is the classical Thomson cross section, with $r_0 = e^2/(m_e c^2) = 2.82 \times 10^{-13}$ cm the classical electron radius.

Note that σ_T is inversely proportional to m_e^2. Therefore the scattering cross sections on charged particles are different from the electron's, smaller by a factor of $(m_e/m_p)^2 \sim 10^{-7}$. That is why Compton scattering by particles other than electrons is negligible because almost no momentum can be transferred.

The probability for a photon to be scattered to an angle θ is given by

$$\sigma_{KN} = \int_{4\pi} \frac{d\sigma_{KN}}{d\Omega}(\theta)d\Omega = \int_0^\pi \frac{d\sigma_{KN}}{d\Omega}(\theta)2\pi\sin\theta d\theta. \tag{2.13}$$

So the total cross section is [Rybicki 1979]

$$\sigma_{KN} = \frac{3}{4}\sigma_T \left[\frac{1+x}{x^3}\left\{\frac{2x(1+x)}{1+2x} - \ln(1+2x)\right\} + \frac{1}{2x}ln(1+2x) - \frac{1+3x}{(1+2x)^2}\right] \tag{2.14}$$

where $x = h\nu/(m_e c^2)$. This yields the following formulae for the total cross-section, in the non-relativistic and extremely relativistic cases respectively:

$$\sigma_{KN} \approx \sigma_T\left(1 - 2x + \frac{26x^2}{5} + ...\right) \text{ for } x \ll 1 \tag{2.15}$$

and

$$\sigma_{KN} = \frac{3}{8}\sigma_T\frac{1}{x}\left(\ln(2x) + \frac{1}{2}\right) \text{ for } x \gg 1 \tag{2.16}$$

At high photon energies, the cross section is therefore reduced, so the Compton scattering becomes less efficient.

For small initial energy $h\nu$, the Klein-Nishina formula approaches the classical Thomson formula

$$\frac{d\sigma_T}{d\Omega} = \frac{3}{8\pi}\sigma_T\left(\frac{1+\cos^2\theta}{2}\right). \tag{2.17}$$

Inverse Compton scattering

In the context of high-energy astrophyiscs, the electron is not at rest, but has an energy substantially greater than that of the photon. When an electron and a photon collide, net energy may be transferred from the electron to the photon. This process is called inverse Compton scattering, to distinguish it from the direct Compton scattering. The Compton scattering formula can be applied in the inverse case if we change the frame of reference in which the electron is at rest. The collision is then viewed in the rest frame. Transformation back to the laboratory or observer frame yields the energy of frequency of the scattered photon.

Here again there are two regimes, depending on the energy of the incoming photon with respect to $m_{e}c^2$. If the photon energy is smaller than $m_{e}c^2$, the Thomson regime is considered. In the opposite case, the recoil of the electron cannot be neglected, and the Klein-Nishina regime is applied. In both regimes, the typical photon gains energy.

The power emitted by Compton scattering by an electron of Lorentz factor γ in the case of an isotropic distribution of photons is [Rybicki 1979]

$$P_{\mathrm{Comp}} = \frac{4}{3}\sigma c U_{\mathrm{rad}}\gamma^2\beta^2 \tag{2.18}$$

where U_{rad} is the radiation energy density of the photon field (before scattering).

If the photons have an energy $E = h\nu$, the average relative gain in energy $\Delta E/E$ during a scattering is:

$$\frac{\Delta E}{E} = \frac{P_{\mathrm{Comp}}}{\sigma c U_{\mathrm{rad}}} = \frac{4}{3}\gamma^2\beta^2. \tag{2.19}$$

Thus a low-energy photon is converted into a high-energy photon by a factor of order γ^2. Inverse Compton scattering process is therefore an effective means of creating very high-energy photons.

Thermal Comptonization

A population of cold photons which encounters a region containing free electrons will find its spectrum modified as a result of inverse Compton scattering given sufficient optical depth. In the case that the electrons are on average more energetic than the photons, the photons will, on average, be scattered to higher energies. In contrast, if the electrons are less energetic, the photons will be scattered to lower energies. When the spectrum of a source is primarily determined by Compton processes, it is said to be Comptonized. In this case, the plasma must be thin enough so that other processes, such as bremsstrahlung, do not dominate the spectrum instead. The hotter the gas, the more chance of Comptonization.

If the electrons are non relativistic and the photons have an energy $h\nu \ll m_{e}c^2$, the relative change in photon energy $\Delta E/E$ is

$$\frac{\Delta E}{E} = \frac{h\nu}{m_{e}c^2}(1 - \cos\theta). \tag{2.20}$$
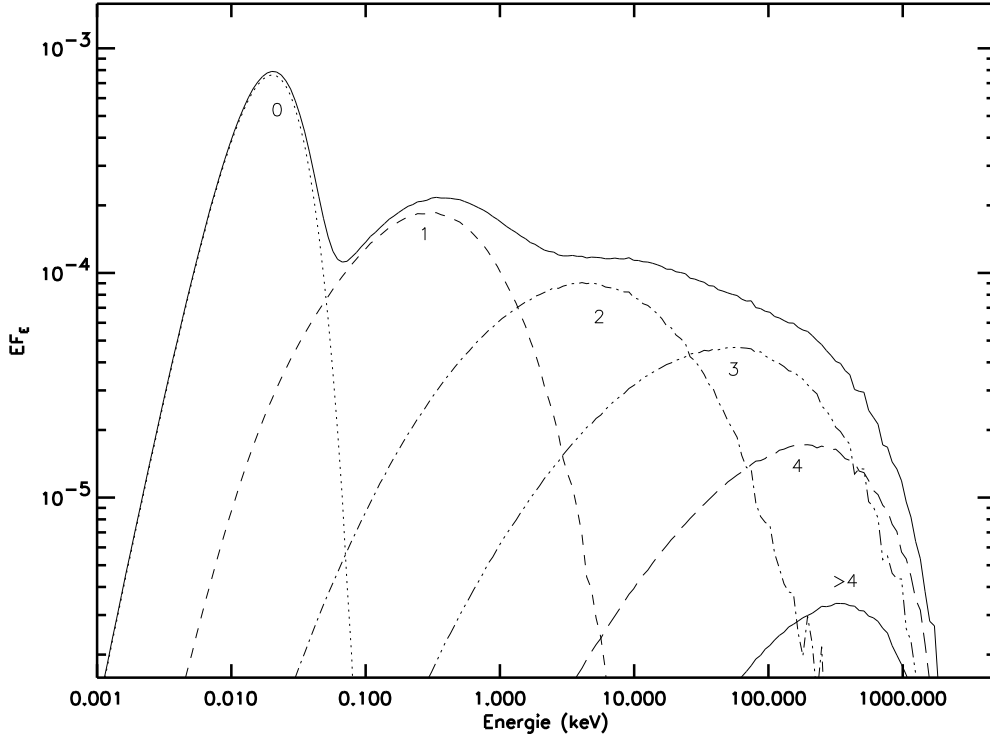
Figure 2.5: Comptonization spectrum arising from seed photons injected with a blackbody temperature $kT_{bb} = 5$ eV in an homogeneous plasma sphere defined by the temperature $kT_e = 300$ keV and the optical depth $\tau = 0.1$. The Compton orders are also represented [Malzac 1999].

In the frame of reference of the electrons, the scattering is Thomson, thus symmetric around the incident direction of the photons. The average energy increase of the electrons is

$$\frac{\Delta E}{E} = \frac{h\nu}{m_e c^2} \text{ for } h\nu \ll m_e c^2. \tag{2.21}$$

This explains the recoil effect undergone by the electrons.

In the opposite case, where the energy is transferred from the electrons to the photons, the average energy gain of the photons per inverse Compton scattering is

$$\frac{\Delta E}{E} = \frac{4}{3} \left(\frac{v}{c}\right)^2 \text{ for } h\nu \gg m_e c^2. \tag{2.22}$$

When the process of multiple scattering of a photon is due to a thermal or quasi-thermal distribution of electrons, the term "thermal Comptonization" is used. Quasi-thermal means a particle distribution that is peaked, even if it is not perfectly Maxwellian, such as the electrons have a thermal distribution of velocities at temperature T_e:

$$\frac{3}{2}kT_e = \frac{1}{2}m_e v^2 \tag{2.23}$$

with v the typical electron velocity. Hence,

$$\frac{\Delta E}{E} = \frac{4kT_\text{e}}{m_\text{e}c^2} \text{ for } h\nu \ll m_\text{e}c^2. \tag{2.24}$$

As a result, the relation describing the average energy change (gain/loss) of the photon per collision, for both the high and low frequency regimes, is

$$\frac{\Delta E}{E} = (4kT_\text{e} - h\nu)/m_\text{e}c^2. \tag{2.25}$$

Therefore, there is no energy transfer if $h\nu = 4kT_\text{e}$, electrons gain energy if $h\nu > 4kT_\text{e}$, and photons gain energy if $h\nu < 4kT_\text{e}$. When the electrons are hotter than the photons, the fractional increase in energy is $4\frac{kT_\text{e}}{m_\text{e}c^2}$ per collision.

In addition to the distribution of the electrons, the determinant parameter for the spectral shapes emerging from the plasma is its optical depth:

$$\tau = n_\text{e}\sigma_\text{T}R \tag{2.26}$$

with n_e the electron density, R the typical radius of the source and σ_T the Thomson cross section. The probability for a photon to cross the plasma without interacting is $e^{-\tau}$.

The average number of scatters can be calculated assuming that the photon, before leaving the source, experiences a sort of random walk inside the source. The more important the optical depth, the higher the number of scatters before escaping. When $\tau < 1$ most of the photons leave the source directly, without any scattering. When $\tau > 1$, the mean free path is $d = R/\tau$ and the photon will experience, on average, τ^2 scatters before leaving the source.

The fundamental parameter which measures the importance of the Inverse Compton process is the Compton parameter y. It quantifies the average energy gain of a photon when crossing the medium. This parameter is defined as the product of the average energy change per scatter with the mean number of scatters N. Brownian motion theory gives an estimate of the number of scatters: $\max(\tau, \tau^2)$. For a non-relativistic temperature and photons at low energy, y is defined by

$$y = 4\frac{kT_\text{e}}{m_\text{e}c^2} \times \max(\tau, \tau^2). \tag{2.27}$$

If $y \geq 1$, the Comptonization process is important, because the Comptonized spectrum has more energy than the spectrum of seed photons. As a result, the total photon energy and spectrum will be significantly altered, whereas for $y \ll 1$ the total energy is not much changed. For more details, see [Ghisellini 2012].

In conclusion, soft photons from the disk gain energy by multiple Compton scattering with the hot electrons forming a corona. This leads to a power-law spectrum with a high-energy cutoff at $\sim 3\,kT_\text{e}$ when the source is in the soft state, and $\sim kT_\text{e}$ when the source is in the hard state. The spectral shapes depend mainly on the temperature and the optical depth of the plasma. The spectral slope becomes harder

(i.e. the spectral index of the power law decreases $\Gamma < 2$) when these parameters increase. The energy cutoff is determined essentially by the electrons temperature; its shape also depends on the optical depth. If the optical depth is sufficient, photons will have time to thermalize at the electron temperature, and a saturation bump will be visible at high energy (as illustrated in Fig. 2.5).

2.2.2 Photoelectric absorption

Photoelectric absorption (or photoabsorption) is observed in the spectra of X-ray sources at low energy. Some of the X-ray photons are absorbed by particles in the interstellar medium, between the source and the observer, such as the interstellar dust, or material in dense molecular clouds. Furthermore, X-ray binaries may suffer extra absorption from the companion star or from material in the accretion disk. It is the dominant process at low photon energies (for $E < 1 - 10$ keV). keV

This process corresponds to the absorption of a photon of energy $h\nu$ by an atom or an ion, and to the ejection of a bound electron. That is why this effect is also named "bound-free" absorption. The incident photon transfers the totality of its energy to the atom. If the energy of the photon is greater than the energy of the X-ray atomic energy level E_I, an electron is ejected from that level. A large amount of the remaining energy is carried away as the kinetic energy of the ejected electron E_e:

$$E_e = h\nu - E_{\mathrm{nlj}} \tag{2.28}$$

with E_{nlj} the bond dissociation energy of the electron in the atom. The higher the energy of the photon, the more likely it is for it to eject electrons that are more bound to the nucleus.

The probability of absorbing photons is energy dependent; low-energy X-rays are more absorbed than high-energy X-rays, since the cross section for photoelectric absorption decreases as roughly ν^{-3}. Moreover, the absorption cross section strongly depends upon the atomic number Z of the elements (such as H, He, C, O, ...). Hence, although heavier elements are less abundant than hydrogen, their contributions to the total absorption cross section is more significant at X-ray energies. These factors are combined into the photoelectric absorbing cross section defined by [Heitler 1954]

$$\sigma_K = 4\sqrt{2}\sigma_T\alpha^4 Z^5 \left(\frac{m_e c^2}{h\nu}\right)^{7/2} \propto \frac{Z^5}{(h\nu)^{7/2}} \tag{2.29}$$

where $\alpha = e^2/4\pi\varepsilon_0\hbar c$ is the fine structure constant and $\sigma_T = 8\pi r_e^2/3 = e^2/6\pi\varepsilon_0^2 m_e^2 c^4$ the Thomson cross section. This is the analytic solution for the absorption cross section for photons with energies $h\nu \gg E_I$ and $h\nu \ll m_e c^2$ due to the ejection of electrons from K-shells of atoms (from 1s level). For more details about the calculations of these cross sections, see [Karzas 1961].

Absorption cross sections are then summed, weighted by the cosmic abundance of the different elements

$$\sigma_e(E) = \frac{1}{n_H} \sum_i n_i \sigma_i(E). \tag{2.30}$$

As hydrogen is the most abundant element, it is customary to express the observed absorption as N_H, the equivalent number of neutral atoms per cm^2 in a column between the source and the observer.

2.2.3 The reflection component

Relatively cold matter forming the accretion disk is irradiated by hard X-rays in the vicinity of the compact object. It results in a reflected spectrum whose most notable signature is the iron Kα line at $6.4 - 7$ keV. This emission line provides an extremely useful spectral diagnostic for matter in the innermost regions of the accretion flow around the compact object [Fabian 1989]. Other notable features are emission lines at lower energy, a Compton hump at ~ 30 keV, and Fe absorption edges, as shown in Fig. 2.6.
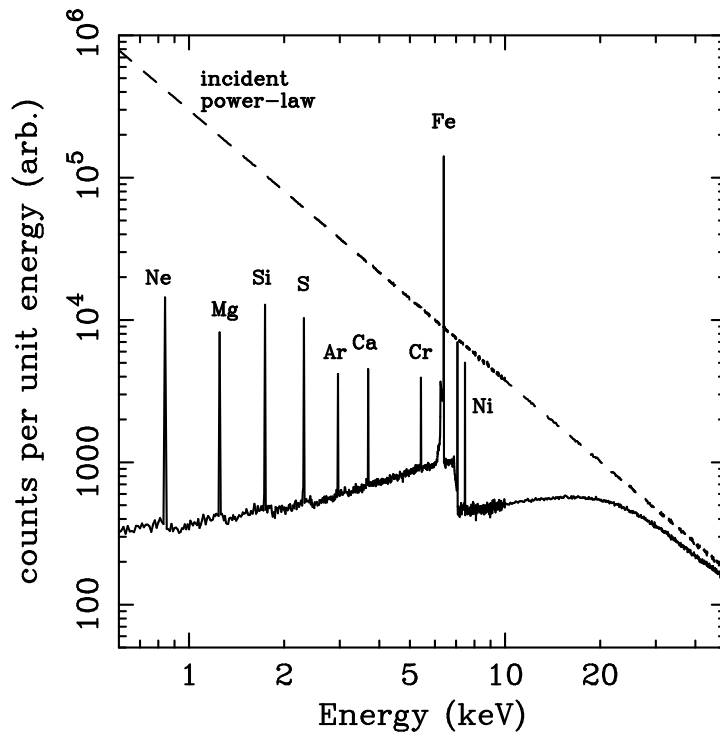
Figure 2.6: Monte Carlo simulation showing the reflection spectrum obtained by an incident power-law X-ray spectrum (dashed line) on a cold gas with cosmic abundances. The main reflected features are the Fe Kα fluorescent line at 6.4 keV, the Fe absorption edge at 7.1 keV, and the Compton reflection hump peaking at ~ 30 keV [Reynolds 1996].

The Fe line

The study of the Fe emission line shape constitutes a fantastic tool to infer properties of the innermost regions of the accretion disk in AGN, X-ray binary systems, and cataclysmic variables. It provides one of the most direct ways to probe the physics of the region of strong gravity in the close environment of the compact object. In the following, we discuss the origin of the Fe line, the influence of the inclination of the system with respect to the line of sight and the ionization state of the matter in the disk, on the line profile [Reynolds 2003, Fabian 2000].

Fluorescent and recombination emission lines are produced by irradiation of the cold matter in the near vicinity of the compact object. Following the K-shell photoabsorption by a high-energy X-ray photon, the inner shell electron of an atom or an ion is removed. De facto, the ion becoming highly unstable, electron cascades from higher shells of the ion will fill the vacancy. This process is accompanied either by a radiative transition, such a Kα line photon (fluorescence), or by radiationless transfer of energy to an electron (Auger effect) [Bambynek 1972]. Fig 2.7 illustrates the atomic processes occuring in the disk. The probability that the ion de-excites via fluorescence rather than Auger effect is given by the fluorescent yield, which depends mainly on the nuclear charge ($\propto Z^4$). Low-Z elements overwhelmingly tend to ionize, while iron and much heavier elements strongly tend towards fluorescence.
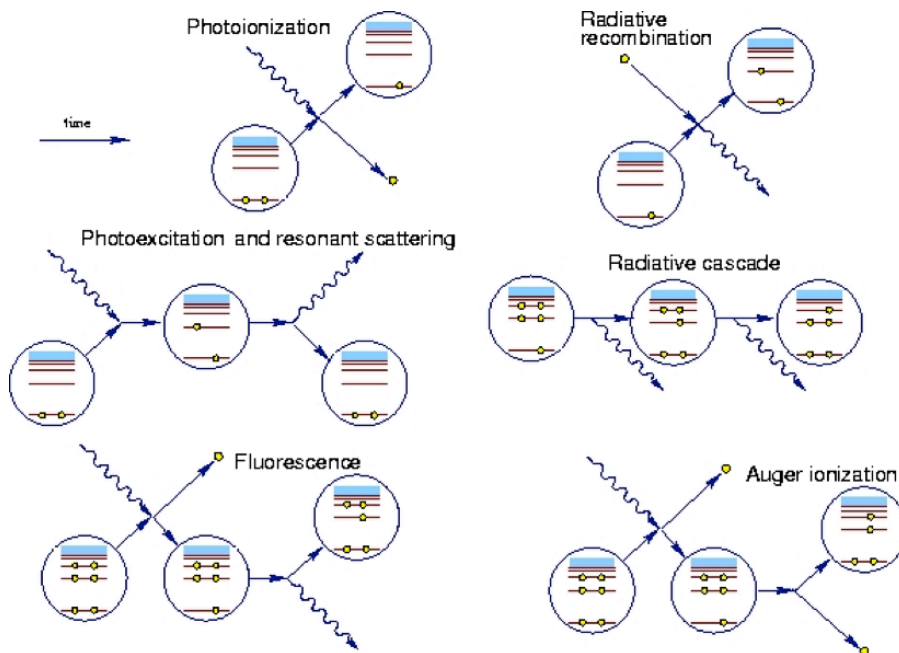
Figure 2.7: Illustration of the possible atomic processes in the accretion disk.

Fluorescence lines are described first by the shell of the electron hole. In addition, in analogy with hydrogen-like ions, α and β indicate the Δn of the transition. Hence,

Table 2.1: Emission lines from neutral or weakly ionized iron (Fe I-XVII), and highly ionized iron (Fe XXV and Fe XXVI). Adapted from [Arnaud 2011].

Spectral line	Origin	Transitions	Energy (keV)
Fe	Fluorescence	$K\alpha_1$	6.4038
		$K\alpha_2$	6.3908
Fe XXV	Recombination/Fluorescence	R	6.7000
		I_2	6.6823
		I_1	6.6676
		F	6.6365
Fe XXVI	Recombination	$Ly\alpha_1$	6.9732
		$Ly\alpha_2$	6.9520

a Kα transition arises from $n = 2 \to 1$ and Kβ transition from $n = 3 \to 1$, with $n = 1, 2, 3$ corresponding to the K, L, M shells of the atom/ion, respectively. The probability to emit a Kβ photon is much lower than a Kα photon [Kikoin 1976].

Due to the combination of high fluorescent yield ($\omega_{K,Fe} = 34\%$ probability, [Kaastra 1993]) and its comparatively high cosmic abundance, the most prominent line is the Fe Kα fluorescent line emitted at ~ 6.40 keV.

Depending on the ionization state of the plasma forming the accretion disk, highly ionized iron can be detected at $6.67 - 6.70$ keV and $6.95 - 6.97$ keV, and is associated with Fe XXV (He-like) and Fe XXVI (H-like), respectively. The lines of He-like ions are formed partly by recombination of hydrogenic ions and partly by fluorescence following K-shell photoionization of Li-like ions:

$$hv + \mathrm{Fe\,XXIV} \leftrightarrows e + \mathrm{Fe\,XXV}, \qquad (2.31)$$

whereas H-like lines are only formed by recombination [Hatchett 1976]. These lines are reported in Table 2.1.

The iron line is intrinsically narrow but may appears broadened and skewed toward low energies. Indeed, the line probably originates from the inner part of the accretion disk (although this is still being discussed), where the effects of Doppler broadening and gravitational redshifts produce strong distorsions onto its profile, as illustrated in Fig. 2.8. Each "radius of disk" produces a symmetric double peaked line profile by Doppler effect, with the emission from matter moving in the direction of the observer (blue-shifted) and receding (red-shifted). Going closer to the compact compact, matter moves faster and undergoes relativistic effects. Hence, in addition to producing a broader profile in the innermost part of the disk, special relativistic beaming enhances the blue peak of the line. Moreover, gravitational redshift shifts the line to lower energy. Consequently, summing all the effects, the iron line appears as a broad and asymmetric line.

In addition, the resulting shape of the line depends upon the inclination of the system with respect to the line of sight. Consequently, the main parameters that
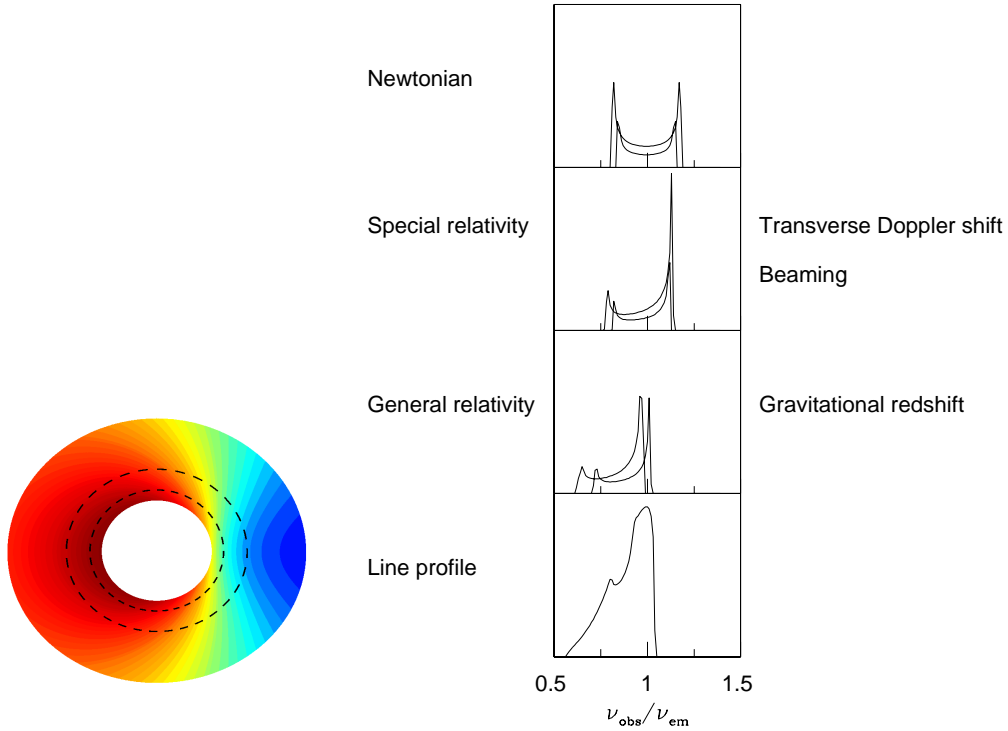
Figure 2.8: Left panel: representation of the accretion disk from the top, with matter approaching (blue) and receding (red). The dashed lines indicate two radii of the disk. Righ panel: in the three upper squares, the effects produced on the emission line profile (Doppler and relativistic effects) are represented. The two line profiles indicate the emission from the radii represented on the disk (on the left), the broadest one corresponding to the inner radius. The sum of these effects gives rise to a broad and skewed Fe line shape, as shown in the fourth square [Fabian 2000].

determine the line profile are the inner radius and the outer radius of the disk, the inclination of the system, and the radial dependence of the line emissivity. The effects of these parameters are shown in Fig. 2.10 [Fabian 1989]. The line emissivity is assumed to vary as r^q, since the geometry of the inner accretion disk surrounding the compact object is poorly understood.

Moreover, the emission line depends on the ionization state of the surface layers of the disk (due to the photoionization by X-ray irradiation). The ionization parameter is defined as :

$$\xi(r) = \frac{4\pi F_X(r)}{n_e} \tag{2.32}$$

where $F_X(r)$ is the X-ray flux received by unit area of the disk at a radius r, and n_e is density of electrons [Reynolds 2003]. It measures the ratio of the photoionization rate (proportional to n_e) to the recombination rate (proportional to n_e^2). Four

regimes can be distinguished depending upon the value of the ionization parameter [Matt 1993, Fabian 2000] (see Fig 2.9):

- $\xi < 100$ erg cm s^{-1} : the neutral regime. The iron line is expected at 6.4 keV in addition to a weak Fe absorption edge at 7.1 keV. This regime is also called "cold" reflection.

- $100 < \xi < 500$ erg cm s^{-1} : the intermediate ionization regime. Fe XVII−Fe XXIII[1] and a moderate absorption edge should be visible in the reflection spectrum. Since there is a vacancy in the L-shell of the Fe ions, ions can resonantly absorb the corresponding Kα line photons. Successive fluorescent emission occur, followed by resonant absorption, until the photon is destroyed by the Auger effect. Therefore a few line photons can escape the disk, resulting in a weak iron line.

- $500 < \xi < 5000$ erg cm s^{-1} : the high ionization regime. The ions are too highly ionized to permit the Auger effect. Line photons are subjected to resonant scattering. The lack of a destruction mechanism implies that they can escape the disk and produce a "hot" iron line. Fe XXV and Fe XXVI should be emitted at 6.67 and 6.97 keV, respectively, in addition to a large iron absorption edge.

- $\xi > 5000$ erg cm s^{-1} : the fully ionized regime. No atomic signature should be visible since the disk is too highly ionized. Consequently no iron line emission or edge are produced.

The other emission lines

Besides the detection of the strong Fe line, other emission lines are sometimes observed at lower energies, as shown in Fig 2.6. These lines are believed to have the same origin than the Fe line, i.e. in the inner part of the accretion disk, following the irradiation by hard X-rays. Their detection depends on their fluorescent yield and on the ionization state of the disk.

The Compton hump

Photoabsorption and Compton scattering are the two main processes in competition in the accretion disk. Depending on their energy, incident photons will undergo one or the other one of these processes. For photon energies smaller than ~ 15 keV, photons will be predominantly absorbed in the cold medium, whereas when $E > 15$ keV, photons will be mostly Compton scattered until they either escape the system or are photoabsorbed. The result of both effects is a broad hump in the spectrum at about 30 keV, also called a Compton reflection hump (see Fig. 2.6).

---

[1]Fe XXIII is a spectroscopic notation describing an emission or absorption line arising from electronic transitions within an Fe^{+22} ion.
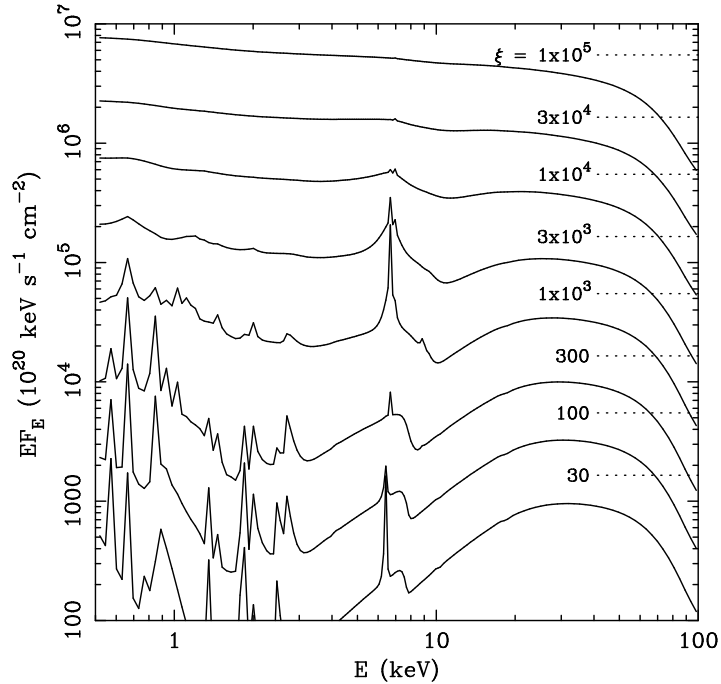
Figure 2.9: Reflection spectra from ionized matter for different values of the ionization parameter ξ. The dotted lines represent the level of the illuminating power-law continuum associated for each value of ξ [Fabian 2000].

The absorption edge

Another effect of the photoelectric absorption at low energy is the absorption edge. The probability of absorbing photons of a particular energy dramatically increases when the energy corresponds to the ionization state of an absorbing element, such as H, He, C, O, etc. The resulting jump in cross section is called an absorption edge. So the absorption edge may be produced and visible in the spectrum of X-ray sources when the incident photon energy is $h\nu = E_\mathrm{I}$. Ejection of electron from this energy level is impossible if the photons are at lower energy. The strong Fe K edge at ~ 7.1 keV (for neutral iron) can be detected in high resolution X-ray spectra of X-ray binary sources (see Fig. 2.6).

2.3   The states of a source

An X-ray binary source observed at different moments can show a variety of spectral shapes. By looking at its light curve, which represents the flux registered in a defined energy range as a function of time, the X-ray emission is indeed highly variable on time scales of minutes, days, months, or years. The All Sky Monitor (ASM) onboard RXTE enabled the monitoring of the activity of many sources in a continuous way, by
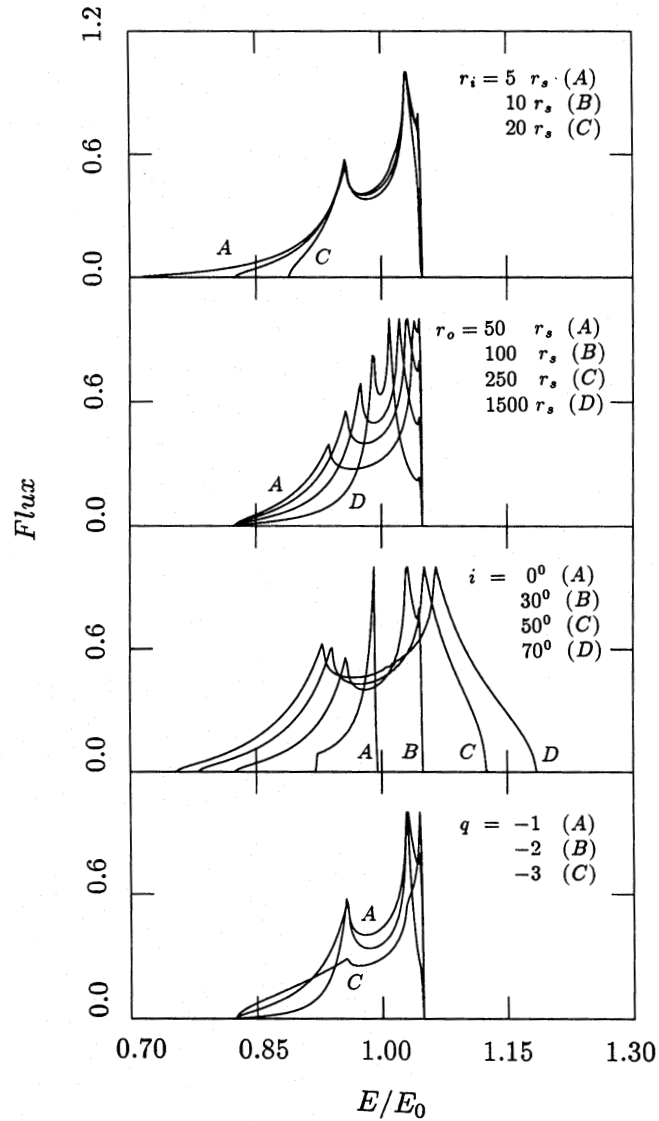
Figure 2.10: Influence of the inner radius of the accretion disk r_i, the outer radius r_o, the inclination i, and the emissivity index q, on the line profile. When one parameter is tested, the other ones are fixed at $r_i = 10\,r_s$, $r_o = 100\,r_s$, $i = 30°$, and $q = -2$ [Fabian 1989].

performing quasi-daily observations. It is now being replaced by the MAXI mission onboard the ISS. Depending on the type of sources, successions of outbursts, which correspond to a high X-ray luminosity and last from several days to several months, are generally visible and are separated by periods of low X-ray luminosity.

Based on the spectral properties of the X-ray emitting components, different spectral states are identified (see [McClintock 2006, Homan 2005]). The two main

states are: the high-soft state, dominated by the thermal emission from the accretion disk and observed during the outbursts; and the low-hard state, dominated by the emission from the corona, during the low X-ray luminosity periods. The intermediate state defines the transition phases between both states, as illustrated in Fig. 2.11.

The different states are most likely related to changes in the accretion physics, such as the rate at which matter is deposited into the accretion disk [Hameury 1986], the amount of matter in the accretion disk, the instabilities in the disk [Mineshige 1989], and/or the way in which the matter moves into the compact object. However, the processes underlying all these are not yet well-understood. That is why it is important to investigate the physical conditions that give origin to the different states.

In addition to spectral analysis, the timing analysis reveals the presence of fast quasi-periodic oscillations (QPOs) in the power density spectra (PDS). PDS describe how the power of a time series is distributed with frequency. Mathematically, it is defined as the Fourier transform of the autocorrelation sequence of the time series. QPOs are believed to originate in the innermost regions of the accretion disk around the compact object.

Moreover, multiwavelength observations (radio, IR, optical, UV, X and gamma-ray) bring a more complete view of what happens in the source, helping in the understanding of state transitions.
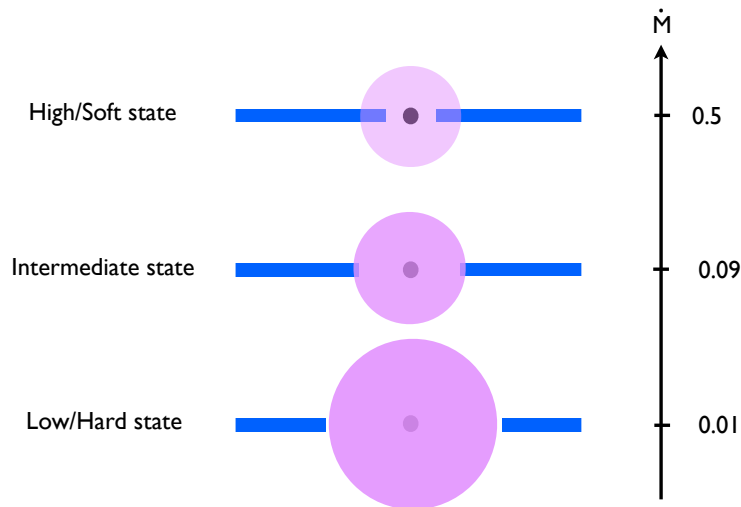
Figure 2.11:   A possible side-view schematic representation of the accretion disk (blue) and the corona (pink) for different states of an X-ray source. From the soft to the hard state, the disk could be truncated farther from the compact object, the corona more opaque, and the mass accretion rate lower.

In the following, the two main spectral states (the high-soft state and the low-hard state) are discussed more in more detail. Then, the general schemes associated with the state transitions for both black hole and neutron star X-ray binaries are

exposed.

2.3.1 The soft state

A source is said to be in the high-soft state, commonly named soft state, because of its brightness in soft X-rays and softness in hard X-rays. The thermal component at ~ 1 keV dominates the spectrum. This component, associated with the geometrically thin optically thick accretion disk, can be fitted by a blackbody or by a multi-temperature blackbody. The disk is thought to extend down to the compact object, i.e. the neutron star surface or the last stable orbit in the case of a black hole.

At higher energy, a non thermal component is detected and is fitted by a weak steep power law with a photon index $\Gamma \sim 2.1 - 3$ (with $N(E) \propto E^{-\Gamma}$ where N is the number of photons of energy E). This soft power law is associated with inverse Compton upscattering of soft photons coming from the disk by non-thermal distribution of electrons in a hot relativistic plasma (the so-called corona). This component illuminates the disk and gives rise to strong reflection features [Done 2007].

The study of sources during the soft state is of great interest to prove the existence of a last stable orbit in black holes, and to estimate black hole spin. In the case of neutron star binary systems, it is also important in order to understand the role of the boundary layer located between the neutron star surface and the inner part of the accretion disk. Moreover it helps to define equations of state of neutron stars with more precision, providing direct values of the radius of these exotic objects. Consequently, the soft state offers a unique opportunity to study accretion processes and relativistic effects very close to the compact object.

2.3.2 The hard state

When the soft X-ray luminosity is faint and the spectrum is hard, the source resides in the low-hard state, also called hard state. The accretion rate is found to be relatively low with respect to the soft state. The spectrum is dominated by a hard power law with a spectral index defined as $\Gamma \sim 1.5 - 1.9$, and a high-energy cutoff.

At low energies, the weak thermal component is consistent with the accretion disk being cooler than in the soft state and thought to be truncated farther from the compact object [Done 2007]. Evaporation of the inner parts of the disk could explain this process but remains a hypothesis for the moment [Meyer 2000, Mayer 2007].

Since the disk is expected to be truncated at a larger radius from the compact object and at a lower temperature than in the soft state, interactions between soft photons from the disk and hot electrons forming the corona are less efficient at cooling the corona by Comptonization. As a result, the corona dominates the spectrum. Moreover, the disk is less ionized and the reflection features are weaker than in the soft state.

Timing analysis reveals that fast time variability is dominated by a strong band-limited noise. Sometimes low frequency QPOs are observed [Wijnands 1999].

The hard state is becoming more studied in the context of multiwavelength observations of X-ray binaries since clear connections have been noticed between X-ray and radio properties with jet detection [Gallo 2012, Corbel 2003].

In conclusion, the hard and soft states represent two different behaviors of the source in the spectral and timing domains. The study of these correlations in each state is important in order to better understand the accretion processes. We note that the spectral and timing variablities are easily observed in X-ray binaries whereas it is more difficult in AGN, since the time scales in which changes occur are much higher.

2.3.3 General schemes for spectral transitions

As explained previously, the spectral and timing analyses reveal that black hole and neutron star binaries reside in different states. It is possible to follow the activity of a source through the hardness intensity diagram (HID) in case of black holes, and the color-color diagram (CD) for neutron stars, making the other intermediate states appear.

Black hole binaries

The state transitions in black hole binaries are often divided into four or five canonical states [McClintock 2006, Belloni 2010] related to the luminosity of the source, the spectral and timing dominant signatures, and the presence or not of jets visible in radio and near IR. With its "q shape", as illustrated in Fig. 2.12, the HID is the most famous diagram capable to reconstruct the different phases of a source during an outburst. In this diagram, the total count rate is plotted as a function of hardness, which is defined as the ratio of the observed counts in two different energy bands. Each side of the "q" represents a distinct state of the source:

- Low/Hard state (HS): associated with the vertical-right side of the "q", it corresponds to the start and the end of an outburst. The spectrum is usually hard, with a power-law index $\Gamma \sim 1.6 - 1.7$. The timing analysis (performing the PDS decomposition in some Lorentzian components) reveals type C QPO peaks. Compact jets can be observed in radio and IR [Gallo 2003, Fender 2004].

- Hard intermediate state (HIS): marks the first transition between the hard state and the soft state, on the top horizontal side of the "q". The spectrum becomes softer, with $\Gamma \sim 2.4 - 2.5$, and the disk component is more visible at low energy. The PDS looks like that in the hard state, however the characteristic frequencies are higher.

- Soft intermediate state (SIS): the spectrum is slighlty softer than in the HIS, however the timing properties differ from the previous states, with the appearance of type A or type B QPOs in the PDS.

- High/Soft state: the spectrum is dominated by a thermal disk component, leading at a very soft spectrum. Weak QPOs can be observed in the PDS, with notably type B QPOs. When the source is in this state, no jet is detected in radio wavelengths.

See [Casella 2004, Casella 2005] and references therein for explanations of the different QPO types.
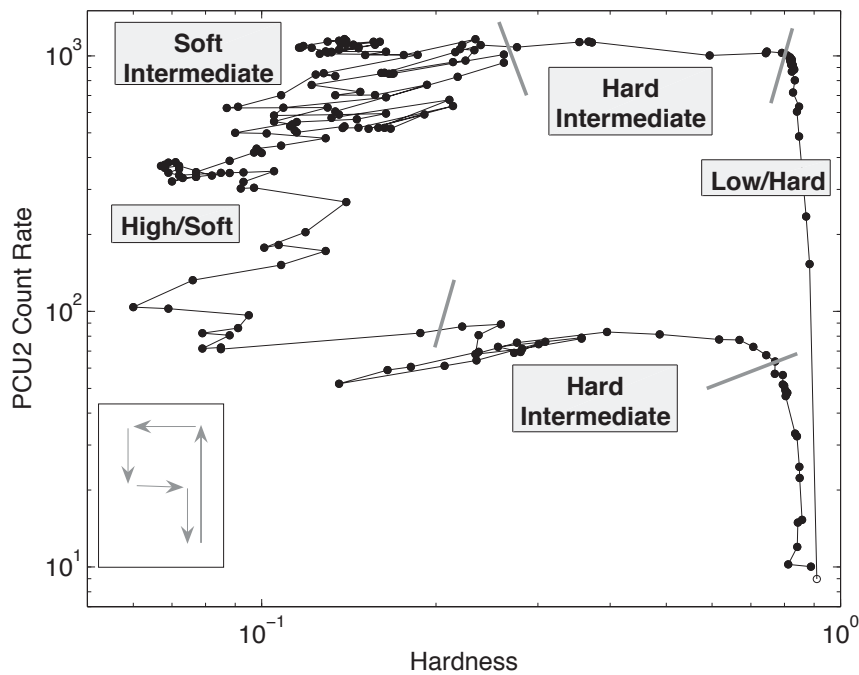
Figure 2.12: Hardness-Intensity diagram (HID) corresponding to the outburst of GX 339-4 observed in 2002/2003 with RXTE/PCA. The grey lines indicate the state transitions presented in the text. The arrows on the bottom-left of the figure represent the time evolution of the outburst, forming a "q-shape" [Belloni 2005].

Neutron star LMXBs

The HID with the "q-shape" previously described for black hole binaries is also valid for neutron star LMXBs. However it is more widespread to trace the color-color diagram (CD) of a source to follow its evolution and to classify sources into two sub-classes: atolls and Z sources, named after the path they describe in the diagram [Hasinger 1989] (see Fig. 2.13).

This diagram represents the soft color (ratio of count rates in the two lowest energy bands) plotted against the hard color (ratio of count rates in the two highest

energy bands). Atoll and Z sources differ mainly in terms of luminosity and magnetic field, Z-sources having higher mass accretion rate and magnetic field ($B \geq 10^9$ G) than atoll sources [Gierlinski 2002]. While Z sources are typically brighter ($>$ 0.5 L_{Edd}) with a higher mass accretion rate, atolls are seen over the same range of luminosity as black hole binaries ($< 0.1\, L_{\text{Edd}}$). Thus, atoll sources constitute a nice sample of sources to compare the state transitions with black hole binaries.

Interestingly, atoll sources present two distinct spectral states: the soft "banana" and the hard "island", named so from their shapes in the CD (see Fig. 2.13). Such sources perform transitions between these states, tracing a C (or atoll) shaped path from the hard island state at the top right of the C, down to the lower and then upper banana branch at the bottom of the C, with the source luminosity and mass accretion rate increasing. The correlation with the black hole binaries states is clear, with the island state corresponding to the hard state and the banana branch corresponding to the soft states.

In both atoll and Z sources, most of the X-ray spectral and timing properties depend only on the position of a source in this diagram. The main parameter that determines these properties and thus the evolution on the diagram is probably the mass accretion rate $\dot{m}$, which is linked to the accretion luminosity as $L_{acc} = \eta \dot{m} c^2$, where η is the accretion efficiency.
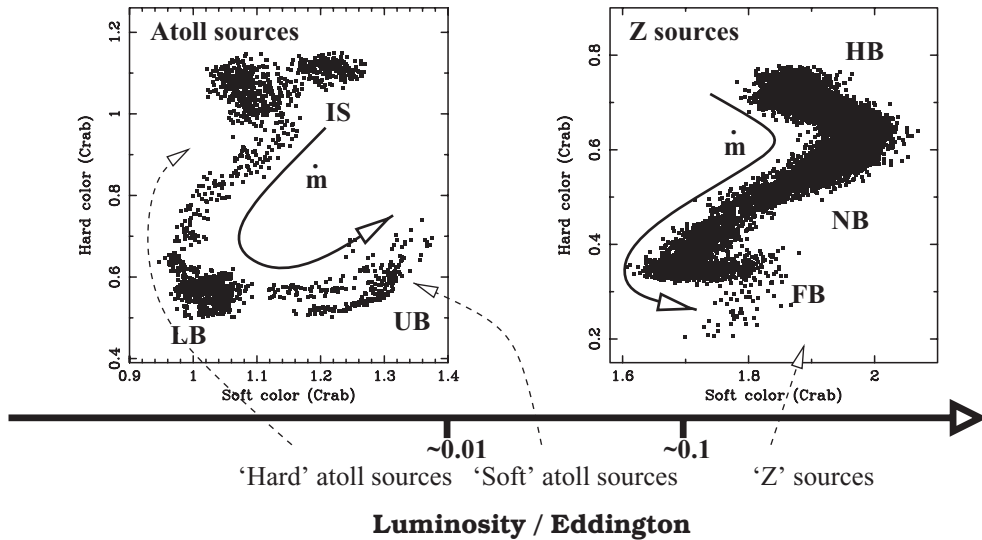
Figure 2.13: Comparison of color-color diagrams (CDs) associated with atoll and Z sources. The increasing mass accretion rate is indicated by the arrows. Two states are clearly defined for atoll sources, the island state (IS) and the banana state (LB Lower Banana and UB Upper Banana), corresponding to the hard and soft states, respectively. As for Z sources, three branches are distinguishable: the horizontal branch (HB), the normal branch (NB), and the flaring branch (FB) [Migliari 2006].

Part II

Data analysis

Although the broad aspects of X-ray binaries are well understood today, many questions remain unanswered especially regarding the regions closest to the compact object. The main physical questions that motivated my work concern the physics of the accretion flow in the innermost region of the accretion flow. I have particularly focused on the diagnostics brought by the study of the broad iron line that somehow traces the interaction of the corona and the disk (reflection), but also helps us to probe the effect of the huge gravitational potential through distortion of the line. Some of the key questions are: do we find the same exact processes than in black hole binaries? What is going on very close to the compact object? What is at the origin of the spectral changes in such sources?

After ten years of operation, the X-ray satellite XMM-Newton offers an ample archive of public data, which is extremely useful for determining the properties of X-ray binary systems. In particular, it provides most of the detections of well-determined profiles corresponding to broad iron lines. Thus XMM-Newton represents one of the best instruments at present to thoroughly study the iron line shape.

In this section dedicated to data analysis, I first explain the progression from the detection of X-ray photons (with satellites such as XMM-Newton) to the data reduction. Then, I present the work I performed on two neutron star LMXBs, MXB 1728-34 and 4U 1705-44, followed by a chapter devoted on the tests I performed on the reflection model called Xillver.
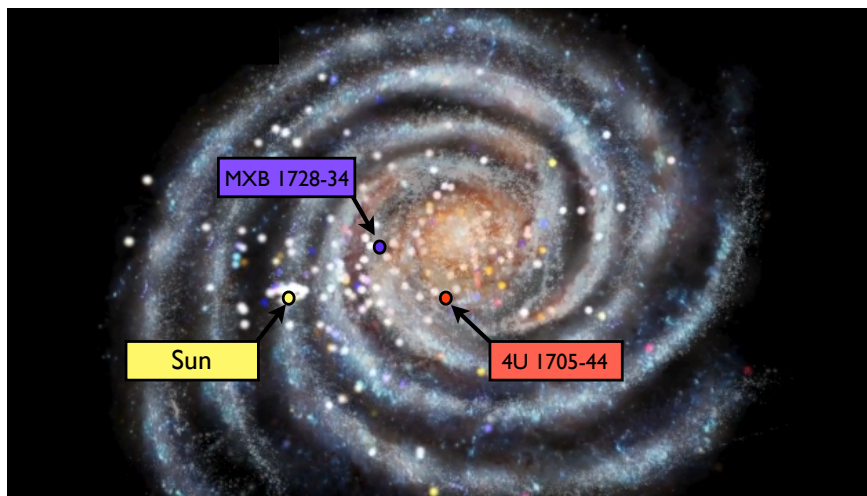
Figure 2.14: Illustration of the Galaxy with the positions of the Sun and the two LMXBs studied: MXB 1728-34 and 4U 1705-44. The other circles indicate the position of high-energy X-ray and gamma-ray sources observed with the INTEGRAL satellite. All sources are represented by "big" circles for clarity. To respect their real size, they should appear as very small points, like the rest of the stars on the arms of the Galaxy. Adapted from an animation created by ESA: C. Carreau & E. Kuulkers.

The detection of X-ray photons

Contents

X-ray astrophysics is a relatively new field (1960's), which represents a real challenge for astronomers, since observations are possible only above the Earth's atmosphere. The X-ray band is located between the ultra-violet and the gamma-ray bands (see Fig 3.1), corresponding to $0.1 < E < 100$ keV (or $9 > \lambda > 0.01$ nm). X-rays at low energy (corresponding to long wavelengths) are called soft X-rays and those at high energy (short wavelengths), hard X-rays.

X-ray detectors count photons, which implies that X-ray astronomy is a Poissonian science. An incoming X-ray photon is related to "an event" characterized by its position on the detector, its pulse height (connected to the X-ray energy of the incoming photon), its arrival time at the spacecraft, and its shape (used to separate X-ray events from particles). Data from X-ray observatories allow us to better understand the nature of sources and the mechanisms by which X-rays are emitted.

I first give a bief review on the evolution of X-ray missions, from the first exploration of the X-ray sky, to the current satellites operating in orbit around the Earth. Then I present the XMM-Newton observatory, since my work was mainly based on its observations.

3.1 X-ray missions

The Earth's atmosphere is opaque to X-rays (and that is essential for the appearance and subsistence of life). Indeed, X-ray photons are absorbed by atoms present in the atmosphere through photoelectric absorption. Consequently, X-ray observatories
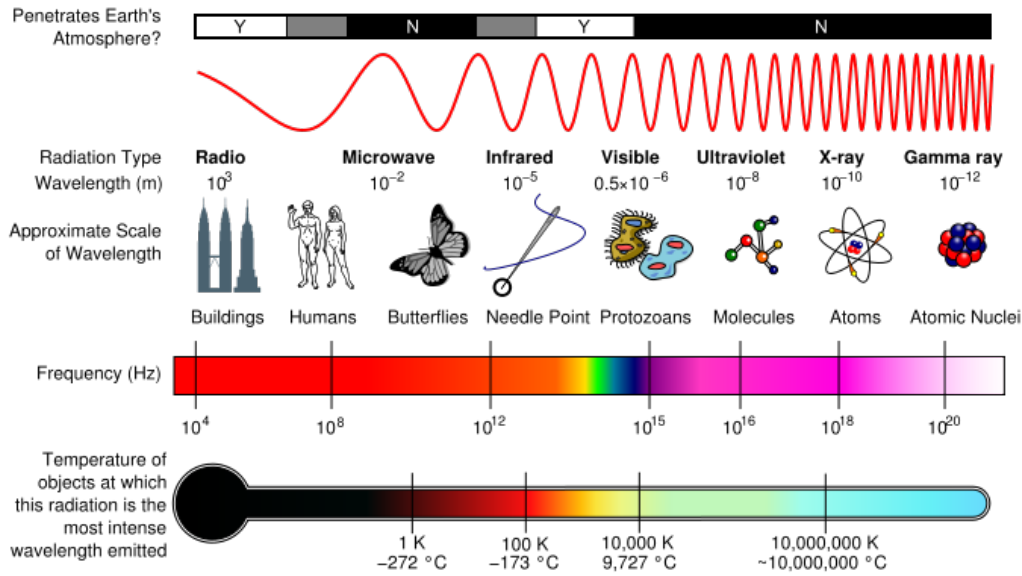
Figure 3.1:   Illustration of the electromagnetic spectrum and some of its properties across the range of frequencies and wavelengths. From Wikipedia.

have to be launched above the atmosphere, as illustrated in Fig 3.2. Therefore, they are subjected to huge constraints on weight, size and cost.
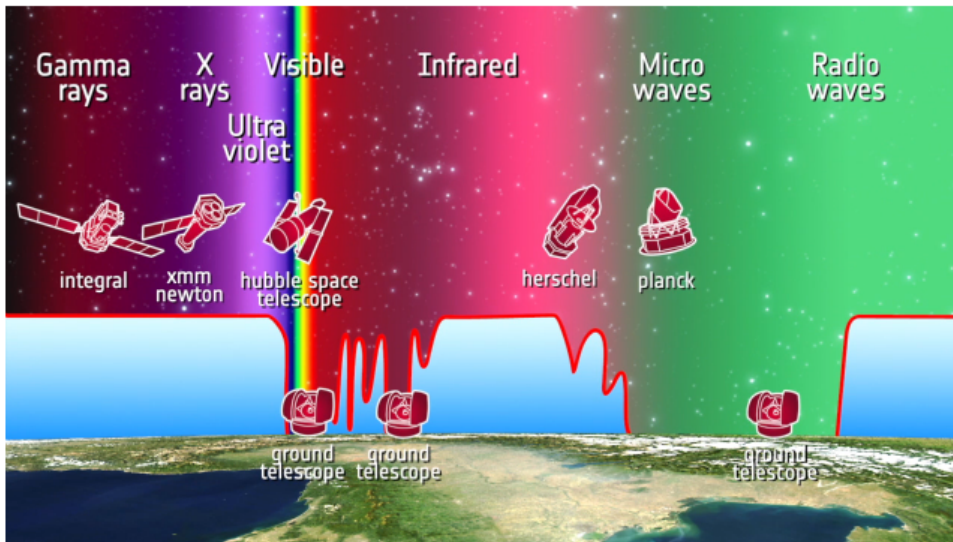
Figure 3.2:   Electromagnetic spectrum with the Earth's atmospheric opacity and the types of telescopes used to study different parts of the spectrum. X-rays are blocked by the upper atmosphere. Credits: ESA C. Carreau & E. Kuulkers.

In high energy astrophysics we use the corpuscular nature of the photons rather than the wave one (as opposition to optical or radio astronomy). Because of the weak flux emitted by an X-ray source (a flux of one photon per square centimeter per second in the $1-10$ keV range constitutes a bright X-ray source), individual X-ray photons can be detected. Hence X-ray detectors look like those used in particle physics experiments, such as proportional counters and scintillation detectors. More recently, CCDs (Charge Coupled Devices) have been introduced. The instrument detects the charge deposited on the detector by the incoming photon.

An ideal detector would possess a high spatial resolution, a large collecting area, and good temporal and energy resolutions. However, reality is different; such detectors do not exist even as they become more and more advanced thanks to technological advances.

3.1.1 History

X-ray astronomy was mainly born in a military context after the Second World War. The beginning of the exploration of the X-ray sky was marked by the launch of rocket flights above the atmosphere for a few minutes, used to study the X-ray emission from the solar corona. Then in 1962, R. Giacconi and his team, composed of H. Gursky, F. Paolini and B. Rossi, detected a very bright, non-solar X-ray source later designated as Scorpius X-1 (because of its location in the Scorpius constellation). He subsequently won the Nobel Prize for Physics in 2002 for his development of X-ray astronomy.

With the improvement of detectors, offering in particular a better spatial resolution, Scorpius X-1 was later identified as a binary system containing a neutron star. Then, other X-ray binaries were detected in addition to X-ray emission from supernovae and radio galaxies (e.g. M87, Cygnus-A).

In 1970, NASA launched the first satellite (called "Uhuru") dedicated to X-ray astronomy. Developed by Giacconi's team, Uhuru performed a map of the X-ray sky, detecting more than 300 individual sources and providing systematic monitoring of variable X-ray sources. Its main discoveries include the pulsations from X-ray binaries and the X-ray emission from galaxy clusters. During the following years, new satellites were built (ANS, Ariel-V, SAS-3, OSO-8, and HEAO-1), each time more sophisticated, with more efficient X-ray detectors. They helped to identify new classes of astronomical objects as X-ray sources, observed more types of time variability from X-ray binaries, and detected the iron emission line.

A revolution in X-ray astronomy was engendered with the Einstein Observatory in 1978. Thanks to the combination of an X-ray telescope and an imaging detector, it provided the first X-ray images of many objects, and had the necessary sensitivity for the observing of stars, binaries, galaxies, galaxy clusters and AGN. Moreover the Einstein Observatory was a real innovation since the data-reduction pipeline became automated and the archive became public.

The 1980's were years of progress for Europe and Japan in X-ray astronomy, with the launch of Hakucho, Tenma, EXOSAT (ESA), and Ginga. Notably, these

X-ray observatories permitted the discovery of quasi-periodic oscillations (QPOs) in X-ray binaries, iron emission and absorption lines from AGN, and iron emission lines from the Galactic center.

At the beginning of the 1990's, the ROSAT satellite, which was the fruit of a German, US, and UK collaboration, enabled the production of a catalog listing more than 150 000 objects thanks to its all-sky-survey during the first six months. The satellite was also used for targeted observations, such as supernova remnants, clusters of galaxies, structure in the interstellar medium, and comets.

Launched in 1989, the Russian X-ray/gamma ray mission Granat operated for almost 9 years. Using the coded-mask technique, the SIGMA instrument was the predecessor of the current INTEGRAL mission. Granat performed a very deep imaging of the galactic center region and enabled the discovery of electron-positron annihilation lines from the Galactic microquasar 1E 1740-294 and the X-ray Nova Muscae.

In 1993, ASCA (resulting from a collaboration between ISAS and NASA) was the first satellite to use X-ray sensitive CCDs instead of proportional counters or scintillators, providing better imaging and spectroscopic properties. The capabilities of X-ray CCDs revolutionized X-ray astronomy, thanks to their sensitivity and linear brightness response. They represent an important step in the advancement of technology and allowed us to study the iron in binary sytems with more accuracy.

Two years later, the RXTE satellite was launched by NASA. Designed to collect many events from bright sources in order to examine their variability down to microsecond timescales, the satellite was endowed with large area proportional counters. The all-sky monitor (ASM) onboard RXTE was of great interest for the tracking of the brightest sources on day to year timescales, allowing us to follow the evolution of their X-ray emission with time and the discovery of many new transient objects. Amongst the numerous results from RXTE, two of the most important are the determination of spin periods in LMXBs and the detection of kHz QPOs in many sources. The RXTE mission ended on January 2012 and the ASM, which was operational for 16 years, was relayed by the Japanese MAXI detector installed onboard the International Space Station (ISS) in 2009.

In 1996, the Italian-Dutch BeppoSAX satellite became the first X-ray mission with the capability of observing sources over more than three orders of magnitude of energy, from 0.1 to 200 keV, with a relatively large area and quite good energy resolution. The wide spectral coverage permitted the study of several areas of X-ray astronomy such as compact galactic sources (shape and variability of the continuum, iron line, cyclotron lines, study of X-ray transients), AGN, clusters of galaxies, supernova remnants, normal galaxies, stars and gamma-ray bursts.

The current generation of X-ray satellites is composed of the Chandra X-ray Observatory, XMM-Newton, INTEGRAL, Swift, Suzaku, MAXI and NuSTAR. These satellites offer a better resolution than the previous ones, and are discussed in more detail in the following section.

Table 3.1: Completed and operating X-ray satellite missions (adapted from [Arnaud 2011] and NASA's HEASARC. Only the main space agencies are reported for each X-ray mission, however there are often collaborations with other agencies which are not mentioned here.

Name	Operation years	Bandpass (keV)	Main Space Agency
Uhuru	$1970 - 1973$	$1.7 - 18$	NASA
ANS	$1974 - 1976$	$0.2 - 30$	NISR/NASA
Ariel-V	$1974 - 1980$	$0.9 - 1\,200$	SRC/NASA
SAS-3	$1975 - 1979$	$0.1 - 60$	NASA
OSO-8	$1975 - 1978$	$0.15 - 1\,000$	NASA
HEAO-1	$1977 - 1979$	$0.15 - 10\,000$	NASA
Einstein	$1978 - 1981$	$0.15 - 20$	NASA
Hakucho	$1979 - 1985$	$0.1 - 100$	ISAS
Tenma	$1983 - 1985$	$0.1 - 100$	ISAS
EXOSAT	$1983 - 1986$	$0.05 - 50$	ESA
GINGA	$1987 - 1991$	$1.5 - 500$	ISAS
Granat	$1989 - 1998$	$2 - 100\,000$	RSA
ROSAT	$1990 - 1999$	$0.1 - 2.4$	GAC/NASA
ASCA	$1993 - 2000$	$0.4 - 10$	ISAS
BeppoSAX	$1996 - 2002$	$0.1 - 300$	ASI/NIVR
RXTE	$1995 - 2012$	$2 - 250$	NASA
Chandra	$1999-$	$0.06 - 10$	NASA
XMM-Newton	$1999-$	$0.15 - 15$	ESA
INTEGRAL	$2002-$	$4 - 10\,000$	ESA
Swift	$2004-$	$0.2 - 150$	NASA
Suzaku	$2005-$	$0.2 - 600$	JAXA/NASA
MAXI	$2009-$	$0.5 - 30$	JAXA
NuSTAR	$2012-$	$5 - 80$	NASA

NASA: National Aeronautics and Space Administration; NISR: The Netherlands Institute for Space Research; SRC: Science Research Council (UK); ISAS: Institute of Space and Astronautical Science; ESA: European Space Agency; RSA: Russian Space Agency; GAC: German Aerospace Center; ASI: Italian Space Agency; NIVR: The Netherlands Agency for Aerospace Programs; JAXA: Japan Aerospace Exploration Agency; RIKEN: Institute of Physical and Chemical Research

3.1.2   The current generation of satellites

The current period is a "Golden age" for X-ray astronomy. It is the first time that so many X-ray missions perform observations at the same time. Chandra, XMM-Newton, Swift, Suzaku, INTEGRAL, MAXI and the recent NuSTAR, enable the combination of high angular resolution, large effective area, agility, high resolution spectroscopy, the observation of broad-band X-rays to hard X-rays, the monitoring, and the observation of hard X-rays respectively. They cover an extremely large energy range and allow the study of all types of X-ray sources, from the most luminous to the most faint and mysterious ones.
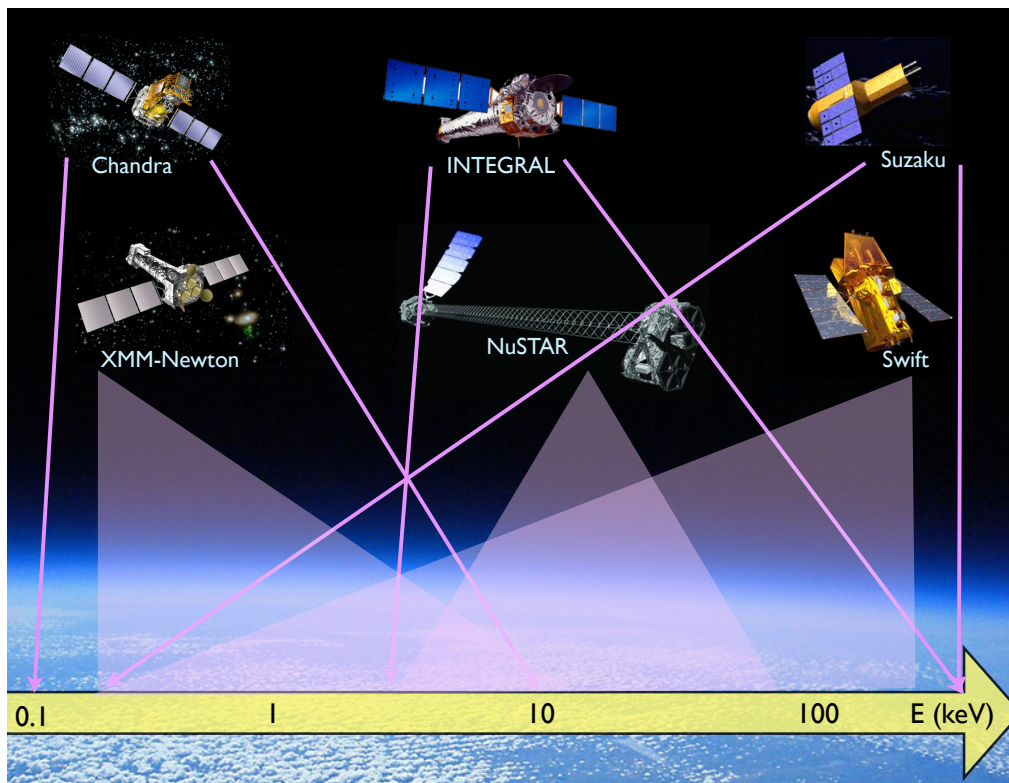
Figure 3.3: The current generation of X-ray satellites (2012) covering a wide spectral range, from 0.1 to 200 keV. The X-ray all-sky monitor MAXI onboard the ISS is not represented here for more clarity; it covers the energy band 0.1-30 keV. Details of the satellites's energy ranges are given in Table 3.1.

Most of these current missions are equipped with X-ray CCDs. They provide a substantially better spectral resolution than proportional counters, allowing us to measure with a higher precision absorption and/or emission lines such as the Fe line at $6.4 - 7$ keV, the column density of absorbing material, the electron temperature of hot diffuse plasmas, the power-law photon index in non-thermal plasmas, and the detection of exponential cut-offs (if they occur in or near the CCD bandpass).

Launched in 1999, Chandra (a NASA observatory) and XMM-Newton (an ESA mission) represent the beginning of the area of powerful telescopes for the exploration of the X-ray sky. The Chandra X-ray observatory is designed to detect X-ray emission from very hot regions of the Universe such as exploded stars, clusters of galaxies, and matter around stellar-mass and supermassive black holes. This high resolution imaging telescope provides images with angular resolution $\Theta \sim 0.5$ arcsec, comparable to the best images obtained by large ground-based optical telescopes.

Thanks to its large collecting aperture, XMM-Newton performs observations of X-ray sources with high spectral resolution. It is one of the most successful X-ray missions, due to its weight (it is the heaviest satellite) and onboard technology. More information on XMM-Newton is given later, in a section dedicated to this satellite.

Swift is a NASA mission launched in 2004 and dedicated for answering and solving the gamma-ray burst (GRB) mystery. GRBs are the most powerful explosions in the Universe seen since the Big Bang, and are most likely associated with the birth of a black hole in a massive stellar explosion, or the collision of two neutron stars. These explosions approximately occur once per day and are brief (from a few milliseconds to a few hundred seconds) but intense flashes of gamma radiation. As soon as Swift detects a burst, it relays its location to ground stations, allowing both ground-based and space-based telescopes around the world the opportunity to observe the burst's afterglow.

Suzaku is the fifth Japanese X-ray satellite. Since 2005, it has performed various observational studies for a wide variety of X-ray sources, with a high energy resolution and a high sensitivity over a wide energy range from 0.3 to 600 keV. Suzaku is dedicated to the study of hot plasmas in various X-ray sources, the structure and evolution of galaxy clusters, and the spectroscopy and accretion flow of black hole candidates, neutron star binaries and AGN.

INTEGRAL (INTErnational Gamma-Ray Astrophysics Laboratory) celebrated the 10th anniversary of its launch in October 2012. Initially planned for a duration of 2 years, this ESA scientific mission dedicated to studying hard X-rays and gamma-rays is still operating. INTEGRAL uses the coded aperture mask technique for three of its instruments. Its main science objectives are compact objects, extragalactic astronomy, stellar nucleosynthesis, the Galactic center, identification of high energy sources, particle processes and acceleration.

MAXI (Monitor of All-sky X-ray Image) is a JAXA instrument onboard the ISS that has continuously monitored astronomical X-ray objects over a broad-energy band from 0.5 to 30 keV since 2009. MAXI enables the scan of almost the entire sky once every 96 minutes. The monitoring of $\sim 1\,000$ X-ray sources allows us to follow their evolution and to be warned when significant changes in the flux of X-ray sources are detected.

NuSTAR (Nuclear Spectroscopic Telescope ARray) focuses on the hard X-ray sky. Launched on June 13, 2012 by NASA, it uses grazing incidence optics with long focal lengths (> 10 m) to obtain both a good angular resolution and a low background. NuSTAR aims to study the hidden Universe; the distribution of black holes through the cosmos in order to understand how they affect the formation of

galaxies; what powers the most extreme active galactic nuclei; but also the distribution of stellar remnants in the Galaxy, the chemical enrichment from star explosions, non-thermal processes, etc.

3.1.3   Future generation of satellites

A dark future for X-ray astronomy? The current world wide economic crisis context has had a serious impact on the next generation of satellites; it is becoming very difficult for some countries to fund space missions. Unfortunately, some countries have stopped investing in missions, and mission projects have to be re-evaluated, with some goals or instruments being cancelled. However, it is very important to keep a few satellites in orbi, so as to cover the whole spectral X-ray range, and to pursue the multi-wavelength observation campaigns which enable us to understand the complex emission processes of many sources.

The future generation of X-ray satellites should help to answer some of the key science questions in the context of accreting objects such as: what happens close to the compact object? Is there an accretion flow between the inner part of the disk and the compact object? What is its nature? How does accretion affect the immediate environment? How does a black hole evolve with time? In addition, they should help to better constrain the EOS of neutron stars, and to measure black hole spins with more accuracy.

For this purpose, new X-ray observatories should provide a better low-energy response, faster readout rates, a larger effective area to collect more photons, keeping in mind that there is an upper mass limit for a satellite. For instance, XMM-Newton and Chandra were designed with the maximum mass possible. Hence new technologies must be used in order to decrease their mass, such as silicon pore, as proposed for the ATHENA mission. Moreover, it is important to have a good angular resolution. Among the projects proposed for future X-ray satellites, we have:

- ASTROSAT, "A Satellite Mission for Multi-wavelength Astronomy", is an Indian mission which has some similarities with RXTE and SWIFT. It is designed to conduct the simultaneous multi-wavelength monitoring of the intensity variations of cosmic sources; a sky survey in hard X-ray and UV ranges; broadband spectroscopic studies of X-ray binaries, AGN, supernova remnants (SNRs), clusters of galaxies, and stellar coronae; and studies of periodic and non-periodic variability of X-ray sources. The launch of this X-ray mission is planned for mid-2013.

- ASTRO-H, formerly known as "NeXT", is a Japanese mission (JAXA) which aims to provide insights into the behavior of matter in extreme gravitational fields; to determine the spin of black holes and the equations of state of neutron stars; to trace shock acceleration structures in clusters of galaxies and SNRs; to investigate the detailed physics of jets; and to trace the growth

history of the largest structures in the Universe. The launch of ASTRO-H is planned for mid-2014.

- SVOM, the Chinese-French "Space-based multi-band astronomical Variable Objects Monitor" mission has been designed to study and better understand Gamma-ray bursts (GRBs). It will permit us to measure the broadband spectral shape of the prompt emission and its temporal properties from visible to MeV. Additionally, it will enable us to quickly identify the afterglows of the detected GRBs in the X-ray and optical bands, including those that are highly redshifted (z>6), and it will measure the broadband spectral shape of the early and late afterglows in addition to its temporal evolution. The launch of the SVOM mission is planned for 2018.

- HXMT, the "Hard X-ray Modulation Telescope" is a collaboration between China and the UK. Its high sensitivity and spatial resolution will enable the production of an all-sky hard X-ray survey, the study of AGN; hard X-ray spectra and temporal variability of X-ray binaries; the nonthermal X-ray emission properties of SNRs; Soft Gamma-ray burst Repeaters (SGR); the structure of magnetars; the matter state equation in strong, high density magnetic fields; the hard X-ray emission of clusters of galaxies; and Gamma-ray bursts (GRBs). The spacecraft is planned for launch between 2014 and 2016.

- LOFT, "The Large Observatory for X-ray Timing" was selected by ESA as one of the four mission projects of the Cosmic vision plan 2015-2025. Its main scientific aim is to investigate the motion of matter down to the compact object by studying the very rapid X-ray flux and spectral variability. Thanks to its large area detector, it provides a fantastic tool to detect high frequency QPOs; the iron line; the study of the neutron star surface and EOS of ultra-dense matter; and the properties of the neutron star crust.

- ATHENA, the "Advanced Telescope for High ENergy Astrophysics", using spectral, timing and imaging spectroscopy, is devoted to exploring the extreme physical conditions around supermassive black holes, and to determining the contribution of the accretion power to the energy budget of the Universe. Moreover, it will map the large scale structure of the Universe, and it will study the physical state and cosmic evolution of the hot gas that forms the major baryonic component of the cosmos.

Unfortunately, in May 2012, ESA's Science Programme Committee decided to select the Jupiter mission "JUICE", which was in competition with ATHENA. ATHENA will have another chance to be selected and launched in 2028.

New projects are in the conception phase, as for instance XTP "X-ray Timing and Polarization", a chinese satellite, seen as a large area successor to RXTE.

3.2   XMM-Newton

The X-ray Multi-Mirror Mission[1] (XMM-Newton) [Jansen 2001] is a product of the European Space Agency (ESA), resulting from a consortium of 35 European companies. Launched on December 10th, 1999 by an Ariane 5 rocket from Kourou, French-Guyana, XMM-Newton represents a technological breakthrough. It is the largest scientific European spacecraft to date.

With a mass of $\sim 3\,800$ kg for a length of 10 meters, XMM-Newton follows an eccentric 48-hour elliptical orbit. It travels at nearly one third of the distance Earth-Moon when it reaches its apogee ($114\,000$ km), then it passes at about $7\,000$ km above Earth when it is at its perigee, flying nine times faster ($\sim 24\,000$ km/h) than when it is at its farthest distance from Earth.

Figure 3.4:   Artist's conception of the XMM-Newton observatory in orbit around the Earth. Image from the ESA website (D. Ducros).

The space observatory carries three X-ray telescopes equipped with three imaging cameras (EPIC-pn, EPIC-MOS1, EPIC-MOS2) and two reflection grating spectrometers (RGS1 and RGS2) that can simultaneously operate, together with a co-aligned optical telescope (OM). The configuration of the spacecraft is shown in Fig 3.5. The unprecedented combination of a large collecting area with the high resolution of the cameras, and the possibility to make long uninterrupted exposures, provide highly valuable observations.

The XMM-Newton mission has been designed to study a large range of objects, from enigmatic black holes to the origins of the Universe. Observing time is however quite difficult to obtain because of the large number of competitive projects proposed by the scientific community.

---

[1]http://xmm.esac.esa.int/
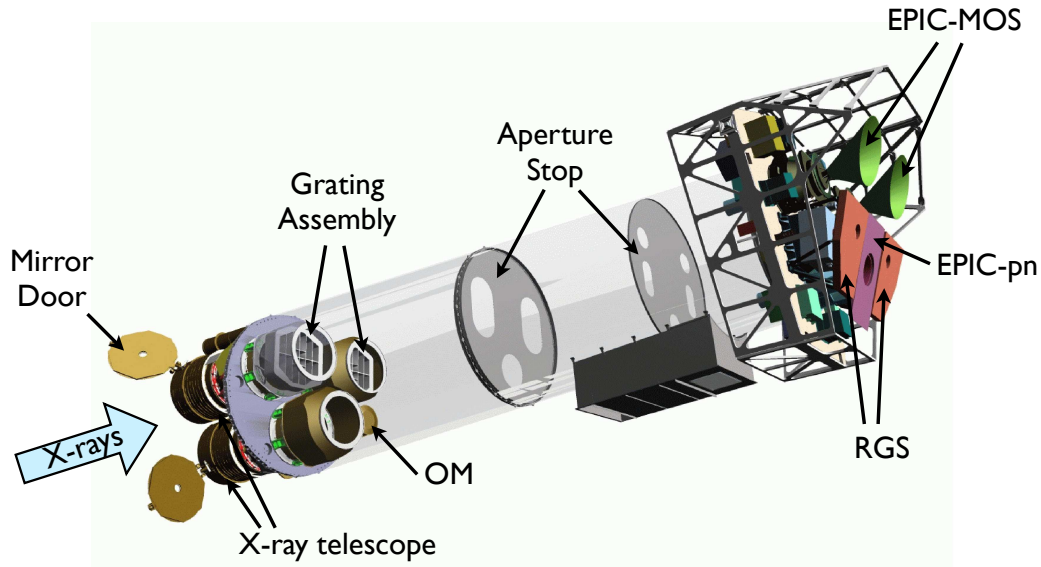
Figure 3.5: Sketch of the XMM-Newton payload. On the lower left: the aperture doors and the mirror modules with the two Reflection Grating Arrays. The optical monitor is obscured by the lower mirror module. On the upper right: the EPIC MOS cameras (green), the EPIC pn camera (purple), and the RGS detectors (red). The direction of the incoming X-rays is indicated by the blue arrow on the left. Figure adapted from the VILSPA XMM-Newton Science Operations Center (Dornier Satellitensysteme GmbH).

3.2.1 How does it work?

XMM-Newton is equipped with solar panels to provide power (see Fig 3.4). The ESA ground stations at Perth (Australia) and Kourou are continuously in contact with the spacecraft, for real-time interaction over almost the entire orbit. The following subsections regard the instruments onboard XMM-Newton.

The X-ray telescopes

The performance of X-ray telescopes is determined by three fundamental parameters: image quality, effective area, and straylight rejection efficiency. The image quality of an X-ray mirror depends on its ability to focus photons. Each X-ray telescope has its own point-spread function (PSF). The PSF can be severely affected if the source is too bright, when the count rate exceeds a few counts per frame.

The effective area characterizes the capacity of detectors to collect radiation at different photon energies (see Fig 3.6). The effective area is folded through the response of the different focal instruments. The effective area of the EPIC-pn camera is higher than those of the two EPIC-MOS cameras. Indeed, light does not follow

the same path in the three Wolter-type X-ray telescopes; the pn camera is at the
focus of one of the X-ray telescope (Fig 3.7), whereas the two others telescopes have
grating assemblies that diffract a part of the incoming radiation onto their secondary
focus (Fig 3.8). The non-intercepted light, representing $\sim 50\%$ of the incident light,
passes through the primary MOS focus, while 40% is intercepted by grating plates of
the RGAs. The remaining light is absorbed by the support structures of the RGAs.
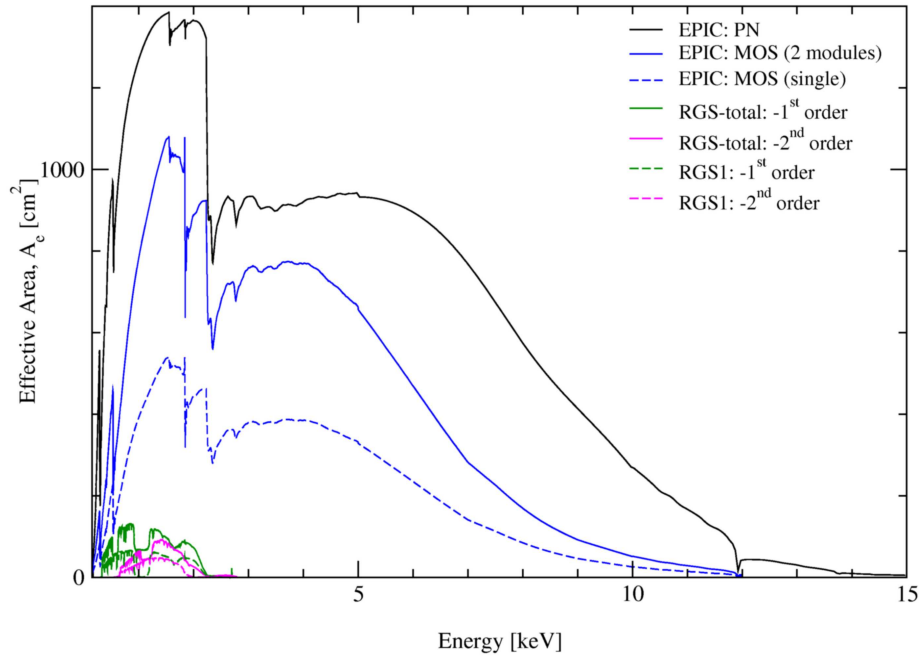
Figure 3.6:   Effective area of the XMM-Newton X-ray telescopes, EPIC-pn, EPIC-
MOS, and RGS. The efficiency of the mirrors is higher in the energy range from
0.1 to 10 keV, with a maximum at about 1.5 keV. A pronounced edge near 2 keV
is associated with the Au edge. The effective areas of the two MOS cameras are
lower than that of the pn, since only part of the incoming radiation falls onto these
detectors. From the XMM-Newton Users' handbook.

Last but not least, the efficiency of the stray-light rejections is an important
parameter that defines the performance of the telescopes. XMM-Newton mirror
modules are equipped with X-ray baffles (Fig 3.9) acting as collimators to consider-
ably reduce the amount of stray-light in the field of view of the focal plane cameras,
and with an electron deflector, which produces a circumferential magnetic field that
prevents low energy electrons reflected by the mirrors from reaching the focal plane
detectors.

XMM-Newton was built in conditions of exceptional cleanliness to preserve its
200 square meters of ultra-polished gold forming the telescope mirrors. These are
the most sensitive ever developed in the world.
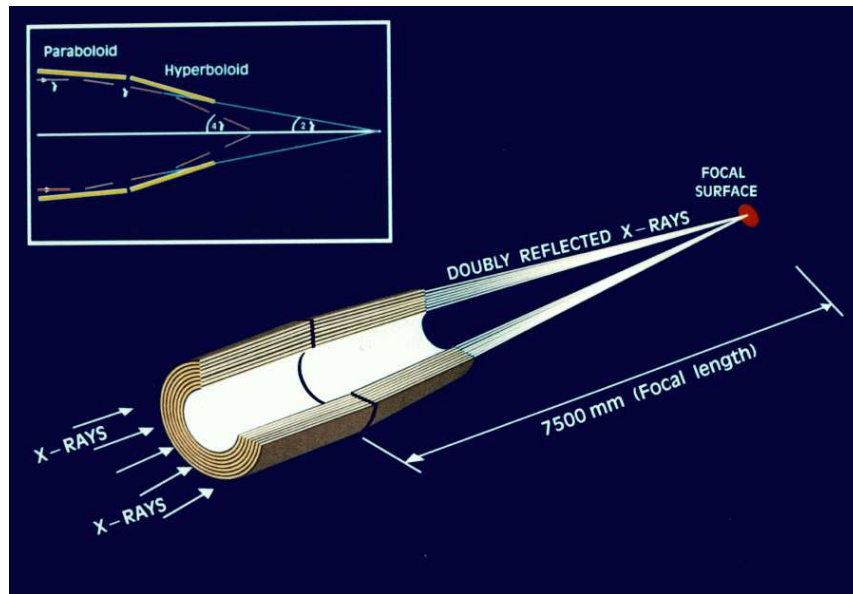
Figure 3.7: Light path in XMM-Newton's open X-ray telescope with the pn camera in focus. From the XMM-Newton Users' handbook.
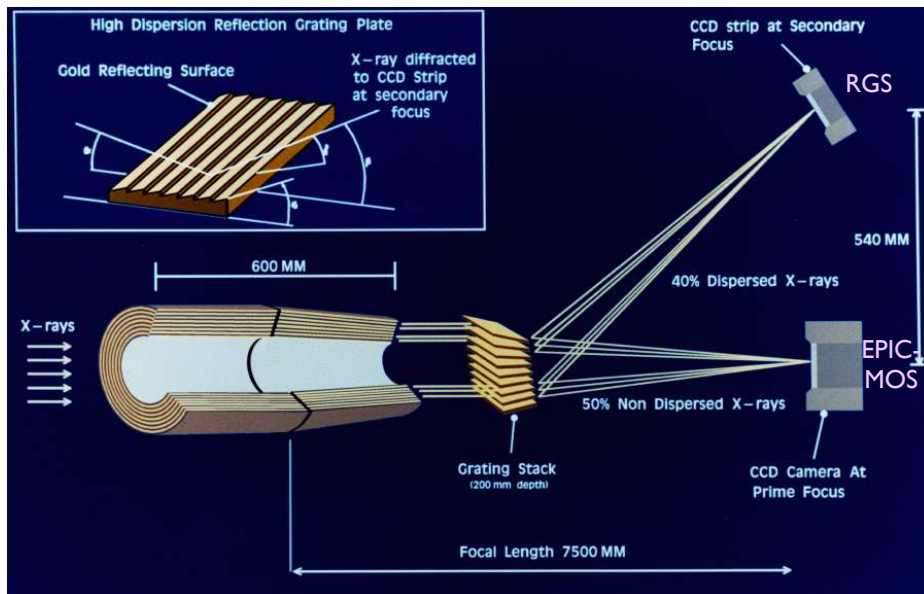
Figure 3.8: The light path in the two XMM-Newton telescopes with grating assemblies. About 50% of the non-intercepted light passes through the primary MOS focus while 40% of the incident light is intercepted by the RGA grating plates. From the XMM-Newton Users' handbook.
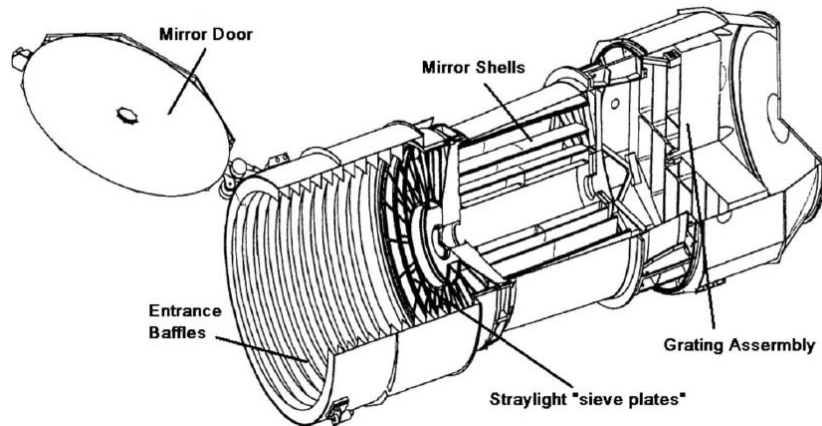
Figure 3.9: Representation of one XMM-Newton telescope that consists of a mirror assembly door (which protected the optics during integration, launch and early orbit phase), the entrance baffle, the X-ray baffle, the mirror module, the Reflection Grating Array (only in two of the telescopes) [Lumb 2012].

The EPIC cameras

The three European Photon Imaging Camera's (EPIC) perform extremely sensitive imaging observations over a field of view of 30', providing a moderate spectral ($E/\Delta E \sim 20 - 50$) and angular resolution ($\sim 6''$ FWHM) in the energy range from 0.15 to 12 keV. All of the EPIC CCDs operate in photon counting mode with a fixed, mode-dependent frame readout frequency, producing event lists.

A selection of filters of different thickness mounted on a wheel in front of each camera enables the rejection of long wavelength optical and UV radiation, so as to optimize the low energy response of the instrument.

Two of the EPIC instruments consist of arrays of Metal-Oxide-Silicon (MOS) technology [Turner 2001], while the third EPIC detector is a pn CCD [Struder 2001]. These two types of cameras are fundamentally different. The readout of the pn chips is much faster than that of the MOS cameras, each pixel column having its own readout node. Another important difference is that the MOS chips are front-illuminated, while the pn CCDs are back-illuminated, which strongly affects the detector quantum efficiencies. We outline below a few more details about these cameras:

- EPIC-pn cameras are composed of X-ray CCDs. The heart of the pn camera is a single Silicon wafer with 12 integrated CCDs (6×2 chips), as displayed in Fig 3.10. With 64×200 pixels per chip, the pn camera offers a field of view similar to that of the MOS cameras.

- EPIC-MOS cameras are rotated by $90°$ with respect to each other (see Fig 3.11). Each camera consists of an array of 7 CCD chips of 600×600
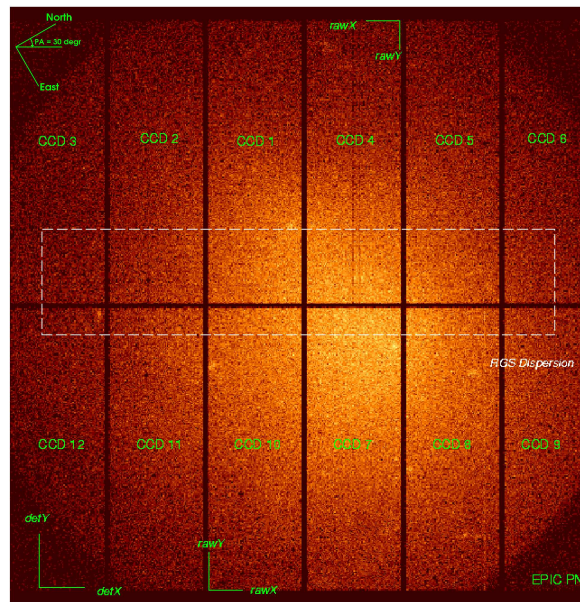
Figure 3.10: EPIC-pn chip array consisting of 12 CCDs each of 13.6×4.4 arcmin. From the XMM-Newton Users' handbook.

pixels each. The physical size of each pixel is 40 μm, corresponding to 1.1 arc seconds on the sky.
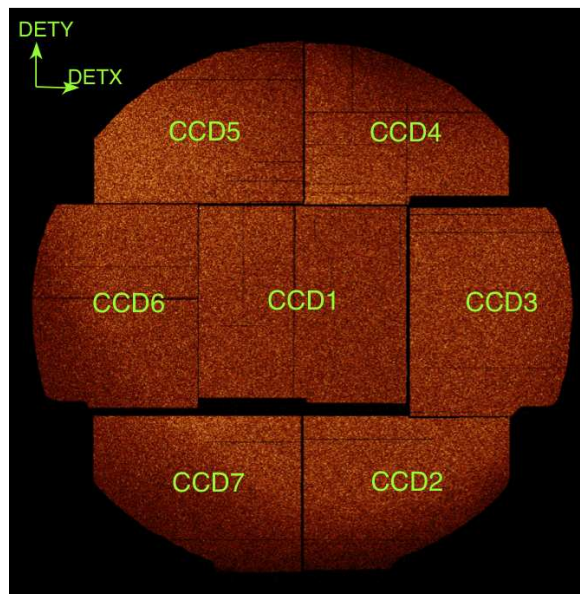
Figure 3.11: EPIC-MOS chip array composed of 7 CCDs each of 10.9×10.9 arcmin. From the XMM-Newton Users' handbook.

EPIC cameras offer the possibility to work in a variety of modes of data acquisition: the "imaging mode", "timing mode", and "burst mode" (see Fig 3.12), associated with different imaging performance, timing resolution and maximum count rate. The burst mode is only possible for the EPIC-pn camera. The imaging mode is composed of the full frame mode (all of the CCDs operate simultaneously), the extended full frame mode (for EPIC-pn only; the image collection time is longer than in the full frame mode), the small window mode (only one CCD is used), and the large window mode (a portion of the area of the CCDs is read-out). The read-out times differ from each other; the values are tabulated in Table 3.2 in addition to the live time and the count rate capability. The live time corresponds to the ratio between the time needed for the CCD to collect X-ray photons also called events (integration time, including the time to shift events towards the read-out), and the frame time, which also includes the time necessary for the read-out of the events. The count rate capability refers to the maximum count rate possible for a point source to avoid pile-up. This effect is discussed later in the chapter 5 dedicated to the study of 4U 1705-44.
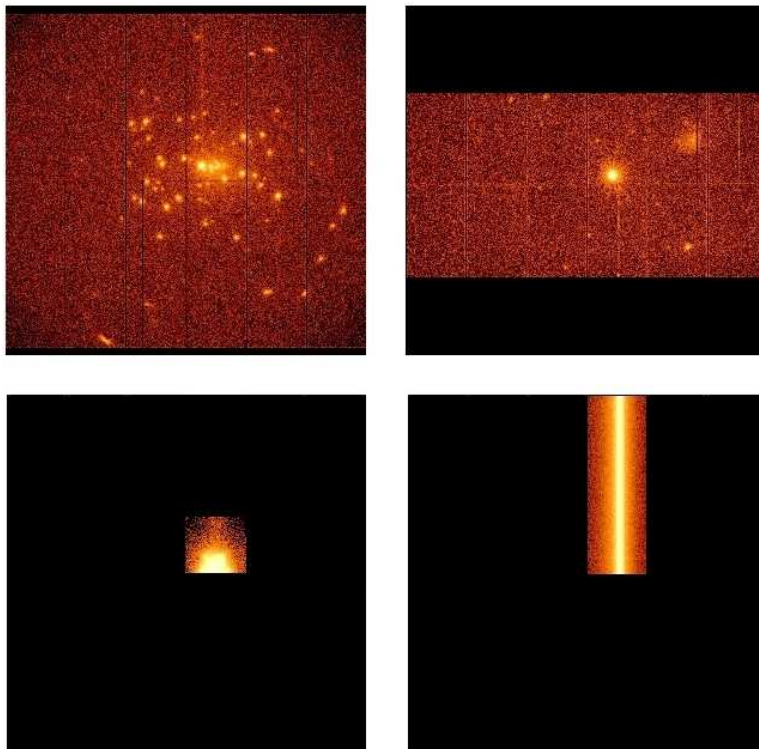
Figure 3.12: Operating modes for the EPIC-pn camera. Top left: Full frame mode (all of the 12 CCDs operate); Top right: Large window mode (half the area of the 12 CCDs); Bottom left: Small window mode (a portion of one CCD operates); Bottom right: Timing mode (a single CCD is used). From the XMM-Newton Users' handbook.

Table 3.2: Characteristics of the EPIC-pn modes. Adapted from the XMM-Newton Users' handbook.

Mode (pixels) [1 pixel = 4.1"]	Time res. [ms]	Live time [%]	Max count rate [s^{-1}]
Full frame (376 ×384)	73.4	99.9	6
Extended full frame (376×384)	200	100.0	1
Large window (198×384)	48	94.9	6
Small window (63×64)	6	71.0	50
Timing (64×200)	0.03	99.5	800
Burst (64×180)	0.007	3.0	60000

The reflection grating spectrometers

The reflection grating spectrometers (RGS) [den Herder 2001] are only present on two out of the three XMM-Newton X-ray telescopes. The RGS units consist of the Reflection Grating Assemblies (RGAs) and the RGS Focal Cameras (RFCs). The RGAs are mounted in the light path of the two X-ray telescopes with EPIC MOS cameras at their primary foci, intercepting $\sim 50\%$ of the incoming radiation.

The RGS were designed for high-resolution X-ray spectroscopy and spectrophotometry. They offer a high spectral resolution, with a resolving power $E/\Delta E$ from 200 to 800 over the energy range $0.35 - 2.5$ keV. This energy band is particularly interesting for performing detailed measurements of emission and absorption features in a large variety of stellar, interstellar and extragalactic hot, ionized plasmas.

The optical monitor

Although XMM-Newton is an X-ray observatory, it is equipped with an optical monitor (OM) [Mason 2001] co-aligned with the three X-ray telescopes. The OM is dedicated to the detection of the optical/UV counterparts of X-ray sources seen by the X-ray telescopes.

The instrument is a 30 cm Ritchey-Chretien telescope with a focal length of $\sim$ 3.8 m, associated with a photon counting detector operating in UV and the blue region of the optical spectrum. This allows us to know the optical state of the X-ray object that the observer is looking at, since the majority of X-ray sources are variable. The OM reaches a limit sensitivity at B=24 (magnitude) for a star viewed with the detector in unfiltered light.

3.2.2 Data analysis

Since there is no data storage capacity onboard the satellite, the data are transmitted in real time to the ground, to the European Space Astronomy Centre (ESAC) in

Spain. The science data are then processed at the XMM-Newton Survey Science Centre (SSC) at the University of Leicester, England.

The SSC, in collaboration with the Space Operations Centre (SOC) in Darmstadt, Germany, developed software dedicated to the reduction and analysis of data collected by XMM-Newton, called the Science Analysis Software[2] (SAS). Released periodically, SAS contains more than 125 programs and scripts allowing astronomers to extract and reduce data. It does not include tools for spectral, timing or image analysis; that is performed as a second step (see the section dedicated to spectral analysis). It generates spectra, light curves, detector response matrices, etc., which are needed to perform the analysis. In other terms, SAS allows the conversion from instrumental quantities into physical ones, in order to derive astrophysical information.

XMM-Newton data are available in two formats: the Observation Data Files (ODF), and the Pipeline Processing System (PPS). ODF data contain all data necessary for processing an observation. PPS data contain calibrated photon event files, source lists, and images, among other things.

There is a procedure to follow for each instrument in order to obtain the final spectrum corresponding to an observation. Below are the main steps associated with the EPIC data reduction[3] [4]:

1. Generation of event files with the most recent calibration files corresponding to the instrument, in order to obtain calibrated photon event files. The resulting files are then used to produce light curves, spectra, etc.

2. Application of filters to the data, by selecting the energy range of the future spectrum, the number and the pattern of the CCD pixels triggered for a given event. Of course, the filters depend on each instrument, and so are different for the EPIC-pn and the EPIC-MOS. Sometimes additional filters are needed, such as the temporal filters. They allow us to remove soft proton flares for example, which can be registered during an observation.

3. Extraction of the source spectrum. To do so, one needs to produce an image, and to take the coordinates (the size and the position) of the region that has to be extracted, centered on the object.

4. Extraction of the background spectrum, following the same method used for the extraction of the source spectrum, but in a region far from the object.

5. Estimation of the amount of pile-up affecting the observation. Pile-up depends on the brightness of the source, but also on the modes that the EPIC detectors are in. This effect occurs when a source is so bright that incoming X-rays arrive on two pixels of the CCD, or on the same one more than once, skewing the spectrum to higher energies.

---

[2]http://xmm.esac.esa.int/sas/
[3]http://xmm.esac.esa.int/sas/current/documentation/threads/
[4]http://heasarc.gsfc.nasa.gov/docs/xmm/abc/

6. Generation of the detector response file RMF (Redistribution Matrix File), which describes the response of the instrument as a function of energy and PI channel.

7. Generation of the effective area ARF (Ancillary Response File), also including also the transmissions of the filters and the quantum efficiency curve of the detector.

In the end we obtain high level scientific products (image, net light curves and calibrated spectra) in a standard format (fits) that are usable by analysis softwares that are common to all X-ray observatories.

3.3 Spectral analysis

X-ray spectral analysis is performed using interactive X-ray spectral-fitting programs, such as Xspec[5] [Arnaud 1996] or ISIS[6] [Houck 2000]. These programs can be used for all X-ray satellites, since they do not depend on one detector in particular.

One first loads the source spectrum, the associated background, the detector response matrix and effective area files, previously created with SAS. If necessary, data can be rebinned, by grouping a certain number of channels (or counts) per bin. The energy range in which the analysis will be performed must then be specified.

However, the source spectrum obtained with SAS is not the real spectrum, but the total photon counts (C) detected by the instrument in a given channel (PI). The observed spectrum is related to the real spectrum S(E) by:

$$C(PI) = T \int RMF(PI, E) \, . \, ARF(E) \, . \, S(E) \, . \, dE, \qquad (3.1)$$

where T is the exposure time (in seconds), RMF(PI,E) is the instrumental response matrix (unitless), ARF(E) the energy-dependent effective area of the telescope and detector system (in cm^2), and S(E) the source flux (in photon/cm^2/s/keV).

Ideally, one would like to determine the real spectrum of the source S(E) corresponding to an observed number of counts per channel C(PI). Since the response matrix is usually not diagonal, the equation cannot be inverted. An alternative method consists of assuming a physical model S(E), convolving it with the instrument response files (RMF and ARF), and then comparing the result with the observed counts. To do so, a "fit statistic" is computed from the comparison to evaluate whether the model spectrum correctly fits the real data. This technique is called the forward-folding approach.

The aim is then to adjust a model based on the physics of the source to the data, in order to have an acceptable fit from a statistical point of view. The initial parameters corresponding to the spectral model are modified until the best value

---

[5]http://heasarc.gsfc.nasa.gov/xanadu/xspec/
[6]http://space.mit.edu/cxc/isis/

of the statistic is found. If this value is unacceptable, a new model must be chosen and the procedure must be repeated (see Fig 3.13). Finding the best fit means minimizing the difference between the observed data and the predicted data. An important problem that usually occurs in X-ray fitting is that the minimization algorithms usually find best-fit parameters that correspond to local minima, and not global minima, of the fit statistic used.

Xspec and ISIS include a wide range of spectral models, and use non-linear fitting routines to find the best-fit parameters for each model. Other models can be used by downloading tables and can be used without any problem.
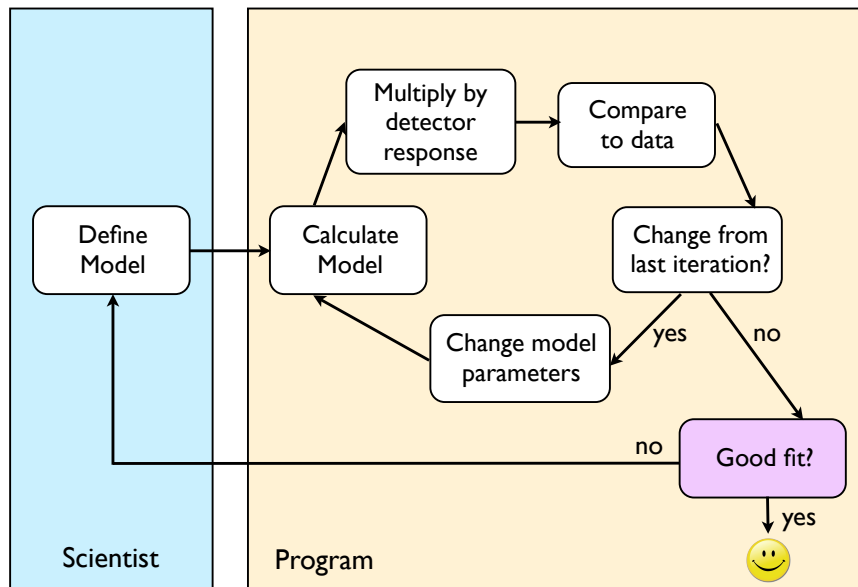
Figure 3.13:   Forward-fitting technique used by Xspec. The scientist determines a model that is calculated and compared to the observed data. The model is acceptable if the resulting fit is statistically good and if it is physically plausible. Otherwise, another model has to be chosen for the data. Adapted from [Arnaud 2011].

3.3.1   Models

As the statistician George Box said, "Essentially, all models are wrong, but some are useful" [Box 1987]. The aim of spectral fitting is to understand the behaviour of a source, of matter, using physical insight. However there does not exist a perfect model since they are all oversimplified, even if one tries to make them closer and closer to reality.

Because many physical processes are occuring in a given source, an X-ray spectroscopic model generally results from the multiplication and the addition of different components. Multiplicative components modify the whole spectrum, such as the photoabsorption of the interstellar medium, or a normalizing factor which takes the

different cross-calibrations of the instruments into account when data from different instruments or satellites are combined together. Thus they modify the model by a certain factor depending on the energy. An additive component acts only locally at the given energy, as for example a Gaussian line or a blackbody. The resulting model can be written as:

$$S(E) = M_1 * M_2 * (A_1 + A_2 + M_3 * A_3) + A_4, \qquad (3.2)$$

where $M_i(E)$ are multiplicative components and $A_i(E)$ are additive ones.

The model parameters converge towards the values that give the best fit statistic. These values are called the best-fit parameters.

To calculate the goodness-of-fit, i.e. to evaluate how well the model describes the observed data, a statistical test needs to be used. The most common one is the χ^2 statistic, defined as:

$$\chi^2 = \sum \left(C_{\text{data}}(PI) - C_{\text{model}}(PI)\right)^2 / (\sigma(PI))^2, \qquad (3.3)$$

where $C_{\text{data}}(PI)$ is the observed counts, $C_{\text{model}}(PI)$ is the predicted counts assuming a particular model, and $\sigma(PI)$ is the error for channel PI.

The χ^2 statistic provides a goodness-of-fit criterion for a given number of degrees of freedom ν and for a given confidence level. ν corresponds to the number of channels minus the number of model parameters. A fit is considered good if $\chi^2/\nu \sim 1$. The ratio χ^2/ν is called the "reduced χ^2": χ^2_{red}. If χ^2_{red} is much greater than 1, this indicates a poor fit, whereas a χ^2_{red} much less than 1 indicates that the errors on the data have probably been over-estimated.

3.3.2 Parameter errors

Once a model fits the data well, one can evaluate the values obtained for each parameter of the model. To do so, it is important to know the parameter errors. XSPEC and ISIS propose a command to derive the confidence intervals for each parameter. The considered parameter is fixed at a particular value and the other parameters are re-fitted. New values can be found. XSPEC uses a bracketing algorithm followed by an iterative cubic interpolation to find the parameter value at each end of the confidence interval.

The Fe line in MXB 1728-34

Contents

I dedicated the first part of my PhD to the spectral analysis of the low-mass X-ray binary system MXB 1728-34, also named 4U 1728-34 or GX 354-0. Using the data obtained with XMM-Newton, I mainly focused on the iron line, for which a long discussion is still being relevant. I investigated its nature and deduced some information from the Fe line profile, such as the inclination of the source and some properties about the inner part of the accretion disk.

XMM-Newton is one of the best X-ray observatories available at present to perform such study, since its instruments (in particular the EPIC-pn) offer a high effective area below and above the Fe line energy, allowing us to determine the shape and width of the line, as well as the continuum.

4.1   MXB 1728-34

Discovered in 1976 by W. H. Lewin, MXB 1728-34 is classified as a neutron star binary, since type-I X-ray bursts have been observed in the energy range $1 - 18$ keV with the Small Astronomy Satellite SAS-3 [Lewin 1976, Hoffman 1976]. With an intensity comparable to that of the Crab Nebula, the bursts are quite frequent and often separated by several hours (average time separation ~ 5 h).

Since the source is located between 4.1 and 5.1 kpc in the direction of the Galactic center, the nature of the companion star is still unknown because of the high optical extinction. Looking at the path that the source follows in the color-color diagram, the system is classified as an atoll source.

4.1.1 The choice of the source

MXB 1728-34 is a source of particular interest for different aspects. First, because the neutron star is weakly magnetized, the accretion disk can approach considerably closer to the compact object, as in the case of black hole binary systems. The study of this kind of sources enables a direct comparison of the X-ray emission between neutron star and black hole binaries.

In addition to its frequent well-studied bursts, MXB 1728-34 is interesting for its timing properties. It is one of the best case where ultra-fast variations in the X-ray light curve became evident through the detection of kilohertz quasi-periodic oscillations (kHz QPOs), and nearly coherent oscillations during type-I X-ray bursts in the power density spectra [Strohmayer 1996]. Different studies were performed on these oscillations and revealed that the difference between the frequencies of twin kHz QPO features, thought to be associated with the spin of the neutron star, does not always remain constant [Mendez 1999]. The observed changes in the frequency of the kHz QPOs seem to be driven by changes in the mass accretion rate in the innermost part of the accretion disk.

Moreover, an observation of MXB 1728-34 was performed by XMM-Newton in 2002. An iron line seems to be detected, but no paper was published on these data until 2010, when a catalog paper appeared, dedicated to the nature and the origin of the Fe Kα line in neutron star LMXBs observed with XMM-Newton [Ng 2010]. However, the source shows a different behavior with respect to the other ones, especially with respect to the continuum study. The authors mentioned: *"The fits to the XMM-Newton spectrum have significantly different continuum parameters when fitting the residuals at the Fe band with Models 1a or 1b, in contrast to all other observations. This indicates that after including the line, the parameters of the fit change significantly so the line fit may not be realistic."*. They explained such a behavior with the low luminosity of MXB 1728-34 in comparison to the other sources. Thus, the nature of the Fe line in MXB 1728-34 did not seem to be clear and the data warrant particular attention.

4.1.2 The data

MXB 1728-34 was observed by XMM-Newton on October 2002 for a total exposure time of 28 ks, using the five X-ray instruments onboard the satellite, i.e. the reflection grating spectrometers RGS1 and RGS2, and the cameras EPIC-pn, MOS1 and MOS2. The corresponding X-ray energy range covered was $1 - 11$ keV. The EPIC-pn camera was operated in timing mode to prevent photon pile-up.

I carried out the standard extraction of the XMM-Newton data, by following all steps described in the XMM manual[1]. After having checked that the data were not contaminated by solar flares during the observation time, I extracted the spectrum corresponding to each instrument, the associated backgrounds, and I checked that pile-up did not affect the data.

---

[1] ftp://legacy.gsfc.nasa.gov/xmm/doc/xmm_abc_guide.pdf

The EPIC-pn data have already been studied by [Ng 2010]. However I propose another analysis and interpretation of the data, using all X-ray instruments and applying different models for both the continuum and the Fe line.

4.2 Is the Fe line relativistic?

The relativistic nature of the Fe line has been clearly confirmed in a large number of AGN, for instance in MCG-6-30-15 [Tanaka 1995, Wilms 2001, Miniutti 2007] (see Fig 4.1), 1H0707-495 [Fabian 2009], and others [Nandra 2007], and black hole binaries such as Cygnus X-1 [Fabian 1989, Miller 2002], GX 339-4 [Miller 2004b], or GRS 1915+105 [Martocchia 2002] (see Fig 4.2). Nevertheless, it is still an object of debate for neutron star binaries.
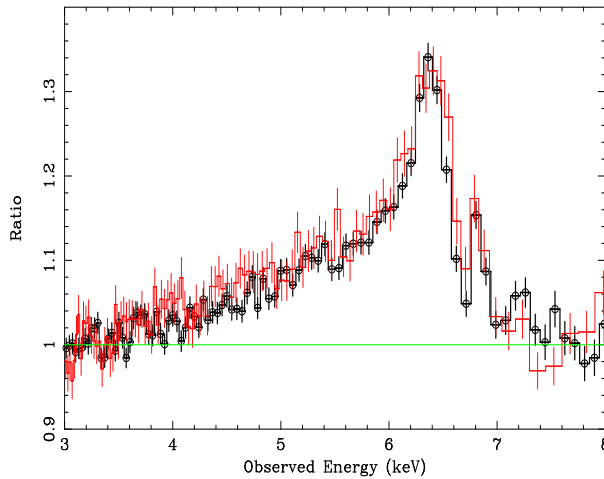
Figure 4.1: Fe line profile in the Seyfert 1 galaxy MGC-6-30-15 obtained from XMM-Newton/EPIC-pn (red) and Suzaku/XIS (black) [Miniutti 2007].

The Fe Kα line is thought to be produced in the inner part of the accretion disk. Thus, it is expected to be broadened and distorted due to gravitational effects induced by the presence of the compact object. The shape of the line differs upon the spin of the compact object and the direction of rotation of the accretion disk. Fig 4.3 illustrates the changes in the shape of the Fe line of an accreting black hole, in the cases of a fast rotating spin; no spin; and fast retrograde spin. In accreting neutron stars, the spin is usually not maximal, but in the case of a high rotation, the neutron star may be oblated because of centrifugal forces. It results that the equatorial radius can be up to 1.5 times the radius at rest. However, in LMXBs, the neutron star is accelerated by the accretion of matter from the disk, which transfers angular momentum to the compact object and determines its spin. Therefore, the resulting spin of an old neutron star should have the same direction than that of the disk. A counter-rotating disk should only be present in young systems where
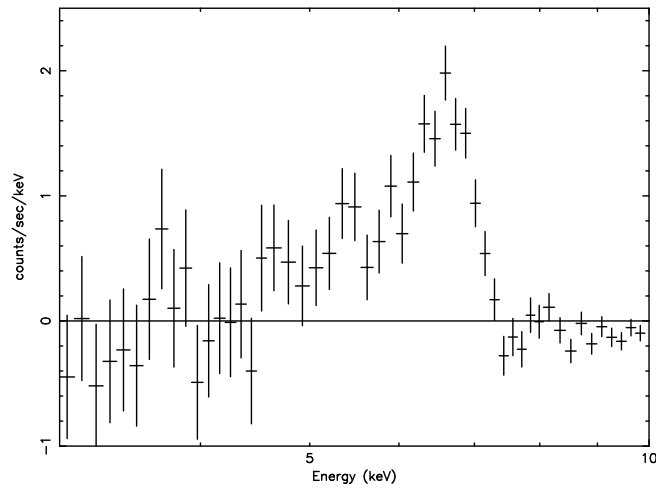
Figure 4.2:   Fe line profile of the microquasar GRS 1915+105 observed by Bep-poSAX [Martocchia 2002].

the neutron star has an intrinsic spin.

As a consequence, the iron line in LMXBs containing a neutron star is expected to be distorted, even if the distorsions should not be as extreme as in black hole accreting systems.
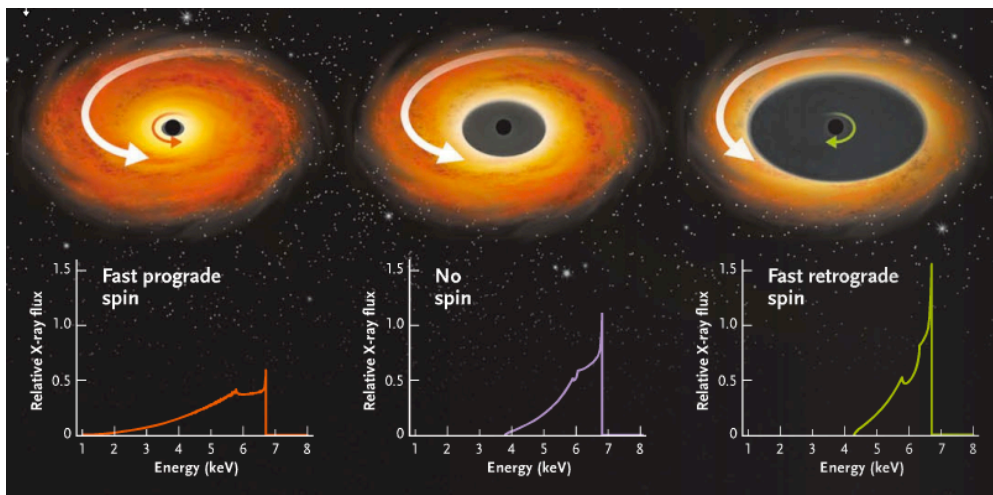
Figure 4.3:   Black hole spin determines the radius of the last stable orbit of the accretion disk. The profile of the Fe line is more or less affected by gravitational effects, in particular the low energy extent of the line (Credit: Sky & Telescope May 2011).

4.2.1   A debate on the (a)symmetry of the Fe line

Recently, [Ng 2010] performed a systematic study of the Fe line using 16 sources observed by XMM-Newton (see Table 4.4). They concluded that the Fe Kα line did not show any asymmetry, and that its origin in the inner part of the accretion disk may be controversial. Fig 4.5 displays the Fe line profiles of the sources studied. In parallel, [Cackett 2010] carried out a similar systematic analysis on Suzaku and XMM-Newton spectra of 10 neutron star LMXBs (see Table 4.6). They obtained different conclusions from [Ng 2010]: the Fe line was found broad and asymmetric, as illustrated in Fig 4.7. We note that 6 sources are part of both selected samples: Ser X-1, 4U 1636-53, 4U 1705-44, GX 340+0, GX 349+2, and SAX J1808.4-3658. Therefore, the nature of the Fe line inferred from the different studies does not depend on a particular instrument, but mainly depends on the way the data are analyzed (such as the pile-up evaluation, the continuum applied, and the models used to fit the Fe line).

Source	Class	Observation ID	Observation times (UTC) Start (year mon day)	(hr:mn)	End (hr:mn)	T (ks)	$C\,[\sigma]$ (s^{-1})	Pile-up	Columns removed
4U 0614+09	A,UCXB	0111040101	2001 Mar. 13	12:27	17:11	10	240 [8]	N	0
Cen X−4	T	0144900101	2003 Mar. 01	15:11	14:48	−	−	−	−
4U 1543−62	UCXB	0061140201	2001 Feb. 04	13:16	03:13	46	203 [5]	N	0
4U 1608−52	A, T	0074140101	2002 Feb. 13	16:04	20:57	−	−	−	−
		0074140201	2002 Feb. 15	01:34	06:22	−	−	−	−
4U 1636−536	A	0303250201	2005 Aug. 29	17:47	02:47	29	243 [15]	N	0
		0500350301	2007 Sep. 28	15:07	00:17	19	507 [11]	Y	1
		0500350401	2008 Feb. 27	03:38	15:01	37	652 [24]	Y	3
GX 340+0	Z	0505950101	2007 Sep. 02	12:40	02:34	40	801 [50]	Y	8
GX 349+2	Z	0506110101	2008 Mar. 19	15:07	23:00	7	2043 [69]	Y	8
4U 1705−44	A	0402300201	2006 Aug. 26	04:27	14:57	35	30 [1]	N	0
		0551270201	2008 Aug. 24	01:41	17:15	45	742 [31]	Y	7
GX 9+9	A	0090340101	2001 Sep. 04	09:37	15:17	1	1380 [11]	Y	4
		0090340601	2002 Sep. 25	09:15	16:10	5	1458 [25]	Y	5
4U 1728−34	A	0149810101	2002 Oct. 03	21:48	05:55	26	88 [1]	N	0
4U 1735−44	A	0090340201	2001 Sep. 03	02:57	09:06	5	1198 [23]	Y	3
Ser X−1	A	0084020401	2004 Mar. 22	14:58	21:18	6	1074 [23]	Y	4
		0084020501	2004 Mar. 24	14:47	21:10	7	925 [14]	Y	4
		0084020601	2004 Mar. 26	14:18	20:41	5	1014 [32]	Y	4
Aql X−1	A, T	0112440101	2002 Oct. 27	01:03	03:30	−	−	−	−
		0112440301	2002 Oct. 15	01:55	04:17	−	−	−	−
		0112440401	2002 Oct. 17	01:42	05:52	−	−	−	−
		0303220201	2005 Apr. 07	14:30	18:58	3	228 [6]	N	0
IGR J00291+5934	AMXP, T	0560180201	2008 Aug. 25	04:45	14:25	−	−	−	−
XTE J1807−294	AMXP, T	0157960101	2003 Mar. 22	13:40	18:40	9	41 [1]	N	0
SAX J1808.4−3658	AMXP, T	0560180601	2008 Sep. 30	23:15	17:19	43	550 [10]	Y^a	2

Figure 4.4: Neutron star LMXBs observations selected by [Ng 2010] to study the Fe line profile. All of these sources were observed by the XMM-Newton/Epic-pn in timing mode. The source classes are A (atoll), Z (Z source), UCXB (ultra-compact X-ray binary), or AMXP (accreting millisecond X-ray pulsar). T means "transient system". The last column shows the number of columns excised from the centre of the PSF to remove the pile-up effects in spectral analysis.

I re-analyzed the XMM-Newton data of MXB 1728-34, and using different models such as diskline and reflection models, I showed that the iron line was broad
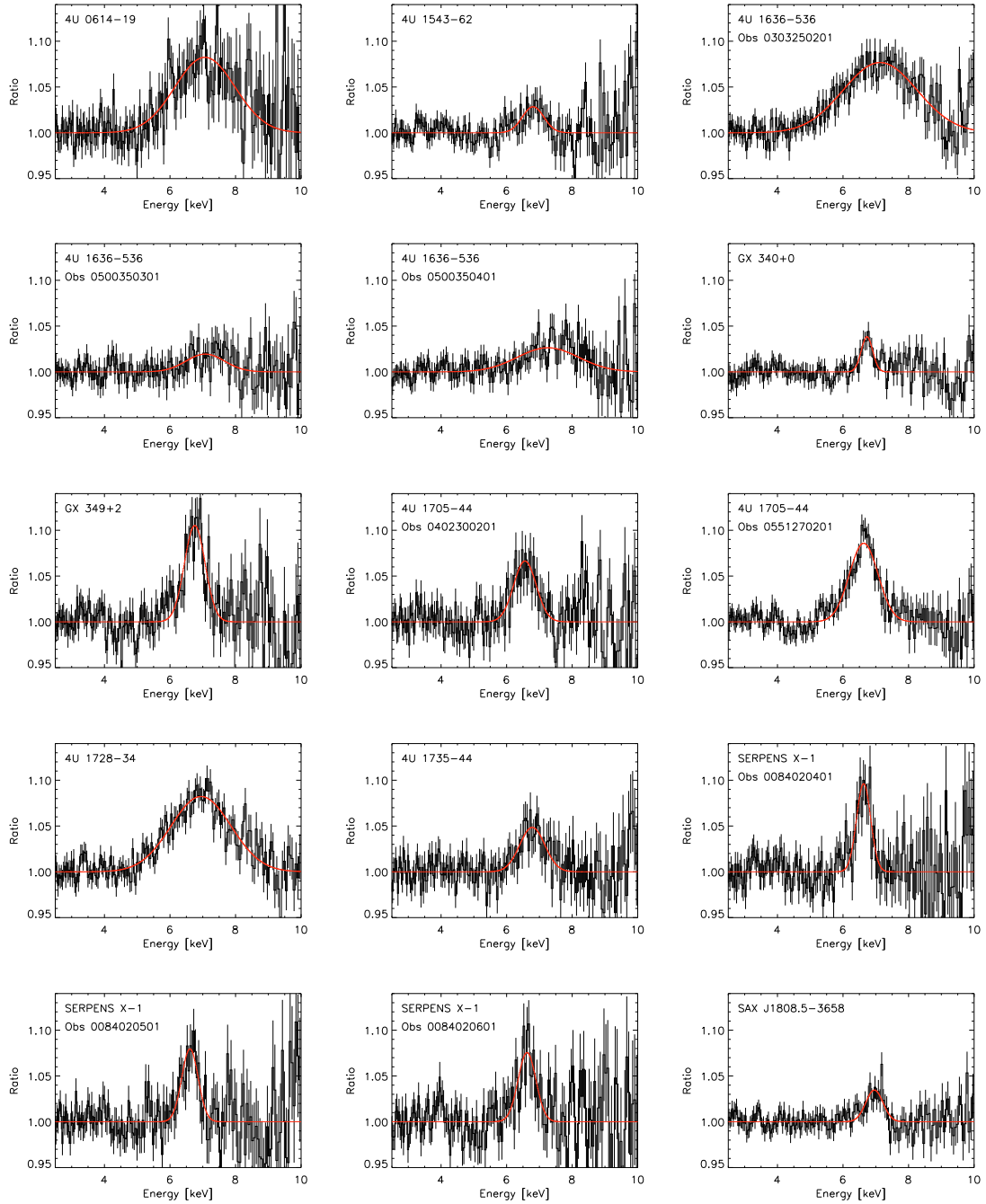
Figure 4.5: Ratio of the data to the continuum model for all neutron star LMXBs analysed by [Ng 2010] for which significant Fe Kα emission is detected. The line is fitted by a Gaussian profile plotted in red.

and relativistic. This is consistent with a line produced in the innermost part of the disk, and which is distorted by relativistic effects induced by the presence of the

Source	Class	Mission	Obs. ID	Obs. Start Date (dd/mm/yyyy)	Exp. Time (ks)
Serpens X-1	A	*Suzaku*	401048010	24/10/2006	18/29
		XMM-Newton	0084020401	22/03/2004	6
		XMM-Newton	0084020501	24/03/2004	7
		XMM-Newton	0084020601	26/03/2004	7
4U 1636−53	A	*XMM-Newton*	0303250201	29/08/2005	29
		XMM-Newton	0500350301	28/09/2007	26
		XMM-Newton	0500350401	27/02/2008	37
4U 1705−44	A	*Suzaku*	401046010	29/08/2006	14/14
		Suzaku	401046020	18/09/2006	17/15
		Suzaku	401046030	06/10/2006	18/17
		XMM-Newton	0402300201	26/08/2006	34
4U 1820−30	A	*Suzaku*	401047010	14/09/2006	10/30
GX 17+2	Z	*Suzaku*	402050010	19/09/2007	5/15
		Suzaku	402050020	27/09/2007	6/18
GX 340+0	Z	*XMM-Newton*	0505950101	02/09/2007	33
GX 349+2	Z	*Suzaku*	400003010	14/03/2006	8/20
		Suzaku	400003020	19/03/2006	8/24
		XMM-Newton	0506110101	19/03/2008	10
Cyg X-2	Z	*Suzaku*	401049010	16/05/2006	< 0.5
	Z	*Suzaku*	403063010	01/07/2008	20/82
SAX J1808.4−3658	AMXP	*Suzaku*	903003010	02/10/2008	21/31
		XMM-Newton	0560180601	30/09/2008	43
HETE J1900.1−2455	AMXP	*Suzaku*	402016010	16/10/2007	42/37

Figure 4.6: Selection of neutron star LMXBs observations performed by Suzaku and XMM-Newton to study the Fe line profile [Cackett 2010].
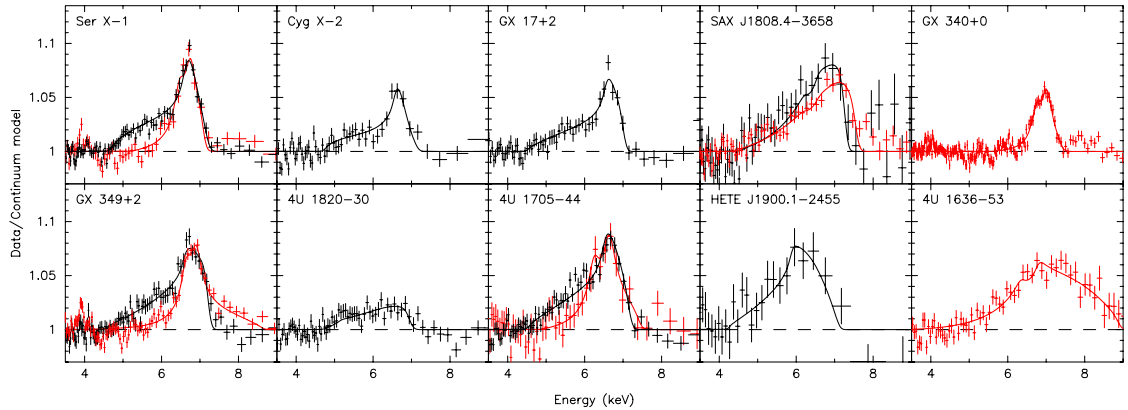
Figure 4.7: Ratio of the data to the continuum model showing the Fe Kα emission lines in the neutron star LMXBs studied by [Cackett 2010]. Data from Suzaku are plotted in black (combined front-illuminated detectors), and those from XMM-Newton are represented in red (PN camera).The solid lines indicate the best-fitting diskline model.

neutron star.

4.2.2   The models applied to fit the Fe line

To investigate the nature of the iron line, it is important to use adequate models. To perform their analysis, [Ng 2010] used as a continuum model a blackbody and a disk blackbody, both modified by photoelectric absorption from neutral material (tbabs×(bbodyrad+diskbb) in Xspec). They then fitted the excess at $\sim$ 6.6 keV, corresponding to the Fe line, with a Gaussian and with the laor model [Laor 1991], which was initially designed to model an emission line from an accretion disk around a black hole.

They compared the χ^2 obtained by both models and deduced that the Fe line was equally well-fitted using either the Gaussian or the laor component. They therefore concluded that the Fe line did not show an asymmetric profile, usually interpreted as an indication for relativistic effects.

Using a Gaussian line or the laor model makes significantly vary the continuum parameters. This should not be observed when the continuum model is well appropriated. In addition, the values obtained for the black-body temperature and the disk black-body temperature are much higher than those of the other sources studied, with larger error bars. This indicates that the parameters are not well-constrained; an other model should be tested in order to better fit the continuum.

The continuum I applied to the data consists of a Comptonization of soft photons in a hot plasma (compTT; [Titarchuk 1994]), multiplied by the photoelectric absorption (phabs; photoelectric cross-sections of [Balucinska-Church 1992] with a new He cross-section based on [Yan 1998] and standard abundances of [Anders 1989]). We note that for dim sources such as MXB 1728-34, Compton scattering is expected to play an important role. This is included in compTT, whereas it was not included in the model used by [Ng 2010].

A blackbody is usually needed to represent the accretion disk, but its addition did not improve the fit in a significant way. I applied different models to fit the iron line in order to understand whether the line was relativistic. First, I used a simple Gaussian to fit the line. Then, more complex models were tested, such as relativistic line coming from the accretion disk (diskline and relline) and a reflection model (reflionx).

Gaussian

The Gaussian line profile is the simplest model one can apply to an emission line. It is defined by:

$$A(E) = K \frac{1}{\sigma\sqrt{2\pi}} \exp\left(-\frac{(E-E_l)^2}{2\sigma^2}\right) \tag{4.1}$$

where E_l is the line energy in keV, σ the line width in keV, and K the normalization given by the total photons cm^{-2} s^{-1} in the line.

I added this component to the continuum model in order to fit the excess at $6.4-6.6$ keV. The Gaussian is found to be at 6.57 $\pm$0.05 keV and the σ parameter is frozen

at 0.6 keV, since the width of the line is poorly constrained. This value corresponds to the lower limit on the σ found from the MOS data fitted independently of the EPIC-pn data. The addition of the Gaussian improved the fit significantly; the resulting χ^2/dof is 1489/901, with the $\Delta\chi^2 = 243$ for the addition of 2 parameters. Fig 4.8 shows the data, the model (the Gaussian component is represented by a dotted line), and the obtained residuals.

Figure 4.8: Top panel: EPIC-pn (black), MOS1 (red), MOS2 (green), RGS1 (cyan), RGS2 (blue) data points of MXB 1728-34 in the range $1 - 11$ keV. Bottom panel: residuals (data-model) in units of sigmas for the Gaussian model (plus the continuum).

Diskline

Although a Gaussian line provides an acceptable fit of the line profile, I tried to physically interpret its large width using models for a relativistically-smeared line in an accretion disk.

The diskline model describes the emission line profile from a relativistic accretion disk around a non-rotating (Schwarzschild) black hole. Due to the employed approximations, it does not include relativistic light bending, but does include all other relativistic effects induced by the compact object in the accretion disk [Fabian 1989].

The diskline model can be obtained from a Gaussian profile, by fixing the

width of the Gaussian to zero $\sigma = 0$, and by multiplying it by the kernel rdblur [Fabian 1989].

The parameters associated with the diskline model are the line energy, the emissivity law, the inner and outer radii of the accretion disk (in units of GM/c^2), the inclination of the system, and the normalization.

I applied the diskline component to the data instead of the Gaussian. The outer radius of the disk was fixed at $1\,000\ \mathrm{R_g}$ and the inclination of the system with respect to the line of sight at $60°$, since the source does not show any dip in its light curve (implying an upper limit $i < 60°$; see the illustration in Fig 4.10). The line centroid energy is found to be 6.45 ± 0.07 keV and is consistent with a fluorescent Kα transition from mildly-ionized iron. The inner radius of the disk is such that $R_\mathrm{in} = 12 - 21\ \mathrm{R_g}$. The improvement of this fit with respect to the Gaussian corresponds to $\Delta\chi^2 = 26$ for the addition of two parameters, the χ^2/dof being $1463/899$. Fig 4.9 shows the results obtained with the diskline component, which can be compared with those including the Gaussian and presented in Fig 4.8.

Figure 4.9: Top panel: EPIC-pn (black), MOS1 (red), MOS2 (green), RGS1 (cyan), RGS2 (blue) data points of MXB 1728-34 in the range 1-11 keV. Bottom panel: residuals (data-model) in units of sigmas when the diskline component is added to the continuum.
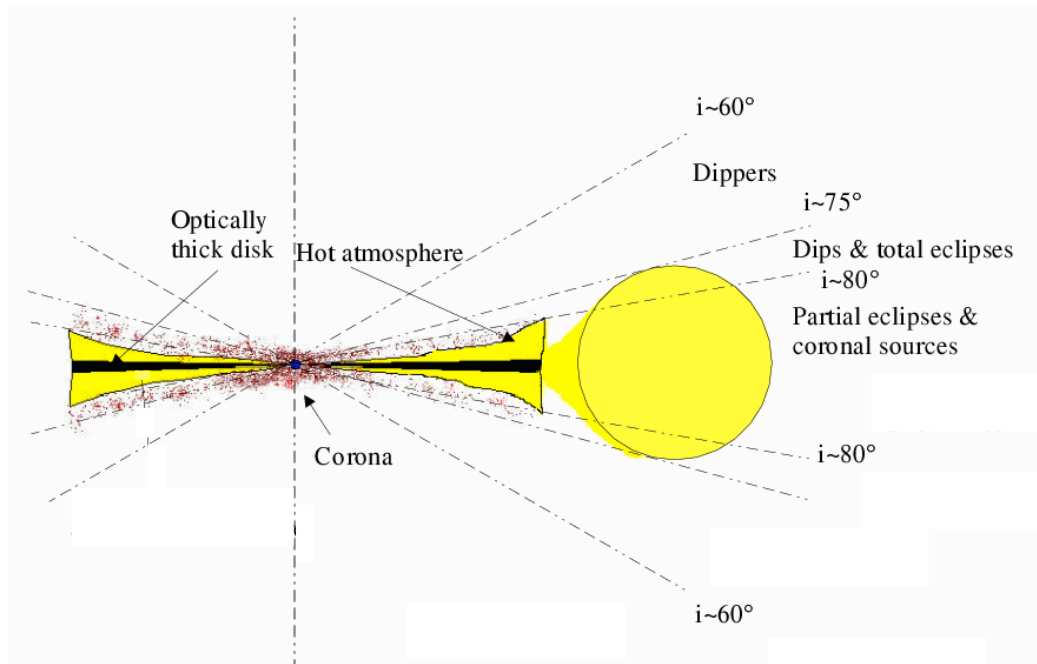
Figure 4.10: Illustration of the "dip source" definition. An X-ray binary system is called "X-ray dipper" when its inclination angle with respect to the line of sight of the observer is $i > 60°$. We note that $0°$ correponds to an observer placed at the normal to the disk plane and $90°$ to an observer in the disk plane. Figure adapted from Jimenez-Garate.

Relline

I also used a recent model for a relativistically-distorted diskline called relline[2] [Dauser 2010]. This model includes all relativistic distortions produced in a disk around the compact object. I tested this model which gave results that are fully consistent with diskline (in particular the energy of the line and inner radius of the disk) which confirms the relativistic nature of the iron line at $6.4 - 6.6$ keV.

Reflionx

To test the consistency of the broad iron line with a reflection component, I applied a self-consistent reflection model, which takes both the reflection continuum and the corresponding discrete features into account [Ross 2005]. Because a broad iron line was identified in previous models, I included relativistic smearing using the rdblur component. The fit is significantly improved: $\chi^2/dof = 1463/900$, so the $\Delta\chi^2 = 89$ for the addition of 2 parameters, which proves that the iron line is indeed broad and smeared in the disk.

---

[2]http://www.sternwarte.uni-erlangen.de/research/relline/

In this energy range, the reflection model is mainly dominated by the iron line. However, it is interesting to compare the values of the parameters with those obtained with the previous models. Some information was derived, such as a lower limit on the inclination of the source: $i > 44°$, and constraints on the inner radius of the accretion disk: $R_{in} = 14 - 49\,R_g$. These values are consistent with those found using a diskline or a relline profile, even if the uncertainties are larger with this model. Assuming a neutron star of 1.4 $M_\odot$, the inner disk radius is estimated to be at $\sim 25 - 100$ km from the neutron star center, therefore the disk would be truncated at a certain distance from the neutron star surface. Moreover, the inclination angle of the system: $44° < i < 60°$ is compatible with the absence of dips in its light curve.

Fig 4.11 presents the results obtained when reflionx is applied to the data. This self-consistent reflection model gives similar values for the spectral parameters, which indicates that the fit is stable and does not depend on the particular choice of the model used to fit the continuum or the iron line. Above all, this shows that relativistic disortions are present in the accretion disk, favoring the relativistic nature of the iron line.
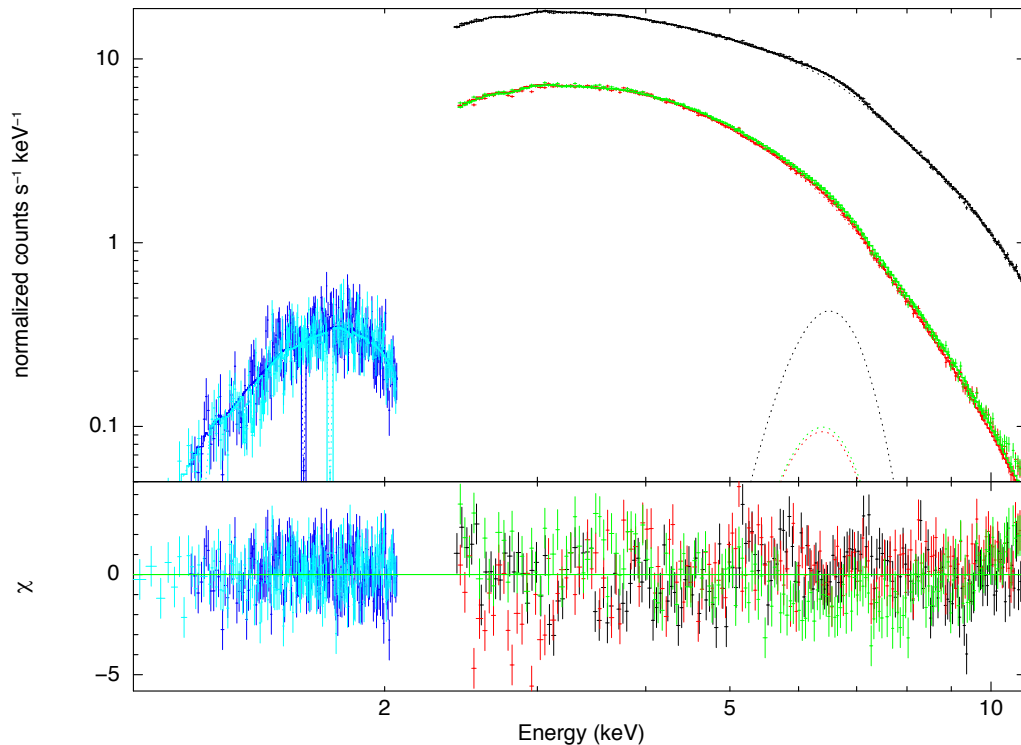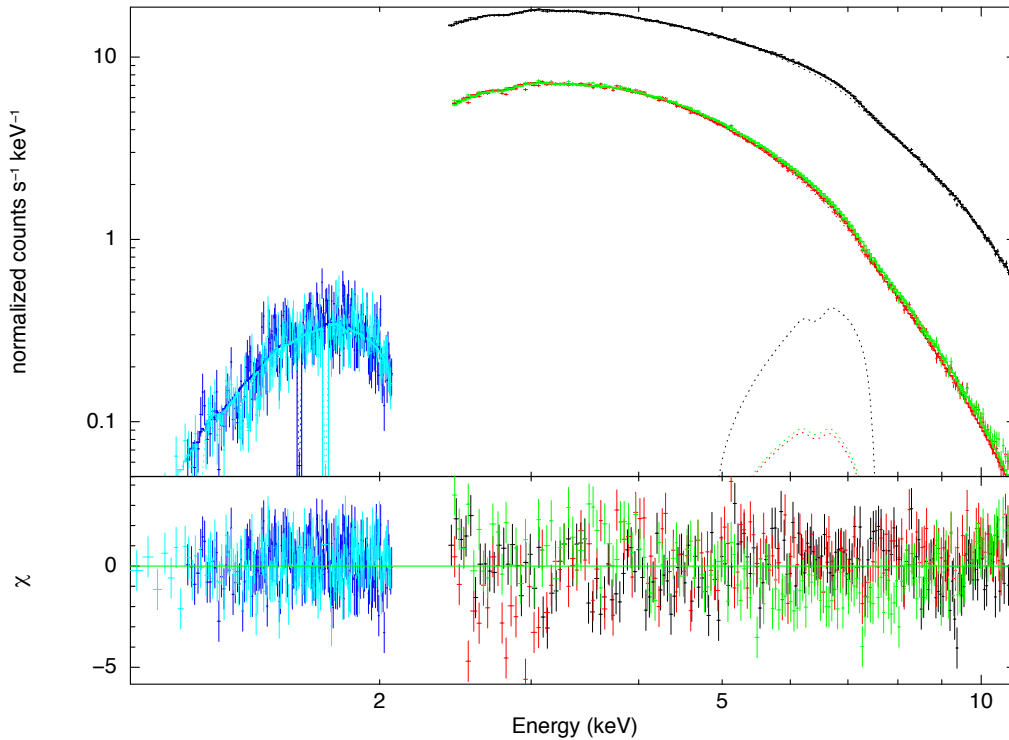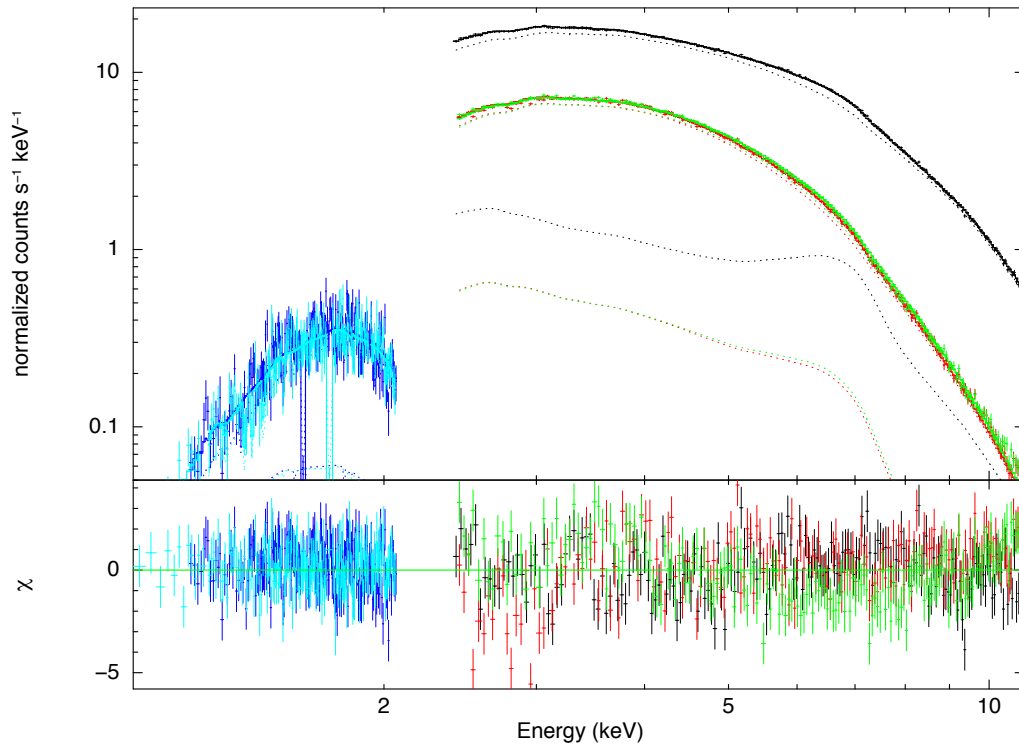

Figure 4.11:   Top panel: EPIC-pn (black), MOS1 (red), MOS2 (green), RGS1 (cyan), RGS2 (blue) data points of MXB 1728-34 in the range 1-11 keV. Bottom panel: residuals (data-model) in units of sigmas when the reflection component reflionx is added to the continuum.

4.2.3 Different methods to compare the models

A relevant question in the context of data analysis is how well a model fits the data, and how we can judge whether a model is preferable to another one. Different tools and methods are available. The easiest one is to have a look at the residuals obtained for different models, and to compare them "by eye". Of course, this only gives a general idea, since most of the time, models give similar residuals. Other methods use a statistic and so may include a possible error. However, they represent the best tool until now. Here I present a brief introduction to the methods I used in the analysis of MXB 1728-34 to infer the validity of the models applied on the XMM-Newton data.

F-test

The F-test is a very common test based on the F-statistic, which consists in comparing two models by their χ^2 and degrees of freedom. The F-test gives the probability that the model that has the smallest reduced χ^2 (the second model) is a chance improvement with respect to the other model (the first one). In other words, it indicates whether the improvement is statistically real. In principle, the second model contains additional components with respect to the first model. These components can also come from thawing a frozen parameter in the first model. The general limit is 10^{-4}. If the F-test gives a value much inferior to this limit, the second model is statistically better than the first one. However, there are some conditions to respect in order to apply this test (see [Protassov 2002]), in particular:

- the compared models must be nested

- the null values of the additional parameters should not be on the boundary of the set of possible parameter values.

Bootstrap

A second method (more rigorous but more fastidious) estimates the variance or other properties using an approximation to a distribution created by resampling the observed data themselves. Concretely, it consists in producing Monte Carlo simulations of a sample of data of equal size to the observed dataset, and comparing models through their $\chi^2_{\rm red}$. Of course the larger the sample, the more valid the test is. The operation is repeated many times in order to obtain a result which is statistically correct.

4.2.4 Results

All of the models tested are consistent with a broad and relativistic iron line. However, in order to assess the significance of the relativistic line smearing, I first compared the diskline model with the Gaussian one using an F-test. It gives a probability of chance improvement of the diskline with respect to the Gaussian of about 10^{-4}.

To test the robustness of the previous results, I used the bootstrap method, which is based on the posterior predictive p values [Hurkett 2008]. For simplicity, I restricted the data to the pn and the MOS2, since they give the best constraints on the iron line parameters. These data were fitted with a simple Gaussian. By substituting the Gaussian with the diskline model, the improvement of the fit corresponds to a $\Delta\chi^2$ of 18 for the addition of two parameters. Then, I simulated 200 pn and MOS2 spectra, including a Gaussian in the model, which were fitted in a second step using diskline. The $\Delta\chi^2$ was registered for each simulation. Among the 200 simulations, I twice found a $\Delta\chi^2$ higher than 18. Thus the probability of chance improvement is 1%. This is in agreement with the 0.75% calculated using the F-test performed on the real data restricted to two instruments. Therefore, the diskline model is a real improvement with respect to the Gaussian one.

Moreover, I applied an F-test to compare the reflection model reflionx with and without the inclusion of relativistic smearing (rdblur). The F-test gives a probability of chance improvement of 10^{-12}, thus it confirms that the line is broadened by relativistic effects induced by the neutron star.

4.3   Paper published in A&A in 2011

The results were published in the Astronomy & Astrophysics review. The most important conclusions of this work are:

a) the Fe Kα line detected in MXB 1728-34 is asymmetric and relativistic,

b) the inclination of the system is such that $44° < i < 60°$,

c) the disk is truncated at $25 - 100$ km from the neutron star,

d) the blackbody is not necessary in the continuum of the spectrum to correctly fit the data.

The last two results, in addition to the value of the photon index $\Gamma = 1.8$ and the other parameters obtained by the different models, are consistent with an intermediate state of the source.

X-ray spectroscopy of MXB 1728–34 with *XMM-Newton*

E. Egron[1], T. Di Salvo[2], L. Burderi[1], A. Papitto[1], L. Barragán[3], T. Dauser[3], J. Wilms[3], A. D'Aì[2], A. Riggio[1,4], R. Iaria[2], and N. R. Robba[2]

[1] Dipartimento di Fisica, Università degli Studi di Cagliari, SP Monserrato-Sestu, KM 0.7, 09042 Monserrato, Italy
e-mail: `elise.egron@dsf.unica.it`
[2] Dipartimento di Scienze Fisiche ed Astronomiche, Università di Palermo, via Archirafi 36, 90123 Palermo, Italy
[3] Dr. Karl Remeis-Sternwarte and Erlangen Centre for Astroparticle Physics, Friedrich-Alexander-Universität Erlangen-Nürnberg, Sternwartstraße 7, 96049 Bamberg, Germany
[4] INAF – Osservatorio Astronomico di Cagliari, Poggio dei Pini, Strada 54, 09012 Capoterra (CA), Italy

ABSTRACT

We analyzed an *XMM-Newton* observation of the low-mass X-ray binary and atoll source MXB 1728–34. The source was in a low-luminosity state during the *XMM-Newton* observation, corresponding to a bolometric X-ray luminosity of $5 \times 10^{36} \, d^2_{5.1 \, \mathrm{kpc}}$ erg s^{-1}. The 1–11 keV X-ray spectrum of the source, obtained combining data from all the five instruments on-board *XMM-Newton*, is well fitted by a Comptonized continuum. Evident residuals are present at $6-7$ keV, which are ascribed to the presence of a broad iron emission line. This feature can be equally well fitted by a relativistically smeared line or by a self-consistent, relativistically smeared reflection model. Under the hypothesis that the iron line is produced by reflection from the inner accretion disk, we can infer important information on the physical parameters of the system, such as the inner disk radius, $R_{\mathrm{in}} = 25-100$ km, and the inclination of the system, $44° < i < 60°$.

Key words. line: formation – line: identification – stars: neutron – stars: individual: MXB 1728–34 – X-rays: binaries – X-rays: general

1. Introduction

Broad iron emission lines in the energy range $6.4-6.97$ keV have been detected in high-energy resolution spectra of many X-ray sources containing a compact object, such as active galactic nuclei (e.g., Tanaka et al. 1995; Fabian et al. 2000) and X-ray binary systems containing a stellar-mass black hole (e.g., Miller et al. 2002; Miller 2007, for a review), or a weakly-magnetized neutron star (e.g., Bhattacharyya & Strohmayer 2007; Cackett et al. 2008; Di Salvo et al. 2009; Papitto et al. 2009; Iaria et al. 2009; D'Aì et al. 2009, and references therein). Identified with fluorescent Kα transition of iron at different ionization states, these lines are generally interpreted in terms of reflection of the central hard X-ray emission on the accretion disk (Fabian et al. 1989). Under this hypothesis, these lines are made broad and asymmetric by Doppler and relativistic effects induced by the Keplerian motion in the accretion disk near the compact object. The shape of the line is therefore an almost unique proxy of the innermost accretion disk close to the compact object (see Reynolds & Nowak 2003, for a review), and, in particular, on the inner disk radius. It also indicates the inclination angle of the system and the ionization state of the reflecting matter. Other reflection components like absorption edges and the Compton hump, which are usually observed between $20-40$ keV, are also expected to result from photoelectric absorption and Compton scattering of the main Comptonization continuum on the accretion disk matter.

MXB 1728–34 (4U 1728–34, GX 354–0) is a low-mass X-ray binary containing a weakly magnetized accreting neutron star. The optical counterpart of this "galactic bulge" source has not been identified yet, owing to the high optical extinction toward the Galactic center. Discovered in 1976 with the Small Astronomy Satellite SAS-3 (Lewin et al. 1976; Hoffman et al. 1976), this source belongs to the so-called atoll class (Hasinger & van der Klis 1989) and shows frequent type-I X-ray bursts (e.g., Basinska et al. 1984) that are caused by thermonuclear flashes on the neutron star surface. Furthermore, double-peaked burst profiles have been observed (Hoffman et al. 1976), which are explained as caused by photospheric radius expansion during the burst (Taam 1982). These bursts have been used to constrain the distance to the source, between 4.1 and 5.1 kpc (Di Salvo et al. 2000; Galloway et al. 2003). The power spectrum of MXB 1728–34 displays kilohertz quasi-periodic oscillations (QPOs) in the persistent emission, and a nearly coherent oscillation at ~363 Hz during some bursts that has been interpreted as the spin frequency of the neutron star (Strohmayer et al. 1996).

Spectral analysis of MXB 1728–34 has been performed in the past using data from different satellites, such as *Einstein* (Grindlay & Hertz 1981), SAS-3 (Basinska et al. 1984), EXOSAT (White et al. 1986), SIGMA (Claret et al. 1994), ROSAT (Schulz 1999), and more recently using BeppoSAX (Piraino et al. 2000; Di Salvo et al. 2000), ASCA (Narita et al. 2001), RXTE, *Chandra* (D'Aì et al. 2006), INTEGRAL (Falanga et al. 2006), and *XMM-Newton* (Ng et al. 2010). The X-ray spectrum is generally composed of a soft and a hard component. The first one can be described by a blackbody or a multicolor disk blackbody, and may originate from the accretion disk. The second one can be fitted either by a Comptonized spectrum or a thermal bremsstrahlung. The Comptonized model seems to be more realistic, because it is efficiently produced by soft photons coming from the neutron star surface and/or boundary layer

Table 1. Instrument modes, filters and exposure times.

Instrument	Mode	Filter	Exposure (ks)
pn	Timing mode	Thick	26.9
MOS1	Timing mode	Thick	27.5
MOS2	Timing mode	Thick	27.5
RGS1	Standard spectroscopy	–	28.1
RGS2	Standard spectroscopy	–	28.1

between the accretion disk and the neutron star and/or the accretion disk, which are up-scattered by electrons in a hot corona.

A broad emission line at 6.7 keV has been often detected in the X-ray spectra of this source and has been interpreted as emission from highly ionized iron (e.g., Di Salvo et al. 2000). The large width of the line suggests that it could come from an ionized inner accretion disk (Piraino et al. 2000), or alternatively it could be emitted from a strongly ionized corona. D'Aì et al. (2006) have proposed an alternative model to describe the iron line region using two absorption edges associated with ionized iron instead of a Gaussian line.

In this paper, we present a spectral analysis of high-energy resolution data taken by *XMM-Newton* on 2002 October 3 using all five X-ray instruments on-board this satellite. The EPIC-pn data have already been published by Ng et al. (2010), in a "catalog" paper dedicated to the study of the iron line in 16 neutron star LMXBs observed by *XMM-Newton*. Here we present a different approach to the analysis of these data, because we fitted for the first time the *XMM-Newton* data of MXB 1728-34 with a self-consistent modeling of the continuum emission and of the reflection component. We also tried several models to fit the iron line profile, such as diskline or relline, which are different from the models proposed by Ng et al. (2010) (Gaussian or Laor). All our results favor the relativistic nature of the line profile. We simultaneously fitted the spectra from all five X-ray instruments on-board *XMM-Newton*, while the pn data alone are analyzed by Ng et al. (2010).

2. Observation and data reduction

MXB 1728–34 was observed by *XMM-Newton* on 2002 October 3 for a total on-source observing time of 28 ks. The observation details for the instruments on-board *XMM-Newton* including the European Photon Imaging Camera (EPIC-pn, Struder et al. 2001), the MOS1 and MOS2 cameras (Turner et al. 2001), and the Reflection Grating Spectrometer (RGS1 and RGS2, den Herder et al. 2001) are presented in Table 1. The Optical Monitor (OM, Mason et al. 2001) was not active during this observation.

The 1.5−12 keV lightcurve of the All Sky Monitor (ASM) on-board RXTE extracted within ∼450 days the *XMM-Newton* observation indicates that the source was not in a high activity state, because it shows an average count rate of about 3 counts/s.

The *XMM-Newton* data were processed using the Science Analysis Software v. 9. The EPIC-pn camera was operated in timing mode to prevent photon pile-up. We created a calibrated photon event file using the pn processing tool EPPROC. Before extracting the spectra, we checked for contamination from background solar flares by producing a lightcurve in the energy range 10−12 keV. There were no high background periods during this observation. We used the task EPFAST to correct rate-dependent CTI effects in the event list. The source spectrum was extracted from a rectangular area, covering all pixels in the Y direction, and centered on the brightest RAWX column (RAWX = 38),
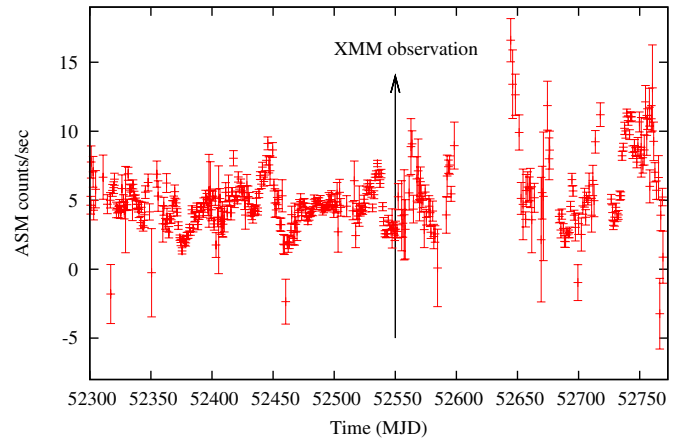
Fig. 1. RXTE/ASM lightcurve covering the 1.5−12 keV energy range. The vertical line indicates the time of the *XMM-Newton* observation performed on 2002 October 3rd.

with a width of 13 pixels around the source position (because 90% of the source counts up to 9 keV is encircled by 53 arcsec, and 1 pn pixel is equivalent to 4.1 arcsec). We selected only events with PATTERN ≤ 4 (single and double pixel events) and FLAG = 0 as a standard procedure to eliminate spurious events. We extracted the background away from the source (in the RAWX = 6−18). We also checked that pile-up did not affect the pn spectrum using the task EPATPLOT. The total count rate registered by EPIC-pn CCDs was around 110 count/s, and was 64 count/s in the 2.4−11 keV range, slightly increasing (by 5%) during the observation.

The MOS data were also taken in timing mode and processed with the routine EMPROC to produce calibrated event list files. The source spectra were extracted from a rectangular box centered on RAWX = 320 (MOS1), and on RAWX = 308 (MOS2), selecting an area 30 pixels wide around the source position, and covering 722 pixels on the Y (PHA) direction. Only events corresponding to PATTERN ≤ 12 and FLAG = 0 were selected, corresponding to standard filters. The background spectra were extracted far from the source, centered on the column RAWX = 240. We checked that the MOS spectra were not affected by pile-up. The count rates were estimated to be around 30 counts/s for each MOS unit (20 counts/s considering 2.4−11 keV energy range).

Spectral channels of EPIC-pn and MOS spectra were rebinned to have three channels per energy resolution element and at least 25 counts per energy channel.

The two RGS were operated in the standard spectroscopy mode. The RGS data were processed using the RGSPROC pipeline to produce calibrated event list files, spectra and response matrices. The count rates measured by RGS1 and RGS2 were around 2.5 and 3.5 counts/s, respectively. The RGS data were rebinned to provide a minimum of 25 counts per energy channel.

3. Spectral analysis

Data were fitted by using XSPEC (Arnaud 1996) v.12.5.1. All uncertainties are given at the 90% confidence level ($\Delta\chi^2 = 2.706$). We simultaneously fitted the broad band energy spectra of the source obtained from all five instruments. Considering the best calibration ranges of the different detectors, the data analysis from EPIC-pn, MOS1 and MOS2 cameras was restricted to the energy range 2.4−11 keV. This excluded the region around the detector Si K-edge (1.8 keV) and the mirror Au M-edge

Table 2. Best-fitting parameters of the continuum emission for the *XMM-Newton* pn, MOS1, MOS2, RGS1 and RGS2 spectra of MXB 1728–34.

Parameter	Value
N_H ($\times 10^{22}$ cm^{-2})	2.4 ± 0.1
kT_{seed} (keV)	0.59 ± 0.02
kT_e (keV)	2.74 ± 0.04
τ	16.5 ± 0.2
Norm	9.54 ± 0.02
Flux 2.0–10.0 keV (pn)	8.06
Flux 2.0–10.0 keV (MOS)	8.17 (MOS1) – 8.07 (MOS2)
Flux 1.0–2.0 keV (RGS)	0.186 (RGS1) – 0.185 (RGS2)
Total χ^2 (d.o.f.)	1732 (903)

Notes. The model used to fit the continuum is cons*phabs*compTT. The absorbed flux is in units of 10^{-10} erg cm^{-2} s^{-1}.

(2.3 keV) that could affect our analysis. This problem was already noticed for the EPIC-pn observations performed in timing mode, e.g., Boirin et al. (2005), Iaria et al. (2009), D'Aì et al. (2009), Papitto et al. (2009), D'Aì et al. (2010), Papitto et al. (2010). We only used the RGS1 and RGS2 data between 1–2 keV to constrain the softest band.

The different cross calibrations of the five instruments were taken into account by including normalizing factors in the model. These factors were fixed to 1 for pn and kept free for the other instruments.

We first fitted the continuum with a thermal Comptonized model using COMPTT (Titarchuk 1994), modified at low energy by the interstellar photoelectric absorption modeled by PHABS using photoelectric cross-sections of Balucinska-Church & McCammon (1992) with a new He cross-section based on Yan et al. (1998) and standard abundances of Anders & Grevesse (1989). The χ^2/degrees of freedom (d.o.f.) of the fit was large, 1732/903. We then tried to add a blackbody component (BBODY model) to improve the fit. The addition of this component turned out to be statistically insignificant, thus we decided not to include the blackbody in our model. The values of the parameters of the continuum emission are reported in Table 2.

With respect to this continuum model, an excess was present in the residuals between 5.5 and 8 keV, probably indicating the presence of iron discrete features. The fit was improved by adding a broad iron emission line, modeled by a simple Gaussian line (Model 1 in Table 3), centered at 6.6 keV with the σ parameter frozen at 0.6 keV. Indeed, the width of the line was poorly constrained, but when we fitted the MOS data independently from the pn data, a significantly broadened line was detected, with a lower limit on σ of 0.55 keV. With the addition of the Gaussian, the fit gave a χ^2/d.o.f. = 1489/901 (resulting in a significant improvement of the fit, with a $\Delta\chi^2 = 243$ for the addition of two parameters). We also tried to fit the line with a combination of two emission lines instead of a broad line, but the χ^2 was worse (χ^2/d.o.f. = 1531/901). So this broad line does not result from a blending of iron line at different ionization state.

We then tried to substitute the Gaussian at 6.6 keV with a diskline profile and obtained a slightly better result with a χ^2/d.o.f. = 1463/899 . The data and the residuals obtained using this model are shown in Fig. 2. Owing to the large uncertainties on the outer radius of the disk and on the inclination of the system if they were let free, we froze the first one at 1000 R_g and the inclination at 60° (the source does not show any dip in its lightcurve, implying $i < 60°$). The improvement of the fit cor-

responds to $\Delta\chi^2 = 26$ for the addition of two parameters (the F-test gives a probability of chance improvement of about 10^{-4}).

The F-test gives a reliable result in this case. In fact, according to Protassov et al. (2002), the conditions that have to be satisfied to use the F-test properly are: i) the two models that are being compared must be nested; ii) the null values of the additional parameters should not be on the boundary of the set of possible parameter values. A comparison between a Gaussian and a diskline satisfies these conditions, because a Gaussian profile can be obtained by a diskline (which is indeed given by a narrow, $\sigma = 0$, Gaussian multiplied by the kernel RDBLUR) and a good approximation of a Gaussian profile is obtained by a diskline for values of the parameters not at their boundary. However, to assess the significance of the relativistic line smearing on a statistical basis, we used another statistical method based on the posterior predictive p values described by Hurkett et al. (2008). For simplicity, we restricted our data to two instruments (pn and MOS2). These data were fitted with Model 1 and Model 2, respectively. We obtained an improvement of the fit corresponding to a $\Delta\chi^2$ of 18 for the addition of two parameters when we substituted Model 1 with Model 2. Then, we simulated 200 pn and MOS2 spectra according to Model 1, which were fitted in a second step using Model 2. The $\Delta\chi^2$ was registered for each simulation. Among the 200 simulations, we twice found a $\Delta\chi^2$ higher than 18. So the probability of chance improvement we gain from these simulations is 1%, which agrees with the 0.75% calculated by the F-test performed on the real data restricted to two instruments. Therefore, we can conclude that the diskline model is to be preferred because it gives a probability of chance improvement of the fit of about 10^{-4} using all instruments.

This model (Model 2 in Table 3) gives an estimate of the inner radius of the disk $R_{in} \sim 18$ R_g ($R_g = GM/c^2$ is the gravitational radius). Fixing the inclination to lower values (i.e. $i < 60°$), worse χ^2 were obtained with the other diskline parameters drifting toward lower R_{in}, higher rest-frame energies, and higher emissivity indices in absolute value. We searched for an absorption edge in the energy range 7–10 keV, but none was significantly detected.

To fit the iron line, we also used a new model for a relativistically distorted diskline, called RELLINE[1] (Dauser et al. 2010), which calculates line profiles taking into account all relativistic distortions in a disk around the compact object. We also fixed the outer radius of the disk and the inclination of the system to the same values used in the diskline model. The χ^2/d.o.f. obtained in these conditions is 1464/899. The best-fit line parameters obtained in this way are perfectly consistent with those obtained using the diskline model. In particular this model (Model 3 in Table 3) estimates the inner radius of the disk to be $R_{in} \sim 19$ R_g.

We tried an alternative model for the iron features (see D'Aì et al. 2006) using two absorption edges (instead of an emission line), which are found at 7.50 keV ($\tau \sim 0.06$) and 8.49 keV ($\tau \sim 0.06$), associated to mildly and highly ionized iron, respectively. The χ^2/d.o.f. for this fit is 1519/899 (which has to be compared to 1489/901 that we obtained fitting the iron line with a Gaussian (Model 1) or to 1463/899 that we obtained fitting the iron line with a diskline (Model 2)). Therefore this model (called Model 4 in Table 3) gives a worse fit of the iron features than the previous ones.

In order to test the consistency of the broad iron line with a reflection component, we fitted the data using REFLION, a self-consistent reflection model including both the reflection

---

[1] http://www.sternwarte.uni-erlangen.de/research/relline/

Table 3. Results of the fitting of MXB 1728–34 *XMM-Newton* data with different models.

Component	Parameter	Model 1: Gaussian	Model 2: Diskline	Model 3: Relline	Model 4: Two edges	Model 5: Reflection
edge	E edge (keV)	–	–	–	7.5 ± 0.1	–
edge	τ ($\times 10^{-2}$)	–	–	–	6 ± 1	–
edge	E edge (keV)	–	–	–	$8.49^{+0.09}_{-0.07}$	–
edge	τ ($\times 10^{-2}$)	–	–	–	6 ± 1	–
phabs	N_{H} ($\times 10^{22}$ cm^{-2})	2.2 ± 0.1	2.2 ± 0.1	2.2 ± 0.1	2.4 ± 0.1	2.7 ± 0.1
compTT	kT_{seed} (keV)	0.69 ± 0.02	$0.69^{+0.01}_{-0.02}$	0.68 ± 0.02	0.62 ± 0.02	–
compTT	kT_{e} (keV)	3.2 ± 0.1	3.3 ± 0.1	3.3 ± 0.1	3.1 ± 0.1	–
compTT	τ	$14.1^{+0.4}_{-0.5}$	$13.9^{+0.5}_{-0.3}$	$14.0^{+0.4}_{-0.2}$	15.2 ± 0.3	–
compTT	Norm ($\times 10^{-2}$)	7.6 ± 0.3	7.4 ± 0.3	$7.5^{+0.3}_{-0.4}$	8.3 ± 0.3	–
nthComp	Γ	–	–	–	–	$1.84^{+0.04}_{-0.01}$
nthComp	kT_{e} (keV)	–	–	–	–	$4.9^{+1.4}_{-0.7}$
nthComp	kT_{bb} (keV)	–	–	–	–	$0.71^{+0.03}_{-0.01}$
nthComp	Norm ($\times 10^{-2}$)	–	–	–	–	4.9 ± 0.2
Gauss	E (keV)	6.57 ± 0.05	–	–	–	-
Gauss	σ (keV)	0.6 (frozen)	–	–	–	-
Gauss	Norm ($\times 10^{-4}$)	8.8 ± 1	–	–	–	-
diskline	E (keV)	–	$6.45^{+0.05}_{-0.07}$	–	–	-
diskline	Betor	–	$(-2.8)^{+0.2}_{-0.3}$	-	–	–
diskline	R_{in} (GM/c^2)	–	18^{+3}_{-6}	–	–	-
diskline	R_{out} (GM/c^2)	–	1000 (frozen)	–	–	-
diskline	i (°)	–	60 (frozen)	–	–	–
diskline	Norm ($\times 10^{-4}$)	–	9.6 ± 1	–	–	–
relline	E (keV)	–	–	6.43 ± 0.07	–	–
relline	Index 1	–	–	$2.8^{+0.2}_{-0.1}$	–	–
relline	i (°)	–	–	60 (frozen)	–	–
relline	R_{in} (GM/c^2)	–	–	19^{+3}_{-4}	–	–
relline	R_{out} (GM/c^2)	–	–	1000 (frozen)	–	–
rdblur	Betor	–	–	–	–	–2.8 (frozen)
rdblur	R_{in} (GM/c^2)	–	–	–	–	20^{+29}_{-6}
rdblur	R_{out} (GM/c^2)	–	–	–	–	1000 (frozen)
rdblur	i (°)	–	–	–	–	>44
reflion	Fe/Solar	–	–	–	–	1 (frozen)
reflion	Γ	–	–	–	–	$1.84^{+0.04}_{-0.01}$
reflion	ξ	–	–	–	–	660 (frozen)
reflion	Norm ($\times 10^{-6}$)	–	–	–	–	$2.2^{+0.5}_{-0.4}$
	Total χ^2 (d.o.f.)	1489 (901)	1463 (899)	1464 (899)	1519 (899)	1463 (900)

Notes. The five models reported in this table mainly differ in the modeling of the iron feature. In the first four models the X-ray continuum is fitted with const*phabs*CompTT, to which a Gaussian line (Model 1), or a diskline (Model 2), or a relativistic line (Model 3) or two edges (Model 4) are used to fit residuals in the iron K-shell range. Model 5 includes a different Comptonization continuum model and a self-consistent, relativistically smeared reflection component: const*phabs*(nthComp + rdblur * reflionx).

continuum and the corresponding discrete features (Ross & Fabian 2005), in addition to a thermally Comptonized continuum modeled with nthcomp, by Zdziarski et al. (1996), and extended by Zycki et al. (1999), instead of comptt. The χ^2/d.o.f. was 1555/901, without the inclusion of relativistic smearing. Because the iron line was found to be significantly broad in the previous models (Model 1, 2, and 3), we added the relativistic smearing using the rdblur component. The addition of this component to the model constitutes Model 5 in Table 3 and led to a χ^2/d.o.f. = 1466/899. The decrease of the χ^2 for the addition of the relativistic smearing was $\Delta\chi^2 = 89$ for the addition of two parameters (corresponding to an F-test probability of chance improvement of $\sim 10^{-12}$). Assuming that iron has a solar abundance and freezing the emissivity betor index to -2.8 (value

obtained with the diskline model) and the ionization parameter $\xi = L_{\mathrm{X}}/(nr^2)$ to 660 (this parameter tends to take high values but is unstable during the fit, which is why we preferred to freeze it), where L_{X} is the ionizing X-ray luminosity, n is the electron density in the reflector, and r the distance of the reflector to the emitting central source, the inner radius was estimated again to be 20 R_{g} and a lower limit to the inclination angle was found to be 44°. In Fig. 3 we plot the residuals obtained with this self-consistent reflection model in comparison with the continuum and the relline model using the EPIC-pn data.

The residuals found with respect to the different models described above do not show any evident systematic trend; the large χ^2 could be due to mismatches in the cross-calibration between the different instruments (for more details, see the
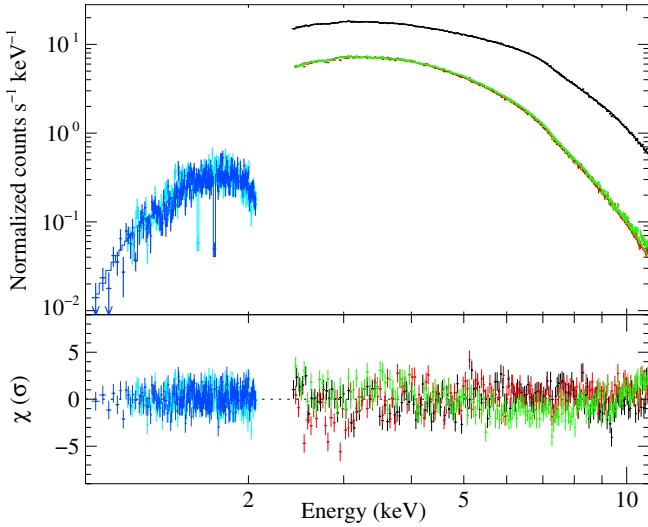
Fig. 2. *Top panel*: EPIC-pn (black), MOS1 (red), MOS2 (green), RGS1 (cyan), RGS2 (blue) data points of MXB 1728–34 in the range 1−11 keV. *Bottom panel*: residuals (data-model) in unit of sigmas for the diskline model (Model 2 in Table 3).
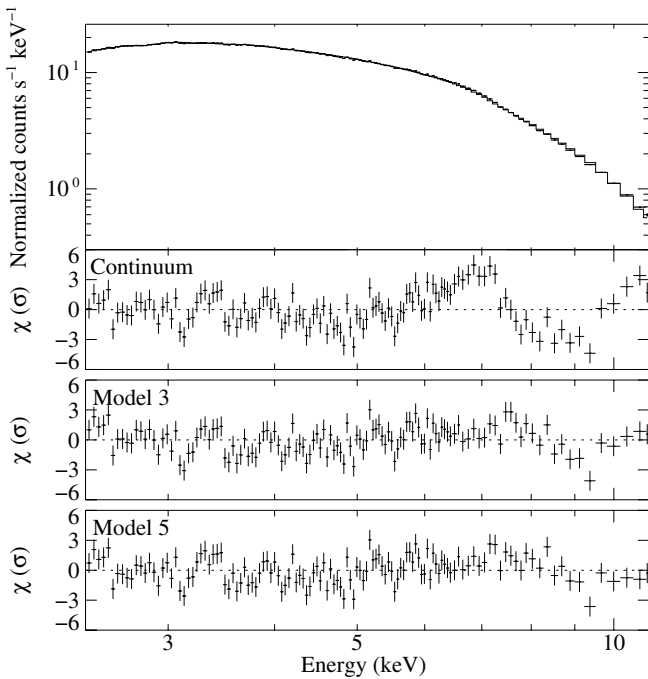

Fig. 3. *Top panel*: EPIC-pn data points of MXB 1728–34 in the range 2.4−11 keV. *Bottom panels*: residuals (data-model) in unit of sigmas for the continuum model reported in Table 2, for Model 3 including a relativistic line (RELLINE), and for Model 5 using a relativistic reflection component (REFLION), respectively. Data were rebinned for graphical purposes.

cross-calibration document available on the *XMM-Newton* web-page[2]) or to unresolved and unfitted features.

4. Discussion

We performed a spectral analysis of MXB 1728–34 observed by *XMM-Newton* on 2002 October 3 in the 1−11 keV energy range. The best-fit continuum model consists of an absorbed Comptonized component; the addition of a soft blackbody component does not improve the fit significantly. With respect to this continuum model, evident residuals are present at 6−8 keV, which can be fitted either by a relativistic line (such as diskline or RELLINE) or by a self-consistent relativistic reflection model.

4.1. The continuum emission

The X-ray spectra of black-hole and neutron star in X-ray binaries are generally described by models that include a soft/thermal and a hard/Comptonized component; the electron temperature of the Comptonized component significantly decreases when the source transits from the hard to the soft state while its optical depth increases. For hard spectra, Comptonization is unsaturated and the spectrum may be approximated by a cutoff power-law. In soft states, Comptonization is saturated and the spectral shape can be approximated with a blackbody emission at the electron temperature. During the observation with *XMM-Newton*, MXB 1728–34 was in a low-luminosity state, and presumably an unsaturated Comptonization is the expected spectral shape. We chose a continuum that consists of an absorbed Comptonization model (COMPTT or NTHCOMP) because these models gave the best fit to the broad-band (0.1−200 keV) BeppoSAX spectrum of MXB 1728–34 (Piraino et al. 2000; Di Salvo et al. 2000).

A different continuum was used by Ng et al. (2010) to fit the sample of neutron star LMXBs. Most of the observations, including MXB 1728–34, were well fitted by a blackbody plus a disk blackbody component, absorbed by neutral interstellar matter. The temperature of the blackbody and of the disk blackbody component had values between 1.5 and 2.8 keV and between 0.6 and 1.3 keV, respectively, except for MXB 1728–34, for which temperatures were found between $3.8^{+8.4}_{-1.1}$ keV and 1.9 ± 0.3 keV, respectively. An alternative model consisting of a blackbody and a power-law was also used to fit the continuum. However, in this case Ng et al. warn the reader that different continuum parameters were found when fitting the residuals at the Fe band with different models, meaning that this line fit may not be realistic. Moreover, it is noted that MXB 1728–34 was in a low-luminosity state during the *XMM-Newton* observation and that for such dim sources Compton scattering is expected to play an important role but was not included in their models. In our case, fitting the X-ray continuum with a Comptonization component, the parameters of the continuum do not change significantly when we add a Gaussian or a relativistic line (such as diskline or RELLINE) to the continuum. Our choice of the continuum modeling allows us to better constrain the profile of the broad iron line. In this context, the choice of a particular fitting to the line does not result in sensible changes of the parameters determining the continuum emission. Moreover, when we tried a self-consistent reflection model, we again found similar values of the spectral parameters, which again indicates that the fit is stable and does not depend on the particular choice of the model used to fit the continuum or the iron line.

The equivalent hydrogen column inferred from the Galactic photoelectric absorption component, $N_H \sim 2.8 \times 10^{22}$ cm^{-2}, agrees with typical values for this source ($N_H \sim 2.6-2.7 \times 10^{22}$ cm^{-2}, Di Salvo et al. 2000; Piraino et al. 2000; D'Aì et al. 2006). The Comptonized component can be produced by inverse Compton scattering from relatively hot electrons ($kT_e \sim$

3.3 keV using the COMPTT model or $kT_e \sim 4.8$ keV using the NTHCOMP model) off soft photons ($kT_{seed} \sim 0.7$ keV using the COMPTT model or the NTHCOMP model). The seed photons for Comptonization are compatible with coming from the neutron star surface. Indeed, we can estimate the size of the emitting region of the soft photons using the formula given by in't Zand et al. (1999). For this, one assumes that the bolometric luminosity of the soft photons is equal to the corresponding blackbody luminosity at the Wien temperature. The relative gain $y = 5.01$ (for a spherical geometry) takes into account the energy gained by the photons scattered off relativistic electrons through the inverse Comptonization process. This leads to a value $R_{seed} = 4.9d_{5.1}$ km, where $d_{5.1}$ is the distance in units of 5.1 kpc, considering the unabsorbed flux that we extrapolated in the energy range 0.1–150 keV, $F_{bol} \sim 1.5(2) \times 10^{-9}$ ergs cm^{-2} s^{-1}.

Usually a soft blackbody component is required to fit the broad band X-ray spectra of LMXBs, most frequently interpreted as emitted by an accretion disk. This component is not significantly detected in the *XMM-Newton* spectrum. This may be ascribed to the relatively low X-ray luminosity of the source during the *XMM-Newton* observation, specially in the soft band. The bolometric X-ray flux in the range 0.1–150 keV also implies a bolometric X-ray luminosity of $L_X \sim 5 \times 10^{36} d_{5.1}^2$ erg s^{-1}, corresponding to 2% of the Eddington luminosity, that is $L_{Edd} = 2.5 \times 10^{38}$ erg s^{-1} for a 1.4 $M_\odot$ neutron star (e.g., van Paradijs & McClintock 1994). Indeed, during the high/soft state the disk is expected to be very close to the compact object, while in the low/hard state the disk should be truncated far from the compact object, and therefore its contribution is expected to be less important. We therefore conclude that the blackbody component is just too weak to be detected. This agrees with the results obtained from the fit of the iron feature with a reflection model. This indicates that the inner accretion disk is probably truncated far from the neutron star ($R_{in} > 25$ km), and with a relatively high value for the system inclination with respect to the line of sight estimated at $44° < i < 60°$, which would further reduce the disk luminosity with respect to the Comptonized component in the hypothesis that the last one has a spherical geometry around the compact object.

4.2. The iron line emission

Recently Ng et al. (2010) and Cackett et al. (2010) presented a spectral analysis of a sample of neutron star LMXBs observed by *XMM-Newton* and *Suzaku,* respectively, with particular interest in the iron discrete features in these sources. While Cackett et al. (2010) conclude that Fe K line profiles are well fitted by a relativistic line model for a Schwarzschild metric in most cases and imply a narrow range of inner disk radii (6–15 GM/c^2), Ng et al. (2010) conclude there is no evidence for asymmetric (relativistic) line profiles in the *XMM-Newton* data, although the line profiles (fitted with a simple Gaussian or a laor model) again appear to be quite broad, with Gaussian sigmas ranging between 0.17 up to 1.15 keV. Another aspect relevant in this context is the impact of photon pile-up on relativistic disk lines and continuum spectra. However, as shown in Miller et al. (2010), while severe photon pile-up may distort relativistic disk lines and continuum shape, a modest pile-up fraction does not sensibly affect the line shape. This is certainly the case of MXB 1728–34.

We tried different models to fit the iron line profile. Although a Gaussian line provides an acceptable fit of the line profile, we tried to physically interpret its large width using models for a relativistically smeared line in an accretion disk.

Using the diskline profile (Model 2), we find the line centroid energy at 6.45 keV, compatible with a fluorescent Kα transition from mildly ionized iron (Fe I–XX). The inner radius is in the range 12–21 R_g. The line profile appears therefore to be significantly broad and compatible with a diskline profile. The results obtained by using a relativistic line profile corresponding to Model 3, which uses the more recent RELLINE instead of diskline, are perfectly consistent with the diskline model. The inner radius is estimated to be in the range 15–22 R_g.

The line profile can be equally well fitted using a self-consistent relativistic reflection model (Model 5). The addition of the RDBLUR component significantly improves the χ^2. This indicates that the line is indeed broad, and that the width of the line agrees with a relativistic smearing in the disk. The value of the inner radius is again consistent with that found using a diskline or a relline profile, even if the uncertainty is larger ($R_{in} = 13$–43 R_g). For a neutron star mass of 1.4 $M_\odot$, the inner disk radius is in the range 25–100 km from the neutron star center, and so the disk would be truncated quite far from the neutron star surface. The inclination angle of the system with respect to the line of sight is found to be >44°, which is still compatible with the absence of dips in its lightcurve (which implies $i < 60°$).

We also attempted to fit the iron feature using an alternative model (Model 4), consisting of two absorption edges instead of a broad emission line (see D'Aì et al. 2006). Their energies correspond to moderately ionized iron, Fe from IX to XVI, and highly ionized iron, Fe XXIII, respectively. The fit was not as good as with the previous models, because the corresponding χ^2 was larger by 56 with the same number of degrees of freedom. We can compare these results with those obtained by (D'Aì et al. 2006), using simultaneous *Chandra* and RXTE observations. The edges were found at slightly different energies of 7.1 and 9.0 keV, corresponding to weakly (Fe I–V) and highly ionized iron (Fe XXV–XXVI), respectively. Although the fitting with two iron edges cannot be completely excluded yet, we think that the most probable explanation is that a couple of edges may mimic the shape of a broad iron line, given the relatively low statistics. We therefore favor the interpretation of the iron feature as a broad and relativistic emission line produced in the accretion disk, because this gives a better fit of the *XMM-Newton* spectrum and very reasonable values of the reflection parameters.

References

Anders, E., & Grevesse, N. 1989, Geochim. Cosmochim. Acta, 53, 197
Arnaud, K. A. 1996, in Astronomical Data Analysis Software and Systems V, ASP Conf. Ser., 101, 17
Balucinska-Church, M., & McCammon, D. 1992, ApJ, 400, L699
Basinska, E. M., Lewin, W. H. G., Sztajno, M., Cominsky, L. R., & Marshall, F. J. 1984, ApJ, 281, L337
Bhattacharyya, S., & Strohmayer, T. E. 2007, ApJ, 664, L103
Boirin, L., Mendez, M., Diaz Trigo, M., Parmar, A. N., & Kaastra, J. S. 2005, A&A, 436, 195
Cackett, E. M., Miller, J. M., Bhattacharyya, S., et al. 2008, ApJ, 674, L415
Cackett, E. M., Miller, J. M., Ballantyne, D. R., et al. 2010, ApJ, 720, L205
Claret, A., Goldwurm, A., Cordier, B., et al. 1994, ApJ, 423, L436
D'Aì, A., Di Salvo, T., Iaria, R., et al. 2006, A&A, 448, 817
D'Aì, A., Iaria, R., Di Salvo, T., Matt, G., & Robba, N. R. 2009, ApJ, 693, L1
D'Aì, A., Di Salvo, T., Ballantyne, D., et al. 2010, A&A, 516, A36
Dauser, T., Wilms, J., Reynolds, C. S., & Brenneman, L. W. 2010, MNRAS, 409, 1534
den Herder, J. W., Brinkman, A. C., Kahn, S. M., et al. 2001, A&A, 365, L7
Di Salvo, T., Iaria, R., Burderi, L., & Robba, N. R. 2000, ApJ, 542, L1034

Di Salvo, T., D'Aì, A., Iaria, R., et al. 2009, MNRAS, 398, 2022
Fabian, A. C., Rees, M. J., Stella, L., & White, N. E. 1989, MNRAS, 238, 729
Fabian, A. C., Iwasawa, K., Reynolds, C. S., & Young, A. J. 2000, PASP, 112, 1145
Falanga, M., Gotz, D., Goldoni, P., et al. 2006, A&A, 458, 21
Galloway, D. K., Psaltis, D., Chakrabarty, D., & Muno, M. P. 2003, ApJ, 590, L999
Grindlay, J. E., & Hertz, P. 1981, ApJ, 247, L17
Hasinger, G., & van der Klis, M. 1989, A&A, 225, 79
Hoffman, J. A., Lewin, W. H. G., Doty, J., et al. 1976, ApJ, 210, L13
Hurkett, C. P., Vaughan, S., Osborne, J. P., et al. 2008, ApJ, 679, L587
Iaria, R., D'Aì, A., di Salvo, T., et al. 2009, A&A, 505, 1143
in't Zand, J. J. M., Verbunt, F., Strohmayer, T. E., et al. 1999, A&A, 345, 100
Lewin, W. H. G., Clark, G., & Doty, J. 1976, 2922, 1
Mason, K. O., Breeveld, A., Much, R., et al. 2001, A&A, 365, 36
Miller, J. M. 2007, ARA&A, 45, 441
Miller, J. M., Fabian, A. C., Wijnands, R., et al. 2002, ApJ, 570, L69
Miller, J. M., D'Aì, A., Bautz, M. W., et al. 2010, ApJ, 724, 1441
Narita, T., Grindlay, J. E., & Barret, D. 2001, ApJ, 547, L420
Ng, C., Daz Trigo, M., Cadolle Bel, M., & Migliari, S. 2010, A&A, 522, A96

Papitto, A., Di Salvo, T., D'Aì, A., et al. 2009, A&A, 493, 39
Papitto, A., Riggio, A., Di Salvo, T., et al. 2010, MNRAS, 407, 2575
Piraino, S., Santangelo, A., & Kaaret, P. 2000, A&A, 360, 35
Protassov, R., van Dyk, D. A., Connors, A., Kashyap, V. L., & Siemiginowska, A. 2002, ApJ, 571, 545
Reynolds, C. S., & Nowak, M. A. 2003, Phys. Rep., 377, 389
Ross, R. R., & Fabian, A. C. 2005, MNRAS, 358, 211
Schulz, N. S. 1999, ApJ, 511, L304
Strohmayer, T. E., Zhang, W., Swank, J. H., et al. 1996, ApJ, 469, L9
Struder, L., Briel, U., Dennerl, K., et al. 2001, A&A, 365, 18
Taam, R. E. 1982, ApJ, 258, L761
Tanaka, Y., Nandra, K., Fabian, A. C., et al. 1995, Nature, 375, 659
Titarchuk, L. 1994, ApJ, 434, L570
Turner, M. J. L., Abbey, A., Arnaud, M., et al. 2001, A&A, 365, 27
van Paradijs, J., & McClintock, J. E. 1994, A&A, 290, 133
White, N. E., Peacock, A., Hasinger, G., et al. 1986, MNRAS, 218, 129
Yan, M., Sadeghpour, H. R., & Dalgarno, A. 1998, ApJ, 496, L1044
Zdziarski, A. A., Johnson, W. N., & Magdziarz, P. 1996, MNRAS, 283, 193
Zycki, P. T., Done, C., & Smith, D. A. 1999, MNRAS, 309, 561

The reflection component in 4U 1705-44

Contents

simultaneously The second source I studied is another well-known neutron star LMXB: 4U 1705-44. The goal of this work was to investigate the changes in the spectral parameters when the source was in two distinct states: the hard and the soft states, in order to understand what could be at the origin of these changes. An hypothesis proposed for black hole binaries suggests that the accretion disk would be truncated farther from the compact object in the hard state. I examined the case of 4U 1705-44 to infer whether this hypothesis could also be valid for neutron star LMXBs.

For this purpose, I constituted a sample of data from different X-ray satellites: XMM-Newton, BeppoSAX, and RXTE, in both states. I applied different models to the data sets, and I compared the obtained parameters.

5.1   4U 1705-44

4U 1705-44, also known as MXB 1705-44 or GX 354-0, is one of the most studied neutron star LMXB. The choice of this source is motivated by different reasons: 1) 4U 1705-44 is a weakly magnetized neutron star, thus similarities with black hole binaries are expected in the accretion disk close to the compact object, 2) the source shows clear spectral transitions from the hard to the soft state, 3) a strong iron line has been detected with XMM-Newton in both states with a well-determined profile, 4) other emission lines and a Compton hump have been detected in the soft and in the hard state, respectively, which gives the possibility to test the common origin of all these features, 5) different observations were performed with different satellites in both states, covering a broad-energy range. Therefore, 4U 1705-44 represents an ideal candidate to perform such study.

5.1.1   The best-studied X-ray burster

Discovered for the first time in 1972 with the Uhuru satellite [Giacconi 1972], 4U 1705-44 is defined as a bright and persistent system showing type-I X-ray bursts [Langmeier 1987]. Some bursts enabled the estimation of the distance of this source at 7.4 kpc in the direction of the Galactic center [Forman 1978, Galloway 2008].

4U 1705-44 is a well-known accreting LMXB that belongs to the class of atoll sources. However, [Barret 2002] noticed that the source sometimes presents a similar color-color diagram with respect to the one associated with Z-sources.

Different spectral and timing studies were performed since the source exhibits two distinct states with a variability on all timescales, from months down to milliseconds. [Olive 2003] looked for correlations between the timing and spectral parameters to get further insights on the accretion flow changes associated with the state transitions.

Spectral analysis were performed using different observatories, such as Chandra [Di Salvo 2005], INTEGRAL [Fiocchi 2007], BeppoSAX [Lin 2010], Suzaku [Reis 2009b], and XMM-Newton [Di Salvo 2009, D'Aì 2010]. A clear Fe line is present in the spectra, in addition to a Compton hump in the hard state.

As for timing properties, they were mainly inferred by RXTE. 4U 1705-44 shows kHz quasi-periodic oscillations (QPOs) [Ford 1998, Olive 2003]. The frequency separation of the two peaks QPOs and the QPOs observed in X-ray bursts suggest a beat-frequency mechanism [Miller 1998]. The frequency separation of the QPOs in 4U 1705-44 implies that the spin period of the neutron star is 3.35 ± 0.12 ms [Ford 1998].

5.1.2   The data selection

As mentioned previously, 4U 1705-44 represents a perfect candidate to study the changes in the spectral parameters from one state to the other one. Unfortunately, there are no simultaneous observations of this source, however, a total of four observations were performed with BeppoSAX and XMM-Newton (two in each state)

at similar flux levels. Fig 5.1 presents the light curve obtained with the All Sky Monitor (ASM) onboard RXTE. The two observations performed in the soft state corresponds at ~ 18 counts/s, and those realized in the hard state at ~ 3 counts/s. This is a very interesting point since properties of the source are expected to be similar for similar flux levels.
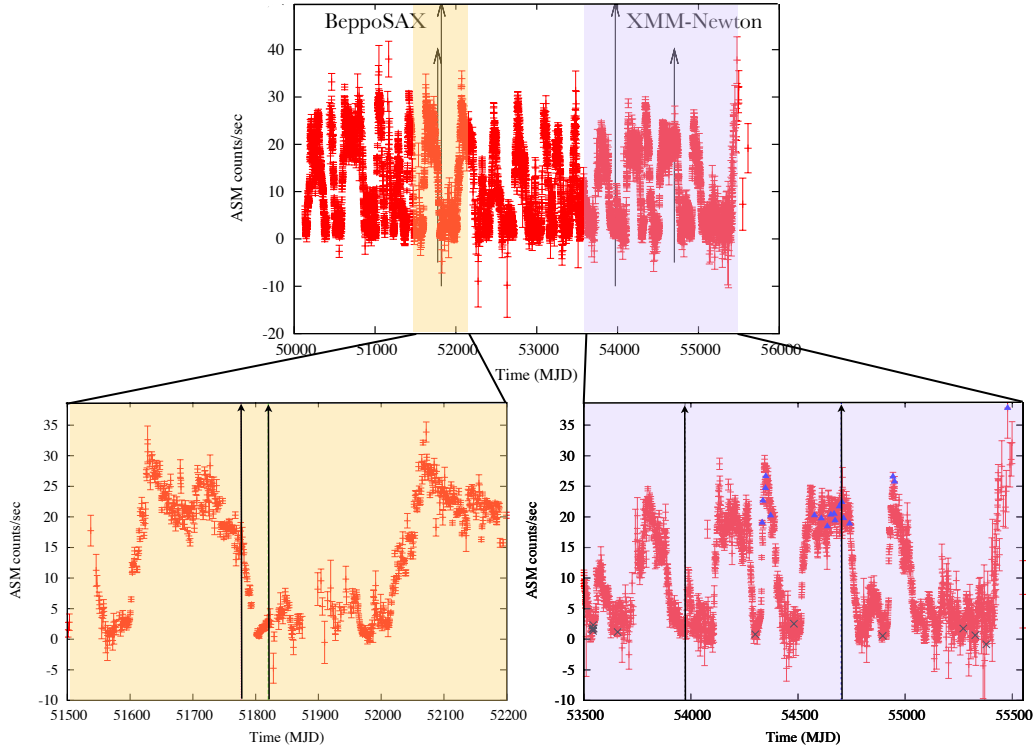
Figure 5.1: The upper panel shows the light curve of 4U 1705-44 obtained with RXTE/ASM on about 16 years. The two first arrows (in the yellow area) mark the observations performed by BeppoSAX in August and October 2000, the two other ones (in the mauve area) indicate the XMM-Newton observations performed in August 2006 and 2008. The lower panels represent two zooms of the light curve of the yellow and mauve areas. The blue triangles and the black crosses correspond to the RXTE observations selected in the soft and in the hard state, respectively.

Moreover, it is very useful to combine advantages of the different instruments to obtain the best constraints on models. XMM-Newton offers a good spectral resolution close to the iron line and BeppoSAX makes the study possible on a large X-ray range, from 0.1 to 200 keV.

Besides studying the spectral changes in 4U 1705-44, it would be interesting to follow the evolution of timing properties from one state to the other one. RXTE data constitute the best opportunity to do so, since this satellite has been designed primarily to study timing properties of binary sources. The difficulty was to cre-
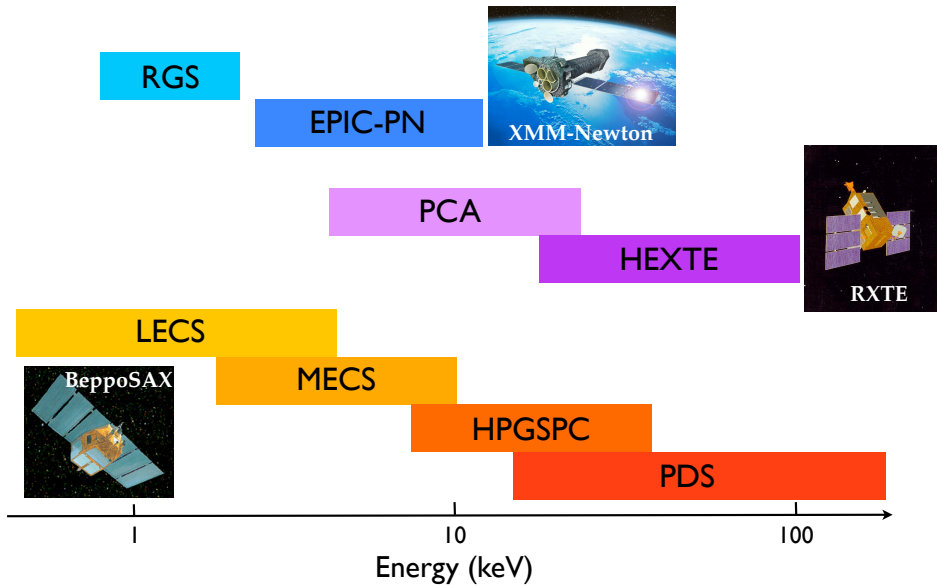
Figure 5.2: Illustration of the energy ranges covered by the different instruments used onboard XMM-Newton, RXTE, and BeppoSAX.

ate a sample of RXTE data with a flux similar to the ones of XMM-Newton and BeppoSAX data. A solution was to produce a color-color diagram (CD) from the XMM-Newton data, and a second one from the RXTE data available, using the same energy bands for the two instruments ($2.47 - 3.68$ keV and $3.68 - 5.31$ keV for the soft color and, $5.31 - 7.76$ keV, $7.76 - 10.22$ keV for the hard color). After having normalized each CD with the Crab colors, they were superimposed on the same figure. As a shift was present between both diagrams, an adjustment by hand was needed, by following their shapes. The resulting CDs are presented in Fig 5.4, and the corresponding RXTE data selected are shown in Fig 5.1.

To summarize, a sample of data has been created in the hard and in the soft states, since no simultaneous observations were performed. The satellites providing the data cover a wide energy range, as illustrated in Fig 5.2, and combine large effective areas (see Fig 5.3) with a high resolution. The aim is then to use the same models in both sets of data, in order to have a direct comparision of the spectral parameters. In the following sections, I present the study performed in each of these states, the reflection components detected, and a possible scenario that can explain the observed changes.

5.2 The soft state

The XMM-Newton/EPIC-pn data associated with the soft state of 4U 1705-44 are of very good quality. The spectrum presents different emission lines, among them
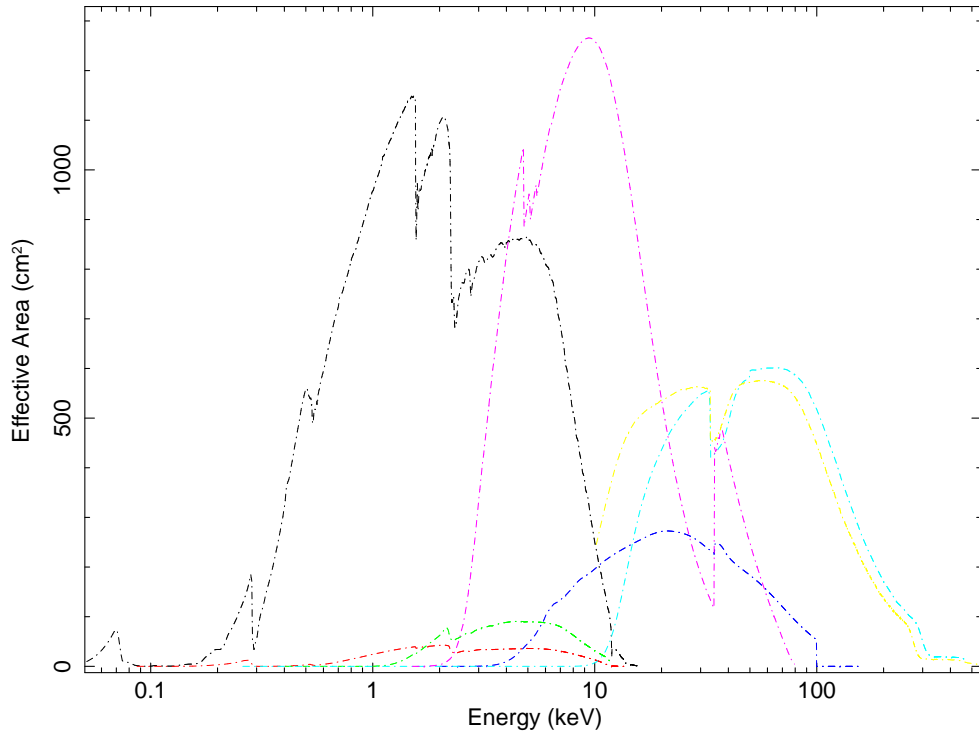
Figure 5.3: Effective area: XMM-Newton/EPIC-pn (black), BeppoSAX/LECS (red), BeppoSAX/MECS (green), BeppoSAX/HPGSPC (blue), BeppoSAX/PDBN (cyan), RXTE/PCA (purple), RXTE/HXTE (yellow).

a strong and extremely well-defined Fe line, in addition to an iron absorption edge. However, the source being very bright during the observation, the question of pile-up must be brought up and discussed.

After having explained what is pile-up and its effects on the data, I present the different models I applied, from the simplest ones (Gaussian, diskline models) to the most complex ones (reflection models). In essence, by comparing the Gaussian and the diskline models, I demonstrate that the iron line is relativistic. Moreover, I show that the application of reflection models is consistent with a common origin of the emission lines in the accretion disk, by processus of reflection of the main component.
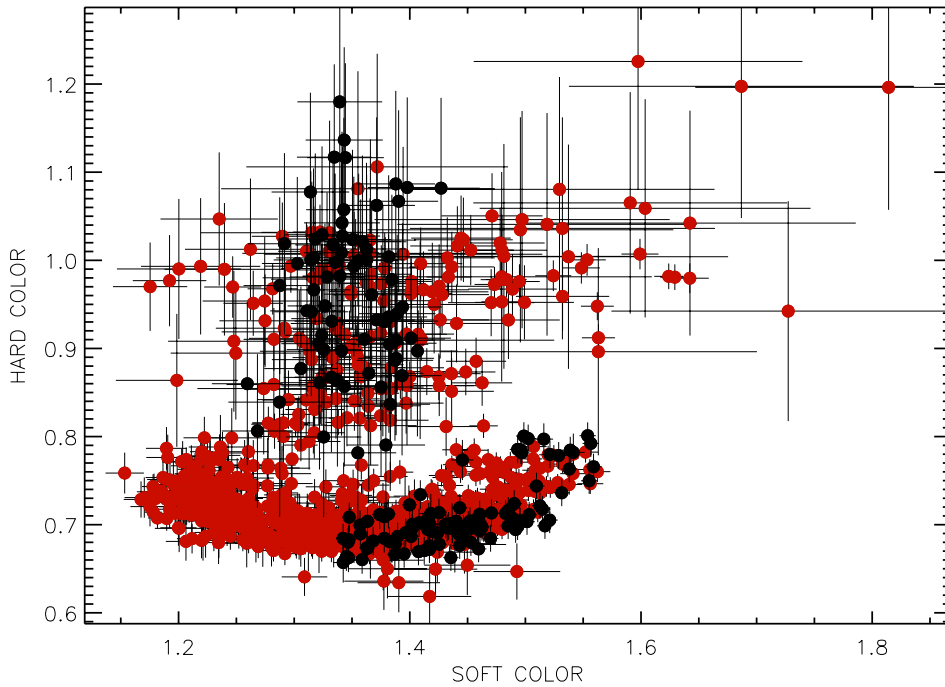
Figure 5.4:   Color-color diagrams of 4U 1705-44 produced by RXTE/PCA (red)
and XMM-Newton/EPIC-pn (black). The RXTE observations have been selected
in such way that they match with those of XMM-Newton, in the hard and soft
states.

5.2.1   Pile-up in the XMM data in the soft state?

Different studies were performed on the XMM-Newton data of 4U 1705-44 by
[Di Salvo 2009, D'Aì 2010, Ng 2010]. However, the authors disagree on the pile-
up fraction detected in this source, and above all, on the way pile-up affects the
data. This has important consequences on the results they obtained, especially
concerning the debate on the iron line: the conclusions are in total contradiction.

What is pile-up?

Pile-up is an important effect to take into account that occurs especially in the case
of bright sources. This is related to a false or a bad photon detection on the camera
CCDs, because of an overexposure effect. Different situations can induce pile-up:

- "energy pile-up": if more than one photon hits the same pixel $\rightarrow$ a single
  photon is read with an energy equal to the sum of the individual energies of
  the incoming photons

- "pattern pile-up": if more than one photon is detected in two or more adjacent
  pixels $\rightarrow$ photons are detected as one individual event having the sum of their
  energies

In both cases, electronics cannot distinguish whether the signal registered corresponds to the original photon energy, or to the combination of different photons. If this happens sufficiently often, the resulting spectrum is erroneous, since some photons are not detected at the correct energy. Therefore, pile-up can affect both the spectral response of EPIC and the point spread function (PSF); see [Read 2011] for a comprehensive description of the EPIC PSF. The main effects observed on a spectrum are a loss of photons, because a single photon can be read instead of several ones, and an energy distorsion (a hardening of the spectrum) due to the charges that are deposited by more than one photon and are associated with an artificial hard photon instead of two or more soft photons.

Timing or burst mode is generally chosen for bright point-like sources in order to avoid pile-up. Timing mode uses a single CCD situated at the center of the pn-camera. The X axis corresponds to the projected image of the source, providing the spatial information, whereas the Y axis is a simple measure of time. This makes the read-out possible at high speed. Burst mode also operates with one CCD, but the source position is not read out (rows 181-200 are dark) to permit a very high time resolution, and the duty cycle is reduced to 3%.

It is possible to qualitatively assess whether an observation is affected by pile-up, thanks to the SAS task "epatplot[1]". This consists in comparing the observed pattern distribution of single, double, triple, and quadruple events versus the expected model pattern distribution within a source extraction region. If the distributions are not consistent, it indicates that data are affected by pile-up (see Fig 5.5).

How to do in case of pile-up?

A common way to overcome pile-up is to exclude photons coming from the brightest part of the source. Indeed, many photons may arrive at almost the same time, thus they represent a strong risk to induce pile-up in the data. To solve the problem, the core of the PSF must be excised.

This implies an iterative approach, where the inner region of the PSF is removed, then the new spectrum is extracted, and the "epatplot" task has to be re-called to check the new pattern distributions. The procedure has to be repeated until the observed and the modeled distribution functions are consistent. Of course, excluding inner parts of the source reduces the number of events for the spectral analysis. Therefore, it is a real compromise between having enough statistics to not distort the data analysis, and excluding a correct fraction of the PSF.

The case of 4U 1705-44

The XMM-Newton/EPIC-pn data were acquired in the timing mode. However, the counts per second registered are at the very limit of the accepted threshold to avoid pile-up (~ 740 c/s for a threshold at ~ 800 c/s).

---

[1]http://xmm.esac.esa.int/sas/current/documentation/threads/epatplot.shtml
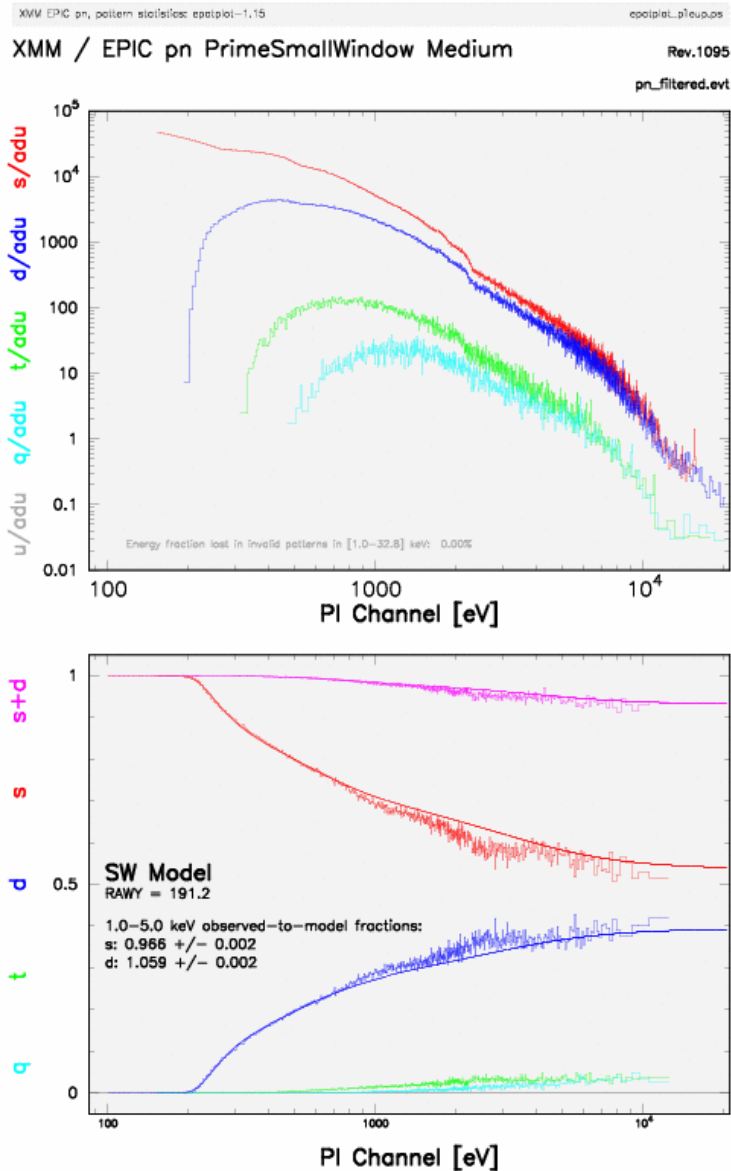
Figure 5.5:   Epatplot outfile of a source suffering from pile-up. The upper panel presents the spectra (distribution of counts as a function of the PI channels) associated with single, double, triple, and quadruple event patterns. The lower panel shows the expected pattern distributions (smooth solid lines) and the observed ones (histogram), in addition to the calculated observed-to-model fractions for single and double events within a certain energy range. In all plots, single, double, triple and quadruple event patterns are represented in red, blue, green and turquoise, respectively.

[Di Salvo 2009, D'Aì 2010, Ng 2010] considered differently pile-up effects in these data. While [Di Salvo 2009] neglected these effects, keeping all central columns of the CCD to extract the spectrum, [D'Aì 2010] excluded the brightest CCD column, and [Ng 2010] excluded 7 central columns, which corresponds to $\sim 90\%$ of the source counts. The conclusions inferred from their spectral analysis are different. [Di Salvo 2009] and [D'Aì 2010] agree on the asymmetry and relativistic nature of the Fe line, whereas [Ng 2010] concluded the Fe line does not show any asymmetry, therefore it is unlikely relativistic.

To definitely disentangle the debate on these data, I carefully studied the consequences that pile-up induces on the EPIC-pn spectrum. For this purpose, I extracted spectra using different selections of the central columns of the CCD, as illustrated in Fig 5.6. In each case, I used the task epatplot to estimate the disortions between the observed spectrum and the expected one, and I evaluated the pile-up fraction close to the iron line energy range. I applied the same model on all spectra, and I compared the spectral parameters and the associated error bars.

pn-all   pn-1   pn-2   pn-3   pn-4   pn-5   pn-6   pn-7
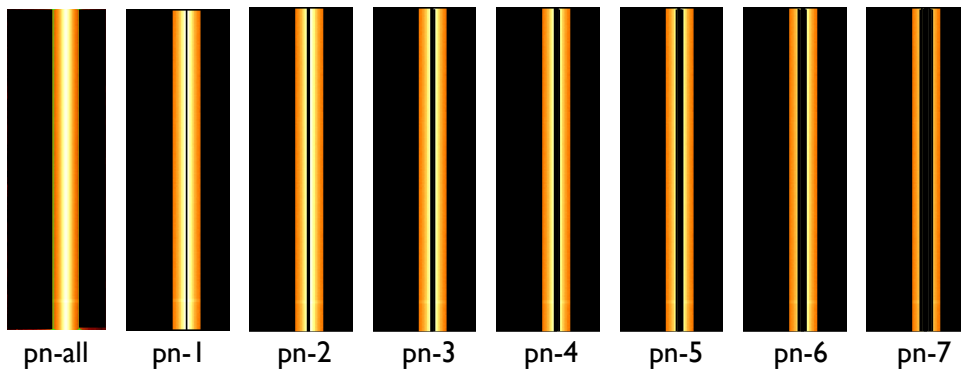
Figure 5.6: Representation of the EPIC-pn CCD in timing mode with different extraction regions. In the first case, all central columns of the CCD are selected to extract the spectrum. In the second one, the brightest column is removed. In the third case, the 2 brightest columns are removed, etc, until the last case where the 7 central columns are removed before extracting the spectrum.

The continuum model I applied on the different spectra consists of a blackbody and a Comptonization model (comptt), modified by the photoelectric absorption (phabs). Given that four emission lines were clearly visible in the data (see Fig 5.7), four Gaussians were added at 2.6 keV, 3.3 keV, 3.9 keV, and 6.6 keV, associated with S XVI, Ar XVIII, Ca XIX, and Fe XXV, respectively, in addition to an iron absorption edge at 8.6 keV. The model was then multiplied by the rdblur component to take relativistic effects produced close to the compact object into account. It gives information on the inclination of the system and on the inner radius of the accretion disk.

The results of the analysis show a variation in some parameters of the continuum in the different cases studied, especially regarding the interstellar absorption column

density, the temperature and normalization of the blackbody component. As for the discrete features and the disk smearing parameters, all values are compatible with each other within the errors. However, the error significantly increases with the decreasing counts, in particular from pn-4 until pn-7.

In order to assess whether the exclusion of some central columns of the CCD has real effects on the spectral shape or simply induces a lack of statistics, I carried out the same analysis than described above but considering also the RGS data together with the EPIC-pn ones. The values of the parameters become much more stable, with the error bars considerably reduced. Therefore, the variation of the parameters and the corresponding error bars fitting the EPIC-pn spectra alone are principally caused by a decrease of the statistics when excluding the central columns of the CCD, thus by a lack of constraints on the parameters.

I compared the deviation of single and double events at the iron line energy, resulting from the task epatplot; the deviation is minimal for the pn-2 spectrum (see Fig 5.10). The continuum parameters obtained from the BeppoSAX spectrum [Piraino 2007] are perfectly consistent with those associated with the pn-2 spectrum. Therefore, this spectrum (without 2 central raws) appears as the best compromise between avoiding any pile-up effects and keeping sufficient statistics to perform the analysis. In the following sections, any reference to the XMM-Newton/EPIC-pn spectrum means the spectrum pn-2.
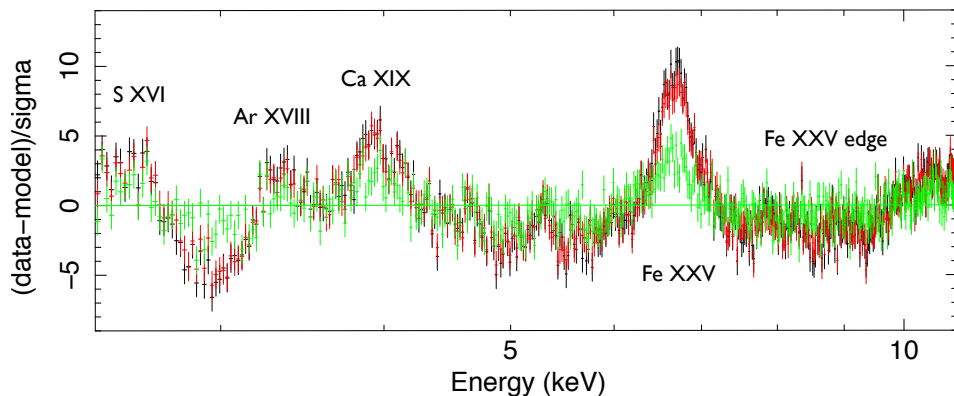
Figure 5.7: Comparison of the residuals of the XMM-Newton/EPIC-pn data considering all rows of the CCD (black; [Di Salvo 2009]), without the brightest CCD column (red; [D'Aì 2010])), and excluding 7 central columns (green; [Ng 2010])), when the continuum model is applied to the data. The continuum consists of a blackbody and a Comptonization model (comptt), modified by photoelectric absorption (phabs).

5.2.2 The detected lines

As shown in Fig 5.7, the EPIC-pn spectrum exhibits a variety of rich features: four emission lines and an absorption edge are clearly present. The most prominent emission line is the Fe line at $\sim 6.6 - 6.7$ keV. The simultaneous study of the detected features offers the possibility to check the hypothesis of a common origin, as reflection component, and to infer information on the accretion disk. Moreover, the detection of the Fe line in the BeppoSAX and RXTE spectra allows us the verification of the conclusions drawn from the XMM-Newton spectrum, and above all, the test of validity of reflection models on a large energy range.

The emission Fe line

A strong Fe line is clearly visible in the EPIC-pn spectrum of 4U 1705-44 in the soft state. This is the highest signal/noise ratio ever detected to date in a neutron star LMXB. It represents a great opportunity to test different models and to obtain important information on the system with high precision.

I first applied a simple Gaussian to fit this feature. The corresponding line centroid and equivalent width are 6.70 ± 0.02 keV and 42 eV, respectively. I then replaced the Gaussian with the diskline model. The line is better fitted with this model, and peaks at 6.66 ± 0.02 keV. The associated equivalent width is 57 eV.

Since the iron line at ~ 6.7 keV very likely corresponds to the Kα transition of Fe XXV, I fitted it with the single components of the triplet, which include the forbidden line (f) at 6.64 keV, the intercombination lines (i) at 6.67 keV and 6.68 keV, and the resonance line (r) at 6.70 keV. I added a line at 6.95 keV to check whether a contribution of the Fe XXVI is also detected. To do so, five Gaussians were used (instead of a single component at 6.7 keV), whose centroid energies were fixed at the expected rest-frame energies. The lines at 6.67 keV and 6.68 keV are indistinguishable with XMM-Newton; the differences in the centroid energies are comparable with the fitting errors on the line energy. I therefore considered only one Gaussian at 6.67 keV to represent the intercombination lines. This line clearly dominates the triplet, although the lines at 6.64, 6.70, and 6.95 keV slightly contribute to the emission. The relative intensities of the Gaussian lines representing the He-like triplet allows us to infer some properties of the plasma (see e.g. [Porquet 2010] and references therein). Since the resonance line intensity is quite negligible with respect to the intercombination line, the plasma is highly photo-ionized. The ratio $R = f/i$ gives constraints on the electronic density and the ratio $G = (f + i)/r$ gives some information on the electronic temperature of the plasma. The relative intensities of the f, i and r lines are $21,4\%$, 71.5% and 7.1%, respectively, which implies that $R \sim 0.3$ and $G \sim 13$. Since the intercombination line is very intense with respect to the other lines and $G > 4$, the electronic temperature is expected to be low. As for the determination of the electronic density diagnostic, the plasma seems to present a relatively high density since the intercombination line is stronger than the forbidden line. In conclusion, the plasma is highly ionized (by a high X-ray luminosity), with a relatively low temperature and a relatively high density.

The BeppoSAX data were studied separately, using the same continuum than the one used for the XMM-Newton data. An iron line is distinctly visible in the residuals and is well fitted by a simple Gaussian. The fit is improved by replacing the Gaussian with a diskline profile at ~ 6.8 KeV (an F-test gives a probability of chance improvement of about 10^{-6}). Thus the iron line profile appears similar in both instruments, although the observations are not simultaneous.

The emission lines at low energy

When the continuum is applied to the Epic-pn data, three emission lines are present in the residuals at 2.6 keV, 3.31 keV, and 3.39 keV, in addition to the Fe line. Associated with S XVI, Ar XVIII, and Ca XIX, respectively, these lines have been detected in other sources such as GX 340+0 [D'Aì 2009], GX 349+2 [Iaria 2009], and GX 3+1 [Piraino 2012].

The simultaneous detection of these lines is of great interest to test and support the reflection scenario, stipulating they would be all produced by reflection in the inner part of the accretion disk, as the Fe line.

I first applied a Gaussian on each of these lines. Using the values of the line width σ and the line centroid energy E, it is possible to infer the velocities associated with the different lines by the relation:

$$\frac{\sigma}{E} = \frac{v_\sigma}{c} \tag{5.1}$$

with c the light velocity.

For instance, as regards the iron line, $E_{\rm Fe} = 6.70 \pm 0.02$ keV and $\sigma_{\rm Fe} \sim 0.25$ keV. The associated velocity is about $v_{\rm Fe} \sim 11\,100$ km/s. In the case of Ar, the line is detected at $E_{\rm Ar} = 3.39 \pm 0.02$ keV and the corresponding $\sigma_{\rm Ar}$ is ~ 0.13 keV. Thus the velocity of the Ar line is $\sim 11\,400$ km/s. In conclusion, the lines having a very similar velocity, they are consistent with coming from the same region of the accretion disk. This is in agreement with the reflection model since the lines are expected to be produced by reflection of the hard X-ray spectrum on relatively cold matter in the accretion disk.

We note that it is also possible to determine the velocity from the full width at half maximum (FWHM), that is different from the velocity inferred using the standard deviation σ.

$$\frac{\rm FWHM}{E} = \frac{v_{\rm FWHM}}{c} \tag{5.2}$$

However the FWHM considers the width caused by positive and by negative velocities. Therefore, to estimate the Keplerian velocity, it is better to use the σ, which is more similar but not equal to the half width height maximum (HWHM), rather than the FWHM.

Then, I added a smearing component (rdblur) to the previous model to take the relativistic distortions induced by the presence of the compact object into account. The same smearing model is applied to all of the Gaussian profiles, to test the common origin of the emission lines. The data are very well fitted and give very

interesting information on the system, such as the inclination of the system with respect to the line of sight $i = 39°\pm2$, and the inner radius of the disk $R_{\mathrm{in}} = 14\pm3\,R_{\mathrm{g}}$.

The iron absorption edge

An iron absorption edge is clearly identified at ~ 8.6 keV in the EPIC-pn data (see Fig 5.7). By adding an edge component to the model, the residuals appear much better. However, there are still a few features left at ~ 9 keV, as presented in Fig 5.11. The addition of another edge at 9.1 keV improves significantly the fit.

As a consequence, using 2 edges and 4 disklines in addition to the continuum, the data are very well fitted. The resulting χ^2_{red} is 1.0026 for 407 dof. Both edges are most likely associated with Fe XXV (8.83 keV in the rest frame energy) and Fe XXVI (9.28 keV).

Fig 5.11 illustrates the comparison of the residuals obtained when no edge is included in the model, when one edge is added, and then when two edges are included.

5.2.3 Reflection models

Different emission lines and absorption edges have been detected in the XMM-Newton/EPIC-pn spectrum of 4U 1705-44 in the soft state. Since the ability of a model to describe the data is the main observational support, it is very important to use models that are as self-consistent as possible.

In order to test the validity of the reflection scenario on these data, I used different reflection models, that include most of the reflection components. To cover a wider energy range and to have better constraints on the parameters, I added the BeppoSAX and RXTE data together with the XMM-Newton ones. In this way, all the data are simultaneously fitted with a same reflection model. Of course, some parameters needs to be let free to obtain a good fit, but in general they are all consistent with each others.

Reflionx

Reflionx contains both the reflection continuum and the corresponding discrete features [Ross 2005]. In addition to fully-ionized species, the following ions are incorporated to the model: C III-VI, N III-VII, O III-VIII, Ne III-X, Mg III- XII, Si IV-XIV, S IV-XVI, and Fe VI-XXVI. However it does not include Ar XVIII and Ca XIX, that is why I added two Gaussians to the model to take these two elements into account.

I multiplied reflionx by a high-energy cutoff where the folding energy is fixed to be 2.7 times the temperature of the electrons, according to the expectation for saturated Comptonization in the soft state. Nthcomp [Zdziarski 1996, Zycki 1999] was used to model the Comptonization continuum instead of comptt in order to have the photon index Γ as fitting parameter of the continuum. Its value is fixed to be equal to the photon index of the illuminating component in the reflection model. I convolved the reflection model and the two Gaussians with the same blurring

component to take the smearing of the reflection component into account. The most interesting results inferred from the reflionx models are:

- the ionization parameter $\xi \sim 3\,500$ is fully consistent with the presence of an iron line at 6.7 keV produced by Fe XXV

- for the first time, there are evidences of an iron overabundance by a factor 2.5 with respect to solar abundance

- the reflection component does not seem to fit correctly the iron edge, since some features are still present in the residuals at about 8.6 keV.

I added an edge to the model, also convolved with the same rdblur component, under the assumption that the edge is also produced in the same region of the accretion disk as the reflection component. The edge is found at 8.7 keV and the associated depth is 0.06.

In order to evaluate the significativity of the edge, two methods are applicable. The first one consists in using the F-test to compare the χ^2 when the edge is included in the model, to the one when the absorption depth is frozen at 0. The edge at 8.6 keV is highly significant since the F-test gives a probability of chance improvement of 10^{-17}.

The second method consists in checking how many σ the depth is from 0. Given that the error bars with Xspec are given at the 90% confidence level, the 1-σ error corresponds to the error estimated by Xspec divided by 1.64. By dividing the best value of the edge depth by the 1-σ error, it indicates how many σ the depth is far from zero. The significance so calculated is 11.6 σ, supporting the evidence of the edge.

Pexriv

To check the consistency of the edge with the reflection continuum, I used the pexriv reflection model [Magdziarz 1995]. This model consists of an exponentially cutoff power-law spectrum reflected by ionized material, and in principle it should include the iron edge and the Compton bump of the reflection component. However this model does not contain any emission line, so four Gaussians corresponding to S, Ar, Ca and Fe were added and convolved with the rdblur component, together with the pexriv component.

The values of the parameters are in agreement with reflionx, in particular the inclination of the system ($i = 38 - 41°$) and the inner radius of the accretion disk ($R_{in} = 12 - 17\,R_g$). Moreover, the features at about 8.6 keV are not visible anymore in the residuals. Therefore, the edge is well fitted by pexriv and is most likely a reflection feature.

Xillver

I also applied another reflection model, called xillver [Garcia 2010]. This model contains among other Compton broadening and emission lines from the same ions than

those included in reflionx, in addition to the Ar and Ca emission lines. Moreover, xillver lets vary the abundances of Ar and Ca with respect to solar abundances.

The addition of the edge at 8.6 keV is needed to improve the fit. The obtained fit is not as good as the one obtained with reflionx, but the values of the parameters are still consistent with each others. An overabundance of Ar and Ca seems to be detected with a factor of $1.5 - 2$ with respect to their solar abundances. One may note that a similar overabundance is also observed for Fe with reflionx. However the statistical significance of the overabundance of Ar and Ca is not very well established. In any case, xillver demonstrates that the Ar and Ca lines are well fitted and are most likely produced by reflection.

5.3   The hard state

The study of the hard state is less complex than that of the soft state. The source being less bright, the statistics is less important. As a consequence, there is no problem of pile-up in the XMM-Newton data.

I first studied the spectra from XMM-Newton, BeppoSAX, and RXTE, separately. I applied the same continuum model than in the soft state (a black body plus a Comptonized component, modified by the photoabsorption). The values of the parameters are similar for the different sets of data, and clearly confirm that 4U 1705-44 was in the hard state during these obervations (the photon index of the power-law $\Gamma = 1.84 \pm 0.01$).

Then I combined all the data together to cover a broad-band energy, to better constrain the reflection models, and to have a direct comparison with the parameters obtained in the soft state. An iron line and a Compton hump at ~ 30 keV are easy to see in the residuals of the spectra.

5.3.1   The iron line

I added a simple Gaussian to fit the excess at ~ 6.4 keV, most likely associated with the iron line. I substituted the Gaussian with the diskline component, to see if any asymmetry can be inferred on the iron line profile. Because of the high uncertainties on the inclination of the system and on the outer radius of the disk, I fixed their values to those obtained in the soft state: $i = 37°$ and $R_{in} = 3\,500\,R_g$, respectively. The resulting χ^2 is very similar in both cases; the Fe line is equally well fitted by a Gaussian or a diskline component.

5.3.2   The reflection models

By including a Gaussian or a diskline profile in addition to the continuum, some features are still present at $\sim 20 - 40$ keV in the residuals corresponding to the BeppoSAX and RXTE data. In order to fit this hard excess, probably ascribed to the Compton bump, I simultaneously applied the self-consistent reflection model reflionx to the whole dataset. Some parameters are left free to vary between the

instruments of the different observatories such as the column density and the black-body temperature.

I convolved the reflection model with the rdblur component, which includes Doppler broadening caused by the motion of matter in the inner disk. This makes the χ^2 decrease from 1126/981 to 1097/980. The corresponding F-test gives a probability of improvement by chance $\sim 10^{-7}$. This result confirms that the iron line and the whole reflection component are significantly broadened also in the hard state, and are consistent with being produced in the accretion disk.

The reflection model provides interesting constraints on the inner disk radius, which appears to be truncated farther from the neutron star surface $R_{in} = 19 - 59\,R_g$. The electron temperature is rather high $kT_e \sim 22 \pm 2$ keV and the ionization parameter attains a quite low value $\xi \sim 210$ erg cm s^{-1}.

Because in the soft state an iron overabundance is detected by at least a factor 2 with reflionx, I fixed this parameter to 2 in order to evaluate the change in the whole spectrum and its effect on the other parameters. The obtained χ^2 is slightly higher (1109 for 981 dof), nevertheless the values of the parameters remain very similar. The inner disk radius is found to be at a slightly larger distance from the compact object $R_{in} = 24 - 79\,R_g$, again in agreement with an accretion disk truncated farther from the neutron star than in the soft state.

To measure the significance of the Compton bump, I substituted the reflionx model with a simple Gaussian line smeared by relativistic and/or Doppler effects, using the rdblur component. The χ^2 is $1299/981 \sim 1.32$, which is much higher than using the reflection model (χ^2 is $1097/980 \sim 1.12$). This means that the Compton bump is significantly detected in these data.

Also, I tested the xillver model on the whole dataset. The parameters are all perfectly consistent with those found with reflionx.

5.4 Results

To summarize, I performed a broad-band and high-energy resolution spectral analysis of 4U 1705-44 using data from XMM-Newton, BeppoSAX, and RXTE, both in the hard and in the soft state. The different models applied on the data give interesting information on the source in both states.

In the following sections, I compare the results obtained with the different models. In particular, I discuss the observed changes regarding the iron line and the spectral parameters of the reflection models.

5.4.1 The iron line

The iron line is an invaluable spectral feature which brings precious information on the system. However its origin and nature are still matter of debate in neutron star LMXBs [Ng 2010, Cackett 2010, Cackett 2012].

After having minutiously studied pile-up effects could induce on the XMM-Newton/EPIC-pn data in the soft state, I demonstrated that the exclusion of the

two central columns is enough to get rid of any effects. This study shows that the iron line profile is robust even with the presence of a small fraction of pile-up, which is in agreement with [Cackett 2010] and [Miller 2010], while the continuum may vary more significantly. Moreover, the best fit parameters of the iron line profile are consistent with the previous studies on 4U 1705-44 (see e.g. [Piraino 2007, Di Salvo 2009, D'Aì 2010], and they turn out to be independent of any particular model neither from the different instruments used.

In the soft state, the Fe line at 6.7 keV is associated with highly ionized Fe XXV. The line is well fitted with a diskline component or reflection models, however, a further smearing is required to properly fit the line complex. This is consistent with a production of the Fe line in the inner part of the accretion disk where the line profile is distorted by Doppler and mildly relativistic effects relatively close to the compact object.

In the hard state, the Fe emission line at $\sim$ 6.4 keV is related to a low ionized Fe fluorescence line. The line does not present a clear asymmetry anymore. It may be due to the relativistic effects becoming less important farther from the compact object since the disk is found slightly at a higher distance from the neutron star surface, and/or simply to the lower statistics in the hard state.
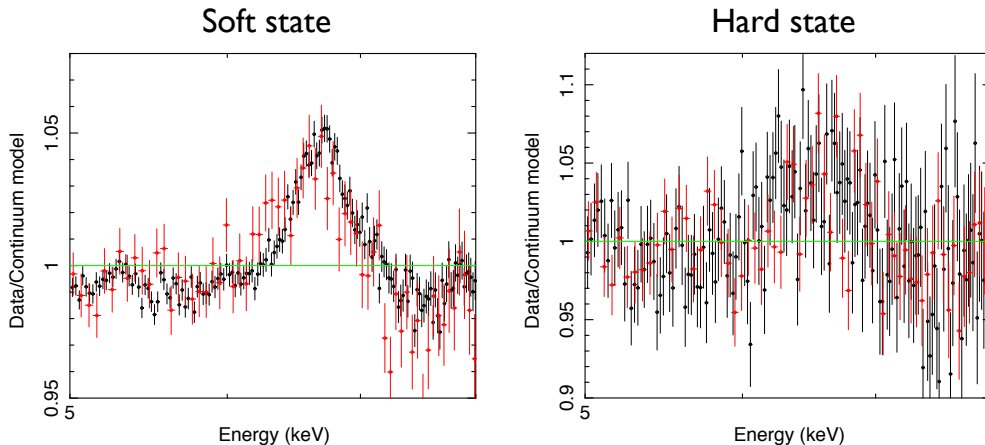
Figure 5.8: Comparison of the Fe line in the soft and in the hard state, representing the ratio of the data to the continuum model for XMM/EPIC-pn (black) and BeppoSAX/MECS (red) in the energy range $5 - 8$ keV. The broad iron line clearly visible in both spectra, although the statistics is much better in the case of the soft state. The continuum consists of a blackbody and a Comptonization component, modified by the photoelectric absorption.

5.4.2   Main changes in the spectral parameters

Using the data from XMM-Newton, BeppoSAX, and RXTE, I tested different self-consistent reflection models on a broad-band range, from 0.3 to 200 keV. These

models allow us to check the hypothesis of a common origin for the detected reflection features, and to directly compare the changes in the spectral parameters from one state to the other one.

In the following section, I report the main differences in the spectral parameters for both the continuum and the reflection models. They mainly concern the photon index of the power law, the electron temperature and the seed photon temperature of the Comptonized component, the inner radius of the disk, and the ionization state of the matter in the disk.

The electron temperature increases from the soft to the hard state, going from $kT_e \sim 2 - 3$ keV to $kT_e \sim 20 - 24$ keV, whereas the power-law photon index and the temperature of the seed photons decrease, from $\Gamma = 2.2 - 2.8$ to $\Gamma = 1.8$ and from $kT_{seed} = 1.1 - 1.4$ keV to $kT_{seed} = 0.7 - 0.8$ keV, respectively. The radius of the emitting region of the seed photons Comptonized in the hot corona is estimated at $R_{seed} \sim 9$ km in the soft state and $R_{seed} \sim 12$ km in the hard state, assuming a distance of 7.4 kpc (the detail of the calculations is given in the paper). Therefore, the seed photons are probably coming from the neutron star surface in both states.

The inner radius of the accretion disk is estimated to be at $R_{in} = 10 - 16\,R_g$ in the soft state, $R_{in} = 19 - 59\,R_g$ when the inclination is fixed at $i = 37°$ in the hard state and $R_{in} = 26 - 65\,R_g$ when $i = 39°$. Hence the accretion disk seems to be truncated farther from the compact object in the hard state. This is in agreement with [Barret 2002, Olive 2003] who interpreted the transitions from one state to the other one in this source with different truncation radii of the accretion disk.

I calculated the mass accretion rate in both states using the typical value of the accretion efficiency $\eta = 0.2$, which corresponds to a neutron star of mass $M_{NS} = 1.4 M_\odot$ and $R_{NS} = 10$ km, and the bolometric luminosities inferred by the spectral modeling used, with the relation:

$$L_{acc} = \eta_{acc} \dot{M} c^2. \qquad (5.3)$$

In the soft state, $\dot{M}_{SS} = 1.6 \times 10^{-8}$ M$_\odot$ yr^{-1}, while in the hard state the accretion rate decreases, $\dot{M}_{HS} = 2 \times 10^{-9}$ M$_\odot$ yr^{-1}. This is consistent with the changes observed in the inner radius of the accretion disk from one state to the other one.

Another parameter very interesting to look at is the ionization state of the matter in the inner part of the accretion disk. The matter is much more ionized in the soft state, $\xi = 3\,600$ erg cm s^{-1}, in comparison with $\xi = 210$ erg cm s^{-1} in the hard state. This is consistent with the values of the energy of the Fe line found to be at $E_{Fe} \sim 6.7$ keV and $E_{Fe} \sim 6.4$ keV in the soft and hard states, respectively. Moreover, the ionization state of the accretion disk seems to have a strong influence on the iron line profile, as already reported in [Reis 2009a].

5.4.3 A possible scenario

How to explain all the changes observed in the spectral parameters? The hypothesis of the truncated disk in the hard state proposed for black hole binaries seems to be relevant also in the context of neutron star LMXBs.

When the source is observed with a low luminosity, the accretion disk is truncated farther from the neutron star. As a consequence, the soft photons emitted are not efficient enough to cool hot electrons forming the corona, thus electrons remain at high temperature. This results in a hard spectrum and a low-ionization reflection. The source is said in the hard state. The iron line produced in such spectra is associated with the fluorescent line at 6.4 keV coming from Fe I-XVII.

When the mass accretion rate increases, the inner radius of the disk moves closer to the compact object; the source becomes brighter in X-rays. The soft photons from the disk are much more efficient in cooling the corona, resulting in a low temperature of the electrons and a softer spectrum. The source is said to be in the soft state. In such a configuration, reflection increases due to a stronger irradiation of the disk, and the matter becomes much more ionized. Moreover, the emission lines are broadened by stronger Doppler effects as the disk approaches the compact object. The most prominent feature of the reflection spectrum is the highly ionized iron line detected at $\sim 6.7 - 7$ keV, associated with Fe XXV (He-like) and/or Fe XXVI (H-like).
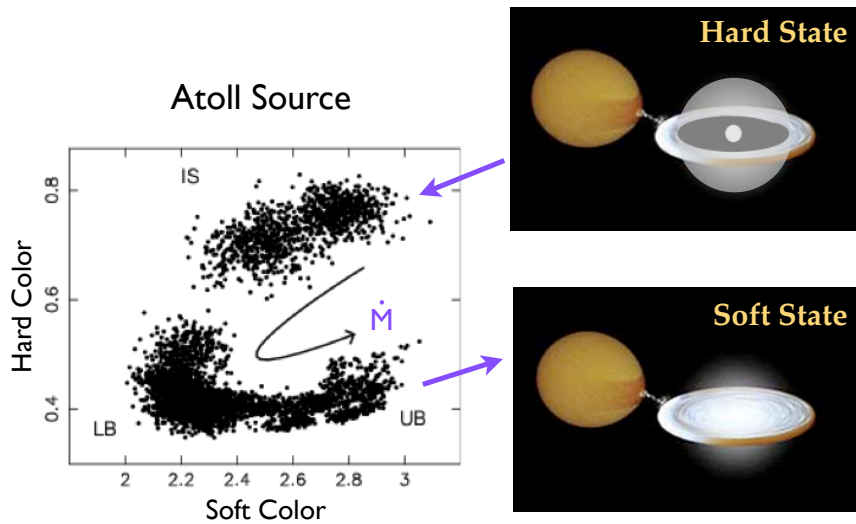
Figure 5.9: Left panel: Color-color diagram of a typical atoll source, where IS, LB and UB indicate the island state (hard state), the lower and upper banana (soft state), respectively. The arrow on the left of $\dot{M}$ indicates the evolution of the mass accretion rate, which increases from the island to the banana. The right panels illustrate the changes in the source in both states, in particular the disk is truncated farther from the neutron star in the hard state, which has direct influences on the temperature of the corona and on the luminosity of the source.

This scenario is generally well supported by the timing analysis through power density spectra, where correlations are observed between the characteristic frequencies of the fast time variability and the position of the source in the CD or its spectral state (e.g. [Olive 2003], with characteristic frequencies increasing with increasing the

inferred mass accretion rate.

Some questions

There are still a lot of questions it would be very interesting to answer, among them, questions about the mass accretion rate, such as: what is really at the origin of changes in the mass accretion rate? Why the time scale is different from one state to the other one for different sources? Could the activity, variability and/or the evolution of the companion star be responsible of these changes? Additionally, there are many questions about the vicinity of the neutron star surface. Is there an accretion flow of particles when the disk is truncated farther from the compact object?

5.5   Paper

The work presented above has been published in Astronomy & Astrophysics in 2013.

Astronomy & Astrophysics

Testing reflection features in 4U 1705−44 with *XMM-Newton*, *BeppoSAX*, and RXTE in the hard and soft states

E. Egron[1], T. Di Salvo[2], S. Motta[3,4], L. Burderi[1], A. Papitto[5], R. Duro[6], A. D'Aì[2], A. Riggio[1,7], T. Belloni[3], R. Iaria[2], N. R. Robba[2], S. Piraino[8,9], and A. Santangelo[9]

[1] Dipartimento di Fisica, Università degli Studi di Cagliari, SP Monserrato-Sestu, KM 0.7, 09042 Monserrato, Italy
e-mail: elise.egron@dsf.unica.it
[2] Dipartimento di Fisica, Università di Palermo, via Archirafi 36, 90123 Palermo, Italy
[3] INAF – Osservatorio Astronomico di Brera, via E. Bianchi 46, 23807 Merate (LC), Italy
[4] Università dell' Insubria, via Valleggio 11, 22100 Como, Italy
[5] Institut de Ciències de l'Espai (IEEC-CSIC), Campus UAB, Fac. de Ciències, Torre C5, parell, 2a planta, 08193 Barcelona, Spain
[6] Dr. Karl Remeis-Sternwarte and Erlangen Centre for Astroparticle Physics, Friedrich-Alexander-Universität Erlangen-Nürnberg, Sternwartstrae 7, 96049 Bamberg, Germany
[7] INAF – Osservatorio Astronomico di Cagliari, Poggio dei Pini, Strada 54, 09012 Capoterra (CA), Italy
[8] INAF – IASF di Palermo, via Ugo La Malfa 153, 90146 Palermo, Italy
[9] Institut für Astronomie und Astrophysik, Kepler Center for Astro and Particle Physics, Sand 1, 72076 Tübingen, Germany

ABSTRACT

We use data from the bright atoll source 4U 1705−44 taken with *XMM-Newton*, *BeppoSAX*, and RXTE both in the hard and in the soft state to perform a self-consistent study of the reflection component in this source. Although the data from these X-ray observatories are not simultaneous, the spectral decomposition is shown to be consistent among the different observations, when the source flux is similar. We have therefore selected observations performed at similar flux levels in the hard and soft states to study the spectral shape in these two states in a broad-band (0.1−200 keV) energy range, with good energy resolution, and using self-consistent reflection models. These reflection models provide a good fit for the X-ray spectrum both in the hard and in the soft state in the whole spectral range. We discuss the differences in the main spectral parameters we find in both states, providing evidence that the inner radius of the optically thick disk slightly recedes in the hard state.

Key words. line: formation – line: identification – stars: neutron – stars: individual: 4U 1705-44 – X-rays: binaries – X-rays: general

1. Introduction

The X-ray emission in low-mass X-ray binaries (LMXBs) comes from the gravitational potential energy released from accretion processes onto black holes or neutron stars. The X-ray spectrum is generally described well by a soft-thermal component such as a blackbody or a multicolor-disk blackbody, originating in the accretion disk, and a hard X-ray component that usually dominates the spectrum. This hard component can be fitted either by a power law with a high-energy cutoff or a unsaturated Comptonization spectrum, when the source is in the so-called hard state, or by a blackbody or a saturated Comptonization spectrum, when the source is in the soft state, where the temperature of the photons is very similar to the electron temperature. The hard component is generally explained in terms of inverse Compton scattering, where soft thermal photons get Compton upscattered by hot electrons forming a corona or a boundary layer between the neutron star surface and the accretion disk, or forming the base of a jet (at least in the hard state, Markoff & Nowak 2004; Markoff et al. 2005).

In addition to this, a broad iron line (associated to the Fe Kα emission) is often detected in the spectra of X-ray binaries. However, the nature of its large width and the (a)symmetric profile of the line are still being debated. In analogy with systems containing stellar mass or supermassive black holes, which show remarkably similar phenomenology

(e.g. Martocchia & Matt 1996; Walton et al. 2012), it can be produced by reflection in the accretion disk (Reynolds & Nowak 2003; Fabian & Miniutti 2005; Matt 2006), or it can arise from an accretion disk corona (Kallman & White 1989; Vrtilek et al. 1993).

The first scenario implies that the iron line is produced in the inner part of the accretion disk. Hard X-rays coming from the corona or from the base of the jet irradiate the relatively cold accretion disk. As a consequence, a broad and asymmetric line is expected due to Doppler and relativistic effects produced close to the compact object. Depending on the ionization state of the disk, this leads to the emission of several emission lines and absorption edges that are more or less strong in the spectrum, depending on the relative abundance of the corresponding ion and/or its fluorescence yield (Kaastra & Mewe 1993). The Fe Kα line at 6.4−7 keV is the most prominent feature (Fabian et al. 2000). It results in a fluorescent line at 6.40 keV from Fe I-XVII or in the recombination lines at 6.67−6.70 keV and 6.95−6.97 keV associated with highly ionized species of Fe XXV (He-like) and Fe XXVI (H-like), respectively. In this scenario other reflection signatures are also expected, such as the emission and/or absorption from several elements at lower energy, and a Compton reflection hump at higher energy (George & Fabian 1991; Ballantyne et al. 2001; Ross & Fabian 2007) if the X-ray continuum spectrum is sufficiently hard.

D'Aì et al. (2009), Iaria et al. (2009), Di Salvo et al. (2009), and Piraino et al. (2012) detect emission lines in GX 340+0, GX 349+2, 4U 1705−44, and GX 3+1 at 2.6, 3.31, and 3.90 keV associated with S XVI, Ar XVIII, and Ca XIX, respectively, and an absorption edge from ionized iron. Moreover, a reflection hump peaking at nearly 30 keV has been found in several sources, such as 4U 1705−44 (Fiocchi et al. 2007). To confirm the common origin of these features, it is important to use self-consistent models that include all the reflection components in order to distinguish among the proposed production mechanisms.

Alternative scenarios explain the line broadening by Compton scattering if the line is emitted in the inner parts of a moderately optical thick accretion disk corona (ADC), formed by evaporation of the outer layers of the disk (White & Holt 1982). Another possibility is that the line profile is red-skewed due to Compton upscattering by a narrow wind shell launched at mildly relativistic velocities at some disk radii where the local radiation force exceeds the local disk gravity (Titarchuk et al. 2009).

Thanks to the good energy resolution capabilities of *Chandra* and to the large effective area of *XMM-Newton* and *Suzaku*, the number of significant detections of these lines is increasing, giving the possibility to study their profile in more detail. Recently, two studies have been performed by Ng et al. (2010) and Cackett et al. (2010) to investigate the nature of the iron line with a large sample of neutron star LMXBs spectra. Using *XMM-Newton* observations of 16 neutron star LMXBs, Ng et al. (2010) conclude that there is no statistical evidence that the iron line profile is asymmetric, and they propose that the observed large width of the line is caused by Compton scattering in the corona. It should be noted that, to eliminate the effects of photon pile-up in the *XMM-Newton* data, Ng et al. (2010) decided to reject up to 90% of the source photons for the brightest sources. Conversely, by studying ten neutron star LMXBs with *Suzaku* (which is less affected by photon pile-up because of a broad point spread function) and *XMM-Newton*, Cackett et al. (2010) confirm that the Fe line is asymmetric, relativistic, and produced by reflection in the inner part of the accretion disk. This result was also achieved by comparing CCD-based spectra from *Suzaku* with Fe K line profiles from archival data taken with gas-based spectrometers Cackett et al. (2012). In general, they find good consistency between the gas-based line profiles from EXOSAT, *BeppoSAX*, RXTE, and the CCD data from *Suzaku*, demonstrating that the broad profiles they see are intrinsic to the line and not because of instrumental issues.

The low-mass X-ray binary system 4U 1705−44 contains a weakly magnetized neutron star. In such systems the accretion disk can extend down to the neutron star surface. This implies a similar configuration with respect to the one envisaged for accreting black holes, since the radius of the neutron star is close to the size of the innermost stable circular orbit (ISCO) of matter around a black hole. Similarities have been observed between these systems (e.g., Maccarone 2012, and references therein), suggesting common physical processes producing X-ray emission and similar properties of the accretion flow around the compact object. Clear observational evidence exists that a neutron star has a solid surface, such as the observations of type I X-ray bursts, which are thermonuclear explosions in the surface layers of the neutron star, or of coherent pulsations, resulting from the magnetic field anchored on the neutron star surface. However, not all systems containing a neutron star show one or more of these characteristics (Done et al. 2007).

4U 1705−44 is a persistent bright source that shows type I X-ray burst (Langmeier et al. 1987) and kHz quasi-periodic oscillations (Ford et al. 1998; Olive et al. 2003). From some bursts that show photospheric radius expansion, its distance is estimated at 7.4 kpc, toward the Galactic ridge (Forman et al. 1978; Galloway et al. 2008).

LMXBs containing a neutron star are divided into two categories (Hasinger & van der Klis 1989) according to the path the source describes in the X-ray color-color diagram (CD) or hardness-intensity diagram (HID): atoll sources (C-like, low luminosity, about $0.001−0.5 L_{Edd}$) or Z-sources (Z-like, high luminosity, close to the Eddington limit). 4U 1705−44 is classified as an atoll source. In the classical CD pattern of these sources, two branches are usually distinguished: the island and the banana. In the island branch, the source presents a low count rate, probably associated to a low-mass accretion rate, and the source is in the low/hard state (low is relative to the X-ray flux, and hard to the spectrum). In this state, it is thought that the accretion disk is truncated relatively far from the compact object. This results in a very hot corona and in a hard spectrum. On the other hand, when the source is in the banana branch, the accretion disk approaches the compact object, the temperature of the corona decreases due to Compton cooling, and the source is in the high/soft state. The mass accretion rate is therefore expected to increase from the island to the banana branch. The Z-sources usually emit persistently at high luminosity and are thought to have a larger magnetic field and/or higher mass accretion rate than atoll sources.

The system 4U 1705−44 has recently been studied thoroughly with the particular objective of understanding the origin of its iron line. A broad Fe line was clearly visible with *Chandra* (Di Salvo et al. 2005), confirming previous studies performed at low-energy resolution by White et al. (1986) and Barret & Olive (2002). The HETG onboard *Chandra* excluded that the large width of the line could be caused by the blending of lines from iron in different ionization states, although it was not possible to distinguish between the two possible origins of the line width (relativistic smearing or Compton broadening). The broad band *BeppoSAX* spectrum of 4U 1705−44 taken during a soft state again showed a broad iron line that could be well fitted by a DISKLINE component with very reasonable smearing parameters (Piraino et al. 2007), and the INTEGRAL spectrum showed clear evidence of a Compton reflection hump (Fiocchi et al. 2007), as well as the *BeppoSAX* spectrum taken during the hard state (Piraino et al., in prep.).

The observations with *XMM-Newton* and *Suzaku* were essential for studying the iron line profile in detail because of their large effective area and good energy resolution. Indeed, Reis et al. (2009b) found a broad (skewed) and asymmetric Fe $K\alpha$ emission line during a *Suzaku* observation of 4U 1705−44. Both Compton broadening and relativistic smearing were needed to account for the large width of the iron line. The best fit value of the inner radius was $R_{in} \simeq 10.5 R_g$, with R_g being gravitational radius ($R_g = GM/c^2$), and the corresponding inclination angle was $i \sim 30°$. Using the observations from *BeppoSAX* and *Suzaku*, Lin et al. (2010) obtained constraints on the broad-band spectrum of 4U 1705−44 and find that the strength of the Fe line correlates well with the boundary layer emission in the soft state, while the Fe line is probably due to illumination of the accretion disk by the strong Comptonization emission in the hard state. An *XMM-Newton* observation performed in 2008 when the source was in a soft state confirmed the results obtained with *Suzaku*, showing a high-statistics Fe line profile and spectrum consistent with a disk-reflection scenario (Di Salvo et al. 2009; D'Aì et al. 2010). The best fit value of the
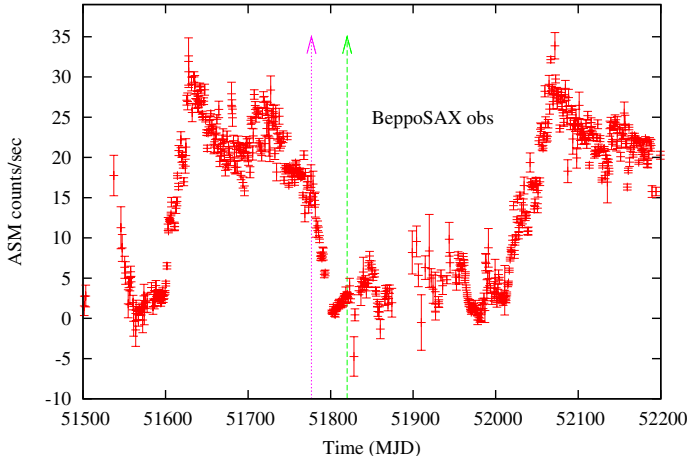
Fig. 1. Light curve of 4U 1705-44 obtained with RXTE/ASM from November 1999 to October 2001. The two arrows show the observations performed by *BeppoSAX* in August and October 2000.

Fig. 2. RXTE/ASM light curve of 4U 1705-44 from May 2005 to November 2010. The arrows mark the two *XMM-Newton* observations performed in August 2006 and 2008. The black crosses and the blue triangles represent the RXTE observations selected in the hard and soft states, respectively.

inner disk radius was $R_{in} \simeq 14 R_g$ and the corresponding inclination angle and index of the emissivity law profile were $i \sim 39°$ and $−2.3$ respectively, in agreement with the *Suzaku* results. In addition, the *XMM-Newton* spectrum shows the presence of several emission lines from elements lighter than iron, such as S, Ar, and Ca at 2.62 keV, 3.31 keV, and 3.90 keV, respectively, and an absorption edge at 8.5 keV probably from ionized iron. All these features were broad and consistent with being produced in the same region where the iron line was produced.

Here we present the spectral analysis of 4U 1705−44 using data from *XMM-Newton*, *BeppoSAX*, and RXTE when the source was both in the hard state and in the soft state. Using the same spectral models to describe the source spectrum in both states, we aim at highlighting the differences in the spectral parameters to find that the accretion disk is truncated farther (but not far) from the compact object in the hard state. Since several reflection features have been detected in 4U 1705−44, we use self-consistent reflection models to fit the broad-band, multimission, X-ray spectrum of this source. We also discuss possible effects of pile-up distortion in the *XMM-Newton* spectrum during the high-luminosity, soft state.

2. Observation and data reduction

The light curve produced from the All-Sky Monitor onboard RXTE allows following the evolution of the source flux for a period of ~16 years. The source shows clear spectral transitions, from the hard (3 counts/s) to the soft state (25 counts/s). A total of four observations were performed with *BeppoSAX* (see Fig. 1) and *XMM-Newton* (see Fig. 2) when the source was in the soft and hard states. The spectral transitions are associated with variations in the X-ray flux, which are most likely proportional to the accretion rate. We select RXTE observations, both in the hard and soft states, as shown in Fig. 2. In this way, the joint spectra from the three satellites cover the full 0.1−200 keV energy range. We explain in detail our methods in the following.

2.1. XMM-Newton

The source 4U 1705−44 was observed twice with *XMM-Newton*. The first observation was performed on 2006 August 26 for an effective exposure of 34.72 ks, when the source was in the hard state. The corresponding RXTE/ASM count rate was 1 c/s. The
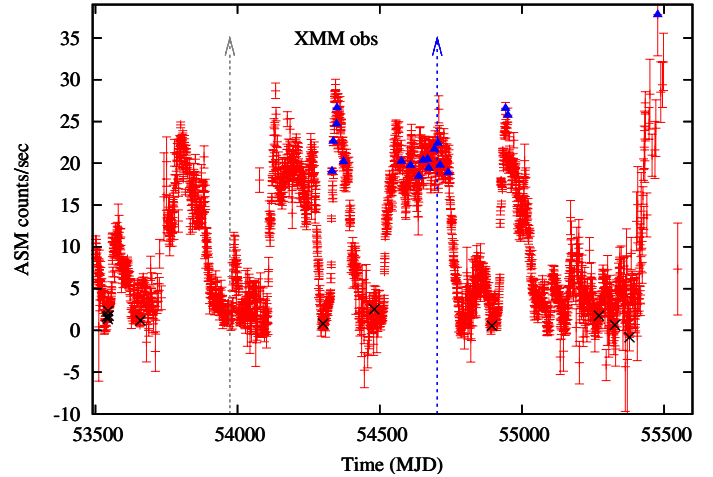
second time, 4U 1705−44 was observed during the soft state (target of opportunity), on 2008 August 24 for a total on-source observing time of 45.17 ks (see Di Salvo et al. 2009, for more details on this observation). The RXTE/ASM was 19 c/s during this observation.

During both observations, the European Photon Imaging Camera pn (EPIC-pn; Struder et al. 2001) and the Reflection Grating Spectrometers (RGS1 and RGS2; den Herder et al. 2001) were used to observe the source. The EPIC-pn camera operated in timing mode to minimize the photon pile-up and telemetry overload that may occur at high count rates, with a thick filter in place, which further reduced the number of low-energy photons. In timing mode only the central CCD is read out with a time resolution of 30 μs. This provides a one-dimensional image of the source with the second spatial dimension being replaced by timing information. The EPIC-MOS and the optical Monitor were off during the second observation in order to avoid telemetry drop-outs in the EPIC-pn.

We produced a calibrated photon event file using the SAS[1] processing tool EPPROC. Before extracting the spectra we checked for contamination from background solar flares by producing a light curve in the energy range 10−12 keV. No solar flare was registered. However, during the first observation (corresponding to the hard state), the EPIC-pn camera registered a type-I X-ray burst at about 11 ks after the start of the observation. We applied temporal filters by creating a good time interval (GTI) file with the task TABGTIGEN in order to remove the burst.

We used the task EPFAST to correct rate-dependent CTI effects in the event list. The source spectra were extracted from a rectangular area covering all the pixels in the Y direction and centered on the brightest RAWX column (36 in the hard state, 38 in the soft state) with a width of 16 pixels, which corresponds to 65.6 arcsec. We selected only events with PATTERN ≤ 4 (single and double pixel events) and FLAG = 0 as a standard procedure to eliminate spurious events. We extracted the background spectra from a box similar to the one used to extract the source photons but in a region away from the source (RAWX = 47−63 and RAWX = 4−12 in the hard and soft states, respectively).

---

[1] The *XMM-Newton* data were processed using the Science Analysis Software v.10, following the *XMM-Newton* ABC guide.

During the first observation, the average count rate registered by EPIC-pn CCDs is around 48 c/s, and 19 c/s in the 2.4−11 keV range, excluding the burst interval. In the soft state, the count rate is much higher: the mean count rate of around 770 count/s, and 425 count/s in the 2.4−11 keV range, slightly increasing in time (by 5%). We also checked for the presence of pile-up using the task EPATPLOT. While the first *XMM-Newton* observation of the source taken in the hard state does not show any significant pile-up, a few percent pile-up affects the second observation taken during a soft state. We discuss the pile-up issue concerning the soft state in the next section. We grouped the EPIC-pn energy channels by a factor of 4 in order to avoid oversampling of the energy-resolution bin of the instrument.

The two RGS units were set in the standard spectroscopy mode. The RGS data were processed using the RGSPROC pipeline to produce calibrated event list files, spectra, and response matrices. The RGS data were rebinned to have at least 25 counts per energy channel.

2.2. BeppoSAX

BeppoSAX performed two observations of 4U 1705−44 in August and October 2000, for total on-source observing times of 43.5 ks and 47 ks, respectively. The count rates registered by the RXTE/ASM associated to these observations were 18 c/s and 3 c/s, respectively.

The four *BeppoSAX* narrow field instruments were on during both the observations. The Low Energy Concentrator Spectrometer (LECS, 0.1−4 keV; Parmar et al. 1997) and the Medium Energy Concentrator Spectrometer (MECS, 1−10 keV; Boella et al. 1997) data were extracted in circular regions centered on the source position using radii of 8′ and 4′, respectively, corresponding to 95% of the source flux. Identical circular regions were used in blank field observations to produce the background spectra. The background spectra of the High Pressure Proportional Gas Scintillation Counter (HPGSPC, 8−50 keV; Manzo et al. 1997) and of the Phoswich Detection System (PDS, 15−200 keV; Frontera et al. 1997) were produced from Dark Earth data and during off-source intervals. The HPGSPC and PDS spectra were grouped using a logarithmic grid.

We did not use data from PDS during the first observation, which corresponds to the soft state, in order to avoid the extra complication of the spectral fit caused by the presence of a hard (power law) spectral component (see Piraino et al. 2007). During the low/hard observation, 6 X-ray bursts were removed from the data.

2.3. RXTE

There was no simultaneous observation performed by RXTE during the *XMM-Newton* and *BeppoSAX* observations. However, the archive has provided us with hundreds of RXTE observations of 4U 1705−44 since RXTE was launched. Therefore, we considered all the observations of 4U 1705−44 collected since 2000 May (corresponding to the 5th epoch of RXTE[2]) and selected RXTE observations during which the source showed the same spectral state of the two *XMM-Newton* observations as mentioned above. To do so we produced a color-color diagram (CD) from all the RXTE observations and a time-resolved CD from the two *XMM-Newton* observations (we separated
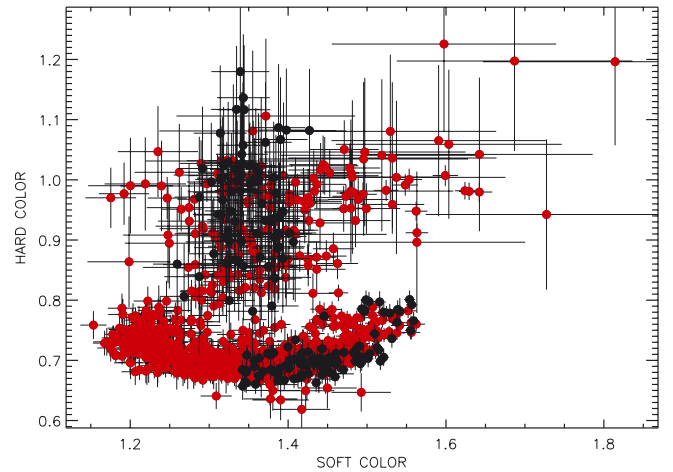
Fig. 3. Color−color diagrams (CDs) of 4U 1705−44 produced by RXTE/PCA and *XMM-Newton*/EPIC-pn, in red and black, respectively. See text for the details.

the *XMM-Newton* observations in intervals 512 s long, and for each of them, we produced a spectrum and measured the colors) using the same energy bands for the two instruments (i.e. 2.47−3.68 keV and 3.68−5.31 keV for the soft color and, 5.31−7.76 keV, 7.76−10.22 keV for the hard color). Since from the RXTE data it is clear that the shape of the CD of 4U 1705−44 remains constant during the period considered, we could directly compare the CD coming from the two instruments. The CDs were normalized to the Crab colors, but an additional correction was needed to precisely match the two diagrams and to take the differences in the gain of the two instruments into account. Figure 3 shows the *XMM-Newton* CD corresponding to the two observations performed in the hard and in the soft state superposed to the RXTE CD. Starting from the two CDs, we selected the RXTE observations that matched the *XMM-Newton* observations. The detail of the RXTE observations selected is given in Table 5.

The RXTE data were obtained in several simultaneous modes. STANDARD 2 mode for PCA and STANDARD for the HEXTE instrument were used to create background and dead-time-corrected spectra. We extracted energy spectra from PCA and HEXTE for each observation using the standard RXTE software within HEAsoft v.6.9 following the standard procedure described in the RXTE cookbook to produce source and background spectra, as well as response matrices. Only Proportional Counter Unit 2 from the PCA was used, since only this unit was on during all the observations. As regards HEXTE data, we used only data coming from HEXTE/Cluster B, which were correctly working in our period of interest.

Then we produced RXTE/PCA and RXTE/HEXTE spectra for each RXTE observation, and we averaged them to obtain a PCA+HEXTE spectrum in the island state (matching *XMM-Newton* observation made in 2006 August 26) and a PCA spectrum in the banana-state (matching *XMM-Newton* observation made in 2008 August 24). In the soft state we did not use RXTE/HEXTE data due to the lack of counts in the HEXTE working enery range (20−200 keV). A systematic error of 0.6% was added to the PCA-averaged spectra to account for residual uncertainties in the instrument calibration[3].

---

[2] We only considered data from the 5th epoch to avoid fluctuations due to the differences in the instrument gain that can be observed in data coming from different epochs.

[3] http://www.universe.nasa.gov/xrays/programs/rxte/pca/doc/rmf/pcarmf-11.7 for a detailed discussion of the PCA calibration.

3. Spectral analysis

Data were fitted by using Xspec (Arnaud 1996) v.12.6. All uncertainties are given at the 90% confidence level ($\Delta\chi^2 = 2.706$). The data analysis of the XMM/EPIC-pn spectrum was restricted to 2.4−11 keV to exclude the region around the detector Si K-edge (1.8 keV) and the mirror Au M-edge (2.3 keV) that could affect our analysis. This problem has already been noticed for the EPIC-pn observations performed in timing mode (e.g., D'Aì et al. 2010; Papitto et al. 2010; Egron et al. 2011). The energy bands used for the other instruments are: 0.3−4 keV for the LECS, 1.8−10 keV for the MECS, 7−34 keV for HPGSPC, 15−200 keV for PDS onboard *BeppoSAX*, and 4−22 keV for PCA, and 15−100 keV for HEXTE onboard RXTE.

The following sections concern the analysis of data associated to the soft and to the hard state of 4U 1705−44. In the first one, we report investigation of the pile-up effects on the *XMM-Newton* data of the soft state to demonstrate that the iron line is always broad and gives consistent spectral parameters that are independent of the extraction region. Then we applied reflection models to fit the *XMM-Newton* data in this state, and finally we included the *BeppoSAX* and RXTE data to extend the analysis to the broad-band, 0.1−200 keV, energy range. In the second one, we applied the same continuum and reflection models to the *XMM-Newton*, *BeppoSAX*, and RXTE data in the hard state, in order to evaluate which spectral parameters change from one state to the other.

4. Soft state

4.1. Pile-up in XMM-Newton /EPIC-pn data?

Pile-up is an important concern for CCD data and may affect the spectral results. It occurs when more than one X-ray photon hits the same pixel or an adjacent one in the same read-out frame. If this happens the CCD will be unable to resolve the individual photon events and instead record a single event with an energy that is roughly the sum of the individual event energies. It results in a shift of the photons to higher energy, which produces an energy-dependent distortion of the spectrum. It is possible to assess the pile-up effects by checking the fraction of single, double, triple, and quadruple events (depending on how many pixels are involved) using the task EPATPLOT (see Appendix).

Di Salvo et al. (2009), D'Aì et al. (2010), and Ng et al. (2010) have studied the iron line in 4U 1705−44 using the same *XMM-Newton* data in the soft state, but considering different extraction regions for the spectra and therefore accepting different pile-up fraction in their spectral analysis. Di Salvo et al. (2009) consider that pile-up effects on spectral results were negligible and thus decided to keep all the central columns of the CCD, whereas D'Aì et al. (2010) excluded the brightest CCD column, and Ng et al. (2010) excluded seven central columns (corresponding to ∼90% of the source counts). In all these cases, the iron line detected in the pn spectra of 4U 1705−44 consistently remains broad, with a Gaussian sigma ∼0.3−0.4 keV. However, the conclusions coming from the spectral analysis differ. While Di Salvo et al. (2009) and D'Aì et al. (2010) deduce that the iron line is clearly asymmetric and compatible with a relativistic line, using the DISKLINE (Fabian et al. 1989) and the reflection model REFBB (Ballantyne 2004), respectively, Ng et al. (2010) find that the iron line can be fit equally well by a Gaussian or using the LAOR model (Laor 1991), concluding that there was no statistical evidence of any asymmetry of the line profile. It is thus important to assess the effects of pile-up in the EPIC-pn spectrum of 4U 1705−44 in the soft state, which shows the highest
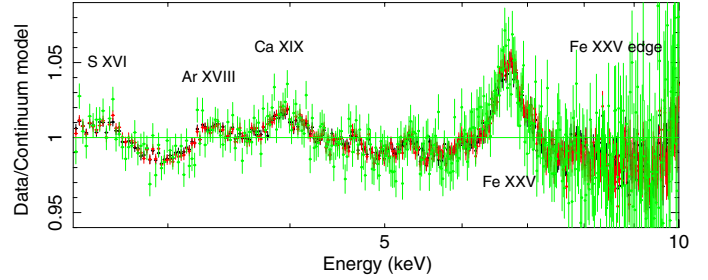
Fig. 4. Comparison of the ratios of the data to the best fit continuum considering all the rows of the CCD (black; Di Salvo et al. 2009), without the brightest CCD column (red; D'Aì et al. 2010), and excluding seven central columns (green; Ng et al. 2010). The continuum model consists of a blackbody and a Comptonization model (comptt) modified by photoelectric absorption (phabs).

signal-to-noise ratio (S/N) iron-line profile ever detected to date in a neutron star LMXB.

To evaluate the pile-up effects on the *XMM-Newton*/pn spectrum, we applied an empirical model that is similar to the one used in Di Salvo et al. (2009), to compare the results obtained when we consider different extraction regions in the CCD. In particular, we consider the extraction region described in Sect. 2, where we exclude from zero up to seven central brightest columns before extracting the pn spectrum. Figure 4 shows the ratios of the data to the continuum obtained for three cases: excluding none, one, and seven of the central brightest columns. The continuum model consists of a blackbody and a Comptonization component (COMPTT; Titarchuk 1994), modified at low energy by the photoelectric absorption (PHABS; photoelectric cross-sections of Balucinska-Church & McCammon 1992 with a new He cross-section based on Yan et al. 1998; and standard abundances of Anders & Grevesse 1989). This model is often used for atoll sources and gives a good fit for the continuum of this source (Barret & Olive 2002; Di Salvo et al. 2005; Piraino et al. 2007; Di Salvo et al. 2009).

Three emission lines are visible at low energy, at 2.62 keV, 3.31 keV, and 3.90 keV, identified by Di Salvo et al. (2009) as highly ionized elements corresponding to S XVI, Ar XVIII, and Ca XIX, respectively. In addition to these lines, an iron emission line and an absorption edge are present. The detection of the iron line is at about 10σ above the continuum when all the columns are considered, whereas it becomes only 5σ when seven columns are removed. In the three cases, the iron line appears broad and the shape is very similar. To fit these residuals we add four Gaussians and an edge to the continuum model, all modified by the same relativistic blurring (modeled with RDBLUR, the DISKLINE kernel, in Xspec) component to consider the relativistic and/or Doppler effects produced by the motion in the inner disk close to the compact object. This model describes the relativistic effects due to the motion of plasma in a Keplerian accretion disk, immersed in the gravitational well of the compact object, in terms of the inner and the outer radius of the disk, R_{in} and R_{out} (in units of the gravitational radius, $R_g = GM/c^2$, where M is the mass of the compact object), of the index of the assumed power-law dependence of the disk emissivity on the distance from the NS, and of the system inclination, i. In this way, all the discrete features present in the model are smeared by the same disk parameters. The only difference with respect to the model used by Di Salvo et al. (2009) is that the RDBLUR component is now also applied to the iron edge, as it should be if the edge is also produced by reflection in the same disk region as the other emission lines.

As expected, we note a variation in the parameters of the continuum when we exclude the columns from 0 to 7, the most affected parameter being the interstellar absorption column density. Its value, and the associated error, progressively increase from $(1.8 \pm 0.1) \times 10^{22}$ cm^{-2} when no central columns are excluded (pn-all) to $(3.5 \pm 0.5) \times 10^{22}$ cm^{-2} when seven central columns are excluded (pn-7). It should be noted here that the best fit value for this parameter obtained with *BeppoSAX* was $(1.9 \pm 0.1) \times 10^{22}$ cm^{-2} (Piraino et al. 2007), compatible with the results obtained for spectra pn-all to pn-2. Other significant changes in the parameter values are in the temperature and normalization of the blackbody component, with the temperature decreasing and the normalization increasing from pn-all to pn-7. Also in this case, the best fit values of these parameters obtained with *BeppoSAX* are compatible with the results obtained for spectra pn-all to pn-2. The temperature of the seed photons of the COMPTT component is quite stable, while some scattering is observed in the values of the electron temperature and optical depth of this component, although the errors are also very large. Regarding the discrete features and the disk-smearing parameters, all the values are compatible with each other within the errors, which of course increase significantly with the decreasing counts. The inclination angle is the parameter that is mostly affected by the choice of the extraction region, with values ranging from $38° \pm 1$ to $58°^{+23}_{-2}$ going from pn-all to pn-7 (the largest increase occurring starting from spectrum pn-4).

To assess whether the exclusion of some central columns of the CCD has noticeable effects on the spectral shape or simply induces a lack of statistics, we carried out the same analysis as described above, but also considering the RGS spectrum, together with the pn spectrum. The uncertainties on the column density and on the inclination decrease strongly. While the value associated to the column density remains constant, $N_{\mathrm{H}} = (1.6 \pm 0.1) \times 10^{22}$ cm^{-2}, the inclination goes from $38° \pm 1$ when no central column is excluded to $40°^{+6}_{-3}$, when seven central columns are excluded. Also, the values of the parameters such as the blackbody temperature, its normalization, and the electron temperature become much more stable, with the error bars considerably reduced. The results are summarized in Table 6. In conclusion, we checked the effect of pile-up in the EPIC-pn spectrum but excluding from none up to seven of the brightest central columns and comparing the best fit spectral parameters. The parameters seem to depend on the extraction region when looking at the EPIC-pn spectra alone. However, the addition of the RGS data clearly stabilizes the values of the parameters. This means that the variation in the parameters and in the corresponding error bars we obtain fitting the EPIC-pn spectra alone are caused by a decrease in the statistics when excluding the central columns of the CCD, hence by a lack of constraints on the parameters.

Moreover, if we look at the plots presented in Appendix, we can see that the deviation of single and double events at the iron line energy has a minimum in correspondence of the pn-2 spectrum, and it increases again when we exclude more than two brightest central columns. This may be ascribed to a mismodeling of the instrumental response and, in particular, of the rate of double events (which involve more than one pixel, and probably more than one column) when too many central columns are excluded. Although most continuum parameters obtained for spectra pn-all to pn-2 are perfectly compatible to those previously obtained with *BeppoSAX* (Piraino et al. 2007), we adopt a conservative approach for the present analysis, to minimize any residual pile-up source of uncertainty. We therefore chose to work with spectrum pn-2.

Table 1. Iron line complex in the XMM/EPIC-pn data fitted by four Gaussians corresponding to the Fe XXV triplet and the Fe XXVI line.

Fe line		Energy (keV)	σ (keV)	Norm $(10^{-3}$ cm^{-2} s$^{-1})$
Fe XXV	F	6.64	$0.11^{+0.05}_{-0.11}$	$0.6^{+0.4}_{-0.5}$
	I_1	6.67	0.36 ± 0.06	2 ± 0.5
	R	6.70	$0.09^{+0.26}_{-0.09}$	$0.2^{+0.6}_{-0.2}$
Fe XXVI	Lyα_2	6.95	$0.14^{+0.12}_{-0.08}$	0.3 ± 0.2

We therefore considered the spectrum pn-2, whose continuum emission is fitted by a blackbody and a comptonized component (COMPTT), both modified at low energy by photoelectric absorption. We first added four Gaussians and an edge to the continuum model to take the emission lines at low energy (S, Ca, Ar), the iron line, and the iron edge at 8.6 keV into account. In this case, the iron line was found at 6.70 ($\pm$0.02) keV, and its equivalent width was 42 eV. The corresponding χ^2_{red} was 1.14 (408).

We also tried to fit the iron line at 6.7 keV, which very likely corresponds to the Kα transition of Fe XXV, with the single components of the triplet (composed of the forbidden line at 6.64 keV, the intercombination lines at 6.67 keV and 6.68 keV, and the resonance line at 6.70 keV). We also added a line at 6.95 keV associated with emission from Fe XXVI. To do so, we used five Gaussians (instead of a single Gaussian at 6.6 keV) whose centroid energies are fixed at the expected rest-frame energies. The lines at 6.67 keV and 6.68 keV are indistinguishable with *XMM-Newton*, since the difference in the centroid energies is comparable to the fitting errors on the line energy. We therefore considered only one Gaussian at 6.67 keV to represent the intercombination lines. This line clearly dominates the triplet, although the lines at 6.64, 6.70, and 6.95 keV contribute slightly to the emission. The results are summarized in Table 1. Accordingly, we used a single Gaussian to describe the Fe complex.

Then we added a smearing component to this model to take relativistic and/or Doppler effects into account close to the compact object, in the hypothesis of a disk origin of the iron line. This component was convolved with all the four Gaussians (associated with S, Ar, Ca, and Fe) and with the edge. We froze the sigma of the Gaussians to zero and applied the same relativistic relativistic smearing parameters to all these features. The iron line is found at $6.66^{+0.01}_{-0.02}$ keV. The equivalent width is 57 eV. The inclination and the inner radius are $39°^{+2}_{-1}$ and 14^{+3}_{-2} R_{g}, respectively. The corresponding χ^2_{red} is 1.03 (409 degrees of freedom, hereafter d.o.f.), and the χ^2 decreases by $\Delta\chi^2 = 44$ for one parameter more with respect to the model without the smearing component. Therefore the addition of a mildly relativistic smearing improves the fit, favoring the interpretation of the discrete features in the pn spectrum of 4U 1705$-$44 as produced by reflection in the inner accretion disk. To support this interpretation, in the next section we fit the broad band (0.3$-$200 keV) spectrum of 4U 1705$-$44 in the soft and in the hard state to self-consistent reflection models.

4.2. Reflection models on pn-2

To test that the iron line, the edge, and the three low-energy emission lines (S XVI, Ar XVIII, and Ca XIX) are consistent with

a reflection scenario, we applied the self-consistent reflection model REFLIONX on the *XMM-Newton*/pn spectrum. REFLIONX is a self-consistent model that includes both the reflection continuum and the corresponding discrete features (Ross & Fabian 2005). In addition to fully-ionized species, the following ions are included in the model: C III-VI, N III-VII, O III-VIII, Ne III-X, Mg III-XII, Si IV-XIV, S IV-XVI, and Fe VI-XXVI. However, it does not include Ar XVIII and Ca XIX. We therefore added two Gaussians to take the emission lines from these two elements into account. We multiplied REFLIONX by a high-energy cutoff (modeled with HIGHECUT in xspec), where the cutoff energy was frozen to 0.1 keV and the folding energy was fixed to be 2.7 times the temperature of the electrons. In fact, for a saturated Comptonization, a Wien bump is formed at the electron temperature, whose peak is at about three times the electron temperature. We used NTHCOMP (Zdziarski et al. 1996; Zycki et al. 1999) to model the Comptonization continuum instead of COMPTT in order to have the photon index Γ as the fitting parameter of the continuum. Its value was fixed to be equal to the photon index of the illuminating component in the reflection model. The χ^2/d.o.f. obtained with this model is 577/413 (~ 1.40).

To take the smearing of the reflection component induced by Doppler and relativistic effects into account in the inner disk close to the compact object, we convolved the reflection model and the two Gaussians with the same RDBLUR component. This gives as best fit parameters the inclination of the system ($38^{\circ+2}_{-1}$), the inner and outer radii of the accretion disk ($R_{in} = 13^{+4}_{-6}$ and R_{out} is fixed at 3500 R_g), and the index of the emissivity law profile (-2.2 ± 0.1). We froze the width of the Gaussian lines at 0 keV to apply the same smearing parameters applied to the RE-FLIONX component. The χ^2/d.o.f. is 523/412 ($\Delta\chi^2 \sim 54$ for the addition of 1 parameter; the corresponding F-test probability of chance improvement is 2×10^{-10}). This attests that the RDBLUR component is statistically required to improve the fit. However, the reflection component does not seem to fit the iron edge correctly, since some features are still present in the residuals at about 8.5 keV. We added an edge to the model, also convolved with the same RDBLUR component (under the assumption that the edge is also produced in the same region of the accretion disk as the reflection component). The edge is found at 8.7 keV and the associated depth is 0.06. The χ^2 decreases by 83 for the addition of two parameters, resulting in a $\chi^2_{red} = 1.07$ (410).

To check the consistency of the edge with the reflection continuum, we used another reflection model, PEXRIV (Magdziarz & Zdziarski 1995), which includes the iron edge and the Compton bump of the reflection component. This model consists in an exponentially cutoff power-law spectrum reflected by ionized material; however, this model does not include any emission lines, so four Gaussians (S, Ar, Ca and Fe) were added and convolved, together with the pexriv component, with the RD-BLUR component. The photon index of PEXRIV is fixed to the one obtained with the NTHCOMP model, and the cutoff energy is 2.7 times the electron temperature obtained with NTHCOMP. The normalization of the PEXRIV model was fixed to the one of the cutoff power-law model included in NTHCOMP. To do so, we applied a cutoff power-law model to the data and calculated the normalization in such a way that the bolometric flux is the same as with NTHCOMP. The χ^2_{red} obtained with this model is 1.06 (410 d.o.f.). The values of the smearing parameters agree with the previous model, and the features at about 8.5 keV are no longer visible in the residuals, so the edge is well fit by PEXRIV and is likely a reflection feature. However, it is not well fit by the REFLIONX component.
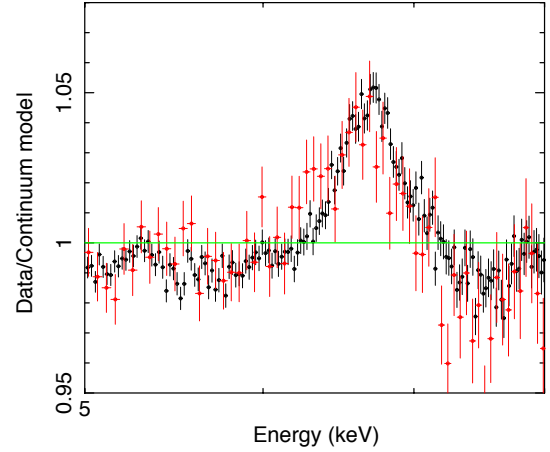
Fig. 5. Ratio of the data to the continuum model for XMM/EPIC-pn (black) and *BeppoSAX*/MECS (red) in the energy range 5−8 keV showing the broad iron line clearly visible in both spectra, although the statistics are much better in the case of the pn spectrum. The continuum is described by the spectral model phabs (bbody + compTT) in Xspec.

4.3. Reflection models on the XMM-Newton, BeppoSAX, and RXTE data

Considering the data of *XMM-Newton* and *BeppoSAX* separately, the continuum of these spectra is well fit by a blackbody plus a thermal Comptonized model (COMPTT or NTH-COMP) modified at low energy by the interstellar photoelectric absorption (PHABS). In both cases, the fit is improved by adding a broad iron line, fitted by a Gaussian line or, even better, by a DISKLINE. The best fit parameters, obtained by fitting the spectra from the two different X-ray observatories separately, are similar to each other and agree with previous results reported by Piraino et al. (2007) and Di Salvo et al. (2009) on 4U 1705−44. Regarding the *BeppoSAX* data, the absorption column density is $N_H = 1.4 \times 10^{22}$ cm^{-2}, the blackbody temperature is 0.56 keV, and the temperatures of the electrons and of the seed photons of the Comptonized component are 3.5 keV and 1.2 keV, respectively. A diskline is found at 6.8 keV, the inclination of the system is $28^{\circ+8}_{-5}$, and the inner radius is about 8^{+4}_{-2} R_g. The χ^2/d.o.f. corresponding to this fit is 584/503 ($\chi^2_{red} \sim 1.16$). This is better than using a Gaussian to fit the iron line (χ^2/d.o.f. is 618/505, $\chi^2_{red} \sim 1.23$; an F-test gives a probability of chance improvement of about 10^{-6}). These results agree perfectly with the results we obtain from the *XMM-Newton* spectrum, independently of the particular model we used to fit the reflection features; however, the uncertainties on the inner radius and on the inclination angle are larger than in the case of *XMM-Newton*. This can be explained by the quality of the data, which is better in the case of *XMM-Newton* thanks to its larger effective area and higher resolution capabilities. In Fig. 5 we show the ratio of the data to the best-fit continuum model in the energy range 5−8 keV to compare the residuals at the iron line as observed by the *XMM-Newton*/EPIC-pn and by the *BeppoSAX*/MECS. The iron line profile appears very similar in the two instruments, although the observations are not simultaneous.

Since the values of the parameters obtained by fitting the *XMM-Newton* and *BeppoSAX* spectra in the soft state are very similar, we fitted these data simultaneously, adding the RXTE data. The different cross calibrations of the different instruments were taken into account by including normalizing factors in the model. This factor was fixed to 1 for pn and kept free for the

Table 2. Parameters left free to vary between *XMM-Newton*, *BeppoSAX*, and RXTE spectra in the soft state.

Parameter	XMM	BeppoSAX	RXTE
N_H ($\times 10^{22}$ cm^{-2})	2.08 ± 0.02	1.96 ± 0.02	3.64 ± 0.02
Γ	2.6 ± 0.1	2.2 ± 0.1	2.4 ± 0.1
kT_e (keV)	3.0 ± 0.1	2.9 ± 0.1	B
kT_seed (keV)	1.30 ± 0.02	$1.13^{+0.01}_{-0.02}$	B
$Norm_\mathrm{nthComp}$	0.14 ± 0.01	0.19 ± 0.01	B

Notes. The whole model is presented in Table 7. B: corresponding parameter has the same value as in the *BeppoSAX* spectrum.

other instruments. We used the self-consistent reflection model REFLIONX, and NTHCOMP instead of COMPTT, to describe the thermal Comptonization component in order to have the photon index as a parameter of the fit. To take the disk smearing into account, which is necessary to obtain a good fit of the reflection component, we convolved the reflection model, the edge, and the two Gaussians used to fit the Ar and Ca lines with the same RDBLUR component.

Since the spectra are not simultaneous, we find small differences in the best fit values of some parameters of the continuum model. We therefore left these parameters free to vary from one instrument to the next, when necessary (see Table 2). These parameters are the column density, the parameters of NTHCOMP (the photon index, the temperature of the electrons and of the seed photons, and the normalization) and the fold energy of the high-energy cutoff (that is fixed at 2.7 times the electron temperature in the soft state, according to the expectation for saturated Comptonization), which are slightly different for *BeppoSAX* and *XMM-Newton*. As regards RXTE, only the column density and the photon index are left free to vary. The other parameters coincide very well with those found for the *BeppoSAX* spectrum, so they are constrained to have the same values. All the other parameters are perfectly consistent with those obtained for *XMM-Newton*, and were forced to have the same values. The total χ^2/d.o.f. obtained in this way is 1839/1573 ($\chi^2_\mathrm{red} \sim 1.17$).

We note that the RDBLUR component is not statistically required to fit the whole dataset in this case. Indeed, if we delete this component from the model, we obtain $\chi^2 = 1835/1574$ (~ 1.17), which is very similar to the one we get when the relativistic smearing is included in the model (χ^2/d.o.f. = 1839/1573). However, if we exclude the relativistic smearing from the model, the ionization parameter gets an extremely high value, ~ 8000 erg cm s^{-1}, that appears to be unphysical. At such a high ionization parameter, Fe XXVI would be the most abundant Fe ion and this would produce a line at 6.97 keV. On the other hand, in the *XMM-Newton* spectrum the iron line is clearly detected at 6.7 keV, suggesting it is produced by Fe XXV. With the inclusion of the relativistic smearing described by the RDBLUR component, the ionization parameter attains a more reasonable value of 3500, fully consistent with the presence of an iron line at 6.6 keV produced by Fe XXV. Moreover, all the smearing parameters are perfectly coherent with those previously obtained (e.g. Di Salvo et al. 2009; D'Aì et al. 2010; Piraino et al. 2007). An additional iron edge is found at 8.7 keV with a significance of 11.6 σ. Finally, we report here, for the first time, evidence of an iron overabundance by a factor 2.5 with respect to its solar abundances. The results of this model are presented in Table 7. To evaluate the statistical significance of the iron overabundance,
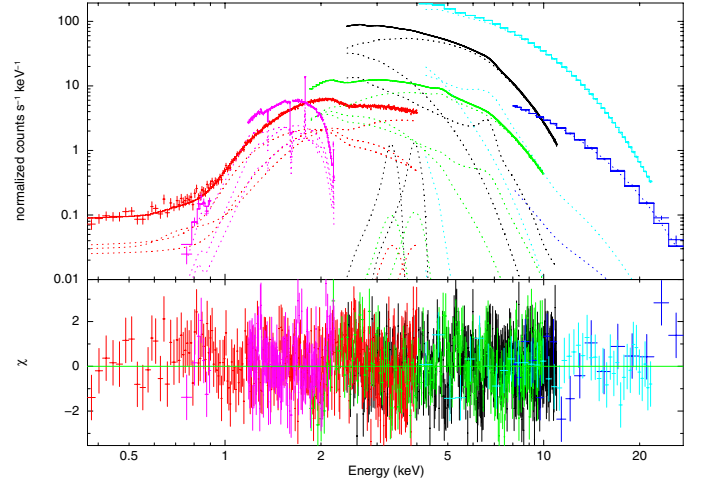
Fig. 6. *Top panel*: XMM/RGS1 (magenta), XMM/EPIC-pn (black), *BeppoSAX*/LECS (red), *BeppoSAX*/MECS (green), *BeppoSAX*/HPGSPC (blue), RXTE/PCA (cyan) data points in the range 0.3–30 keV, when 4U 1705−44 was in the soft state. *Bottom panel*: residuals (data-model) in unit of σ when the REFLIONX model is used to describe the reflection component. The parameters associated to this model are indicated in Table 7. The XMM/RGS1 data have been rebinned for graphical purpose.

we fixed this parameter to one. The χ^2 increases by 48 for the addition of 1 d.o.f. ($\chi^2_\mathrm{red} \sim 1.20$) and the associated probability of chance improvement is 2×10^{-10}, so the iron overabundance is statistically significant.

The EPIC/pn absorbed flux obtained from the *XMM-Newton* best fit spectral parameters is 6.19×10^{-9} erg cm^{-2} s^{-1} and the unabsorbed flux is 7.39×10^{-9} erg cm^{-2} s^{-1} in the 2−10 keV band. We extrapolate this model in the 0.1−150 keV range to estimate the bolometric unabsorbed flux, $F_\mathrm{X} = 2.7(1) \times 10^{-8}$ erg cm^{-2} s^{-1}. The bolometric luminosity associated to the soft state is $L_\mathrm{X} \sim 1.8 \times 10^{38}$ erg s^{-1}, assuming a distance to the source of 7.4 kpc. This value is very close to the Eddington luminosity for a 1.4 $M_\odot$ neutron star.

We also apply another reflection model, XILLVER (Garcia & Kallman 2010), to our dataset of 4U 1705−44 from the three satellites. This model includes Compton broadening, and the illumination spectrum is a power law with a photon index of two, similar to REFLIONX. In this model, the redistribution of the photon energy is achieved by a Gaussian convolution, whose sigma is a function of the energy and the temperature of the gas. The gas temperature changes when going deep inside the disk, and is calculated self-consistently by solving thermal and ionization balance. This model also includes emission lines from the same ions included in REFLIONX and, in addition, emission lines from Ar and Ca. It also allows fitting the abundances of these two elements with respect to the solar abundance. In this case, to obtain a stable fit, we were forced to freeze the photon index Γ associated to the *XMM-Newton* data to the value obtained with REFLIONX ($\Gamma = 2.6$). The addition of the edge at 8.5 keV is again needed to improve the fit, with a significance of 11.1σ. The χ^2_red associated to this fit is 1.26 for 1576 d.o.f. The fit obtained with this model is a bit worse than obtained with REFLIONX, but the values of the parameters are still consistent with those obtained with REFLIONX. We note a lower value of the inclination angle of the system ($i = 25-27°$), while the value of the inner disk radius ($R_\mathrm{in} = 10-13\ R_\mathrm{g}$) is perfectly consistent between
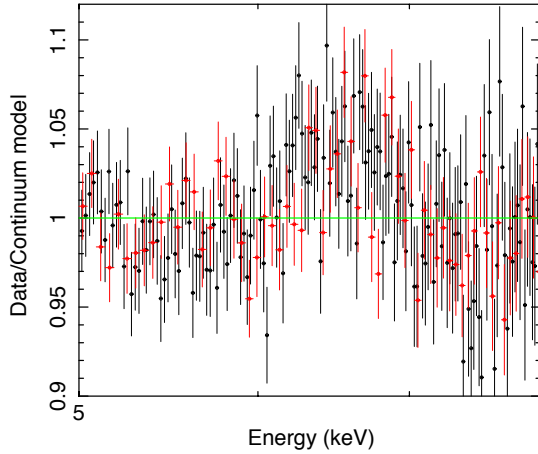
Fig. 7. Ratio of the data to the best-fit continuum model for XMM/EPIC-pn (black) and *BeppoSAX*/MECS (red) in the hard state, in the energy range 5−8 keV. The broad iron line is visible in both spectra, but is not as well defined as in the soft state (see Fig. 5). The continuum is described by phabs (bbody + compTT).

the two cases[4]. We find an overabundance by a factor 1.5−2 of Ar and Ca with respect to their solar abundance; a similar overabundance is also observed for iron (see Table 7). However, the statistical significance of the overabundance of Ar and Ca is not very well established. Indeed, fixing this parameter to 1, we find χ^2/d.o.f. = 1992/1577, the corresponding probability of chance impovement is 2×10^{-2}. In any case, this model allows us to demonstrate that the Ar and Ca lines are probably produced by reflection.

As seen in the previous section, PEXRIV also gives a very good fit of the pn data. We apply this model plus four Gaussians, all convolved with the same rdblur component, to the whole dataset. The results are very similar to REFLIONX, in particular the inclination of the system ($i = 38−41°$) and the inner radius of the accretion disk ($R_{\rm in} = 12−17 \, R_{\rm g}$). The $\chi^2_{\rm red}$ associated is 1.16 for 1570 d.o.f. The best fit parameters corresponding to this model are summarized in Table 7 and compared to REFLIONX and XILLVER.

5. Hard state

In this section we apply the same procedure used for the soft state to the 4U 1705−44 data in the hard state, using the three satellites: *XMM-Newton*, *BeppoSAX*, and RXTE. Regarding the *XMM-Newton* data, we excluded a type-I X-ray burst before performing the spectral analysis. The study of the burst is described by D'Aì et al. (2010).

We use the same continuum model in order to determine the differences in the spectral parameters from one state to the other. The temperature of the electrons is about 14−16 keV, the temperature of the seed photons is 1.0−1.2 keV, the optical depth of the Comptonized component is 5−6, and the blackbody is

Table 3. Parameters left free to vary between *XMM-Newton*, *BeppoSAX*, and RXTE in the hard state.

Parameter	XMM	BeppoSAX	RXTE
$N_{\rm H}$ ($\times 10^{22}$ cm^{-2})	2.0 ± 0.3	1.9 ± 0.1	B
$kT_{\rm bb}$ (keV)	$0.58^{+0.04}_{-0.02}$	$0.24^{+0.02}_{-0.03}$	B
$Norm_{\rm bb}$ ($\times 10^{-3}$)	2.6 ± 0.5	2.0 ± 0.4	B
Γ	B	1.84 ± 0.01	$2.07^{+0.05}_{-0.03}$
$kT_{\rm e}$ (keV)	B	22^{+2}_{-1}	79^{+50}_{-22}

Notes. The complete model is given in Table 8. B: corresponding parameter is fixed to have the same value as in the *BeppoSAX* spectrum. $kT_{\rm bb}$, $Norm_{\rm bb}$: temperature and normalization of the BLACKBODY component. Γ, $kT_{\rm e}$: photon index and electron temperature of the NTHCOMP component.

found at 0.55−0.58 keV. The addition of a Gaussian improves considerably the fit. A broad iron line is present in all the data at 6.4−6.6 keV (see Fig. 7). Using a DISKLINE instead of a Gaussian profile to fit the iron line, we have to freeze the values of the outer radius to 3500 $R_{\rm g}$ and the inclination of the system to 37°, as in the soft state and in agreement with Di Salvo et al. (2009). The χ^2 in this case is the same as using a simple Gaussian line. While for the *XMM-Newton* data, the χ^2/d.o.f. is 407/419 (~0.97) using a Gaussian, there are still some residuals at high energy (>10 keV) in the case of *BeppoSAX* and RXTE. The associated $\chi^2_{\rm red}$ are 1.24 (484 d.o.f.) and 1.15 (65 d.o.f.) for the *BeppoSAX* and the RXTE spectra, respectively.

To fit this hard excess, probably ascribed to the Compton bump of the reflection component, we apply the self-consistent reflection model REFLIONX, with the aim of comparing the values of the parameters in the hard state and in the soft state. In this case we fix the folding energy of the high-energy cutoff to the electron temperature of the NTHCOMP component, as expected for unsaturated Comptonization. We simultaneously fitted the three datasets following the same method as described in previous section. Some parameters are left free to vary between the instruments of the different observatories, such as the column density and the blackbody temperature. Moreover, in the case of the RXTE spectrum, we have to leave the photon index of the power law and the electron temperature free to vary in order to obtain a good fit. These parameters are listed in Table 3. The inclination angle is not well constrained so we freeze its value to 37°, which corresponds to the best fit value obtained in the soft state using REFLIONX to fit the reflection component. The outer radius of the accretion disk is also frozen to 3500 $R_{\rm g}$. This value corresponds to the best estimate obtained using the REFLIONX model to fit the soft state of 4U 1705−44 and is consistent with the results reported by Di Salvo et al. (2009).

We convolve the reflection model with the RDBLUR component to include Doppler broadening caused by the motion of matter in the inner disk. The addition of this component decreases the χ^2/d.o.f. from 1126/981 to 1097/980. The F-test is ~4×10^{-7}. This demonstrates that the iron line and the whole reflection component are also significantly broadened in the hard state, and are consistent with being produced in the accretion disk. Since only the iron line is significantly detected, we do not add any other emission line or edge. To measure the significance of the Compton bump in these data, we replace the REFLIONX model with a simple Gaussian line smeared by relativistic and/or Doppler effects, by using the RDBLUR component. The χ^2 is 1299/981 ~1.32. We compare this result with the previous

---

[4] We use here a test version of the XILLVER model, specifically developed to include Ar and Ca lines. In this version of the model, the illuminating flux is integrated over a different energy range with respect to that used for the REFLIONX model, and this results in a different, lower value of the ionization parameter, which also affects the estimate of the inclination angle (Garcia, priv. comm.). We have checked that, integrating the illumination flux over the same range used for the REFLIONX model, we obtain best-fit parameters that are all compatible with those obtained with REFLIONX.
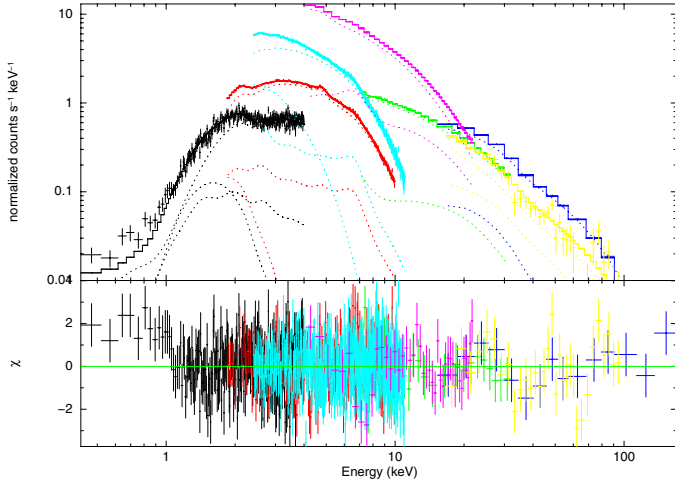
Fig. 8. *Top panel*: XMM/EPIC-pn (cyan), *BeppoSAX*/LECS (black), *BeppoSAX*/MECS (red), *BeppoSAX*/HPGSPC (green), *BeppoSAX*/PDS (blue), RXTE/PCA (magenta), RXTE/HXTE (yellow) data points in the range $0.4-200$ keV, corresponding to the hard state of 4U 1705−44. *Bottom panel*: residuals (data-model) in units of σ when the REFLIONX model is applied. The parameters associated to this model are shown in Table 8.

model where the reflection component is included instead of the simple Gaussian associated to the iron line. The F-test gives a probability of chance improvement equal to 10^{-38}. This shows that there is a reflection signature in the spectrum besides the iron line in the hard state, meaning the Compton bump is significantly detected in these data.

We obtain a good fit of the whole dataset; the best fit parameters are listed in Table 8, where we just show those obtained for the *BeppoSAX* spectrum. (There are small differences in the best-fit parameters related to the fact that the observations are not simultaneous as described above.) From all the instruments, we obtain a constraint on the inner disk radius, which appears to be truncated farther from the neutron star surface ($R_{\rm in} = 19-59\,R_{\rm g}$) with respect to the soft state. We obtain a high temperature of the electrons (about 22 keV) in the hard state, and a low value of the ionization parameter ($\xi \sim 210$ erg cm s^{-1}).

The absorbed flux associated to this model obtained from the *BeppoSAX* best fit parameters in the range $0.1-150$ keV is 2.09×10^{-9} erg cm^{-2} s^{-1}, and the unabsorbed flux is 2.99×10^{-9} erg cm^{-2} s^{-1}. The bolometric luminosity associated to the hard state is $L_{\rm X} \sim 2 \times 10^{37} d_{7.4}^2$ erg s^{-1}, which corresponds to $\sim 11\%\,L_{\rm Edd}$.

Because in the soft state, an iron overabundance has been detected by at least a factor 2, we fixed this parameter to two in order to evaluate the change in the whole spectrum and its effect on the other parameters. The values of the parameters are very similar, even if the χ^2 is a bit higher (1.13 for 981 d.o.f.). The inner disk radius is found at a slightly larger distance from the compact object ($R_{\rm in} = 24-79\,R_{\rm g}$), again in agreement with a geometry where the accretion disk is truncated farther from the neutron star than in the soft state. These results are summarized in Table 8.

6. Discussion

We performed a spectral analysis in the broad band and with high energy resolution of 4U 1705−44 using data from *XMM-Newton*, *BeppoSAX*, and RXTE, both in the hard and in the soft state. We described a method of fitting unsimultaneous

data, which we applied using self-consistent reflection models. Thanks to the good spectral coverage from the low (0.3 keV) to the high (200 keV) energy band, we have obtained good constraints on the continuum emission and on the reflection component, marking the most significant changes in the spectral parameters from the hard state to the soft state. The agreement between the results obtained with different instruments and the possibility of fitting most of the reflection component with self-consistent models, provides further evidence that the broad iron line observed in 4U 1705−44 may be produced by reflection at the inner accretion disk, and indicates that the reported inner disk parameters are indeed reliable. In the following we discuss the main results from this analysis.

6.1. The iron line

The origin of the iron line in neutron star LMXBs is still being debated (Ng et al. 2010; Cackett et al. 2010, 2012). In this paper, we have compared the iron line profile observed by *XMM-Newton* with the one observed by other instruments, and in particular by *BeppoSAX*. We find perfect agreement between the results from these instruments, although the observations were not simultaneous, both in the soft and in the hard state of the source.

We carefully studied the pile-up effects in the XMM/EPIC-pn spectrum of 4U 1705−44 during the soft state, when the count rate was the highest. We demonstrated that the exclusion of the two central columns of the CCD is enough to get rid of pile-up effects, while excluding more CCD rows may underestimate the number of double events with respect to the expected value (see Appendix). In addition to this, we showed that the addition of the RGS data is important to constrain the overall continuum shape well. We find that the iron line parameters are not significantly affected by pile-up. This agrees with Cackett et al. (2010), who also conclude that the iron line profile is robust even if there was a small fraction of pile-up affecting the data, while the continuum may vary significantly. This also agrees with a comprehensive study performed by Miller et al. (2010), who found that severe pile-up may distort disk lines and the continuum shape, whereas a modest pile-up fraction does not noticeably affect the line shape. This is probably the case of 4U 1705−44.The best fit parameters of the iron line profile we find in this way agree perfectly with what has been previously found (see e.g. Piraino et al. 2007; Di Salvo et al. 2009; D'Aì et al. 2010), independently of the particular model used to fit the reflection component.

In the soft state, the Fe line at 6.7 keV is associated with highly ionized Fe XXV, which is a triplet consisting of the following components: at $r = 6.700$ keV, $i_2 = 6.682$ keV, $i_1 = 6.668$ keV, and $f = 6.637$ keV. We also included a Gaussian to consider the H-like Fe XXVI contribution of the Lyα transitions at $Ly\alpha_1 = 6.973$ keV and $Ly\alpha_2 = 6.952$ keV. Unfortunately, the resolution of *XMM-Newton* and *BeppoSAX* does not allow us to resolve the structure of the resulting line, which appears to be dominated by the intercombination line of the triplet, and this is why a single Gaussian or a diskline has been used to take all these components into account. These lines were resolved, for example, in the case of the bright Z-source Cyg X-2 observed with the High Energy Transmission Grating Spectrometer on-board the *Chandra* satellite, which offers very high spectral resolution (Schulz et al. 2009). Also in that case the Fe complex was dominated by the intercombination line of the Fe XXV triplet, and therefore the line was fitted by a single Gaussian. Also a red-skewed wing of the iron line was discovered in a *Suzaku* observation of Cyg X-2 (Shaposhnikov et al. 2009). It should be noted,

Table 4. *XMM-Newton* and *BeppoSAX* journal of observations.

Satellite	Obs. ID	Obs. date	Exp. time (ks)	Count rate ASM (c/s)	State source
XMM-Newton	0402300201	26/08/2006	34.72	1	Hard
	0551270201	24/08/2008	45.17	19	Soft
BeppoSAX	21292001	20/08/2000	43.5	18	Soft
		03/10/2000	48	3	Hard

Table 5. Selected RXTE observation journal.

Source state	Obs. ID	Obs. date (MJD)	Count rate (c/s)	Hardness
SS	93060-01-15-00	54 332.3	642.4	0.613
	93060-01-16-00	54 336.4	804.4	0.647
	93060-01-19-01	54 348.7	1049.0	0.620
	93060-01-19-02	54 349.0	1011.0	0.621
	93060-01-25-00	54 372.5	834.5	0.630
	93060-01-76-00	54 576.5	726.9	0.620
	93060-01-84-00	54 608.5	833.7	0.628
	93060-01-91-00	54 636.8	732.4	0.625
	93060-01-95-00	54 652.6	785.0	0.617
	93060-01-01-10	54 668.1	832.2	0.646
	93060-01-02-10	54 672.3	849.8	0.637
	93060-01-07-10	54 692.5	761.5	0.614
	93060-01-10-10	54 704.4	768.4	0.632
	93060-01-12-10	54 712.2	791.4	0.617
	93060-01-19-10	54 740.3	782.5	0.631
	94060-01-20-00	54 942.5	805.5	0.609
	94060-01-22-00	54 950.6	834.7	0.622
	95060-01-71-00	55 478.6	879.0	0.620
HS	91039-01-01-41	53 541.0	79.7	0.760
	91039-01-01-42	53 543.0	78.1	0.749
	91039-01-01-43	53 544.8	82.6	0.751
	91039-01-01-50	53 546.0	91.3	0.767
	91039-01-02-40	53 658.3	64.9	0.736
	93060-01-07-00	54 300.4	70.6	0.747
	93060-01-52-01	54 480.6	67.1	0.746
	94060-01-08-00	54 894.9	52.1	0.738
	95060-01-19-01	55 270.5	69.6	0.749
	95060-01-33-00	55 326.4	52.5	0.733
	95060-01-46-00	55 378.7	57.7	0.750

however, that these lines are all included in the reflection models we used in our spectral analysis, and a further smearing was required to properly fit the line complex. Consequently, the iron line is consistent with being produced in the inner part of the accretion disk where the line profile is distorted by Doppler and by mildly relativistic effects relatively close to the compact object. At the inner disk radii we find, $R_{in} \sim 10-17\,R_g$, the Keplerian velocities become mildly relativistic, and the Doppler boosting effect yields the blue-shifted horn (produced by matter coming in our direction) brighter than the red-shifted one (produced by receding matter).

In the hard state, the Fe emission line at 6.4−6.6 keV is related to a low ionized Fe fluorescence line. The line does not present clear asymmetry anymore and is equally well fit by a Gaussian or with the diskline model. The apparent symmetry of the line may be due to the relativistic effects becoming less important farther from the compact object and/or to the lower statistics in the hard state. In both states, the broadening of the line is not as extreme as in the case of some black hole X-ray binaries or AGNs (see e.g. Reis et al. 2009a; Fabian et al. 2009). The Compton hump of the reflection component, however, is required with a very high confidence level to get a good fit of the data in the hard state.

6.2. Reflection models

We used data of 4U 1705−44 from three satellites (*XMM-Newton*, *BeppoSAX*, and RXTE) in order to test self-consistent reflection models on a broad-band range from 0.3 to 200 keV. The reflection models we used are calculated for an optically-thick atmosphere (such as the surface of an accretion disk) of constant density illuminated by a power-law spectrum.

In the soft state, we conclude that the reflection model PEXRIV is able to fit the iron edge with smearing parameters that are very similar to those obtained for the iron line profile; the REFLIONX model is able to self-consistently fit the iron line profile and the S XVI line at 2.6 keV; the XILLVER model is able to fit the iron line profile self-consistently with the S XVI, the Ar XVII, and Ca XIX lines. The REFLIONX model suggests an iron overabundance by a factor of about 2 with respect to its solar abundance. A mildly relativistic smearing of the reflection component, described with the RDBLUR component, is statistically required to fit the *XMM-Newton* data with the REFLIONX model, because these data have the best statistics at the iron line energy. Nevertheless, this component is not statistically required when we fit all our dataset with the REFLIONX model. However, if we exclude the RDBLUR component from the model,

Table 6. Evaluation of the pile-up effects on the *XMM-Newton* EPIC-pn data of 4U 1705−44 in the soft state, using the RGS and pn spectra.

Component	Parameter	pn-all	pn-1	pn-2	pn-3	pn-4	pn-5	pn-6	pn-7	BeppoSAX
phabs	N_H (×10^{22} cm^{-2})	1.6 ± 0.1	1.6 ± 0.1	1.6 ± 0.1	1.6 ± 0.1	1.6 ± 0.1	1.6 ± 0.1	1.6 ± 0.1	1.6 ± 0.1	1.9 ± 0.1
rdblur	Betor	$-2.30^{+0.04}_{-0.02}$	-2.32 ± 0.03	$-2.35^{+0.05}_{-0.04}$	$-2.39^{+0.06}_{-0.07}$	$-2.35^{+0.04}_{-0.07}$	$-2.39^{+0.08}_{-0.07}$	-2.4 ± 0.1	-2.4 ± 0.1	-2 (frozen)
rdblur	R_{in} (GM/c^2)	14 ± 2	14^{+1}_{-2}	14^{+3}_{-1}	15 ± 2	15^{+3}_{-2}	16 ± 3	16^{+4}_{-3}	17^{+4}_{-3}	8^{+4}_{-2}
rdblur	i (°)	38 ± 1	39 ± 1	38^{+2}_{-1}	39 ± 2	41^{+2}_{-1}	42 ± 2	40^{+3}_{-2}	40^{+6}_{-3}	28^{+20}_{-8}
edge	E (keV)	8.6 ± 0.1	8.6 ± 0.1	8.6 ± 0.1	8.6 ± 0.1	8.7 ± 0.1	$8.7^{+0.2}_{-0.1}$	8.8 ± 0.2	$8.6^{+0.3}_{-0.5}$	–
edge	Max τ (×10^{-2})	5.1 ± 0.4	5.7 ± 0.4	7 ± 1	7 ± 1	8 ± 2	8 ± 2	7^{+3}_{-2}	5^{+3}_{-2}	–
bbody	kT_{bb} (keV)	0.57 ± 0.01	0.57 ± 0.01	0.57 ± 0.01	0.56 ± 0.01	0.55 ± 0.02	0.55 ± 0.02	0.54 ± 0.01	0.54 ± 0.02	0.56 ± 0.01
bbody	Norm (×10^{-2})	3.0 ± 0.1	2.9 ± 0.1	3.1 ± 0.1	3.0 ± 0.1	3.2 ± 0.1	3.2 ± 0.1	3.4 ± 0.1	3.4 ± 0.1	2.2 ± 0.1
compTT	kT_o (keV)	1.31 ± 0.01	1.29 ± 0.02	$1.30^{+0.02}_{-0.03}$	$1.34^{+0.02}_{-0.05}$	$1.33^{+0.03}_{-0.08}$	$1.35^{+0.05}_{-0.09}$	1.36 ± 0.05	$1.39^{+0.06}_{-0.04}$	$1.13^{+0.05}_{-0.02}$
compTT	kT_e (keV)	6^{+19}_{-2}	4^{+3}_{-1}	4^{+4}_{-1}	4^{+14}_{-1}	4^{+11}_{-1}	4^{+15}_{-2}	4^{+18}_{-1}	4^{+5}_{-1}	2.7 ± 0.1
compTT	τ	$4.7^{+13}_{-0.1}$	6.8 ± 0.1	$6.6^{+0.1}_{-0.3}$	5.9 ± 0.3	6^{+7}_{-1}	$5.2^{+0.6}_{-0.5}$	$5.1^{+0.5}_{-0.6}$	4^{+60}_{-1}	11.0 ± 0.6
compTT	Norm (×10^{-2})	18^{+6}_{-5}	29^{+8}_{-2}	30 ± 1	30^{+65}_{-2}	30^{+1}_{-7}	30^{+1}_{-12}	33^{+170}_{-12}	32^{+411}_{-8}	35 ± 2
gauss	E (keV)	2.64 ± 0.03	2.67 ± 0.03	2.65 ± 0.03	2.65 ± 0.03	2.67 ± 0.05	2.66 ± 0.05	$2.7^{+0.9}_{-0.7}$	$2.8^{+0.1}_{-0.2}$	–
gauss	Norm (×10^{-3})	0.9 ± 0.2	1.3 ± 0.2	2.1 ± 0.3	$1.6^{+0.5}_{-0.3}$	1.7 ± 0.6	$1.8^{+0.8}_{-0.7}$	$1.8^{+0.8}_{-0.9}$	$1.3^{+0.9}_{-0.7}$	–
gauss	E (keV)	3.29 ± 0.01	$3.29^{+0.01}_{-0.02}$	3.29 ± 0.02	$3.30^{+0.03}_{-0.02}$	$3.30^{+0.03}_{-0.02}$	$3.27^{+0.04}_{-0.02}$	3.27 ± 0.03	$3.28^{+0.03}_{-0.04}$	–
gauss	Norm (×10^{-3})	1.9 ± 0.2	2.1 ± 0.2	2.4 ± 0.2	2.6 ± 0.3	$3.2^{+0.3}_{-0.5}$	3.1 ± 0.6	$3.4^{+0.5}_{-0.7}$	2.8 ± 0.7	–
gauss	E (keV)	$3.89^{+0.01}_{-0.02}$	$3.87^{+0.04}_{-0.01}$	3.89 ± 0.02	3.88 ± 0.02	3.88 ± 0.02	3.86 ± 0.03	$3.84^{+0.03}_{-0.02}$	$3.87^{+0.03}_{-0.05}$	–
gauss	Norm (×10^{-3})	1.7 ± 0.1	2.0 ± 0.1	2.1 ± 0.2	2.4 ± 0.2	2.9 ± 0.4	$3.0^{+0.5}_{-0.2}$	3.3 ± 0.6	$3.1^{+0.9}_{-0.6}$	–
gauss	E (keV)	6.64 ± 0.01	6.64 ± 0.01	6.64 ± 0.01	6.62 ± 0.02	$6.62^{+0.03}_{-0.02}$	$6.59^{+0.02}_{-0.03}$	6.58 ± 0.04	6.58 ± 0.04	$6.7^{+0.2}_{-0.5}$
gauss	Norm (×10^{-3})	$3.8^{+0.1}_{-0.2}$	4.1 ± 0.2	4.3 ± 0.1	$4.1^{+0.3}_{-0.2}$	4.4 ± 0.4	4.7 ± 0.4	$4.9^{+0.5}_{-0.4}$	$4.6^{+0.6}_{-0.4}$	$4.7^{+2}_{-0.6}$
	χ^2_{red} (d.o.f.)	1.20 (1024)	1.15 (1024)	1.14 (1024)	1.15 (1024)	1.13 (1024)	1.11 (1024)	1.13 (1024)	1.14 (1024)	1.18 (524)

Notes. We compare the parameters obtained when we exclude 0, 1, 2, until the 7 brightest central columns in the pn CCD, which correspond to spectra named pn-all, pn-1, pn-2, up to pn-7, respectively (see text). The last column contains the results from *BeppoSAX* data in the soft state as reported by Piraino et al. (2007), to compare the values of the parameters obtained with *XMM-Newton* with those obtained with non-CCD instruments. The model applied on the pn and RGS data consists of const*phabs*rdblur*edge*(bbody+compTT+gauss+gauss+gauss+gauss). The model used to fit the *BeppoSAX* data is phabs*(bbody+compTT+powerlaw+diskline).

Table 7. Comparison of three different self-consistent, relativistically smeared reflection models (reflionx, xillver and pexriv) applied to the *XMM-Newton*, *BeppoSAX*, and RXTE spectra of 4U 1705−44 in the soft state.

Component	Parameter	Reflionx	Xillver	Pexriv
phabs	N_H ($\times 10^{22}$ cm^{-2})	2.08 ± 0.02	2.04 ± 0.01	1.91 ± 0.02
bbody	kT_{bb} (keV)	0.56 ± 0.01	$0.67^{+0.02}_{-0.01}$	0.52 ± 0.01
bbody	Norm ($\times 10^{-2}$)	2.58 ± 0.01	1.7 ± 0.01	2.94 ± 0.01
nthComp	Γ	2.6 ± 0.1	2.6 (frozen)	2.3 ± 0.1
nthComp	kT_e (keV)	3.0 ± 0.1	2.9 ± 0.1	2.6 ± 0.1
nthComp	kT_{seed} (keV)	1.30 ± 0.02	$1.39^{+0.04}_{-0.01}$	$1.18^{+0.03}_{-0.02}$
nthComp	Norm	0.14 ± 0.01	0.11 ± 0.01	0.17 ± 0.01
rdblur	Betor	-2.1 ± 0.1	-2.1 ± 0.1	-2.3 ± 0.1
rdblur	R_{in} (GM/c^2)	13 ± 3	11^{+2}_{-1}	15^{+2}_{-3}
rdblur	R_{out} (GM/c^2)	3500 (frozen)	3500 (frozen)	3500 (frozen)
rdblur	i (°)	37 ± 2	26 ± 1	40^{+1}_{-2}
edge	E (keV)	8.7 ± 0.1	8.5 ± 0.1	–
edge	Max τ ($\times 10^{-2}$)	4.2 ± 0.6	3.4 ± 0.5	–
gauss	E (keV)	–	–	2.6 (frozen)
gauss	Norm ($\times 10^{-3}$)	–	–	1.4 ± 0.2
gauss	E (keV)	3.31 ± 0.01	–	$3.31^{+0.02}_{-0.03}$
gauss	Norm ($\times 10^{-3}$)	1.4 ± 0.2	–	1.9 ± 0.2
gauss	E (keV)	3.92 ± 0.02	–	$3.88^{+0.01}_{-0.03}$
gauss	Norm ($\times 10^{-3}$)	1.4 ± 0.2	–	2.0 ± 0.2
gauss	E (keV)	–	–	6.63 ± 0.01
gauss	Norm ($\times 10^{-3}$)	–	–	4.1 ± 0.1
highecut	cutoff$_E$ (keV)	0.1 (frozen)	0.1 (frozen)	–
highecut	fold$_E$ (keV)	8.1 (2.7*kT_e of nthComp)	7.7 (2.7*kT_e of nthComp)	7.0 (2.7*kT_e of nthComp)
reflection	Γ	2.6 (=Γ of nthComp)	–	2.3 (=Γ of nthComp)
reflection	Norm	$(8 \pm 1) \times 10^{-6}$	$(1.5 \pm 0.1) \times 10^{-5}$	1.218 (frozen)
reflection	Fe/Solar	$2.5^{+0.4}_{-0.5}$	1 (frozen)	$1.4^{+0.6}_{-0.1}$
reflection	Ar, Ca Abund	1 (frozen)	$1.8^{+0.2}_{-0.3}$	1 (frozen)
reflection	ξ (erg cm s^{-1})	3578^{+1184}_{-847}	1349^{+31}_{-90}	3081^{+2488}_{-1954}
pexriv	Rel-refl	–	–	$-1^{+1}_{-0.02}$
	Total χ^2_{red} (d.o.f.)	1.17 (1573)	1.26 (1576)	1.16 (1570)

Notes. The model used is const*phabs*rdblur*edge*(bbody+nthcomp+gauss+gauss+ gauss+gauss+highecut*reflection). For the pexriv model, the disk inclination is fixed to cos i = 0.78 and the disk temperature to 10^6 K. Here we present the best fit parameters we obtain for the *XMM-Newton* spectrum. A few parameters of the continuum got different best fit values for the nonsimultaneous *BeppoSAX* and RXTE spectra, as detailed in Table 2.

we find that the ionization attains very high (unphysical) values. It should be noted here that both REFLIONX and XILLVER include Compton broadening, which is higher for higher ionization parameters (Reis et al. 2009b). This means that to adequately fit the width of the line with Compton broadening alone, we have to dramatically increase the ionization parameter to values that appear too high to be compatible with the observed energy of the iron line. This is why we decided to include the relativistic smearing in the reflection model. The smearing parameters are determined well and appear very similar regardless of the particular reflection model adopted. They are congruent with previous results reported for this source (Piraino et al. 2007; Di Salvo et al. 2009; D'Aì et al. 2010), and are very similar for all the datasets used here (from *XMM-Newton*, *BeppoSAX*, and RXTE satellites).

In the hard state, we significantly detect the iron line at 6.4 keV and the Compton bump of the reflection component, while the other low-energy emission lines and the iron edge were not significantly detected. We just used the REFLIONX model to fit the reflection component self-consistently (i.e. just the iron line and the Compton bump in this case). As before, we obtain a very good fit of the whole spectrum in the broad-energy band between 0.4 and 200 keV. We note that the relativistic smearing

is statistically required for the hard state. In fact the iron line is found to also be broad in this state (although not as broad as in the soft state), but in that case the ionization parameter has a particularly low value, and Compton broadening is negligible so cannot explain the width of the line. Our results for the hard state of 4U 1705-44 coincide with the results obtained by Piraino et al. (in preparation). These authors fit the *BeppoSAX* data in the hard state with an alternative reflection model, where COMPPS (Poutanen & Svensson 1996) is used to model the primary Comptonization spectrum. Their results are consistent with the disk-reflection scenario we favor in this paper.

Our results agree with Reis et al. (2009b), who applied RE-FLIONX on three datasets of 4U 1705−44 obtained by *Suzaku* at different periods. A relativistic broadening was also required to obtain a good fit, as in our analysis. Therefore different instruments get similar values for the reflection component in 4U 1705−44, indicating that the iron line shape as seen by these instruments is similar, and demonstrating that pile-up is not responsible for the observed iron line shape.

D'Aì et al. (2010) and Cackett et al. (2010) also applied a reflection model, REFBB (Ballantyne 2004), to fit the spectrum of this source, restricted to the *XMM-Newton* data in the energy range 2–12 keV. In this model a blackbody component, very

Table 8. Self-consistent, relativistically smeared reflection model (reflionx) applied to the 4U 1705−44 spectra from the three satellites (*XMM-Newton*, *BeppoSAX*, and RXTE) when the source was in the hard state.

Component	Parameter	Reflionx (Fe/sol = free)	Reflionx (Fe/sol = 2)
phabs	$N_{\rm H}$ ($\times 10^{22}$ cm^{-2})	1.9 ± 0.1	1.9 ± 0.1
bbody	$kT_{\rm bb}$ (keV)	$0.24^{+0.02}_{-0.03}$	0.26 ± 0.02
bbody	Norm ($\times 10^{-3}$)	2.0 ± 0.4	1.7 ± 0.3
nthComp	Γ	1.84 ± 0.01	1.83 ± 0.01
nthComp	$kT_{\rm e}$ (keV)	22^{+2}_{-1}	21 ± 1
nthComp	$kT_{\rm seed}$ (keV)	$0.69^{+0.02}_{-0.01}$	0.70 ± 0.02
nthComp	Norm ($\times 10^{-2}$)	$3.9^{+0.1}_{-0.2}$	4.0 ± 0.2
rdblur	Betor	-3 (frozen)	-3 (frozen)
rdblur	$R_{\rm in}$ (GM/c^2)	31^{+28}_{-12}	39^{+40}_{-15}
rdblur	$R_{\rm out}$ (GM/c^2)	3500 (frozen)	3500 (frozen)
rdblur	i (°)	37 (frozen)	37 (frozen)
highecut	$cutoff_E$ (keV)	0.1 (frozen)	0.1 (frozen)
highecut	$fold_E$ (keV)	22 (=$kT_{\rm e}$ of nthComp)	21 (=$kT_{\rm e}$ of nthComp)
reflionx	Fe/Solar	$1.1^{+0.5}_{-0.3}$	2 (frozen)
reflionx	Γ	1.84 (=Γ of nthComp)	1.83 (=Γ of nthComp)
reflionx	ξ (erg cm s^{-1})	209^{+9}_{-5}	204^{+4}_{-3}
reflionx	Norm ($\times 10^{-5}$)	1.7 ± 0.3	$1.8^{+0.6}_{-0.3}$
	Total $\chi^2_{\rm red}$ (d.o.f.)	1.12 (980)	1.13 (981)

Notes. The model consists of const*phabs*(bbody + nthComp + rdblur*highecut*reflionx). The inclination angle is fixed at 37°, while the Fe/sol ratio is left free to vary or is fixed to 2. Here we show the best fit parameters we obtain for the *BeppoSAX* spectrum. A few parameters of the continuum got different best fit values for the nonsimultaneous *XMM-Newton* and RXTE spectra, as detailed in Table 3.

likely associated to the boundary layer, provides the illuminating flux. In this energy band, the reflection model parameters are mainly determined by the shape of the iron line and are perfectly compatible with the results described in this work. In other words, the inner disk parameters we obtain for this source under the hypothesis that the line is produced by reflection of the primary Comptonization spectrum on the inner accretion disk, are always compatible with each other, independently of the particular model used to fit the reflection component (such as DISKLINES, REFBB, PEXRIV, REFLIONX, XILLVER).

To support this disk-reflection scenario, all the reflection component should be fitted by a self-consistent reflection model. Unfortunately, no reflection model includes all the reflection features. In the case of REFLIONX, two emission lines are needed to reproduce Ar XVIII and Ca XIX emission lines detected in the soft state. We also needed to add an edge at ∼8.5 keV. To check whether the edge was consistent with a disk origin, we used another reflection model: PEXRIV. The edge is taken into account correctly by this model, but the model does not include any emission line. The XILLVER model includes S, Ar, Ca, and Fe lines, but the addition of an edge at ∼8.5 keV was again necessary to obtain a good fit.

As shown by our analysis, the quality reached by today's observatories is such that it is now compelling to calibrate the reflection broad band spectrum better, because important features are clearly present (like emission lines from low Z-elements) and others are not accounted for well enough (as absorption edges of highly ionized elements).

6.3. The continuum parameters

The main differences between the spectral parameters obtained from the soft and the hard states are discussed in the following. They concern the electron temperature and the seed photon temperature of the Comptonized component, the inner radius of

the disk as derived from the smearing of the reflection component, and the ionization of the reflection component. We note here that we had to fix the parameters of the continuum of the reflection component to the parameters of the NTHCOMP component used to represent the primary Comptonization spectrum. In this case, to obtain a good fit, we had to fix the folding energy parameter to 2.7 times the electron temperature in the soft state and to the electron temperature in the hard state, in agreement with the fact that the peak of a saturated Comptonization spectrum is at 2.7 $kT_{\rm e}$, while the peak of an unsaturated Comptonization spectrum is at $kT_{\rm e}$.

We observe a clear difference in the spectral parameters from the soft to the hard state. The electron temperature increases from $kT_{\rm e} = 2−3$ keV in the soft state to ∼20−24 keV in the hard state, whereas the power-law photon index and the temperature of the seed photons decrease from $\Gamma = 2.2−2.8$ to $\Gamma = 1.8$ and from $kT_{\rm seed} = 1.1−1.4$ keV to 0.7−0.8 keV, respectively.

To evaluate the changes in the optical depth and the region of the seed photons from one state to the other, we use the parameters obtained by the NTHCOMP model. This model specifies the Comptonization via the electron temperature in the corona $kT_{\rm e}$, the temperature of photons injected in the corona $kT_{\rm seed}$, and the spectral slope Γ. These parameters are related to the optical depth τ as

$$\Gamma = -\frac{1}{2} + \left[\frac{9}{4} + \frac{1}{\frac{kT_{\rm e}}{m_{\rm e}c^2} \tau \left(1 + \frac{\tau}{3}\right)} \right]^{1/2} \quad (1)$$

(Lightman & Zdziarski 1987). We use the values of the NTHCOMP components reported in the first column of Tables 7 and 8, which correspond to the REFLIONX model for the reflection component in both states. The optical depth decreases from the soft to the hard state, from $\tau \sim 7$ to $\tau \sim 3$. Moreover, we

compute the Comptonization parameter y defined by

$$y = 4 \frac{kT_e}{m_e c^2} \times \max(\tau, \tau^2) \qquad (2)$$

and obtain $y \sim 1$ and $y \sim 2$ in the soft and hard states, respectively. To estimate the radius of the emitting region of the seed photons that are Comptonized in the hot corona, we assume their emission as a blackbody and the bolometric Comptonized flux as $F_{Compt} = F_{seed}(1 + y)$ since we have to correct for energy gained by the photons in the inverse Compton scattering. As a result, F_{seed} is defined by

$$F_{seed} = \sigma T_{seed}^4 \left(\frac{R_{seed}}{d} \right)^2, \qquad (3)$$

so the region of the seed photons is obtained by

$$R_{seed} = 3 \times 10^4 d \frac{[F_{Compt}/(1 + y)]^{1/2}}{(kT_{seed})^2} \text{ km} \qquad (4)$$

(see in't Zand et al. 1999) with d the distance in kpc, F_{Compt} in erg cm^{-2} s^{-1}, and kT_{seed} in keV. By considering the F_{Compt} obtained with *BeppoSAX* that is 8.84×10^{-9} and 2.09×10^{-9} erg cm^{-2} s^{-1} in the soft and hard states, respectively, and a distance of 7.4 kpc, we obtain $R_{seed} \sim 9$ km in the soft state and $R_{seed} \sim 12$ km in the hard state, so the seed photons are compatible with coming from the neutron star surface in both states. These results are consistent with a corona above the disk and/or between the disk and with the stellar surface that is hotter in the hard state than in the soft state. This is likely due to the interactions with the soft photons from the disk that are more or less intense depending upon the geometry of the disk-corona system. It can also be connected with the energetic balance between the Compton cooling provided by the soft photons (which acts as the photon number, so with the fourth power of the temperature) and the coronal heating (maybe through shock dissipation).

For the blackbody component, in the soft state kT_{bb} is 0.57 keV. Assuming a distance of 7.4 kpc, the region associated with the blackbody has an apparent radius $\sim R_{bb} = 30$ km, in agreement with the emission coming from the hottest part of the accretion disk, which corresponds to the inner part of the disk close to the neutron star. In the hard state, the blackbody temperature is $kT_{bb} = 0.25$ keV for all the instruments except for *XMM-Newton*, for which $kT_{bb} = 0.57$ keV. The radius associated to the first value is $\sim R_{bb} = 160$ km, again compatible with a truncated accretion disk, whereas the second one is $\sim R_{bb} = 30$ km. It is not clear whether the temperature of the blackbody component changes between the soft and the hard states, since for this parameter we find a very similar value for the hard state to what is found for the soft state for the *XMM-Newton* dataset, while the other instruments suggest a lower value. However, in the hard state, we note similar values of the blackbody normalization for different temperatures. The reason *XMM-Newton* gives a much higher blackbody temperature than *BeppoSAX* and RXTE may be a contamination from the boundary layer emission visible during the *XMM-Newton* observation and not during the other ones (of course the boundary layer emission may be directly visible when it is not completely comptonized in the corona).

6.4. The inclination of the system

The inclination angle of the system with respect to the line of sight, the inner radius of the disk, the emissivity index, and the centroid energy of the line are determined by the profile of the

lines (Fabian et al. 1989). These parameters are mutually correlated, and it may be difficult to disentangle their contribution to the overall line shape. For example, as discussed by Cackett et al. (2010), the inclination and the emissivity index play similar roles in determining the line profile. A high value of these parameters makes the line broad and less peaked, so a high value of the inclination and a low value of the emissivity index will give a similar profile to one with a low value of the inclination and a high value of the emissivity index.

In the soft state the observed emission lines, especially the iron line profile, allow us to obtain a good constraint on the inclination angle of the system. Using REFLIONX, we find $i = 35-40°$. Applying XILLVER instead of REFLIONX to the data, we obtain $i = 25-27°$. (The difference between the best fit values of the inclination angle and the ionization parameter obtained with XILLVER and REFLIONX are caused by the different energy range used to extrapolate the illuminating flux in the two models, Garcia, priv. comm.) However, using other models on the *XMM-Newton* data, which are the best-quality data obtained on 4U 1705−44, such as DISKLINE and PEXRIV, the inclination is found at $38-41°$, in agreement with REFLIONX. Because the χ^2/d.o.f. is higher in the case of XILLVER and because all the other models indicate the same range of values for the inclination, we conclude that the inclination of 4U 1705−44 is between $35-41°$ with respect to the line of sight.

6.5. Geometry of the accretion disk

In all the models, the RDBLUR component was needed to improve the fit. The mildly relativistic blurring was applied to the entire reflection spectrum, confirming the common origin of the reflection features in the inner part of the accretion disk, where strong relativistic effects broaden emission and absorption features. This component gives us information on the inner radius of the accretion disk, $R_{in} = 10-16$ R_g in the soft state, and $R_{in} = 19-59$ R_g ($R_{in} = 26-65$ R_g for the inclination fixed at $39°$) in the hard state, so we have an indication that the accretion disk is close to the neutron star surface in the soft state and truncated farther from the compact object in the hard state. This agrees with Barret & Olive (2002) and Olive et al. (2003), who interpret the transitions from one state to the other in this source with different truncation radii of the accretion disk. This is also a possible interpretation for black hole binaries that show clearer transitions from the soft to the hard state and vice versa (e.g. Done et al. 2007).

The spectral state transitions are also associated with variations in the overall X-ray luminosity. We calculated the accretion rate in both states using the typical value of the accretion efficiency $\eta = 0.2$, corresponding to a neutron star ($M_{NS} = 1.4$ $M_\odot$ and $R_{NS} = 10$ km), and to the bolometric luminosities inferred by our spectral modeling. In the soft state, $\dot{M}_{SS} = 1.6 \times 10^{-8}$ $M_\odot$ yr^{-1}, while in the hard state the accretion rate decreases, $\dot{M}_{HS} = 2 \times 10^{-9}$ $M_\odot$ yr^{-1}. This difference in the accretion rate is consistent with changes in the flow geometry, hence with a different inner radius of the accretion disk. The evaporation of the inner part of the accretion disk may lead to a truncated disk at low-mass accretion rates (e.g. Meyer et al. 2000).

We therefore infer a similar geometry to what has been proposed for black hole binaries where the accretion disk is truncated at low luminosity (Barrio et al. 2003; Done & Diaz Trigo 2010); however, some differences should be observed between these systems, especially in the soft state, because of the boundary layer in the case of the neutron star binaries. And in fact we

find that the disk is truncated in 4U 1705−44 relatively far from the compact object (at more than $10\,R_g$ both in the soft and in the hard state) as is inferred by the fact that the observed distortion of the iron line profile is never extreme.

6.6. The ionization parameter

Reflection models give an indication of the ionization state of the matter in the inner part of the accretion disk: $\xi = 4\pi F_X/n_H$, where F_X is the total illuminating flux (erg cm^{-2} s^{-1}) and n_H is the hydrogen number density. We note that the matter is much more ionized in the soft state, $\xi = 3600$ erg cm s^{-1}, in comparison with $\xi = 210$ erg cm s^{-1} in the hard state. This again agrees with the disk-reflection scenario for a truncated disk and with a lower illuminating flux in the hard state. When the accretion rate is high, the disk penetrates the hot flow, favoring the interactions between the inner disk and the illuminating flux and resulting in a high ionization and of the matter in the disk and, possibly, in a high reflection amplitude (e.g. Poutanen et al. 1997). In contrast, when the accretion rate is low, the disk is truncated farther from the compact object, disk matter is less ionized, and the amount of reflection is intrinsically low (e.g. Barrio et al. 2003). This is consistent with the observed energy of the iron line found in the soft state, $E_{Fe} = 6.6$–6.7 keV, and in the hard state, $E_{Fe} = 6.4$–6.5 keV (see also Reis et al. 2009b, who emphasize the influence of the ionization state of the accretion disk on the iron line profile).

6.7. Overabundance of some elements

Determination of the abundances of heavy elements is important for inferring how they originated. Most heavy elements from Si to Fe develop from explosive nucleosynthesis in supernovae. Type Ia supernovae, which correspond to the explosion of an accreting white dwarf in a binary system when its mass becomes superior to 1.4 $M_\odot$ via mass transfer, mainly provide Fe, whereas core collapse supernovae (SN II, Ib, IIb) associated to the gravitational collapse of the iron core of a massive star after successive stages of hydrostatic burning, provide intermediate elements, from Si to Ca.

In the soft state of 4U 1705−44, *XMM-Newton* detected emission lines corresponding to S, Ca, Ar, and Fe. Using reflection models we have investigated a possible overabundance of some elements with respect to their solar abundance. Applying REFLIONX we have an indication of an iron overabundance by a factor 2–3, probably responsible for the apparent large edge observed in the soft state (Ross & Fabian 2005). This result agrees with D'Aì et al. (2010), who evaluated the iron overbundance by a factor ~3 by using REFBB, in addition to an overabundance of S with respect to the other elements (or solar abundance).

In the hard state, the lower statistics do not allow us to detect other emission lines than Fe, so it is difficult to estimate any overabundance. When this parameter (Fe/sol) is free to vary in REFLIONX, its value is close to 1, and the inner radius of the disk is found at about $R_{in} = 19$–$59\,R_g$. When we fix the abundance of iron to a factor 2 with respect to the solar abundance, the inner radius is found at a slightly greater distance from the neutron star $R_{in} = 24$–$79\,R_g$, confirming the evidence of a truncated disk in the hard state. It is therefore important to obtain good constraints on the abundance of Fe and other elements, if possible, because this parameter also has a direct effect on the estimate of the inner radius of the disk.

6.8. Comparison with Cyg X-2 and GX 3+1

Both Cygnus X-2 and GX 3+1 are bright neutron star LMXBs showing spectral features similar to those observed in 4U 1705−44. The Z-source Cyg X-2 is one of the rare persistent LMXB whose secondary star is easily observed. It appears to be a high-inclination system ($i > 60°$) since short-duration dips have been detected in its light curve (Vrtilek et al. 1988; Orosz & Kuulkers 1999). The width of the brightest spectral lines of Mg XII, Si XIV, S XVI, Fe XXV, and Fe XXVI resolved by Chandra indicate velocity dispersion ranging from 1000 to 3000 km s^{-1} (Schulz et al. 2009), and they are consistent with a stationary, dense, and hot accretion-disk corona. Moreover, a *Suzaku* observation reveals the presence of a red-skewed wing of the Kα iron line in this source (Shaposhnikov et al. 2009), possibly explained by reflection of X-ray radiation from a cold accretion disk or by Compton down-scattering in a mildly relativistic wind outflow (Laurent & Titarchuk 2007). In the case of 4U 1705−44, the observed emission lines could not be resolved into blending of different lines, whether with *XMM-Newton* (Di Salvo et al. 2009) or with the *Chandra* High Energy Transmission Grating (Di Salvo et al. 2005). We infer velocities associated with the different emission lines of ~11 000 km s^{-1} ($E_{Fe} = 6.69 \pm 0.01$ keV, $\sigma_{Fe} \sim 0.25$ keV; $E_{Ar} = 3.31 \pm 0.02$ keV, $\sigma_{Ar} \sim 0.13$ keV) and a red-skewed Kα iron line, with a line width similar to the one observed in Cyg X-2 ($\sigma_{Fe} \sim 0.22$–0.25 keV). In both sources, the intercombination line dominates the Fe XXV triplet. However, the width measured for the 6.68 keV line is much more in 4U 1705−44 than in the case of the *Chandra* observation of Cyg X-2, but it is similar to the line width measured in the *Suzaku* observation of Cyg X-2. Because of the lower statistics of Chandra grating spectra, it may be possible that the red wing of the line is not easily observed by Chandra and is better detected by the large-area instruments of *Suzaku* and *XMM-Newton*.

Another peculiar system presenting very similar features to those observed in 4U 1705−44 is the type-I X-ray burster GX 3+1. Recently, a broad and asymmetric iron line, in addition to Ar XVIII and Ca XIX lines, has been detected with *XMM-Newton* in this persistent and bright atoll source (Piraino et al. 2012). The iron line profile is well fitted by a relativistically smeared profile and is thought to come from reflection in the inner parts of the accretion disk. As in 4U 1705−44, the line profile does not depend upon the photon pile-up fraction in the EPIC-pn spectrum, in agreement with Miller et al. (2010). The parameters obtained from the line profile modeled with a Gaussian or a diskline, such as the emission line width, the inclination of the system with respect to the line of sight, $35° < i < 44°$, and the inner disk radius, are remarkably similar to those we find for 4U 1705−44, indicating similar geometry and physical parameters of the disk-corona system in these bright sources.

7. Conclusions

Reflection features present complex profiles that mainly depend on the relativistic blurring, caused by Doppler effects of the high Keplerian velocities and, possibly, gravitational redshift at the inner disk radius, on the incident flux, on the ionization state of the matter in the disk, on the abundance of the elements, and on the inclination of the system with respect to the line of sight. The study of these features gives invaluable information on the system. We performed a broad band (0.4–200 keV) and moderately high-energy resolution spectral analysis of the X-ray burster 4U 1705−44 both in the soft and in the hard states using data

from *XMM-Newton*, *BeppoSAX*, and RXTE observatories. This source is particularly interesting since it shows several reflection features observed at a high S/N. We fitted these features with several self-consistent reflection models in order to test the common origin of all these features, which are all compatible with being produced by reflection of the primary Comptonization spectrum on the inner accretion disk. In this scenario we inferred the main parameters of the inner accretion disk. In particular, we found (i) the inclination of the system with respect to the line of sight that is constrained in the range 35−41°, (ii) the inner radius of the disk that increases from 10−16 R_g in the soft state up to 26−65 R_g in the hard state, and (iii) the ionization parameter that decreases from ~3600 erg cm s^{-1} in the soft state to 210 erg cm s^{-1} in the hard state. We also find an indication of an iron overabundance by a factor 2−3 with respect to its solar abundance. All these results appear to be strong against the particular reflection model used to fit these features and against possible distortion caused by photon pile-up in the *XMM-Newton*/EPIC-pn CCDs.

We have also discussed the differences in the spectral parameters between the soft and the hard states. The results found are consistent with the following scenario. At low luminosity, the accretion disk is truncated farther from the neutron star, so the interaction efficiency of the disk photons with the hot electrons of the corona is lower. The rate of photons coming from the disk is also lower because of the cooler temperature of the disk. This results in a hard spectrum and a low-ionization reflection. At higher luminosity, the mass accretion rate increases and the inner radius of the disk moves closer to the compact object. The soft photons from the disk are much more efficient at cooling the corona, resulting in a softer spectrum. In addition to this, reflection increases due to a stronger irradiation of the disk, and the matter becomes more ionized. Moreover, the emission lines are broadened by stronger Doppler effects as the disk approaches the compact object.

This scenario is generally well supported by the timing analysis through power density spectra where correlations are observed between the characteristic frequencies of the fast time variability and the position of the source in the CD or in its spectral state (e.g. Olive et al. 2003), with characteristic frequencies increasing when increasing the inferred mass accretion rate.

Appendix A: Pile-up

The task EPATPLOT offers the possibility to check whether an observation suffers from pile-up. Here we compare the following different cases, when all the columns of the CCD are used (pn-all), when the brightest central column is excluded (pn-1), when the two brightest central columns are excluded (pn-2), and finally when the seven brightest columns are excluded (pn-7, as proposed by Ng et al. 2010) in order to determine if the 4U 1705−44 spectra were affected by significant pile-up during the *XMM-Newton* observation in the soft state. We note the presence of some pile-up below 2 keV and above 10 keV, unless 7 central columns are excluded. We specify that we have restricted our spectral analysis between 2.4 and 11 keV, which is the range of interest for the study of the iron Kα line complex.
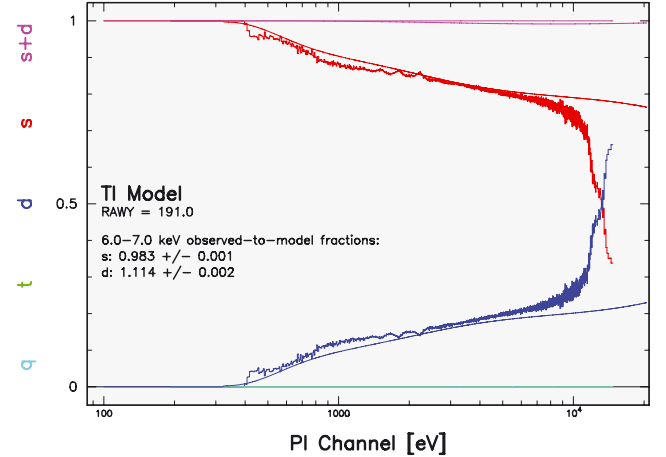

Fig. A.1. Estimation of the pile-up fraction in the EPIC-pn through the epatplot tool at the 6−7 keV iron line energy range when all the columns of the CCD are considered. The plot represents the spectra of the single (red) and double (blue) events. Solid lines indicate the expected fraction from the model curves.
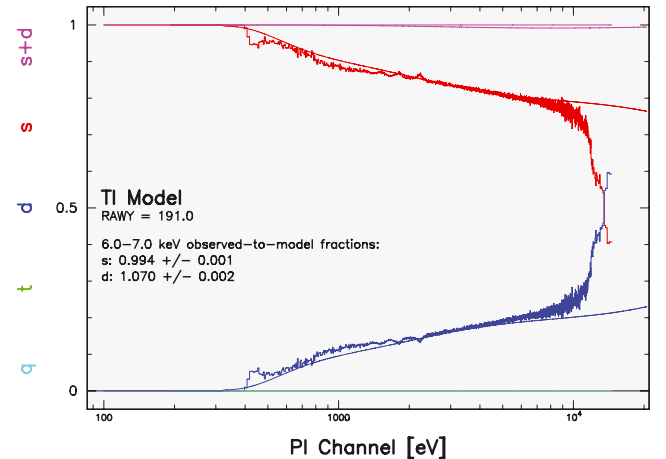
Fig. A.2. Same as in Fig. A.1 for pn-1, in which the brightest central column has been excluded.

Moreover, it is possible to quantify the amount of pile-up in a given energy range. By default this range is from 0.5 to 2 keV, which corresponds to the softest part of the spectrum, which is where it is the most sensitive to pile-up. We estimate the amount of pile-up in the energy band of the iron emission line (6−7 keV).

When we use all the columns of the CCD, we note a deviation between the observed and the expected distribution that testifies to the presence of pile-up in the spectrum (Fig. A.1). The observed-to-model fractions of the single and double are 0.98 and 1.11, respectively, in the 6−7 keV band. If we exclude the central column, the deviation is less important, especially for the single events (Fig. A.2). The observed-to-model fractions corresponding to the single and double events are 0.99 and 1.07. When we exclude two central columns, the single and double distributions follow the expected models, meaning that the observation no longer suffers from pile-up (Fig. A.3). The corresponding ratios are 1.00 and 1.04. Finally we exclude the seven brightest columns. The single and double distributions are overestimated in comparison to the models (Fig. A.4). The associated ratios are 1.03 and 0.91, respectively, in the 6−7 keV energy band. We therefore conclude that the best solution is to exclude two central columns of the CCD in order to avoid pile-up and to have the most correct distribution of single and double events at

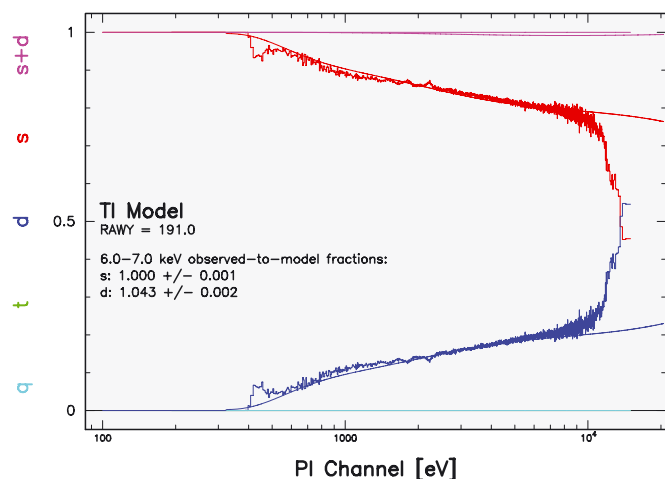**Fig. A.3.** Same as in Fig. A.1 for pn-2, in which the 2 brightest central columns of the CCD have been excluded.
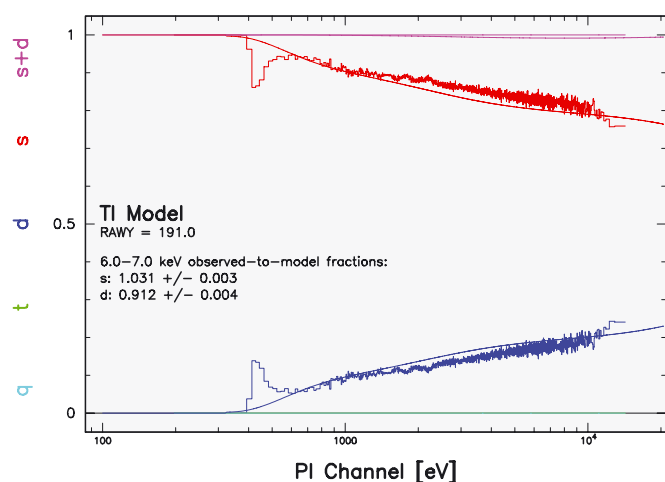

Fig. A.4. Same as in Fig. A.1 for pn-7, in which the 7 brightest central columns of the CCD have been excluded.

the iron-line energy band. Note also that the range below 2 keV is covered by the RGS, and it is therefore not necessary to eliminate more central columns in the pn CCD with the aim to reduce the pile-up fraction below 2 keV. In other words, we prefer to exclude from our spectral analysis the softer energy range in the pn spectrum, which is covered by the RGS, in order to maximize the statistics of the pn spectrum and the quality of the instrumental response reconstruction in the range of interest for iron line studies.

References

Anders, E., & Grevesse, N. 1989, Geochim. Cosmochim. Acta, 53, 197
Arnaud, K. A. 1996, in Astronomical Data Analysis Software and Systems V, ASP Conf. Ser., 101, 17
Ballantyne, D. R. 2004, MNRAS, 351, 57
Ballantyne, D. R., Ross, R. R., & Fabian, A. C. 2001, MNRAS, 327, 10
Balucinska-Church, M., & McCammon, D. 1992, ApJ, 400, L699
Barret, D., & Olive, J. F. 2002, ApJ, 576, 391

Barrio, F. E., Done, C., & Nayakshin, S. 2003, MNRAS, 342, 557
Cackett, E. M., Miller, J. M., Ballantyne, D. R., et al. 2010, ApJ, 720, L205
Cackett, E. M., Miller, J. M., Reis, R. C., Fabian, A. C., & Barret, D. 2012, ApJ, 755, 27
D'Aì, A., Iaria, R., Di Salvo, T., Matt, G., & Robba, N. R. 2009, ApJ, 693, L1
D'Aì, A., Di Salvo, T., Ballantyne, D., et al. 2010, A&A, 516, A36
Di Salvo, T., Iaria, R., Mendez, M., et al. 2005, ApJ, 623, L121
Di Salvo, T., D'Aì, A., Iaria, R., et al. 2009, MNRAS, 398, 2022
Done, C., & Diaz Trigo, M. 2010, MNRAS, 407, 2287
Done, C., Gierlinski, M., & Kubota, A. 2007, A&ARv, 15, 1
Egron, E., Di Salvo, T., Burderi, L., et al. 2011, A&A, 530, A99
Fabian, A. C., & Miniutti, G. 2005 (Cambridge Univ. Press) [arXiv:astro-ph/0507409]
Fabian, A. C., Rees, M. J., Stella, L., & White, N. E. 1989, MNRAS, 238, 729
Fabian, A. C., Iwasawa, K., Reynolds, C. S., & Young, A. J. 2000, PASP, 112, 1145
Fabian, A. C., Zoghbi, A., Ross, R. R., et al. 2009, Nature, 459, 540
Fiocchi, M., Bazzano, A. P. U., & Zdziarski, A. A. 2007, ApJ, 657, 448
Ford, E., van der Klis, M., & Kaaret, P. 1998, ApJ, 498, L41
Forman, W., Jones, C., Cominsky, L., et al. 1978, ApJ, 38, 357
Galloway, D. K., Muno, M. P., Hartman, J. M., Psaltis, D., & Chakrabarty, D. 2008, ApJ, 179, 360
Garcia, J., & Kallman, T. R. 2010, ApJ, 718, 695
George, I. M., & Fabian, A. C. 1991, MNRAS, 249, 352
Hasinger, G., & van der Klis, M. 1989, A&A, 225, 79
Iaria, R.and D'Aì, A., di Salvo, T., et al. 2009, A&A, 505, 1143
in't Zand, J. J. M., Verbunt, F., Strohmayer, T. E., et al. 1999, A&A, 345, 100
Kaastra, J. S., & Mewe, R. 1993, A&AS, 97, 443
Kallman, T., & White, N. E. 1989, ApJ, 341, 955
Langmeier, A., Sztajno, M., Hasinger, G., Truemper, J., & Gottwald, M. 1987, ApJ, 323, 288
Laor, A. 1991, ApJ, 376, 90
Laurent, P., & Titarchuk, L. 2007, ApJ, 656, 1056
Lightman, A. P., & Zdziarski. 1987, ApJ, 319, 643
Lin, D., Remillard, R. A., & Homan, J. 2010, ApJ, 719, 1350
Maccarone, T. J. 2012 [arXiv:1204.3154]
Magdziarz, P., & Zdziarski, A. A. 1995, MNRAS, 273, 837
Markoff, S., & Nowak, M. 2004, ApJ, 609, 972
Markoff, S., Nowak, M., & Wilms, J. 2005, ApJ, 635, 1203
Martocchia, S., & Matt, G. 1996, MNRAS, 282, L53
Matt, G. 2006, AN, 327, A96
Meyer, F., Liu, B. F., & Meyer-Hofmeister, E. 2000, A&A, 361, 175
Miller, J. M., D'Aì, A., Bautz, M. W., et al. 2010, ApJ, 724, 1441
Ng, C., Diaz Trigo, M., Cadolle Bel, M., & Migliari, S. 2010, A&A, 522, A96
Olive, J. F., & Barret, D. M. G. 2003, ApJ, 583, 416
Orosz, J. A., & Kuulkers, E. 1999, MNRAS, 305, 132
Papitto, A., Riggio, A., Di Salvo, T., et al. 2010, MNRAS, 407, 2575
Piraino, S., Santangelo, A., Di Salvo, T., et al. 2007, A&A, 471, L17
Piraino, S., Santangelo, A., Kaaret, P., et al. 2012, A&A, 542, L27
Poutanen, J., & Svensson, R. 1996, ApJ, 470, 249
Poutanen, J., Krolik, J. H., & Ryde, F. 1997, MNRAS, 292, L21
Reis, R. C., Fabian, A. C., Ross, R. R., & Miller, J. M. 2009a, MNRAS, 395, L1257
Reis, R. C., Fabian, A. C., & Young, A. J. 2009b, MNRAS, 399, L1
Reynolds, C. S., & Nowak, M. A. 2003, Phys. Rep., 377, 389
Ross, R. R., & Fabian, A. C. 2005, MNRAS, 358, 211
Ross, R. R., & Fabian, A. C. 2007, MNRAS, 381, 1697
Schulz, N. S., Huenemoerder, D. P., Ji, L., et al. 2009, ApJ, 692, L80
Shaposhnikov, N., Titarchuk, L., & Laurent, P. 2009, ApJ, 699, 1223
Titarchuk, L., Laurent, P., & Shaposhnikov, N. 2009, ApJ, 700, 1831
Vrtilek, S. D., Swank, J. H., Kelley, R. L., & Kahn, S. M. 1988, ApJ, 329, 276
Vrtilek, S. D., Soker, N., & Raymond, J. C. 1993, ApJ, 404, 696
Walton, D. J., Reis, R. C., Cackett, E. M., Fabian, A. C., & Miller, J. M. 2012, MNRAS, 422, 2510
White, N. E., & Holt, S. S. 1982, ApJ, 257, 318
White, N. E., Peacock, A., Hasinger, G., et al. 1986, MNRAS, 218, 129
Yan, M., Sadeghpour, H. R., & Dalgarno, A. 1998, ApJ, 496, L1044
Zdziarski, A. A., Johnson, W. N., & Magdziarz, P. 1996, MNRAS, 283, 193
Zycki, P. T., Done, C., & Smith, D. A. 1999, MNRAS, 309, 561
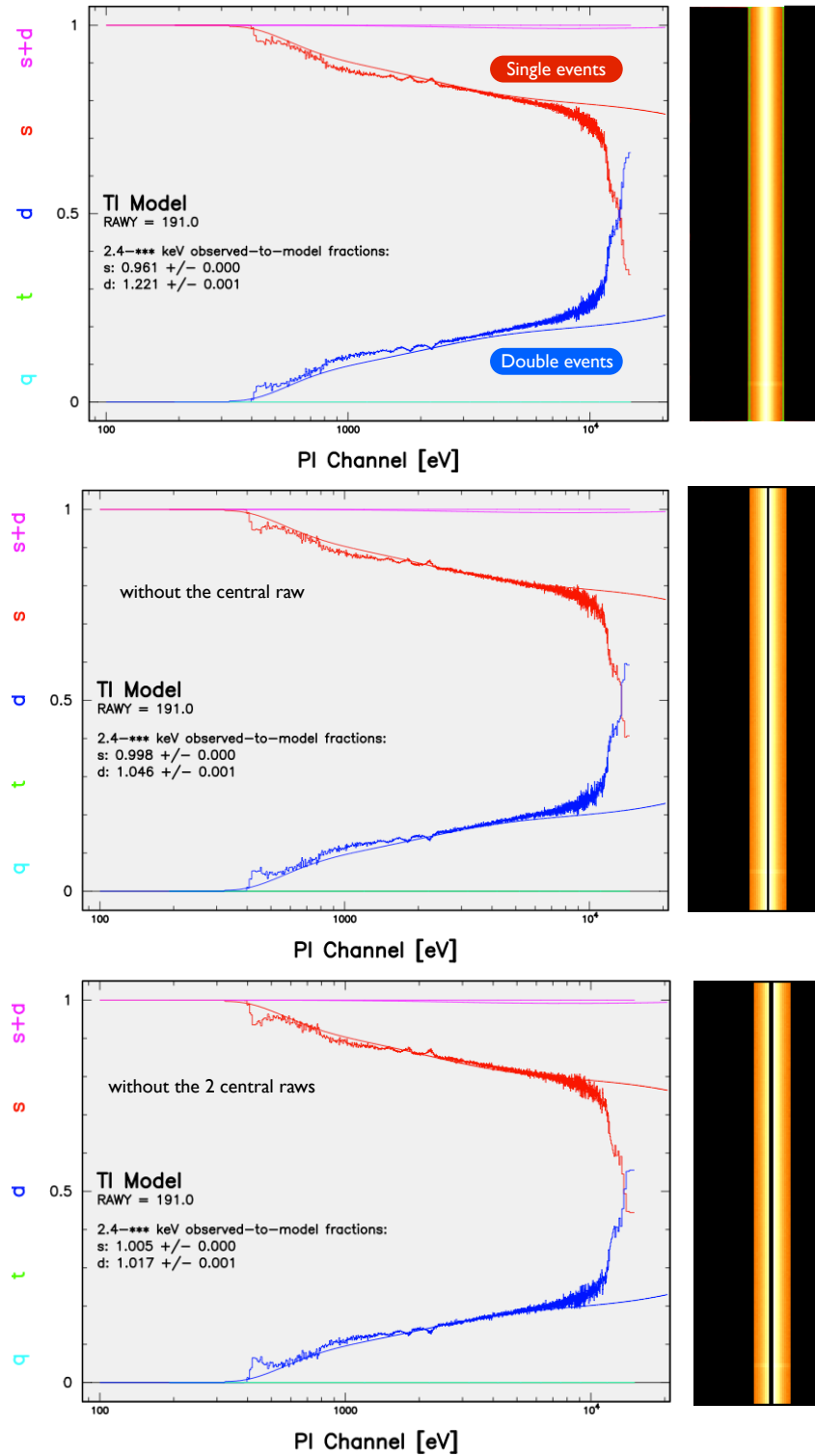
Figure 5.10: The left panels represent the expected pattern distribution functions (smooth solid lines) superposed to the observed ones for single (red) and double events (blue) in three different cases: a) when the central raws are used (upper panel), b) without the central raw (second panel), c) without the 2 central raws (lower panel). The rectangulars on the right show the image of the CCD of the EPIC-pn in timing mode corresponding to the three cases previously described.
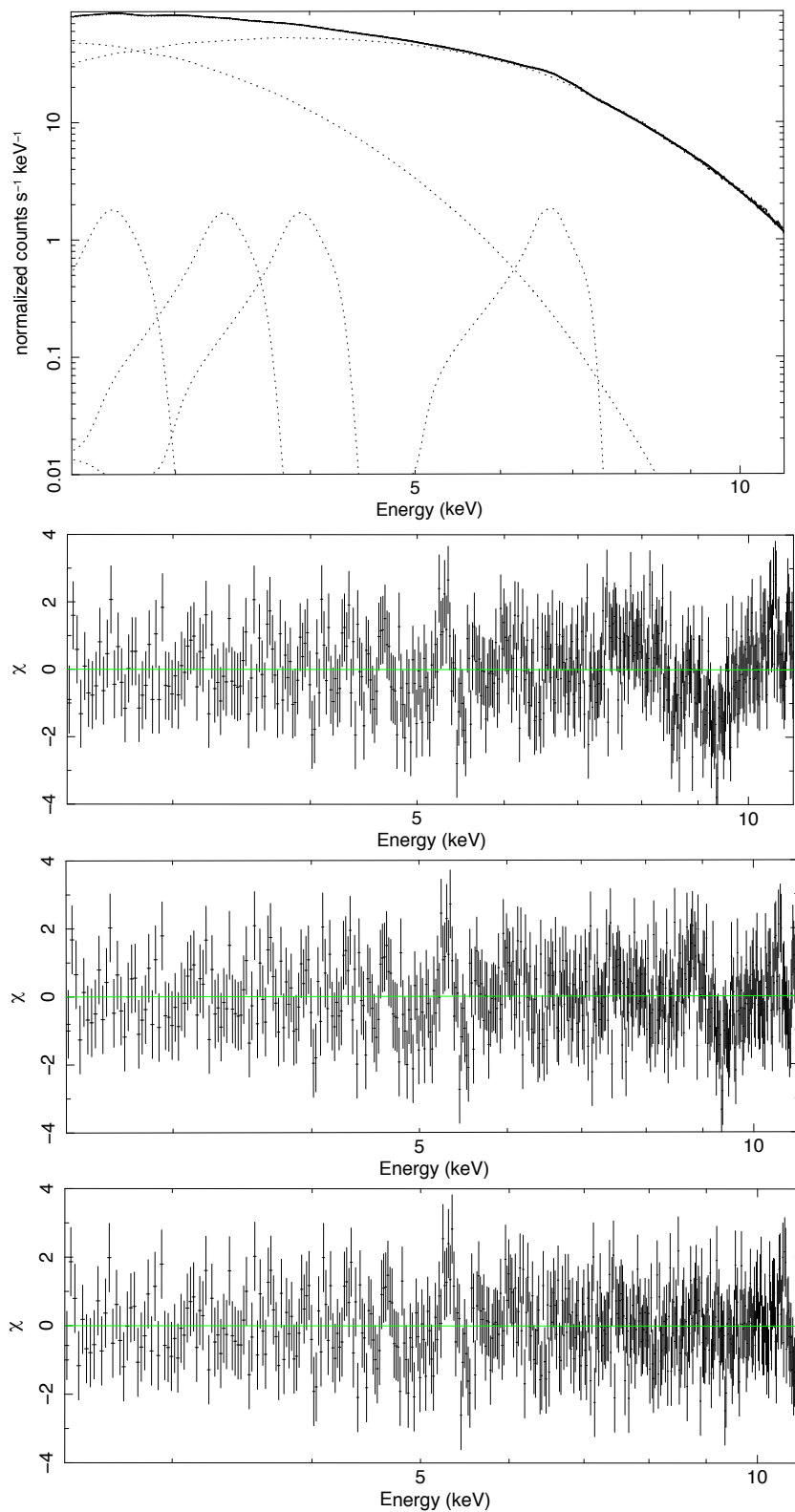
Figure 5.11: Upper panel: XMM-Newton/EPIC-pn data (continuous line) plus the different components of the model in dotted lines. The lower panels represents the residuals when a) no edge is included to the model, b) one edge at 8.6 keV is added, and c) when two edges are included to the model.

Tests on the Xillver reflection model

Contents

At present, there does not exist a fully, self-consistent model able to fit the whole reflection component in X-ray binaries and AGN. The current models present some limits. As seen in the previous chapter, a) reflionx does not include all of the emission lines and the Fe edge is not well taken into account (although this may be caused by small differences in the emission region of the emission lines and absorption edges), and b) pexriv does not contain any emission lines. Many other models do exist that account for the reflection component, but none contains all of the parameters necessary to perfectly fit the data. Therefore, models need to be improved in order to better reconstruct the reality of what happens in X-ray sources.

Xillver [Garcia 2010] is a relatively new model for which I performed some tests, in order to help its author, J. Garcia, adapt it in order to match the soft spectra observed in neutron star LMXBs and to fit all the observed discrete features. After a brief presentation of the model, I discuss the main parameters on which I focused. To test the tables, I used the 4U 1705-44 data in the soft state, since they present many reflection features of high quality. Moreover, thanks to the work performed on these data with the other reflection models, I can make a direct comparison between xillver and these models.

6.1 Xillver

6.1.1 Brief description of the model

Xillver is a recent model that seeks to reproduce reflected spectra from X-ray illuminated accretion disks. It assumes that the density is constant along the vertical direction of the disk. The theory used to design this model is based on the radiation transfer equation, ionization equilibrium, energy conservation, and atomic data. The structure of the gas is determined by the photoionization code XSTAR [Kallman 2001], considering different states of the gas, which isdefined by its temperature and the level of ion population. The vertical structure of the gas is found by solving ionization and thermal balance for different zones, using XSTAR.

The xillver model proposes a grid of parameters, which can take a certain range of values. Some parameters are fixed, such as the photon index of the power law $\Gamma = 2$, the other ones are free to vary, like for instance the ionization parameter ξ.

The energy resolution associated with the reflection spectra is higher than in the previous models, as well as the resolution of the detectors on current X-ray observatories, such as XMM-Newton, Suzaku and Chandra; it is comparable to the expected resolving power of the new generation of X-ray missions (as IXO for instance). Fig 6.1 shows the comparison between xillver and reflionx for three different values of the ionization parameter. The most prominent lines are identified in Fig 6.2.

6.1.2 Differences between xillver and reflionx, pexriv

Some differences have been highlighted between xillver and other reflection models (reflionx and pexriv) from the spectral analysis performed on the 4U 1705-44 data in the soft state [Egron 2012]. In this study, four emission lines were detected at 2.62, 3.31, 3.90 and 6.66 keV, probably associated with S XVI, Ar XVIII, Ca XIX, and Fe XXV respectively, in addition to an iron aborption edge at ~ 8.6 keV. Different reflection models (reflionx, xillver and pexriv) were applied to the data to confirm the common origin of these features. All of them were convolved with the rdblur component to take the relativistic effects into account close to the compact object. The main conclusions of the analysis are:

- the inner radius of the disk is found to be between 10 and 17 R_g in all of the models

- the edge at 8.6 keV is not well-included in reflionx and xillver

- an overabundance of Fe is detected with reflionx and as well as Ar, Ca with xillver.

- there is a difference in the inclination between xillver (26°) and reflionx/pexriv (37° and 40° respectively).

- the ionization parameter is found to be higher with reflionx, including higher error estimates than with xillver

- a blackbody is found to be at a slightly higher temperature in the case of xillver (0.67 keV) in the continuum. By comparison, the associated temperature is 0.56 keV and 0.52 keV, for reflionx and pexriv respectively.

6.2 Parameters tested

I tested different tables built by J. Garcia for the 4U 1705-44 data, in order to understand which parameters can improve the xillver reflection model. We note that the creation of a new table requires a lot of time and cpu's to be produced.

In the following, I present the main parameters on which I focused. They concern the Ar, Ca, and Fe abundances, and the Fe absorption edge. Furthermore, I introduce a new version of xillver, which includes a new treatment of the illumination of the accretion disk, and the first tests I performed with these new tables. Then, I mention some changes which will be needed to be taken into account in the future, such as the ionization parameter.

6.2.1 The abundance parameter

Reflionx and xillver show an overabundance of Ar, Ca, and Fe with respect to the solar abundance in the 4U 1705-44 data. In the version of xillver used, the iron abundance is set to 1, whereas the Ar and Ca abundances constitute a single parameter that is free to vary [Egron 2012]. The total $\chi^2_{\rm red}$ obtained is 1.26 for 1576 dof. Ar and Ca overabundances are detected with a factor of $1.8^{+0.2}_{-0.3}$. The Ca and Ar lines are well-fitted, but some residuals are still present at ~ 6.7 keV in the EPIC/pn data, corresponding to the iron line energy.

I tested different tables where the Ar, Ca, and Fe abundances are all grouped into a unique parameter, and then, when the Fe abundance is free to vary whereas the Ar and Ca abundances are fixed to 1 (solar abundances). The results are summarized in Table 6.1, where they are compared with the initial version of xillver (Ar and Ca abundances are free to vary as a unique parameter).

In the first table, the Ar, Ca, and Fe elements are forced to have the same abundance. An overabundance of these elements is found with a factor of 2.8 ± 0.1. However the S and Ar lines are still visible in the residuals. The $\chi^2_{\rm red}$ obtained using the XMM-Newton, BeppoSAX, and RXTE data is higher than in the previous case (1.38 for 1576 dof). The residuals corresponding to the XMM-Newton/EPIC-pn data are shown in the upper panel of Fig 6.4.

In the second table, where only the iron abundance can vary, and the Ar and Ca abundances are fixed to 1, the result should in principle be very similar to that of the reflionx model. The iron is detected with an overabundance of a factor $4.0^{+0.3}_{-0.1}$. The $\chi^2_{\rm red}$ associated with the fit is better than in the previous cases (1.24 for 1579 dof). The iron line is fitted in a nice way, but some residuals are still apparent at ~ 3.3 and

3.9 keV, which means that the Ca and Ar lines are not well-fitted. However, the $\chi^2_{\rm red}$ is still higher than that obtained with reflionx, where two Gaussians were added at 3.31 and 3.9 keV to fit the Ar and Ca lines, respectively. The corresponding residuals associated with the EPIC-pn data are illustrated in the upper panel of Fig 6.5.

I proposed to create another table that considers two different parameters for the element abundances: one for Ar and Ca, and another one for Fe. Indeed, these elements should not necessarily have the same abundance, since they do not have the same origin. Type Ia supernovae, which correspond to the explosion of an accreting white dwarf in a binary system when its mass becomes superior to 1.4 $M_{\rm sol}$ via mass transfer, provide mainly Fe. On the other hand, core collapse supernovae (SN II, Ib, IIb) associated with the gravitational collapse of the iron core of a massive star after successive stages of hydrostatic burning, provide intermediate elements, from Si to Ca. Therefore, it seems judicious to produce another xillver table which includes 2 different parameters: one for Fe abundance and the other one for Ar and Ca abundance, in order to let these parameters vary separately. These tables are currently under construction.

6.2.2   The Fe edge

As seen in the case of 4U 1705-44, the iron absorption edge is not well-fitted whether with reflionx or xillver. Pexriv is the only model which does it correctly.

I tested different xillver tables in order to understand whether the influence of the abundance parameter could have direct effects on the iron edge. I only used the XMM/EPIC-pn data in order to better see the comparisons. For each xillver table, I compared the residuals, with and without the addition of an edge (cf Fig 6.3, 6.4, and 6.5), and the associated χ^2. The values are reported in Table 6.2.

From this analysis, we note that the addition of an Fe absorption edge is necessary in the models to obtain a better fit. The only table that fits quite well the iron edge is the one which includes the Fe abundance parameter (Fe overabundance ~ 3) as a free parameter. Thus, the Fe edge seems to be correctly fitted only when the iron emission line is perfecty fitted (see Fig 6.5).

Additionally, the line at 2.6 keV probably associated to S XVI is not really well fitted by the different xillver tables. We suggest an overabundance of this element with respect to the solar abundance. This element could perhaps be added to the Ca and Ar in a same parameter, which could vary independently of the iron abundance parameter.

6.2.3   A new treatment of the illumination

The new xillver tables contain some modifications with respect to the previous ones, in particular with respect to the treatment of the illumination of the accretion disk. In the previous versions, the incident power law illuminating the disk was used for all energies in the spectrum, down to 0.1 eV. For any photon index Γ larger than 2, this induced too many photons in the low energy part of the spectrum, which was

Table 6.1: Comparison of the three versions of xillver (Xillver 1, Xillver 2, and Xillver 3), applied to the XMM-Newton, BeppoSAX, and RXTE data of 4U 1705-44 in the soft state. The abundance parameter differs from one version to another, such as a) **Xillver 1**: Ca and Ar abundances are grouped to one parameter, b) **Xillver 2**: Ca, Ar, and Fe abundances constitute one parameter, and c) **Xillver 3**: only the Fe abundance can vary, while the Ca and Ar abundance are fixed to 1.

Component	Parameter	Xillver 1	Xillver 2	Xillver 3
phabs	$N_{\rm H}$ ($\times 10^{22} cm^{-2}$)	2.04 ± 0.01	2.35 ± 0.01	1.99 ± 0.01
bbody	$kT_{\rm bb}$ (keV)	$0.67^{+0.02}_{-0.01}$	0.51 ± 0.01	0.59 ± 0.01
bbody	Norm ($\times 10^{-2}$)	1.70 ± 0.01	0.36 ± 0.01	1.95 ± 0.01
nthComp	$kT_{\rm e}$ (keV)	2.9 ± 0.1	3.2 ± 0.1	3.2 ± 0.1
nthComp	$kT_{\rm bb}$ (keV)	$1.39^{+0.04}_{-0.01}$	1.43 ± 0.01	$1.31^{+0.02}_{-0.01}$
nthComp	Norm	0.11 ± 0.01	0.099 ± 0.003	0.14 ± 0.01
rdblur	Betor	-2.1 ± 0.1	-2.8 ± 0.1	-2.3 ± 0.1
rdblur	$R_{\rm in}$ (GM/c^2)	11^{+2}_{-1}	11^{+1}_{-2}	11 ± 1
rdblur	i (°)	26 ± 1	22 ± 1	22 ± 1
edge	E (keV)	8.5 ± 0.1	9.1 ± 0.1	9.2 ± 0.1
edge	Max τ ($\times 10^{-2}$)	3.4 ± 0.5	$6.9^{+0.6}_{-0.4}$	$2.7^{+0.3}_{-0.4}$
highecut	fold$_E$ (keV)	7.7	8.8	8.6
xillver	Γ	-	2.6 (fixed)	2.6 (fixed)
xillver	Norm ($\times 10^{-6}$)	15 ± 1	84^{+7}_{-4}	8.4 ± 0.3
xillver	Fe/Solar	1 (frozen)	2.8 ± 0.1	$4.0^{+0.3}_{-0.1}$
xillver	Ar, Ca Abund	$1.8^{+0.2}_{-0.3}$	= abund Fe	1 (frozen)
xillver	log ξ (erg cm s^{-1})	$3.13^{+0.01}_{-0.03}$	3.50 ± 0.01	3.20 ± 0.01
	Total $\chi^2_{\rm red}$ (dof)	1.26 (1576)	1.38 (1576)	1.24 (1579)

Notes. The model is const*phabs*rdblur*edge*(bbody+nthcomp+highecut*xillver). The fold energy is fixed at 2.7 times the electron temperature given by the nthcomp component. The outer radius is frozen at 3500 Rg. The photon index Γ of the nthComp component is fixed at 2.6, and the high-energy cutoff at 0.1 keV.

Table 6.2: Comparison of the three versions of xillver, applied to the XMM-Newton data of 4U 1705-44 in the soft state. The model is the same as the one used in the first part: phabs*rdblur*edge*(bbody+nthcomp+highecut*xillver). We report only the values relative to the edge, the χ^2 associated, and the χ^2 when we delete the edge from the model. We also compute the F-test in order to check whether the addition of the edge is statistically significant.

Table	**edge** E (keV)	**edge max** τ ($\times 10^{-2}$)	χ^2/ **d.o.f.** with edge	χ^2/ **d.o.f.** without edge	F-test
Ar, Ca	8.6 ± 0.1	9 ± 0.1	$503/415$	$656/417$	1×10^{-24}
Ar, Ca, Fe	8.6 ± 0.1	9 ± 0.1	$565/414$	$665/416$	2×10^{-15}
Fe	9.1 ± 0.1	4 ± 0.1	$618/415$	$644/417$	2×10^{-4}

somehow unphysical. This had important consequences on the ionization balance calculations, and thus on the final predicted spectrum. In the reflionx model, the incident power law is cut at ~ 100 eV to avoid this issue. The new xillver models take this modification into account and contain the latest version of the atomic database (the newest XSTAR version). Moreover, the energy has been extended to 1 MeV (as in reflionx). The old and new versions of xillver, referred as versions 1 and 2, are shown in Fig 6.6.

The new xillver tables are currently re-calculated. For the moment, the abundances of S, Ar, Ca and Fe are all grouped in a single parameter, since producing a table in which the Ar and Ca abundance varies independently of the Fe abundance wouldl take too much time. Until now, we do not obtain a better fit compared to the previous xillver tables applying this new table to the XMM-Newton data of 4U 1705-44. The Ca line (at ~ 3.9 keV) does not seem to be well fitted and they are still some residuals at the Ar and Fe line energies (see Fig 6.7).

Interestingly, the S line seems to be well taken into account. We note that the abundance of S, Ar, Ca and Fe tends to reach the maximal value authorized ($\sim 9-10$) and the inclination of the system with respect to the line of sight becomes very similar to that obtained with reflionx (about $39° \pm 2$). However, by constraining the abundance parameter to be between 1 and 5 (to be physically possible), its value is found to be at $4.1^{+0.5}_{-1}$, but the inclination increases: $i = 65°^{+7}_{-2}$. The associated ionization parameter is $\xi = 3.5^{+0.1}_{-0.3}$. The edge is found to be at $8.8^{+0.2}_{-0.3}$ and the blackbody temperature at 0.43 ± 0.03 keV. The other parameters are fully consistent with the reflionx model. The total $\chi^2_{\rm red}$ is $596/414 = 1.44$. When we delete the iron absorption edge at ~ 8.8 keV the $\chi^2_{\rm red}$ slightly increases ($607/416 = 1.46$), and the F-test $= 2 \times 10^{-2}$ indicates that the edge is not statistically required in the model. Consequently, the iron absorption edge seems to be quite well fitted with this xillver table, although several problems appear still present in this table model, as shown by the mismatches still visible with respect to the reflionx model. We note that

the two models are very similar, the only differences are the presence of Ar and Ca emission lines and the intrinsic energy resolution.

6.3 Conclusions

The X-ray spectral analysis of 4U 1705-44 has allowed us to show an overabundance of Ar, Ca, and Fe with reflionx and xillver, with a higher factor for Fe ($2.5^{+0.4}_{-0.5}$ against $1.8^{+0.2}_{-0.3}$ for Ar and Ca). This statement seems to be confirmed by the tests we performed on new xillver tables, where these three elements were forced to have the same abundance. The overabundance is estimated at 2.8 ± 0.1, but some features are still visible in the residuals corresponding to the S, Ar, and Ca line energies. Another test performed when only the Fe abundance is free to vary whereas the Ar and Ca abundances are fixed with the solar abundances, shows that the S, Ar, and Ca lines are still apparent in the residuals. As a consequence, it would be interesting to test new tables where the abundance of these elements are independently treated, to see if the fit is improved.

At present, xillver uses a new treatment of the illumination of the disk that should be more similar than reflionx. The first results obtained from the new tables are inconclusive. Nonetheless, some features in the residuals at the Ca line energy seem to indicate that the line is not correctly fitted. By contrast, the Fe edge is well taken into account.

New tables are currently tested for variable photon index Γ and Fe abundance, and for fixed $\Gamma = 2.6$ and where the abundances of S, Si, Ar, Ca and Fe are grouped to form a single variable parameter. We are also trying to combine different tables, however, the ionization parameter in all these fits is too large ($\log(\xi) > 3$). For those values, the gas is too ionized and thus all the lines from low Z elements, like the ones we are looking for, get diminished a lot. For example, in the case of the Ca line, a much sensitive value will be around $\log(\xi) \sim 2.8$, where the line is more intense.

Therefore, separating the Fe abundance with the S, Ar, and Ca abundance and leaving the spectral photon index free to vary would probably improve the fit. It should then be interesting to see whether the Ca line is better fitted when its abundance is independent of A and Ar.

Furthermore, the ionization parameter is considered as a constant parameter in the current reflection models. However, this parameter should vary with the radius of the accretion disk, the ionization being more important at a smaller distance from the compact object.
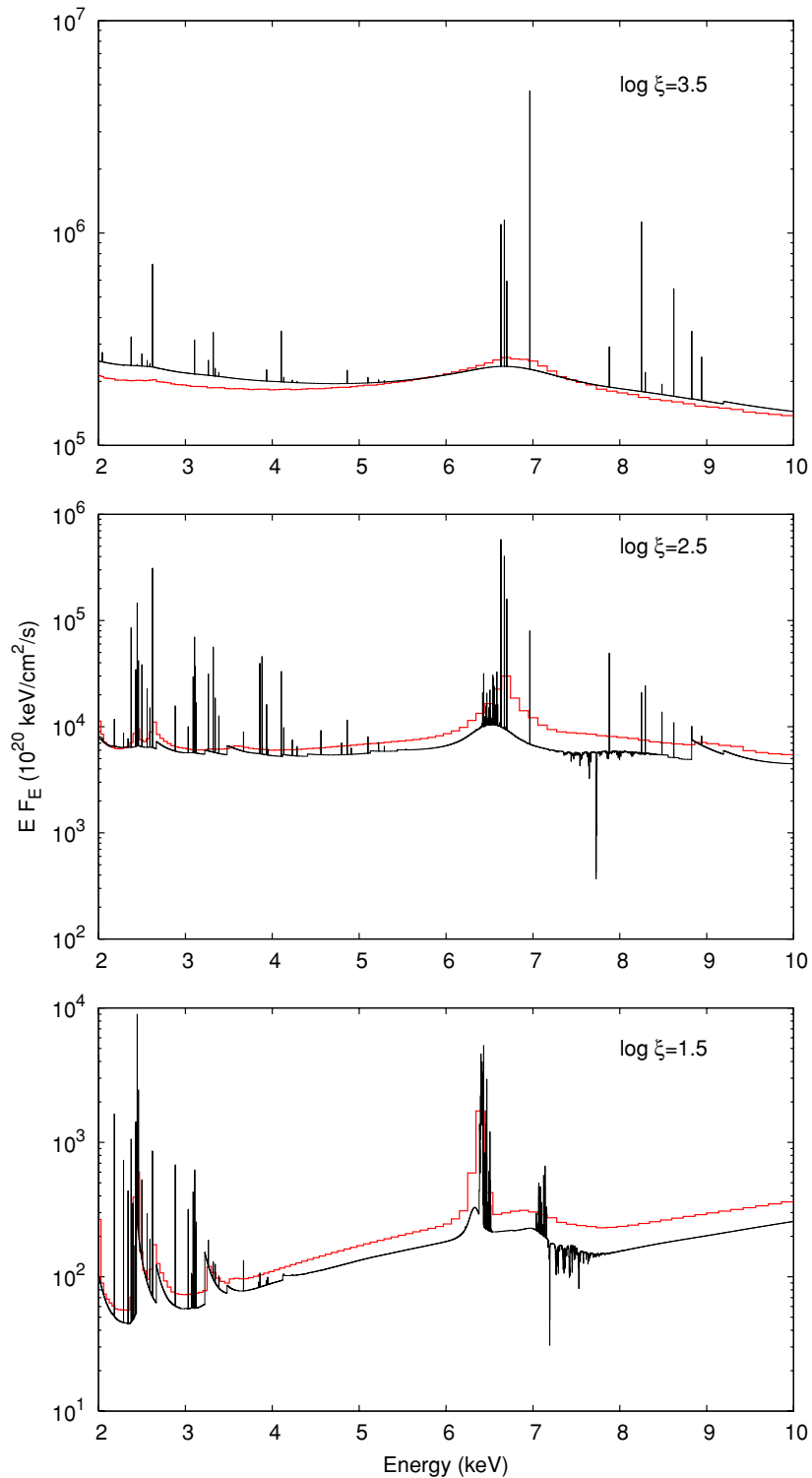
Figure 6.1: Comparison of xillver (black) and reflionx (red) using the same input parameters, for three different ionization parameters [Garcia 2010]. The prominent emission lines appearing on these spectra are identified on Fig 6.2.
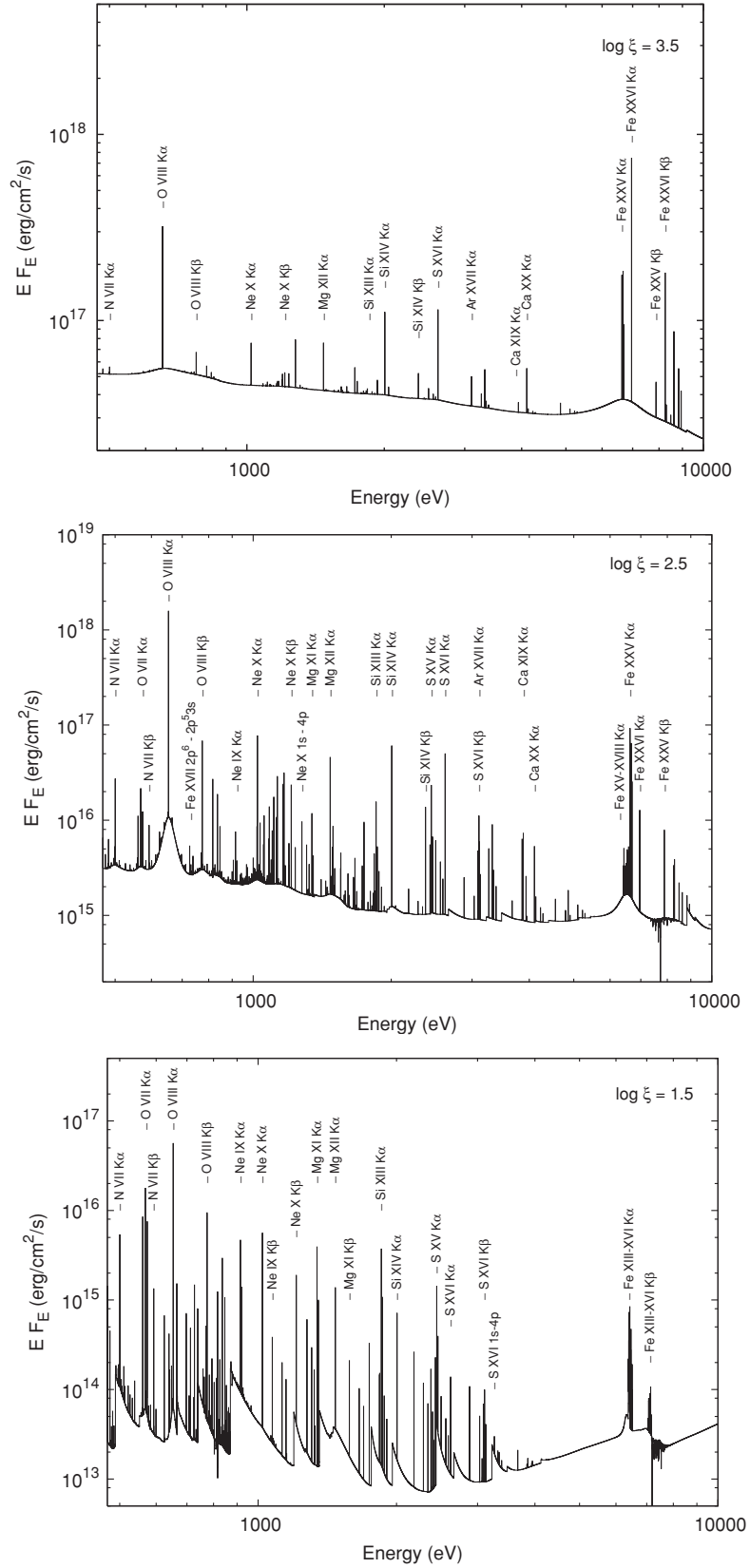
Figure 6.2: Comparison of xillver reflected spectra for three different ionization parameters [Garcia 2010].
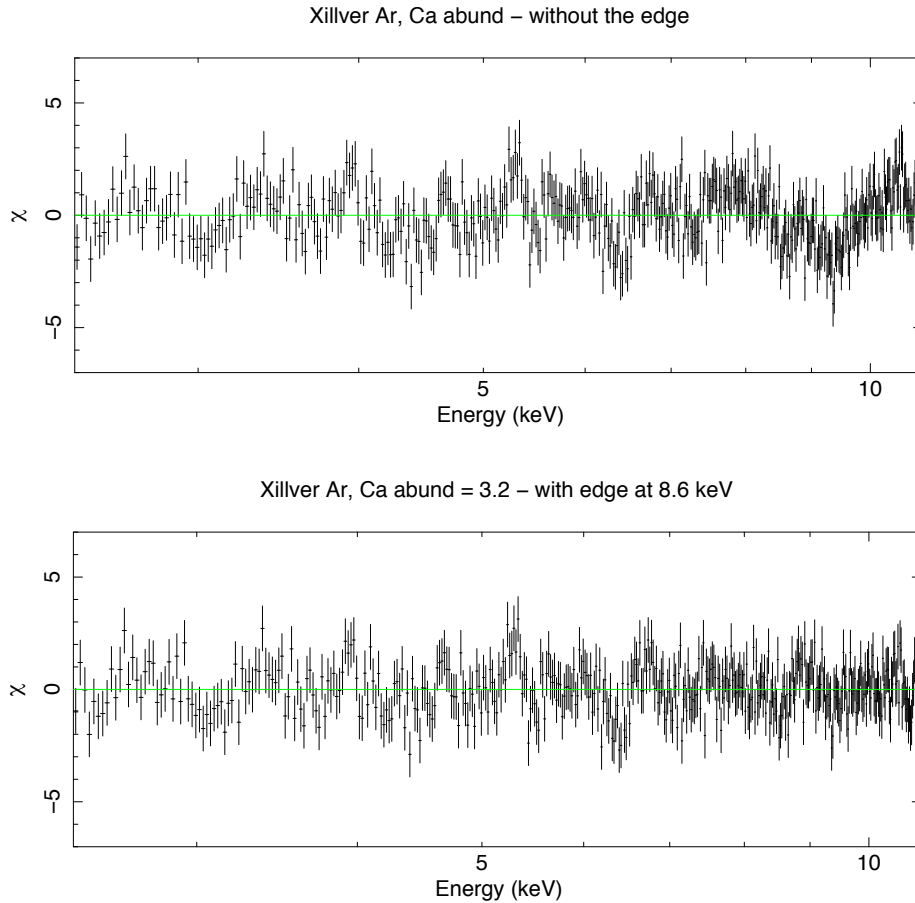
Figure 6.3: Comparison of the residuals, with and without an additional edge, when the Ar and Ca abundances form a same parameter free to vary, whereas the Fe abundance is set to 1. The Ar and Ca overabundance is $\sim 3.2 \pm 0.3$, the inclination is 40 ± 1, and the χ^2_{red} is 1.21 (415) when the edge is added (lower panel).

Xillver Ar, Ca, Fe abund – without the edge

Xillver Ar, Ca, Fe abund = 3 – with edge at 8.6 keV
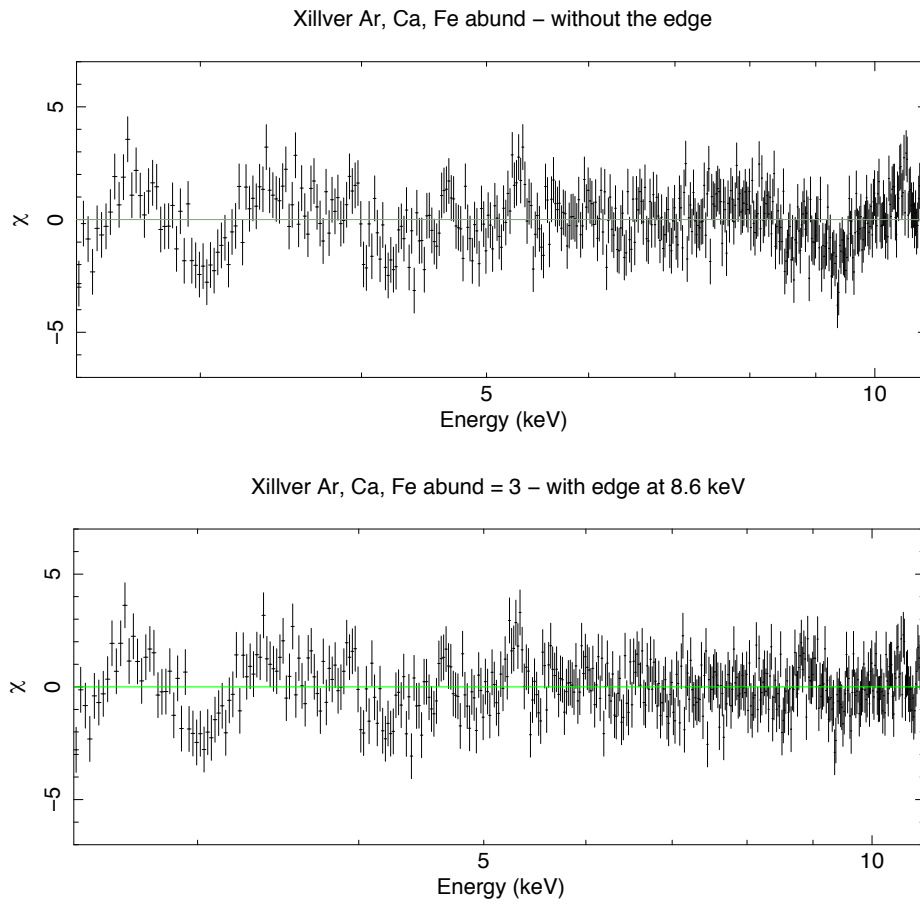
Figure 6.4: Comparison of the residuals, with and without an additional edge, when the Ar, Ca, and Fe abundances formed a single parameter. This parameter is found at $\sim 3^{-3}_{-0.8}$, $i = 37 \pm 1$, and χ^2_{red} is 1.36 (414) when the edge is added (lower panel).

Xillver Fe abund – without the edge

Xillver Fe abund = 3.4 – with edge at 9.1 keV
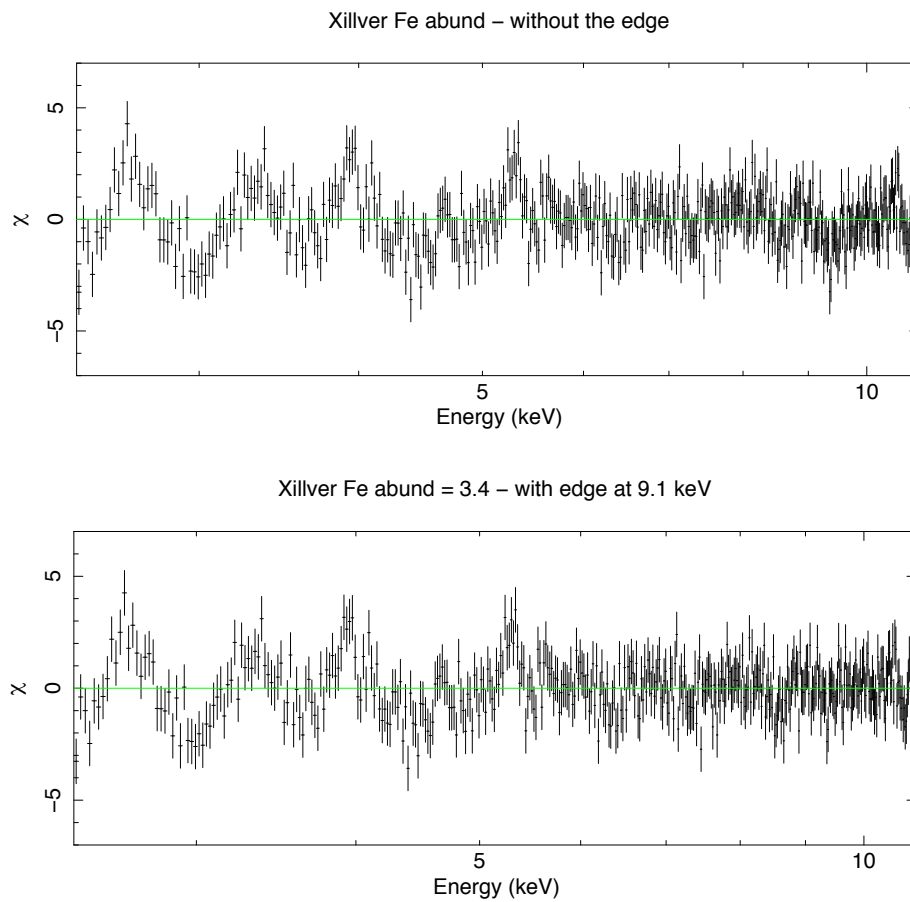
Figure 6.5: Comparison of the residuals, with and without an additional edge, when the Fe abundance can vary whereas the Ar and Ca abundances are fixed to 1. The Fe is detected with an overabundance of a factor of $\sim 3.4^{+0.7}_{-1}$, $i = 22 \pm 1$, and χ^2_{red} is 1.49 (415) when the edge is added (lower panel).
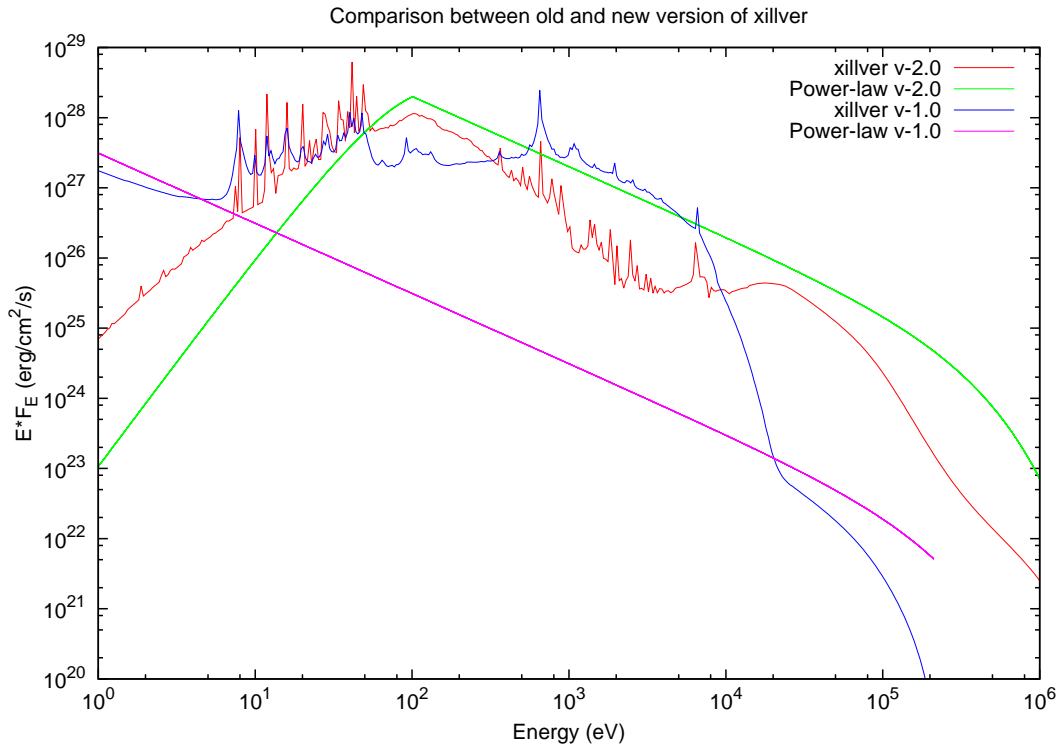
Figure 6.6: Comparison of the previous version of xillver (v-1.0) with the new one (v-2.0), which includes a new treatment of the illumination of the disk (appearing in green on the figure). Figure from J. Garcia.
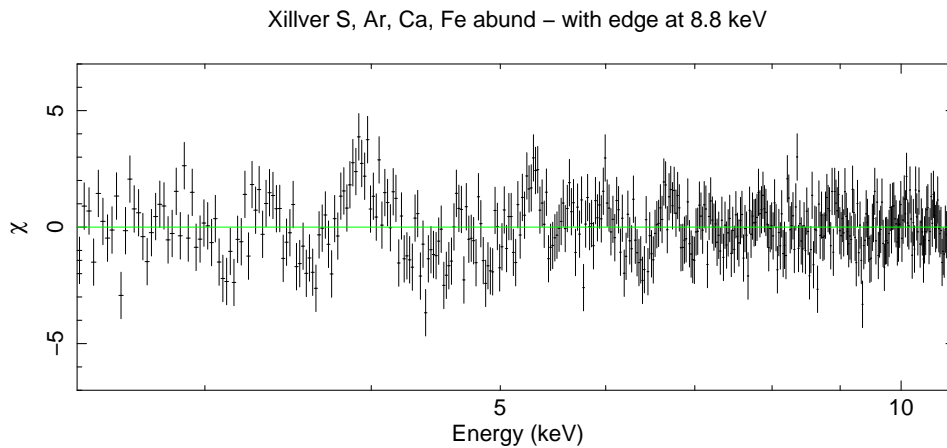
Figure 6.7: Residuals with the edge in the XMM/EPIC-pn data, including the new treatment of the illumination of the disk. The Ca line at 3.9 keV is not correctly fitted.

Part III

Conclusion

General conclusions

Contents

This chapter is devoted to the conclusions drawn from the work performed on the two neutron star LMXBs studied, and more generally on the differences and similarities between neutron star LMXBs and black hole X-ray binaries, deduced by X-ray spectral analysis.

7.1 Conclusions on the sources studied

The aim of my PhD was to perform a spectral comparison of neutron star LMXBs with the better-known black hole binaries, specifically by studying the reflection component in neutron star LMXBs. The observation of the two atoll sources MXB 1728-34 and 4U 1705-44 with different X-ray telescopes allowed me to investigate the inner parts of the accretion disk and to obtain interesting results about the nature and the origin of the iron line, for which a debate is still on-going, and more generally concerning the reflection component. Also, I inferred physical and geometrical information on the systems when the sources were in different states, such as the inner radius of the disk, the inclination angle of the system, the state of ionization of the disk, and the electron temperature forming the corona.

By performing the spectral analysis of the XMM-Newton data of MXB 1728-34, I showed that the Fe Kα line is broad and asymmetric, contrary to a previous analysis performed on part of these data by [Ng 2010]. Different reasons can explain this divergence: a) the previous analysis was done using only the EPIC-pn data, whereas I used these data in addition to the MOS1, MOS2, RGS1, and RGS2 data in order to better constrain the models; b) different models were used to fit the continuum and the Fe line. I carefully compared the different applied models, which are all consistent with a relativistically smeared Fe line. These models give first estimates of the inclination of the system: $44° < i < 60°$, and the inner radius of the accretion disk: $25 < R_{in} < 100$ km from the neutron star center, assuming the neutron star mass to be 1.4 M$_\odot$.

The second neutron star LMXB I studied is the well-known X-ray burster 4U 1705-44. The main objectives of this study were: a) to study the pile-up effects

on the iron line detected with the XMM-Newton/EPIC-pn; b) to fit the reflection features with a self-consistent reflection model in order to prove their common origin; and c) to study the changes in the spectral parameters when the source was in two distinct states, the so-called soft and hard states.

For this purpose, I selected a sample of data in both states by using XMM-Newton, BeppoSAX, and RXTE observations, so as to cover a high-energy range from 0.1 to 200 keV and to have a high-spectral resolution close to the iron line energy. This last point is important, since a well-determined profile of the iron line constitutes a fantastic tool for inferring information on the inner part of the accretion disk, like the ionization state of matter in the disk, the estimate of the inner radius of the disk, or the inclination angle of the system with respect to the line of sight.

I first studied with caution the effects that pile-up could have on the Fe line and more generally on the XMM-EPIC/pn spectrum when the source was in the soft state. I showed that the iron line profile is robust even with the presence of a small fraction of pile-up, while the continuum may vary more significantly. The broad Fe Kα line detected at 6.7 keV, associated with highly ionized Fe XXV, is consistent with produced in the inner part of the accretion disk, where Doppler and mildly relativistic effects relatively close to the compact object participate in the distortions of its profile. Other emission lines are detected at lower energy, corresponding to S XVI, Ar XVIII, and Ca XIX, in addition to iron absorption edges. All of these components are well fitted with self-consistent reflection models, which supports their common origin in the inner parts of the accretion disk, via the process of X-ray reflection of the power-law continuum illuminating the cold gas. An overabundance of Fe and possibly Ar and Ca is highlighted. Work on the reflection model xillver is still in progress to improve the fit.

In the hard state, the Fe emission line detected at $\sim$ 6.4 keV is related to a low ionized Fe fluorescence line. The line does not present any clear asymmetry anymore. Furthermore, a Compton hump which peaks at $\sim$ 30 keV is visible in the BeppoSAX data and is well fitted with the reflection models. The spectra from XMM-Newton, BeppoSAX, and RXTE were then simultaneously fitted with the same reflection models as those used in the soft state, in order to allow a direct comparison of the parameters.

The source 4U 1705-44 shows clear changes in the spectral parameters when the source resides in the hard and in the soft state. These changes concern mainly the ionization parameter, the energy of the Fe Kα line, the power-law photon index Γ, the electron temperature of the corona, and the inner radius of the accretion disk. The scenario proposed for black hole X-ray binaries seems relevant also in the case of this system: the disk would be truncated at a larger distance from the compact object in the hard state. When the source moves to the soft state, the mass accretion rate increases, and the inner radius of the disk approaches closer to the neutron star surface. The disk becomes hotter and more ionized, which has direct consequences on the temperature of the corona, since the soft photons from the disk are very efficient in cooling the electrons. It would be interesting to perform a similar study

on other neutron star LMXBs to see if this scenario is valid for all of these systems.

To conclude, the study of the two neutron star LMXBs shows that their spectra are very similar to those of black hole X-ray binaries, in particular the reflection component. Moreover, it shows that the deformations of the iron line profile, and so the fact that the Fe line is relativistic, strongly depends on the state of the source. The Fe Kα line present in the MXB 1728-34 data, when the source was in an intermediate state, shows a slightly asymmetric profile. The Fe line in 4U 1705-44 is clearly asymmetric in the soft state, whereas it is not asymmetric anymore in the hard state. Two main hypotheses can explain this: a) depending on the state in which the source resides (soft or hard state), the accretion disk approaches more or less the compact object, thus the deformations of the line profile from the neutron star are more or less strong; b) when the source is in the hard state, fewer photons are received on the X-ray detectors of the telescopes because the source is less bright. In this case, since the statistics is lower, the line profile seems symmetric and the relativistic nature of the line is more difficult to prove since the models are not very well constrained.

Whereas the relativistic nature of the Fe line seems clear when a source is observed in the soft state, where the accretion disk approaches the compact object, hence where relativistic effects are stronger, the mystery of the (a)symmetric Fe Kα line in the hard state will probably be solved with the next generation of X-ray satellites which will offer a higher effective area to collect more photons and a higher energy resolution. Moreover, it will likely be possible to detect clearly and independently the asymmetry of the other emission lines at lower energy. This would constitute the ultimate proof that all of these components are produced with the same reflection processes in the inner parts of the accretion disk. Last but not least, it is of crucial importance to continue the development and improvement of full, self-consistent reflection models, including all of the emission lines with different abundance parameters for each elements, so as to better reproduce the data with more precision.

7.2 Comparison between NS LMXBs and BHXBs

This section is devoted to a more general conclusion on the comparison between neutron star LMXBs and black hole X-ray binaries, based on their X-ray spectral properties. This comparison aims to answer the following question: is it possible to identify the nature of the compact object from the X-ray spectral analysis?

A common way to determine whether the compact object is a black hole or a neutron star is based on the determination of the dynamical mass; for a mass $M > 3M_\odot$, the accreting object is believed to be a black hole. However, the optical counterpart has to be visible in order to calculate the mass function. In many X-ray binaries, it is impossible to get this information, therefore other methods seek to answer it. Spectral and timing analyses are expected to show unequivocal signatures of these systems. Until now, only a few characteristics have been found. The major

signature revealed by timing analysis is the presence of twin kHz QPOs in 26 neutron star LMXBs. What about the spectral analysis? Are there any differences between black hole and neutron star X-ray binaries?

Depending on the type of neutron star (atoll or Z-source), the magnetic field does not have the same intensity, which has direct consequences on the accretion flow. Atoll-type neutron star LMXBs share many X-ray spectral and timing properties with black hole X-ray binaries. Because of the low magnetic field of the neutron star in such systems, the accretion disk approaches very close to the neutron star surface, hence the accretion flow is expected to be very similar to that of black hole binaries. Furthermore, these systems exhibit similar luminosities when the sources are in the soft state (corresponding to the banana branch of the atoll color-color diagram) and hard state (island state of the atoll source).

Two dominant components are generally observed in the spectra of these systems, whose relative strengths vary according to the state of the source. One is a power law characterized with a photon index ranging from ~ 1.5 to ~ 2.5, which dominates the high-energy part of the spectrum ($E > 10$ keV). The other component is approximately described by a blackbody, with a photon temperature of $kT_{\rm bb} < 1$ keV. In addition, a reflection component is often detected and allows one to investigate the structure and the properties of the innermost part of the accretion disk. To this date, reflection spectra have been found to be extremely similar in these systems; a small difference resides in the Fe Kα line profile, whose distorsions are stronger in the case of black hole accreting systems, especially in fast-rotating ones.

Therefore, the similar configuration in these sources, with apparently identical processes involved, leads to very similar spectra. Such tight analogies complicate the identification of the compact object with the spectral analysis. However, there is a major difference between these systems, due to the fact that a neutron star has a solid surface. A direct consequence is the emission of type I X-ray bursts, which corresponds to thermonuclear flashes when a sufficient amount of matter is accreted on the neutron star surface. These have never been observed in black hole binaries, favoring the evidence for an event horizon in such systems. Furthermore, the presence of the neutron surface is expected to have some effects on the X-ray spectra of neutron star LMXBs. It provides an important source of seed photons, in addition to those coming from the boundary layer (located between the accretion disk and the neutron star) and from the disk, to cool the corona of high energy electrons. This explains why the corona in neutron star LMXBs is, in most cases, less hot than in black hole binaries. These observed differences may help to show that the accreting object is a black hole or a neutron star, in particular in the soft state. The new generation of X-ray observatories will probably help to infer more differences in these systems.

We note that another important difference between systems hosting a black hole or an old neutron star is due to the presence of a magnetic field in a neutron star. If strong enough, the magnetic field can affect the accretion flow because of interaction with the neutron star magnetosphere. Coherent pulsations, which are signals resulting from the dipolar magnetic fields anchored in neutron stars, may be

observed and give another criterium to show the presence of a neutron star.

Many questions still remain unanswered about these mysterious X-ray accreting systems, in particular about the origin of the state transitions, the geometry of the corona/accretion disk, and the behavior of the accretion flow close to the compact object. Is the accretion disk truncated in the hard state? By which processes? Additionally, multiwavelength studies of these sources reveal the presence of radio jets in some systems, in particular in black hole accreting systems (the so-called microquasars). What is the role of jets? How are they formed? Some jets have also been detected in a few neutron star accreting systems. Why do we observe jets in a small fraction of neutron star LMXBs compared to black hole binaries? Why is the radio luminosity of atoll sources much lower than Z-sources and black hole binaries? The jet emission could simply be weaker in the case of a neutron star. The understanding of accretion/ejection processes and the role of magnetic field is very important in this context.

Future work

Contents

The end of my PhD marks the beginning of new research projects, which I began in November 2012 as a post-doctoral fellow at the Observatory of Cagliari, with Alberto Pellizzoni. My current research is mainly focused on the X-ray spectral analysis of the double pulsar system PSR J0737-3039, as observed with XMM-Newton. In parallel, I am pursuing tests for the xillver model with Javier Garcia, and the study of the iron line in other neutron star LMXBs such as 4U 1735-44. Moreover, I will perform work in collaboration with Sera Markoff (University of Amsterdam) and Marion Cadolle Bel (ESAC, Madrid) on the multi-wavelength spectral study of black hole binary systems. In the following, I present a brief description of these projects.

8.1 X-ray analysis of the double pulsar

Nowadays, six double-neutron-star binaries have been detected. They provide wonderful laboratories for the study of relativistic gravity, gravitational radiation, equations of state, but they are also fantastic systems for the understanding of evolutionary scenarios of binary systems. Among these rare objects, an amazing system was recently discovered: the double radio pulsar PSR J0737-3039 [Burgay 2003, Lyne 2004]. The properties of these two neutron stars (such as their masses, spin periods, etc) are being constrained with unprecedented precision [Kramer 2008].

High-energy observations of such a system are very interesting to study the physics of the magnetospheric emission and dissipative shocks in the close environment of the two neutron stars [Pellizzoni 2008]. I am currently working on the PSR J0737-3039 data obtained with XMM-Newton.

8.2   Tests on the xillver model

I continue to test new xillver tables in order to try to perfectly fit the reflection features in 4U 1705-44. I am mainly focused on the S, Ar, Ca, and Fe abundances, to understand if vaying the different elements independently can improve the fit.

Moreover, I would like to apply this reflection model to the data of other neutron star LMXB systems, where different emission lines were detected, in order to compare the abundances of the different elements. For instance, GX 3+1 would be a very interesting candidate, since an XMM-Newton observation shows the presence of a relativistically smeared Fe line at $\sim 6 - 7$ keV, in addition to Ar XVIII and Ca XIX lines. We note that this source is surprisingly similar to 4U 1705-44; the inclination of the system is estimated at $35° < i < 44°$, and the inner radius of the disk was inferred at 25 R_g [Piraino 2012].

8.3   Proposal on 4U 1735-44

I wrote a Suzaku proposal on the neutron star LMXB 4U 1735-44, which was accepted as priority C in 2012. For the time being, the observation has not yet been performed. It will be done if there is enough time remaining on the X-ray telescope after having observed the sources accepted as priority A and B.

The idea behind this proposal is to study the iron line and possibly other reflection features, such as the S, Ar and Ca lines, and either a Compton reflection hump at $20-40$ keV or a hard tail at energies above 25 keV depending on the state of the source, using the broad-band capabilities of Suzaku. This will allow us to increase the sample of broad, relativistically smeared iron lines in neutron star X-ray binaries, and to prove the common origin of all these reflection features.

8.4   Multiwavelength spectral study of BHXBs

Black hole X-ray binaries (BHXBs) show a strong correlation between the radio and X-ray fluxes during the hard state, which takes the form of $F_{\rm rad} \propto F_X^b$, where $b \sim 0.5 - 0.7$ [Coriat 2011]. This is interpreted as evidence that the compact jets are strongly connected with the accretion disk and/or corona, and that a dominant fraction of the X-ray spectrum of the hard state is due to optically thin synchrotron emission from the jet base [Markoff 2003, Corbel 2003, Rodriguez 2008]. A similar correlation exists for neutron star X-ray binaries, but with a steeper correlation coefficient ($b \sim 1.4$) than that seen in black holes [Migliari 2006].

Recently, an increasing number of outliers lying well outside the scatter was identified. Therefore, two distinct tracks seem to reflect different accretion regimes within the hard state [Gallo 2012]. I will perform a spectral analysis of black hole X-ray binaries data obtained simultaneously in radio, IR, and X-rays. The aim is to see whether a spectral analysis can help us understand what is really changing in the physics of these objects.

List of refereed and non refereed publications

A.1   Refereed publications

- **Egron E.**, Di Salvo T., Motta S., Burderi L., Papitto A., Duro R., D'Aí A., Riggio A., Belloni T., Iaria R., Robba N.R., Piraino S., Santangelo A., *Testing reflection features in 4U 1705-44 with XMM-Newton, BeppoSAX, and RXTE in the hard and soft state*, A&A, 550, A5, eprint `arXiv:1211.2933` (2013)

- Papitto A., D'Aí A., Di Salvo T., **Egron E.**, Bozzo E., Burderi L., Iaria R., Riggio A., Menna M.T., *The accretion flow to the intermittent accreting millisecond pulsar, HETE J1900.1-2455, as observed by XMM-Newton and RXTE*, MNRAS, eprint `arXiv:1212.2532` (2013)

- Riggio A., Burderi L., Di Salvo T., Papitto A., **Egron E.**, Belloni T., D'Aí A., Iaria R., Floris M., Motta S., Testa V. and Menna M.T., *Sub-arcsecond location of IGR J17480-2446 with Rossi XTE*, ApJ, 754, L11, eprint `arXiv:1206.4878` (2012)

- Piraino S., Santangelo A., Kaaret P., Mück B., D'Aí A., Di Salvo T., Iaria R., Robba N.R., Burderi L., and **Egron E.**, *A Relativistic Iron Emission Line from the Neutron Star Low-Mass X-Ray Binary GX 3+1*, A&A, 542, L27, eprint `arXiv:1205.3348` (2012)

- D'Aí A., Bozzo E., Papitto A., Iaria R., Di Salvo T., Burderi L., Riggio A., **Egron E.**, and Robba N.R., *A complete X-ray spectral coverage of the 2010 May-June outbursts of Circinus X-1*, A&A, 543, A20, eprint `arXiv:1204.2464` (2012)

- **Egron E.**, Di Salvo T., Burderi L., Papitto A., Barragan L., Dauser T., Wilms J., D'Aí A., Riggio A., Iaria R., and Robba N.R., *Spectroscopy of MXB 1728-34 with XMM-Newton*, A&A, 530, A99, eprint `arXiv:1104.0566` (2011)

A.2   Non-refereed publications

Papers appearing in proceeding of conferences:

- **Egron E.**, Di Salvo T., Motta S., Burderi L., *Testing reflection features in 4U 1705-44 with XMM-Newton, RXTE, and BeppoSAX*, Proceedings of Science, Conference "An INTEGRAL view of the high-energy sky", Paris, France, $15 - 19$ October 2012

- Papitto A., Di Salvo T., D'Ai A., Burderi L., Iaria R., **Egron E.**, Riggio A., *Broad iron lines from accreting millisecond pulsars*, 39th COSPAR Scientific Assembly, p.1443, Mysore, India, $14 - 22$ July 2012

- **Egron E.**, Di Salvo T., Motta S., Burderi L., *Self-consistent study of the reflection component in 4U 1705-44 with XMM-Newton, BeppoSAX and RXTE in the hard and soft state*, Proceedings of Science, Extreme sky 2011, Chia Laguna, Italy, $19 - 23$ September 2011

- **Egron E.**, Di Salvo T., Burderi L., Papitto A., Barragan L., Dauser T., Wilms J., D'Aí A., Riggio A., Iaria R., and Robba N.R., *Detection of a relativistic iron line in MXB 1728-34*, Proceeding of SF2A 2011, pp. 567-572, Paris, France, $20 - 23$ June 2011

- **Egron E.**, Di Salvo T., Burderi L., Papitto A., Barragan L., Dauser T., Wilms J., D'Aí A., Riggio A., *X-ray Spectroscopy of MXB 1728-34 with XMM-Newton*, The X-ray Universe 2011, Presentations of the Conference held in Berlin, Germany, $27 - 30$ June 2011. Available online at: http://xmm.esac.esa.int/external/xmm_science/workshops/2011symposium/, article id.065"

Posters presented during conferences:

- **Egron E.**, et al., *Testing reflection features in 4U 1705-44 with XMM-Newton, RXTE, and BeppoSAX*, Conference "An INTEGRAL view of the high-energy sky", Paris, France, $15 - 19$ October 2012

- **Egron E.**, et al., *Study of the reflection component in 4U 1705-44 with XMM-Newton, RXTE, and BeppoSAX*, Conference "IAU XXVIII General Assembly", Beijing, China, $20 - 31$ August 2012

- **Egron E.**, et al., *X-ray Spectroscopy of MXB 1728-34 with XMM-Newton*, Conference "High Energy View of Accreting Objects : AGN and X-ray Binaries", Agios Nikolaos, Crete, Greece, $5 - 14$ October 2010

Papers as co-author

A brief description of the papers for which I am co-author.

B.1 The accretion flow to the intermittent accreting ms pulsar, HETE J1900.1-2455, as observed by XMM-Newton and RXTE

Papitto A., D'Aí A., Di Salvo T., Egron E., Bozzo E., Burderi L., Iaria R., Riggio A., Menna M.T. 2013, MNRAS

We present a study of the accretion flow to the intermittent accreting millisecond pulsar, HETE J1900.1-2455, based on observations performed simultaneously by XMM-Newton and RXTE. The $0.33 - 50$ keV energy spectrum is described by a hard Comptonised component originated in an optically thin $\tau \sim 1$ environment, by a soft thermal $kT_{\rm in} \sim 0.2$ keV component, interpreted as accretion disc emission, and by disc reflection of the hard component. Two emission features are detected at energies of $0.98(1)$ and $6.58(7)$ keV, respectively. The latter is identified as Kα transition of Fe XXIII-XXV, while origin of the former is less certain. A simultaneous detection in EPIC-pn, EPIC-MOS2, and RGS spectra favours an astrophysical origin, and energy of the feature suggests a Fe-Lα line and/or helium-like Ne-Kα line. Broadness of these features, $\tau/E \sim 0.1$, is compatible with reflection in an accretion disc extending down to $R = 25^{+16}_{-11}$ gravitational radii from the compact object. Pulsations at the known 377.3 Hz spin frequency could not be detected, with an upper limit of 0.4 per cent at 3-σ confidence level on the pulsed fractional amplitude. We interpret the inner disc radius estimated from spectral modelling as an indication of a disc accretion flow truncated by some mechanism connected to the overall evolution of the accretion disc, rather than by the neutron star magnetic field. This is compatible with the extremely close similarity of spectral and temporal properties of this source with respect to other, non pulsing atoll sources in the hard state.

B.2 Sub-arcsecond location of IGR J17480-2446 with Rossi XTE

Riggio A., Burderi L., Di Salvo T., Papitto A., Egron E., Belloni T., D'Aí A., Iaria R., Floris M., Motta S., Testa V. and Menna M. T. 2012, ApJ, 754, L11.

On 2010 October 13, the X-ray astronomical satellite Rossi XTE, during the observation of the newly discovered AXP IGR J17480-2446, detected a lunar occultation of the source. From knowledge of lunar topography and Earth, Moon, and spacecraft ephemeris at the epoch of the event, we determined the source position with an accuracy of 40 Milliarcseconds (1σ c.l.), which is astonishing, given the very poor imaging capabilities of RXTE (~ 1 degree). For the first time, using a non-imaging X-ray observatory, the position of an X-ray source with a sub-arcsecond accuracy is derived, demonstrating the amazing capabilities of a technique that can be fruitfully applied to current and future X-ray missions.

B.3   A relativistic iron emission line from the neutron star low-mass X-ray binary GX 3+1

Piraino S., Santangelo A., Kaaret P., Muck B., D'Aí A., Di Salvo T., Iaria R., Robba N. R., Burderi L., and Egron E. 2012, A&A, 542, L27.

We present the results of a spectroscopic study of the Fe Kα emission of the persistent neutron-star atoll low-mass X-ray binary and type I X-ray burster GX 3+1 with the EPIC-PN on board XMM-Newton. The source shows a flux modulation over several years and we observed it during its fainter phase, which corresponds to an X-ray luminosity of $L_X \sim 10^{37}$ ergs s^{-1}. When fitted with a two-component model, the X-ray spectrum shows broad residuals at $\sim 6 - 7$ keV that can be ascribed to an iron Kα fluorescence line. In addition, lower energy features are observed at ~ 3.3 keV, ~ 3.9 keV and might originate from Ar XVIII and Ca XIX. The broad iron line feature is well fitted with a relativistically smeared profile. This result is robust against possible systematics caused by instrumental pile-up effects. Assuming that the line is produced by reflection from the inner accretion disk, we infer an inner disk radius of $25\,R_g$ and a disk inclination of $35° < i < 44°$.

B.4   A complete X-ray spectral coverage of the 2010 May-June outbursts of Circinus X-1.

D'Aí A., Bozzo E., Papitto A., Iaria R., Di Salvo T., Burderi L., Riggio A., Egron E., and Robba N.R. 2012, A&A, 543, A20.

Circinus X-1 is a neutron star accreting X-ray binary in a wide, eccentric, orbit. After two years of relatively low X-ray luminosity, Circinus X-1 went into outburst in May 2010, reaching 0.4 Crab flux. This outburst lasted for about two orbital cycles and was followed by another, shorter and fainter outburst in June. We focus here on the broadband X-ray spectral evolution of the source as

it spans about three order of magnitudes in flux. We aim at giving a description that relates luminosity, spectral shape, local absorption, and orbital phase. We use multiple Rossi-XTE/PCA ($3.0 - 25$ keV), Swift/XRT ($1.0 - 9.0$ keV) and a 20 ks long Chandra/HETGS observation ($1.0 - 9.0$ keV), to comprehensively track the spectral evolution of the source during all the outbursting phases. PCA data mostly cover the major outburst, XRT data cover the declining phase of the major outburst and all the phases of the minor outburst, Chandra data give an essential snapshot at the end of this overall outbursting phase. The X-ray spectrum can satisfactorily be described by a thermal Comptonization model with variable neutral local absorption in all the phases of the outburst. No other additive component is statistically required. The first outburst has a clear linear decay, showing a knee as the source flux goes below 5×10^{-10} erg cm^{-2} s^{-1}. At the same time, the source shows a clear spectral state transition from an optically thick to an optically thin state. While the characteristics of the first, bright, outburst can be interpreted within the disk-instability scenario, the following, minor, outburst shows peculiarities that cannot be easily reconciled in this framework.

Tables: spectroscopy

C.1 Fluorescent emission lines

Table C.1: Fluorescent emission lines (in keV), from [Krause 1979].

Element	Kα_1	Kα_2	Kβ_1	Lα	Lβ
C	0.277				
N	0.3924				
O	0.5249				
Ne	0.8486	0.8486			
Na	1.0410	1.0410	1.0711		
Mg	1.2536	1.2536	1.3022		
Al	1.4867	1.4863	1.5575		
Si	1.7400	1.7394	1.8359		
S	2.3078	2.3066	2.4640		
Ar	2.9577	2.9556	3.1905		
Ca	3.6917	3.6881	4.0127	0.3413	
Fe	6.4038	6.3908	6.4905	0.6374	0.6488
Ni	7.4782	7.4609	8.2647	0.8515	0.8588

C.2 He-like and H-like lines

Table C.2: Helium-like R, I_2, I_1, F lines (in keV) from [Drake 1988]. "R" refers to resonance line, "I" to intercombination lines and "F" to forbidden lines.

Spectral line	R	I_2	I_1	F
C V	0.3079	0.3044	0.3044	0.2990
N VI	0.4307	0.4263	0.4264	0.4198
O VII	0.5739	0.5687	0.5686	0.5610
Ne IX	0.9220	0.9150	0.9148	0.9051
Na X	1.1268	1.1190	1.1187	1.1078
Mg XI	1.3522	1.3435	1.3431	1.3311
Al XII	1.5983	1.5888	1.5881	1.5750
Si XIII	1.8650	1.8547	1.8538	1.8395
S XV	2.4606	2.4488	2.4471	2.4303
Ar XVII	3.1396	3.1262	3.1238	3.1043
Ca XIX	3.9025	3.8879	3.8830	3.8612
Fe XXV	6.7000	6.6823	6.6676	6.6365
Ni XXVII	7.8053	7.7865	7.7660	7.7316

Table C.3: H-like Lyα lines (in keV) from [Johnson 1985] and Lyβ lines (in keV) from [Erickson 1977]

Spectral line	Lyα_1	Lyα_2	Lyβ_1	Lyβ_2
C VI	0.3675	0.3675	0.436	0.436
N VII	0.5004	0.5002	0.593	0.593
O VIII	0.6537	0.6535	0.775	0.775
Ne X	1.0220	1.0215	1.211	1.211
Na XI	1.2370	1.2363	1.466	1.465
Mg XII	1.4726	1.4717	1.745	1.745
Al XIII	1.7290	1.7277	2.036	2.036
Si XIV	2.0061	2.0043	2.377	2.376
S XVI	2.6227	2.6197	3.107	3.106
Ar XVIII	3.3230	3.3182	3.936	3.934
Ca XX	4.1075	4.1001	4.864	4.862
Fe XXVI	6.9732	6.9520	8.252	8.246
Ni XXVIII	8.1017	8.0731	9.586	9.577

Bibliography

[Abbassi 2008] S. Abbassi, J. Ghanbari and S. Najjar. *The effects of thermal conduction on the ADAF with a toroidal magnetic field.* MNRAS, vol. 388, pages 663–668, August 2008. (Cited on page 33.)

[Abramowicz 1995] M. A. Abramowicz, X. Chen, S. Kato, J. P. Lasota and O. Regev. *Thermal equilibria of accretion disks.* ApJ, vol. 438, pages L37–L39, January 1995. (Cited on page 33.)

[Abramowicz 1998] M. A. Abramowicz, I. V. Igumenshchev and J. P. Lasota. *A note on the conditions for SSD-ADAF transitions.* MNRAS, vol. 293, page 443, February 1998. (Cited on page 33.)

[Anders 1989] E. Anders and N. Grevesse. *Abundances of the elements - Meteoritic and solar.* Geochimica Cosmochimica Acta, vol. 53, pages 197–214, January 1989. (Cited on page 88.)

[Arnaud 1996] K. A. Arnaud. *XSPEC: The first ten years.* in ASP Conf. Ser. 101: Astronomical Data Analysis Software and Systems V, page 17, 1996. (Cited on page 77.)

[Arnaud 2011] K. Arnaud, R. Smith and A. Siemiginowska. Handbook of X-ray Astronomy. Cambridge Observing Handbooks for Research Astronomers, November 2011. (Cited on pages 45, 63 and 78.)

[Arnett 1996] D. Arnett. Supernovae and Nucleosynthesis: An Investigation of the History of Matter from the Big Bang to the Present. Princeton University Press, 1996. (Cited on page 13.)

[Baade 1934] W. Baade and F. Zwicky. *Remarks on Super-Novae and Cosmic Rays.* Physical Review, vol. 46, pages 76–77, 1934. (Cited on page 13.)

[Backer 1982] D. C. Backer, S. R. Kulkarni, C. Heiles, M. M. Davis and W. M. Goss. *A millisecond pulsar.* Nature, vol. 300, pages 615–618, December 1982. (Cited on page 14.)

[Balbus 1991] S. A. Balbus and J. F. Hawley. *A powerful local shear instability in weakly magnetized disks. I - Linear analysis. II - Nonlinear evolution.* ApJ, vol. 376, pages 214–233, July 1991. (Cited on page 31.)

[Balbus 1998] S. A. Balbus and J. F. Hawley. *Instability, turbulence, and enhanced transport in accretion disks.* Reviews of Modern Physics, vol. 70, pages 1–53, January 1998. (Cited on page 33.)

[Balucinska-Church 1992] M. Balucinska-Church and D. McCammon. *Photoelectric absorption cross sections with variable abundances.* ApJ, vol. 400, pages L699–L700, December 1992. (Cited on page 88.)

[Bambynek 1972] W. Bambynek, B. Crasemann, R. W. Fink, H. U. Freund, H. Mark, C. D. Swift, R. E. Price and P. V. Rao. *X-Ray Fluorescence Yields, Auger, and Coster-Kronig Transition Probabilities.* Review of Modern Physics, vol. 44, pages 716–813, 1972. (Cited on page 44.)

[Barret 2002] D. Barret and J. F. Olive. *A Peculiar Spectral State Transition of 4U 1705-44: When an Atoll Looks Like a Z.* ApJ, vol. 576, page 391, September 2002. (Cited on pages 104 and 120.)

[Belloni 2005] T. Belloni. *Black Hole States: Accretion and Jet Ejection.* Procs. Interacting Binaries Meeting, Cefalu, Italy, 2005. (Cited on page 53.)

[Belloni 2010] T. Belloni. *States and transitions in black hole binaries.* The Jet Paradigm - From Microquasars to Quasars, 2010. (Cited on page 52.)

[Bhattacharya 1991] D. Bhattacharya and E. P. J. van den Heuvel. *Formation and evolution of binary and millisecond radio pulsars.* Physics Reports, vol. 203, pages 1–124, 1991. (Cited on page 13.)

[Blandford 1999] R. D. Blandford and M. C. Begelman. *On the fate of gas accreting at a low rate on to a black hole.* MNRAS, vol. 303, pages L1–L5, February 1999. (Cited on page 33.)

[Bolton 1972] C. T. Bolton. *Identification of Cygnus X-1 with HDE 226868.* Nature, vol. 235, pages 271–273, February 1972. (Cited on page 20.)

[Box 1987] G. E. P. Box and R. D. Norman. *Empirical Model-Building and Response Surfaces.* Wiley Series in Probability and Statistics, 1987. (Cited on page 78.)

[Bradt 2008] H. Bradt. *Astrophysics Processes.* Cambridge, 2008. (Cited on page 35.)

[Brown 1994] G. E. Brown and H. A. Bethe. *A Scenario for a Large Number of Low-Mass Black Holes in the Galaxy.* ApJ, vol. 423, page 659, March 1994. (Cited on page 20.)

[Burgay 2003] M. Burgay, N. D'Amico, A. Possenti, R. N. Manchester, A. G. Lyne, B. C. Joshi, M. A. McLaughlin, M. Kramer, J. M. Sarkissian, F. Camilo, V. Kalogera, C. Kim and D. R. Lorimer. *An increased estimate of the merger rate of double neutron stars from observations of a highly relativistic system.* Nature, vol. 426, pages 531–533, December 2003. (Cited on pages 11, 14 and 165.)

[Cackett 2010] E. M. Cackett, J. M. Miller, D. R. Ballantyne, D. Barret, S. Bhattacharyya, M. Boutelier, M. C. Miller, T. E. Strohmayer and R. Wijnands. *Relativistic Lines and Reflection from the Inner Accretion Disks Around Neutron Stars.* ApJ, vol. 720, pages L205–L225, September 2010. (Cited on pages 85, 87, 118 and 119.)

[Cackett 2012] E. M. Cackett, J. M. Miller, R. C. Reis, A. C. Fabian and D. Barret. *A Comparison of Broad Iron Emission Lines in Archival Data of Neutron Star Low-mass X-Ray Binaries.* ApJ, vol. 755, page 27, August 2012. (Cited on page 118.)

[Camenzind 2007] M. Camenzind. Compact objects in astrophysics : white dwarfs, neutron stars, and black holes. Astronomy and astrophysics library, Springer-Verlag Berlin Heidelberg, 2007. (Cited on page 16.)

[Casella 2004] P. Casella, T. Belloni, J. Homan and L. Stella. *A study of the low-frequency quasi-periodic oscillations in the X-ray light curves of the black hole candidate XTE J1859+226.* A&A, vol. 426, pages 587–600, November 2004. (Cited on page 53.)

[Casella 2005] P. Casella, Belloni T. and L. Stella. *The ABC of Low-Frequency Quasi-periodic Oscillations in Black Hole Candidates: Analogies with Z Sources.* ApJ, vol. 629, pages 403–407, August 2005. (Cited on page 53.)

[Chen 1995] X. Chen, M. A. Abramowicz, J. P. Lasota, R. Narayan and I. Yi. *Unified description of accretion flows around black holes.* ApJ, vol. 443, pages L61–L64, April 1995. (Cited on page 33.)

[Corbel 2003] S. Corbel, Nowak M. A., R. P. Fender, A. K. Tzioumis and S. Markoff. *Radio/X-ray correlation in the low/hard state of GX 339-4.* A&A, vol. 400, pages 1007–1012, March 2003. (Cited on pages 52 and 166.)

[Coriat 2011] M. Coriat, S. Corbel, L. Prat, J. C. A. Miller-Jones, D. Cseh, A. K. Tzioumis, C. Brocksopp, J. Rodriguez, R. P. Fender and G. R. Sivakoff. *Radio/X-ray correlation in the low/hard state of GX 339-4.* MNRAS, vol. 414, pages 677–690, June 2011. (Cited on page 166.)

[D'Aì 2009] A. D'Aì, R. Iaria, T. Di Salvo, G. Matt and N. R. Robba. *Disk Reflection Signatures in the Spectrum of the Bright Z-Source GX 340+0.* ApJ, vol. 693, pages L1–L5, March 2009. (Cited on page 114.)

[D'Aì 2010] A. D'Aì, T. Di Salvo, D. Ballantyne, R. Iaria, N. R. Robba, A. Papitto, A. Riggio, L. Burderi, S. Piraino, A. Santangelo, M. Matt G.and DovÄiak and V. Karas. *A self-consistent approach to the hard and soft states of 4U 1705-44.* A&A, vol. 516, page id.A36, June 2010. (Cited on pages 104, 108, 111, 112 and 119.)

[Dauser 2010] T. Dauser, J. Wilms, C. S. Reynolds and L. W. Brenneman. *Broad emission lines for a negatively spinning black hole.* MNRAS, vol. 409, pages 1534–1540, December 2010. (Cited on page 91.)

[den Herder 2001] J. W. den Herder, A. C. Brinkman, S. M. Kahn, G. Branduardi-Raymont, K. Thomsen, H. Aarts, M. Audard, J. V. Bixler, A. J. den Boggende, J. Cottam, T. Decker, L. Dubbeldam, C. Erd, H. Goulooze, M. GÃ¼del, P. Guttridge, C. J. Hailey, K. Al Janabi, J. S. Kaastra, P. A. J. de Korte, B. J. van Leeuwen, C. Mauche, A. J. McCalden, R. Mewe, A. Naber, F. B. Paerels, J. R. Peterson, A. P. Rasmussen, K. Rees, I. Sakelliou, M. Sako, J. Spodek, M. Stern, T. Tamura, J. Tandy, C. P. de Vries, S. Welch and A. Zehnder. *The Reflection Grating Spectrometer on board XMM-Newton.* A&A, vol. 365, pages L7–L17, January 2001. (Cited on page 75.)

[Di Salvo 2005] T. Di Salvo, R. Iaria, M. Mendez, L. Burderi, G. Lavagetto, L. Robba N. R.; Stella and M. van der Klis. *A Broad Iron Line in the Chandra High Energy Transmission Grating Spectrum of 4U 1705-44.* ApJ, vol. 623, page L121, April 2005. (Cited on page 104.)

[Di Salvo 2009] T. Di Salvo, A. D'Aì, R. Iaria, L. Burderi, M. DovÄiak, V. Karas, G. Matt, A. Papitto, S. Piraino, A. Riggio, N. R. Robba and A. Santangelo. *A relativistically smeared spectrum in the neutron star X-ray binary 4U 1705-44: looking at the inner accretion disc with X-ray spectroscopy.* MNRAS, vol. 398, pages 2022–2027, October 2009. (Cited on pages 104, 108, 111, 112 and 119.)

[Done 2007] C. Done, M. Gierlinski and A. Kubota. *Modelling the behaviour of accretion flows in X-ray binaries. Everything you always wanted to know about accretion but were afraid to ask.* A&A Review, vol. 15, pages 1–66, December 2007. (Cited on pages 35 and 51.)

[Drake 1988] G. W. Drake. *Theoretical energies for the $n = 1$ and 2 states of the helium isoelectronic sequence up to $Z = 100$.* Canadian Journal of Physics, vol. 66, pages 586–611, July 1988. (Cited on page 174.)

[Egron 2012] E. Egron, T. Di Salvo, S. Motta, L. Burderi, A. Papitto, R. Duro, A. D'Ai, A. Riggio, T. Belloni, R. Iaria, N. R. Robba, S. Piraino and A. Santangelo. *Testing reflection features in 4U 1705-44 with XMM-Newton, BeppoSAX and RXTE in the hard and soft state.* Accepted for publication in A&A, November 2012. (Cited on pages 144 and 145.)

[Erickson 1977] G. W. Erickson. J. Physics Chem. Ref. Data, vol. 6, page 831, 1977. (Cited on page 174.)

[Esin 1996] A. A. Esin, R. Narayan, E. Ostriker and I. Yi. *Hot One-Temperature Accretion Flows around Black Holes.* ApJ, vol. 465, page 312, July 1996. (Cited on page 33.)

[Esin 1997] A. A. Esin, J. E. McClintock and R. Narayan. *Advection-dominated Accretion and the Spectral States of Black Hole X-Ray Binaries: Application to Nova MUSCAE 1991.* ApJ, vol. 489, page 865, November 1997. (Cited on pages 33 and 35.)

[Fabian 1989] A. C. Fabian, M. J. Rees, L. Stella and N. E. White. *X-ray fluorescence from the inner disc in Cygnus X-1.* MNRAS, vol. 238, pages 729–736, May 1989. (Cited on pages 43, 46, 49, 83, 89 and 90.)

[Fabian 2000] A. C. Fabian, K. Iwasawa, C. S. Reynolds and A. J. Young. *Broad Iron Lines in Active Galactic Nuclei.* Astronomical Society of the Pacific, vol. 112, pages 1145–1161, September 2000. (Cited on pages 44, 46, 47 and 48.)

[Fabian 2009] A. C. Fabian, A. Zoghbi, R. R. Ross, P. Uttley, L. C. Gallo, W. N. Brandt, A. J. Blustin, T. Boller, M. D. Caballero-Garcia, J. Larsson, J. M. Miller, G. Miniutti, G. Ponti, R. C. Reis, C. S. Reynolds, Y. Tanaka and A. J. Young. *Broad line emission from iron K- and L-shell transitions in the active galaxy 1H0707-495.* Nature, vol. 459, pages 540–542, May 2009. (Cited on page 83.)

[Fender 2004] R. P. Fender, T. M. Belloni and E. Gallo. *Towards a unified model for black hole X-ray binary jets.* MNRAS, vol. 355, pages 1105–1118, December 2004. (Cited on page 52.)

[Fiocchi 2007] M. Fiocchi, A. Bazzano, Ubertini P. and A. A. Zdziarski. *The First Detection of Compton Reflection in the Low-Mass X-Ray Binary 4U 1705-44 with INTEGRAL and BeppoSax.* ApJ, vol. 657, page 448, March 2007. (Cited on page 104.)

[Ford 1998] E. E. Ford, M. van der Klis and P. Kaaret. *Discovery of Kilohertz Quasi-periodic Oscillations in the Atoll X-Ray Binary 4U 1705-44.* ApJ Letters, vol. 498, page L41, May 1998. (Cited on page 104.)

[Forman 1978] W. Forman, C. Jones, L. Cominsky, P. Julien, G. Murray S.; Peters, H. Tananbaum and R. Giacconi. *The fourth Uhuru catalog of X-ray sources.* ApJ, vol. 38, page 357, December 1978. (Cited on page 104.)

[Frank 1992] J. Frank, A. King and D. Raine. Accretion power in astrophysics. Cambridge University Press, 1992. (Cited on pages 24, 31 and 32.)

[Galeev 1979] A. A. Galeev, R. Rosner and G. S. Vaiana. *Structured coronae of accretion disks.* ApJ, vol. 229, pages 318–326, April 1979. (Cited on pages 34 and 35.)

[Gallo 2003] E. Gallo, R. P. Fender and G. G. Pooley. *A universal radio-X-ray correlation in low/hard state black hole binaries.* MNRAS, vol. 344, pages 60–72, September 2003. (Cited on page 52.)

[Gallo 2012] E. Gallo, B. Miller and R. Fender. *Assessing luminosity correlations via cluster analysis: evidence for dual tracks in the radio/X-ray domain of black hole X-ray binaries.* MNRAS, vol. 423, pages 590–599, June 2012. (Cited on pages 52 and 166.)

[Galloway 2008] D. K. Galloway, M. P. Muno, J. M. Hartman, D. Psaltis and D. Chakrabarty. *Thermonuclear (Type I) X-Ray Bursts Observed by the Rossi X-Ray Timing Explorer.* ApJ, vol. 179, page 360, December 2008. (Cited on page 104.)

[Garcia 2010] J. Garcia and T. R. Kallman. *X-ray Reflected Spectra from Accretion Disk Models. I. Constant Density Atmospheres.* ApJ, vol. 718, page 695, August 2010. (Cited on pages 116, 143, 150 and 151.)

[Ghisellini 2012] G. Ghisellini. *Radiative Processes in High Energy Astrophysics.* 2012. (Cited on page 41.)

[Giacconi 1971] R. Giacconi, H. Gursky, E. M. Kellogg, E. Schreier and H. Tananbaum. *Discovery of Periodic X-Ray Pulsations in Centaurus X-3 from UHURU.* ApJ, vol. 167, page L67, July 1971. (Cited on pages 5 and 14.)

[Giacconi 1972] R. Giacconi, S. Murray, H. Gursky, E. Kellogg, E. Schreier and H. Tananbaum. *The Uhuru catalog of X-ray sources.* ApJ, vol. 178, pages 281–308, December 1972. (Cited on pages 5 and 104.)

[Gierlinski 2002] M. Gierlinski and C. Done. *A comment on the colour-colour diagrams of low-mass X-ray binaries.* MNRAS, vol. 331, pages L47–L50, April 2002. (Cited on page 54.)

[Gilfanov 2010] M. Gilfanov. *X-Ray Emission from Black-Hole Binaries.* The Jet Paradigm, Lecture Notes in Physics, vol. 794, page 17, March 2010. (Cited on page 30.)

[Griffin 1985] R. F. Griffin. The distributions of periods and amplitudes of late-type spectroscopic binaries. Publishing Co., 1985. (Cited on page 5.)

[Haardt 1994] F. Haardt, L. Maraschi and G. Ghisellini. *A model for the X-ray and ultraviolet emission from Seyfert galaxies and galactic black holes.* ApJ, vol. 432, pages L95–L99, September 1994. (Cited on page 35.)

[Haensel 2007] P. Haensel, A. Y. Potekhin and D. G. Yakovlev. NEUTRON STARS 1: Equation of State and Structure. Astrophysics and Space Science Library, 2007. (Cited on page 15.)

[Hameury 1986] J. M. Hameury, A. R. King and J. P. Lasota. *A model for soft X-ray transients.* A&A, vol. 162, pages 71–79, July 1986. (Cited on page 50.)

[Hanke 2011] M. Hanke. *Probing the Environment of Accreting Compact Objects.* PhD thesis, Dr. Karl Remeis-Sternwarte, Astronomisches Institut der Universitat Erlangen-Nurnberg, 2011. (Cited on page 32.)

[Hasinger 1989] G.; Hasinger and M. van der Klis. *Two patterns of correlated X-ray timing and spectral behaviour in low-mass X-ray binaries.* A&A, vol. 225, page 79, November 1989. (Cited on page 53.)

[Hatchett 1976] S. Hatchett, J. Buff and R. McCray. *Transfer of X-rays through a spherically symmetric gas cloud.* ApJ, vol. 206, pages 847–860, June 1976. (Cited on page 45.)

[Heitler 1954] W. Heitler. The Quantum Theory of Radiation. Oxford University Press, 1954. (Cited on page 42.)

[Hellier 2001] C. Hellier. Cataclysmic Variable Stars. Springer, 2001, 2001. (Cited on page 5.)

[Hewish 1968] A. Hewish, S. J. Bell, J. D. H. Pilkington, P. F. Scott and R. A. Collins. *Observation of a Rapidly Pulsating Radio Source.* Nature, vol. 217, pages 709–713, February 1968. (Cited on page 13.)

[Hoffman 1976] J. A. Hoffman, W. H. G. Lewin, J. Doty, D. R. Hearn, G. W. Clark, G. Jernigan and F. K. Li. *Discovery of X-ray bursts from MXB 1728-34.* ApJ Letters, vol. 210, pages L13–L17, November 1976. (Cited on page 81.)

[Homan 2005] J. Homan and T. Belloni. *The evolution of black hole states.* Astrophys. Space, January 2005. (Cited on page 49.)

[Houck 2000] J. C. Houck and L. A. Denicola. *ISIS: An Interactive Spectral Interpretation System for High Resolution X-Ray Spectroscopy.* Astronomical Society of the Pacific, vol. 216, page 591, January 2000. (Cited on page 77.)

[Hulse 1975] R. A. Hulse and J. H. Taylor. *Discovery of a pulsar in a binary system.* ApJ, vol. 195, pages L51–L53, January 1975. (Cited on page 14.)

[Hurkett 2008] C. P. Hurkett, S. Vaughan, J. P. Osborne, P. T. O'Brien, K. L. Page, A. Beardmore, O. Godet, D. N. Burrows, M. Capalbi, P. Evans, N. Gehrels, M. R. Goad, J. E. Hill, J. Kennea, T. Mineo, M. Perri and R. Starling. *Line Searches in Swift X-Ray Spectra.* ApJ, vol. 679, pages L587–L606, May 2008. (Cited on page 94.)

[Iaria 2009] A. Iaria R.and D'Aì, T. Di Salvo, N. R. Robba, A. Riggio, A. Papitto and L. Burderi. *A ionized reflecting skin above the accretion disk of GX 349+2.* A&A, vol. 505, pages 1143–1151, October 2009. (Cited on page 114.)

[Ichimaru 1977] S. Ichimaru. *Bimodal behavior of accretion disks - Theory and application to Cygnus X-1 transitions.* ApJ, vol. 214, pages 840–855, June 1977. (Cited on page 33.)

[Imshennik 1988] V. S. Imshennik and D. K. Nadezhin. *Supernova 1987A and the Emergence of the Blast Wave at the Surface of the Compact Presupernova.* Soviet Astronomy Letters, vol. 14, page 449, December 1988. (Cited on page 13.)

[Imshennik 1992] V. S. Imshennik. *A possible scenario of a supernova explosion as a result of the gravitational collapse of a massive stellar core.* Soviet Astronomy Letters, vol. 18, page 489, June 1992. (Cited on page 16.)

[Jansen 2001] D. Jansen F.and Lumb, B. Altieri, J. Clavel, M. Ehle, C. Erd, C. Gabriel, M. Guainazzi, P. Gondoin, R. Much, R. Munoz, M. Santos, N. Schartel, D. Texier and G. Vacanti. *XMM-Newton observatory. I. The spacecraft and operations.* A&A, vol. 365, pages L1–L6, January 2001. (Cited on page 68.)

[Johnson 1985] W. R. Johnson and G. Soff. Atomic Data Nuclear Data Tables, vol. 33, page 405, 1985. (Cited on page 174.)

[Kaastra 1993] J. S. Kaastra and R. Mewe. *X-ray emission from thin plasmas. I - Multiple Auger ionisation and fluorescence processes for Be to Zn.* A&A Supplememt Series, vol. 97, pages 443–482, January 1993. (Cited on page 45.)

[Kallman 2001] T. Kallman and M. Bautista. *Photoionization and High-Density Gas.* ApJ Supplement Series, vol. 133, pages 221–253, March 2001. (Cited on page 144.)

[Kaper 2006] L. Kaper, A. van der Meer, M. van Kerkwijk and E. van den Heuvel. *Measuring the Masses of Neutron Stars.* The Messenger, vol. 126, pages 27–31, December 2006. (Cited on page 18.)

[Karttunen 2007] H. Karttunen, P. Kruger, H. Oja, M. Poutanen and K. J. Donner. Fundamental Astronomy. Berlin: Springer, 2007. (Cited on page 6.)

[Karzas 1961] W. J. Karzas and R. Latter. *Electron Radiative Transitions in a Coulomb Field.* ApJ Supplement, vol. 6, page 167, May 1961. (Cited on page 42.)

[Kato 1998] S. Kato, J. Fukue and S. Mineshige. Black-Hole Accretion Disks. Kyoto University Press, 1998. (Cited on pages 22 and 33.)

[Kerr 1963] R. P. Kerr. *Gravitational Field of a Spinning Mass as an Example of Algebraically Special Metrics.* Physical Review Letters, vol. 11, pages 237–238, September 1963. (Cited on page 23.)

[Kikoin 1976] I. K. Kikoin. Tables of Physical Quantities. Moscow:Atomizdat, 1976. (Cited on page 45.)

[King 2003] A. King. *Black holes, galaxy formation, and the mass-sigma relation.* ApJ, vol. 596, pages L27–L29, October 2003. (Cited on page 19.)

[Klein 1929] O. Klein and Y. Nishina. Z. Physik, vol. 52, page 853, 1929. (Cited on page 38.)

[Kramer 2008] M. Kramer and I. H. Stairs. *The Double Pulsar*. Annual Review of Astronomy & Astrophysics, vol. 46, pages 541–572, September 2008. (Cited on pages 17 and 165.)

[Krause 1979] M. O. Krause and J. H. Olivier. *Natural widths of atomic K and L levels, Kalpha X-ray lines and several KLL Auger lines*. Journal of Physical and Chemical Reference Data, vol. 8, pages 329–338, April 1979. (Cited on page 173.)

[Landau 1987] L. D. Landau and E. M. Lifshitz. *Course of Theoretical Physics*. Fluid Mechanics 2nd Ed., Pergamon Press, vol. 6, pages 336–343, 1987. (Cited on page 31.)

[Langmeier 1987] A. Langmeier, M. Sztajno, G. Hasinger, J. Truemper and M. Gottwald. *EXOSAT observations of 4U 1705-44 - Type I bursts and persistent emission*. ApJ, vol. 323, page 288, December 1987. (Cited on page 104.)

[Laor 1991] A. Laor. *Line profiles from a disk around a rotating black hole*. ApJ, vol. 376, page 90, July 1991. (Cited on page 88.)

[Lasota 1996] J. P. Lasota, M. A. Abramowicz, X. Chen, J. Krolik, R. Narayan and I. Yi. *Is the Accretion Flow in NGC 4258 Advection Dominated?* ApJ, vol. 462, page 142, May 1996. (Cited on page 33.)

[Lasota 2011] J. P. Lasota, T. Alexander, G. Dubus, D. Barret, S. A. Farrell, N. Gehrels, O. Godet and N. A. Webb. *The Origin of Variability of the Intermediate-mass Black-hole ULX System HLX-1 in ESO 243-49*. ApJ, vol. 735, page 89, July 2011. (Cited on page 20.)

[Lewin 1976] W. H. G. Lewin, G. Clark and J. Doty. *X-Ray Bursts*. IAU Circ. 2922, March 1976. (Cited on page 81.)

[Lewin 1983] W. H. G. Lewin and E. P. J. van den Heuvel. Accretion-driven stellar X-ray sources. Cambridge University Press, 1983. (Cited on page 9.)

[Lewin 1995] W. H. G. Lewin, J. van Paradijs and E. P. J. van den Heuvel. X-ray binaries. Cambridge University Press, 1995. (Cited on page 11.)

[Liang 1977] E. P. T. Liang and R. H. Price. *Accretion disk coronae and Cygnus X-1*. ApJ, November 1977. (Cited on page 34.)

[Lin 2010] D. Lin, R. A. Remillard and J. Homan. *Suzaku and BeppoSAX X-ray Spectra of the Persistently Accreting Neutron-star Binary 4U 1705-44*. ApJ, vol. 719, page 1350, August 2010. (Cited on page 104.)

[Liu 2006] Q. Z. Liu, J. van Paradijs and E. P. J. van den Heuvel. *Catalogue of high-mass X-ray binaries in the Galaxy (4th edition)*. A&A, vol. 455, pages 1165–1168, September 2006. (Cited on page 9.)

[Liu 2007] Q. Z. Liu, J. van Paradijs and E. P. J. van den Heuvel. *A catalogue of low-mass X-ray binaries in the Galaxy, LMC, and SMC (Fourth edition)*. A&A, vol. 469, pages 807–810, July 2007. (Cited on page 7.)

[Longair 2011] M. S. Longair. High Energy Astrophysics. Wiley-Interscience, 2011. (Cited on pages 31 and 35.)

[Lumb 2012] D. H. Lumb, N. Schartel and F. A. Jansen. *XMM-Newton (X-Ray Mulit-Mirror Mission) Observatory*. Opt. Eng. 51, 011009, February 2012. (Cited on page 72.)

[Lynden-Bell 1974] D. Lynden-Bell and J. E. Pringle,. *The evolution of viscous discs and the origin of the nebular variables*. MNRAS, vol. 168, pages 603–637, September 1974. (Cited on page 27.)

[Lyne 2004] A. G. Lyne, M. Burgay, M. Kramer, A. Possenti, R. N. Manchester, F. Camilo, M. A. McLaughlin, D. R. Lorimer, N. D'Amico, B. C. Joshi, J. Reynolds and P. C. C. Freire. *A Double-Pulsar System: A Rare Laboratory for Relativistic Gravity and Plasma Physics*. Science, vol. 303, pages 1153–1157, February 2004. (Cited on pages 11, 14 and 165.)

[Magdziarz 1995] P. Magdziarz and A. A. Zdziarski. *Angle-dependent Compton reflection of X-rays and gamma-rays*. MNRAS, vol. 273, page 837, April 1995. (Cited on page 116.)

[Malzac 1999] J. Malzac. *Modelisation de l'emission X et gamma des objets compacts par des methodes Monte-Carlo*. PhD thesis, Universite Paul Sabatier - Toulouse III, 1999. (Cited on pages 36 and 40.)

[Manmoto 1997] T. Manmoto, S. Mineshige and M. Kusunose. *Spectrum of Optically Thin Advection-dominated Accretion Flow around a Black Hole: Application to Sagittarius A**. ApJ, vol. 489, page 791, November 1997. (Cited on page 33.)

[Markoff 2003] S. Markoff, M. Nowak, S. Corbel, R. Fender and H. Falcke. *Exploring the role of jets in the radio/X-ray correlations of GX 339-4*. A&A, vol. 397, pages 645–658, January 2003. (Cited on page 166.)

[Martocchia 2002] A. Martocchia, G. Matt, V. Karas, T. Belloni and M. Feroci. *Evidence for a relativistic iron line in GRS 1915+105*. A&A, vol. 387, pages 215–221, May 2002. (Cited on pages 83 and 84.)

[Mason 2001] K. O. Mason, A. Breeveld, R. Much, M. Carter, F. A. Cordova, M. S. Cropper, J. Fordham, H. Huckle, C. Ho, H. Kawakami, J. Kennea,

T. Kennedy, J. Mittaz, D. Pandel, W. C. Priedhorsky, T. Sasseen, R. Shirey, P. Smith and J. M. Vreux. *The XMM-Newton optical/UV monitor telescope.* A&A, vol. 365, pages L36–L44, January 2001. (Cited on page 75.)

[Matt 1993] G. Matt, A. C. Fabian and R. R. Ross. *Iron K-alpha lines from X-ray photoionized accretion discs.* MNRAS, vol. 262, pages 179–186, May 1993. (Cited on page 47.)

[Mayer 2007] M. Mayer and J. E. Pringle. *Time-dependent models of two-phase accretion discs around black holes.* MNRAS, vol. 376, pages 435–456, March 2007. (Cited on page 51.)

[McClintock 2006] J. E. McClintock and R. A. Remillard. Compact stellar X-ray sources. Cambridge Astrophysics Series, 2006. (Cited on pages 18, 49 and 52.)

[Mendez 1999] M. Mendez and van der Klis M. *Precise Measurements of the Kilohertz Quasi-periodic Oscillations in 4U 1728-34.* ApJ, vol. 517, pages L51–L54, May 1999. (Cited on page 82.)

[Meyer 2000] F. Meyer, B. F. Liu and E. Meyer-Hofmeister. *Evaporation: The change from accretion via a thin disk to a coronal flow.* A&A, vol. 361, page 175, September 2000. (Cited on page 51.)

[Migliari 2006] S. Migliari and R. P. Fender. *Jets in neutron star X-ray binaries: a comparison with black holes.* MNRAS, vol. 366, pages 79–91, February 2006. (Cited on pages 54 and 166.)

[Mignani 2011] R. P. Mignani. *Optical, ultraviolet, and infrared observations of isolated neutron stars.* Advances in Space Research, vol. 47, pages 1281–1293, April 2011. (Cited on page 14.)

[Miller 1998] M. C. Miller, F. K. Lamb and D. Psaltis. *Sonic-Point Model of Kilohertz Quasi-periodic Brightness Oscillations in Low-Mass X-Ray Binaries.* ApJ, vol. 508, pages 791–830, December 1998. (Cited on page 104.)

[Miller 2002] J. M. Miller, A. C. Fabian, R. Wijnands, R. A. Remillard, P. Wojdowski, N. S. Schulz, T. Di Matteo, H. L. Marshall, C. R. Canizares, D. Pooley and W. H. G. Lewin. *Resolving the Composite Fe Kalpha Emission Line in the Galactic Black Hole Cygnus X-1 with Chandra.* ApJ, vol. 578, pages 348–356, October 2002. (Cited on page 83.)

[Miller 2004a] J. M. Miller, A. C. Fabian and M. C. Miller. *A Comparison of Intermediate-Mass Black Hole Candidate Ultraluminous X-Ray Sources and Stellar-Mass Black Holes.* ApJ, vol. 614, pages L117–L120, November 2004. (Cited on page 19.)

[Miller 2004b] J. M. Miller, A. C. Fabian, C. S. Reynolds, M. A. Nowak, J. Homan, M. J. Freyberg, M. Ehle, T. Belloni, R. Wijnands, M. van der Klis, P. A.

Charles and W. H. G. Lewin. *Evidence of Black Hole Spin in GX 339-4: XMM-Newton/EPIC-pn and RXTE Spectroscopy of the Very High State.* ApJ, vol. 606, pages L131–L134, May 2004. (Cited on page 83.)

[Miller 2010] J. M. Miller, A. D'Aì, M. W. Bautz, S. Bhattacharyya, D. N. Burrows, E. M. Cackett, A. C. Fabian, M. J. Freyberg, F. Haberl, J. Kennea, M. A. Nowak, R. C. Reis, T. E. Strohmayer and M. Tsujimoto. *On Relativistic Disk Spectroscopy in Compact Objects with X-ray CCD Cameras.* ApJ, vol. 724, pages 1441–1455, December 2010. (Cited on page 119.)

[Mineshige 1989] S. Mineshige and J. C. Wheeler. *Disk-instability model for soft-X-ray transients containing black holes.* ApJ, vol. 343, pages 241–253, August 1989. (Cited on page 50.)

[Miniutti 2007] G. Miniutti, A. C. Fabian, N. Anabuki, J. Crummy, Y. Fukazawa, L. Gallo, Y. Haba, K. Hayashida, S. Holt, H. Kunieda, J. Larsson, A. Markowitz, C. Matsumoto, M. Ohno, J. N. Reeves, T. Takahashi, Y. Tanaka, Y. Terashima, K. Torii, Y. Ueda, M. Ushio, S. Watanabe, M. Yamauchi and T. Yaqoob. *Suzaku Observations of the Hard X-Ray Variability of MCG -6-30-15: the Effects of Strong Gravity around a Kerr Black Hole.* Publications of the Astronomical Society of Japan, vol. 59, pages pp.315–325, January 2007. (Cited on page 83.)

[Mirabel 1998] I. F. Mirabel and L. F. Rodriguez. *Microquasars in our Galaxy.* Nature, vol. 392, pages 673–676, April 1998. (Cited on page 22.)

[Morisson 1983] R. Morisson and D. McCammon. ApJ, vol. 270, page 119, 1983. (Cited on page 36.)

[Mukhopadhyay 2012] B. Mukhopadhyay and P. Dutta. *Variation of the gas and radiation content in the sub-Keplerian accretion disk around black holes and its impact to the solutions.* New Astronomy, vol. 17, pages 51–60, February 2012. (Cited on page 25.)

[Nagase 1986] F. Nagase, S. Hayakawa, N. Sato, K. Masai and H. Inoue. *Circumstellar matter in the VELA X-1/HD 77581 system.* Astronomical Society of Japan, vol. 38, pages 547–569, 1986. (Cited on page 9.)

[Nandra 2007] K. Nandra, P. M. O'Neill, I M. George and J. N. Reeves. *An XMM-Newton survey of broad iron lines in Seyfert galaxies.* MNRAS, vol. 382, pages 194–228, November 2007. (Cited on page 83.)

[Narayan 1994] R. Narayan and I. Yi. *Advection-dominated accretion: A self-similar solution.* ApJ, vol. 428, pages L13–L16, June 1994. (Cited on page 33.)

[Narayan 1995a] R. Narayan and I. Yi. *Advection-dominated accretion: Self-similarity and bipolar outflows.* ApJ, vol. 444, pages 231–243, May 1995. (Cited on page 33.)

[Narayan 1995b] R. Narayan and I. Yi. *Advection-dominated Accretion: Underfed Black Holes and Neutron Stars.* ApJ, vol. 452, page 710, October 1995. (Cited on page 33.)

[Narayan 1996] R. Narayan. *Advection-dominated Models of Luminous Accreting Black Holes.* ApJ, vol. 462, page 136, May 1996. (Cited on page 33.)

[Narayan 1998] R. Narayan, R. Mahadevan and E. Quataert. Advection-dominated accretion around black holes. Cambridge University Press, 1998. (Cited on page 33.)

[Ng 2010] C. Ng, M. Diaz Trigo, M. Cadolle Bel and S. Migliari. *A systematic analysis of the broad iron K-alpha line in neutron-star LMXBs with XMM-Newton.* A&A, vol. 522, page A96, November 2010. (Cited on pages 82, 83, 85, 86, 88, 108, 111, 112, 118 and 159.)

[Olive 2003] J. F. Olive, D. Barret and Gierlinski M. *Correlated Timing and Spectral Behavior of 4U 1705-44.* ApJ, vol. 583, page 416, January 2003. (Cited on pages 104, 120 and 121.)

[Pellizzoni 2008] A. Pellizzoni, A. Tiengo, A. De Luca, P. Esposito and S. Mereghetti. *PSR J0737-3039: Interacting Pulsars in X-Rays.* ApJ, vol. 679, pages 664–674, May 2008. (Cited on page 165.)

[Piraino 2007] S. Piraino, A. Santangelo, T. Di Salvo, P. Kaaret, D. Horns, R. Iaria and L. Burderi. *BeppoSAX observation of 4Uâ1705-44: detection of hard X-ray emission in the soft state.* A&A, vol. 471, page L17, August 2007. (Cited on pages 112 and 119.)

[Piraino 2012] S. Piraino, A. Santangelo, P. Kaaret, B. Muck, A. D'Aì, T. Di Salvo, R. Iaria, N. R. Robba, L. Burderi and E. Egron. *A relativistic iron emission line from the neutron star low-mass X-ray binary GX 3+1.* A&A, vol. 542, page L27, June 2012. (Cited on pages 114 and 166.)

[Porquet 2010] D. Porquet, J. Dubau and N. Grosso. *He-like Ions as Practical Astrophysical Plasma Diagnostics: From Stellar Coronae to Active Galactic Nuclei.* Space Science Reviews, vol. 157, pages 103–134, December 2010. (Cited on page 113.)

[Pringle 1972] J. E. Pringle and M. J. Rees. *Accretion Disc Models for Compact X-Ray Sources.* A&A, vol. 21, page 1, October 1972. (Cited on pages 27 and 31.)

[Protassov 2002] R. Protassov, D. A. van Dyk, V. L. Connors A. Kashyap and A. Siemiginowska. *Statistics, Handle with Care: Detecting Multiple Models Components with the Likelihood Ratio Test.* ApJ, vol. 571, pages 545–559, May 2002. (Cited on page 93.)

[Quataert 2000] E. Quataert and A. Gruzinov. *Convection-dominated Accretion Flows*. ApJ, vol. 539, pages 809–814, August 2000. (Cited on page 33.)

[Read 2011] A. M. Read, S. R. Rosen, R. D. Saxton and J. Ramirez. *A new comprehensive 2D model of the point spread functions of the XMM-Newton EPIC telescopes: spurious source suppression and improved positional accuracy*. A&A, vol. 534, page 13, October 2011. (Cited on page 109.)

[Reig 2011] P. Reig. *Be/X-ray binaries*. Astrophysics and Space Science, vol. 332, pages 1–29, March 2011. (Cited on page 10.)

[Reis 2009a] R. C. Reis, A. C. Fabian, R. R. Ross and J. M. Miller. *Determining the spin of two stellar-mass black holes from disc reflection signatures*. MNRAS, vol. 395, pages L1257–1264, October 2009. (Cited on page 120.)

[Reis 2009b] R. C. Reis, A. C. Fabian and A. J. Young. *Relativistically broadened iron line in the Suzaku observation of the neutron star X-ray binary 4U 1705-44*. MNRAS, vol. 399, page L1, October 2009. (Cited on page 104.)

[Remillard 2006] R. A. Remillard and J. E. McClintock. *X-ray properties of black-hole binaries*. Annual Review of Astronomy and Astrophysics, vol. 44, pages 49–92, September 2006. (Cited on pages 20 and 21.)

[Reynolds 1996] C. S. Reynolds. *X-Ray Emission and Absorption in Active Galaxies*. PhD thesis, University of Cambridge, 1996. (Cited on page 43.)

[Reynolds 2003] C. S. Reynolds and M. A. Nowak. *Fluorescent iron lines as a probe of astrophysical black hole systems*. Physics Reports, vol. 377, page 389, April 2003. (Cited on pages 44 and 46.)

[Roberts 2007] T. P. Roberts. *X-ray observations of ultraluminous X-ray sources*. Astrophysics and Space Science, vol. 311, pages 203–212, October 2007. (Cited on page 19.)

[Rodriguez 2008] J. Rodriguez, S. E. Shaw, D. C. Hannikainen, T. Belloni, S. Corbel, M. Cadolle Bel, J. Chenevez, L. Prat, P. Kretschmar, H. J. Lehto, I. F. Mirabel, A. Paizis, G. Pooley, M. Tagger, P. Varniere, C. Cabanac and O. Vilhu. *2 Years of INTEGRAL Monitoring of GRS 1915+105. II. X-Ray Spectro-Temporal Analysis*. ApJ, vol. 675, pages 1449–1458, March 2008. (Cited on page 166.)

[Ross 2005] R. R. Ross and A. C. Fabian. *A comprehensive range of X-ray ionized-reflection models*. MNRAS, vol. 358, pages 211–216, March 2005. (Cited on pages 91 and 115.)

[Rybicki 1979] G. B. Rybicki and A. P. Lightman. Radiative Processes in Astrophysics. Wiley-Interscience, 1979. (Cited on pages 35, 38 and 39.)

[Salpeter 1964] E. F. Salpeter. *Accretion of Interstellar Matter by Massive Objects.* ApJ, vol. 140, pages 796–800, August 1964. (Cited on page 20.)

[Shadmehri 2005] M. Shadmehri and F. Khajenabi. *Self-similar structure of magnetized radiation-dominated accretion discs.* MNRAS, vol. 361, pages 719–724, August 2005. (Cited on page 33.)

[Shakura 1973] N. I. Shakura and R. A. Sunyaev. *Black holes in binary systems. Observational appearance.* A&A, vol. 24, pages 337–355, January 1973. (Cited on pages 27, 31 and 34.)

[Shapiro 1983] S. L. Shapiro and S. A. Teukolsky. Black Holes, White Dwarfs, and Neutron Stars: The Physics of Compact Objects. Wiley-VCH, 1983. (Cited on pages 15 and 22.)

[Stairs 2004] I. H. Stairs. *Pulsars in Binary Systems: Probing Binary Stellar Evolution and General Relativity.* Science, vol. 304, pages 547–552, April 2004. (Cited on page 18.)

[Stern 1995] B. E. Stern, J. Poutanen, M. Svensson R. Sikora and M. C. Begelman. *On the Geometry of the X-Ray-Emitting Region in Seyfert Galaxies.* ApJ, vol. 449, pages L13–L16, 1995. (Cited on page 34.)

[Storm 1967] E. Storm and H. Israel. Photon Cross Sections from 0.001 to 100 MeV for Elements 1 to 100. Technical Report LA-3753, Los Alamos Scientific Laboratory, 1967. (Cited on page 36.)

[Strohmayer 1996] T. E. Strohmayer, W. Zhang, J. H. Swank, A. Smale, L. Titarchuk, C. Day and U. Lee. *Millisecond X-Ray Variability from an Accreting Neutron Star System.* ApJ Letters, vol. 469, pages L9+, September 1996. (Cited on page 82.)

[Struder 2001] L. Struder, U. Briel, K. Dennerl, R. Hartmann, E. Kendziorra, N. Meidinger, E. Pfeffermann, C. Reppin, B. Aschenbach, W. Bornemann, H. Brauninger, W. Burkert, M. Elender, M. Freyberg, F. Haberl, G. Hartner, F. Heuschmann, H. Hippmann, E. Kastelic, S. Kemmer, G. Kettenring, W. Kink, N. Krause, S. Muller, A. Oppitz, W. Pietsch, M. Popp, P. Predehl, A. Read, K. H. Stephan, D. Stotter, J. Trumper, P. Holl, J. Kemmer, H. Soltau, R. Stotter, U. Weber, U. Weichert, C. von Zanthier, D. Carathanassis, G. Lutz, R. H. Richter, P. Solc, H. Bottcher, M. Kuster, R. Staubert, A. Abbey, A. Holland, M. Turner, M. Balasini, G. F. Bignami, N. La Palombara, G. Villa, W. Buttler, F. Gianini, R. Laine, D. Lumb and P. Dhez. *The European Photon Imaging Camera on XMM-Newton: The pn-CCD camera.* A&A, vol. 365, pages 18–26, January 2001. (Cited on page 72.)

[Tanaka 1995] Y. Tanaka, K. Nandra, A. C. Fabian, H. Inoue, C. Otani, T. Dotani, K. Hayashida, K. Iwasawa, T. Kii, H. Kunieda, F. Makino and M. Matsuoka.

Gravitationally redshifted emission implying an accretion disk and massive black hole in the active galaxy MCG-6-30-15. Nature, vol. 375, pages 659–661, June 1995. (Cited on page 83.)

[Tananbaum 1972] H. Tananbaum, E. M. Gursky H.and Kellogg, R. Levinson, E. Schreier and R. Giacconi. *Discovery of a Periodic Pulsating Binary X-Ray Source in Hercules from UHURU.* ApJ, vol. 174, page L143, June 1972. (Cited on page 5.)

[Timmes 1996] F. X. Timmes, S. E. Woosley and T. A. Weaver. *The Neutron Star and Black Hole Initial Mass Function.* ApJ, vol. 457, page 834, February 1996. (Cited on page 20.)

[Titarchuk 1994] L. Titarchuk. *Generalized Comptonization models and application to the recent high-energy observations.* ApJ, vol. 434, pages L570–L586, October 1994. (Cited on page 88.)

[Turner 2001] M. J. L. Turner, A. Abbey, M. Arnaud, M. Balasini, M. Barbera, E. Belsole, P. J. Bennie, J. P. Bernard, G. F. Bignami, M. Boer, U. Briel, I. Butler, C. Cara, C. Chabaud, R. Cole, A. Collura, M. Conte, A. Cros, M. Denby, P. Dhez, G. Di Coco, J. Dowson, P. Ferrando, S. Ghizzardi, F. Gianotti, C. V. Goodall, L. Gretton, R. G. Griffiths, O. Hainaut, J. F. Hochedez, A. D. Holland, E. Jourdain, E. Kendziorra, A. Lagostina, R. Laine, N. La Palombara, M. Lortholary, D. Lumb, P. Marty, S. Molendi, C. Pigot, E. Poindron, K. A. Pounds, J. N. Reeves, C. Reppin, R. Rothenflug, P. Salvetat, J. L. Sauvageot, D. Schmitt, S. Sembay, A. D. T. Short, J. Spragg, J. Stephen, L. Struder, A. Tiengo, M. Trifoglio, J. Trumper, S. Vercellone, L. Vigroux, G. Villa, M. J. Ward, S. Whitehead and E. Zonca. *The European Photon Imaging Camera on XMM-Newton: The MOS cameras : The MOS cameras.* A&A, vol. 365, pages L27–L35, January 2001. (Cited on page 72.)

[van den Heuvel 1992] E. P. J. van den Heuvel. Proc. Internat. Space Year Conf. ed. T. D. Guyenne & J. J. Hunt (Noorwijk:ESA Publ. Div., ESTEC), 1992. (Cited on page 20.)

[Verbunt 1993] F. Verbunt. *Origin and evolution of X-ray binaries and binary radio pulsars.* Annual review of A&A, vol. 31, pages 93–127, 1993. (Cited on page 6.)

[Warner 1995] B. Warner. Cataclysmic variable stars. Cambrige Univ. Press., 1995. (Cited on page 5.)

[Webster 1972] B. L. Webster and P. Murdin. *Cygnus X-1-a Spectroscopic Binary with a Heavy Companion?* Nature, vol. 235, pages 37–38, January 1972. (Cited on page 20.)

[Wheeler 1968] J. A. Wheeler. *Our Universe: The known and the unknown.* American Scientist, vol. 56, pages 1–20, 1968. (Cited on page 20.)

[White 1982] N. E. White and S. S. Holt. *Accretion disk coronae.* ApJ, vol. 257, pages 318–337, 1982. (Cited on page 34.)

[Wijnands 1999] R. Wijnands and M. van der Klis. *The Broadband Power Spectra of X-Ray Binaries.* ApJ, vol. 514, pages 939–944, April 1999. (Cited on page 51.)

[Wilms 2001] J. Wilms, C. S. Reynolds, M. C. Begelman, J. Reeves, S. Molendi, R. Staubert and E. Kendziorra. *XMM-EPIC observation of MCG-6-30-15: direct evidence for the extraction of energy from a spinning black hole?* MNRAS, vol. 328, pages L27–L31, December 2001. (Cited on page 83.)

[Yan 1998] M. Yan, H. R. Sadeghpour and A. Dalgarno. *Photoionization Cross Sections of He and H 2.* ApJ, vol. 496, page L1044, March 1998. (Cited on page 88.)

[Yuan 2001] F. Yuan. *Luminous hot accretion discs.* MNRAS, vol. 324, pages 119–127, June 2001. (Cited on page 33.)

[Zavlin 2002] V. E Zavlin and G. G. Pavlov. *Modeling Neutron Star Atmospheres.* Proceedings of the 270 WE-Heraeus Seminar on Neutron Stars, Pulsars, and Supernova Remnants, page 263, June 2002. (Cited on page 15.)

[Zdziarski 1996] A. A. Zdziarski, W. N. Johnson and P. Magdziarz. *Broad-band gamma-ray and X-ray spectra of NGC 4151 and their implications for physical processes and geometry.* MNRAS, vol. 283, page 193, November 1996. (Cited on page 115.)

[Zycki 1999] P. T. Zycki, C. Done and D. A. Smith. *The 1989 May outburst of the soft X-ray transient GS 2023+338 (V404 Cyg).* MNRAS, vol. 309, page 561, November 1999. (Cited on page 115.)

Spectral comparisons of neutron star low-mass X-ray binaries with black hole X-ray binaries

Abstract:

The study of high-resolution X-ray spectra of neutron star low-mass X-ray binaries (LMXBs) allows the investigation of the innermost parts of the accretion disk and immediate surroundings of the compact object. The weak magnetic field of old neutron stars present in such systems allows the accretion disk to approach very close to the compact object, like in black hole X-ray binaries.

Using data from X-ray satellites such as XMM-Newton, RXTE, and BeppoSAX, I studied the reflection component in two neutron star LMXBs: MXB 1728-34 and 4U 1735-44. I showed that the iron line at $6.4 - 7$ keV is broad and relativistically smeared, as in black hole binary systems and active galactic nuclei. This is compatible with an interpretation where the line is emitted in the innermost part of the accretion disk. Moreover, I studied the changes in the spectral parameters in 4U 1705-44, in both the hard and soft states of the source. I derived physical and geometrical parameters for the system in both states, such as the state of ionization of the disk, the inner radius of the disk, the inclination angle of the system, and the temperature of the electrons composing the corona.